A NUMERICAL STUDY OF HEAT AND MASS TRANSFER IN POROUS-FLUID COUPLED DOMAINS

CHEN XIAOBING

NATIONAL UNIVERSITY OF SINGAPORE

2009

A NUMERICAL STUDY OF HEAT AND MASS TRANSFER IN POROUS-FLUID COUPLED DOMAINS

CHEN XIAOBING

(***B. Eng., University of Science and Technology of China***)

A THESIS SUBMITTED

FOR THE DEGREE OF DOCTOR OF PHYLOSOPHY

DEPARTMENT OF MECHANICAL ENGINEERING

NATIONAL UNIVERSITY OF SINGAPORE

2009

ACKNOWLEDGEMENTS

I wish to express my deepest gratitude to my Supervisors, Associate Professor Low Hong Tong and Associate Professor S. H. Winoto, for their invaluable guidance, supervision, patience and support throughout the research work. Their suggestions have been invaluable for the project and for the result analysis.

I would like to express my gratitude to the National University of Singapore (NUS) for providing me a Research Scholarship and an opportunity to do my Ph.D study in the Department of Mechanical Engineering. I wish to thank all the staff members and classmates, Sui Yi, Cheng Yongpan, Zheng Jianguo, Shan Yongyuan, Qu Kun, Xia Huanmin and Huang Haibo in the Fluid Mechanics Laboratory, Department of Mechanical Engineering, NUS for their useful discussions and kind assistances. Thanks must also go to Dr. Yu Peng and Dr. Zeng Yan, who helped me overcome many difficulties during the PHD research life.

Finally, I wish to thank my dear parents and brother for their selfless love, support, patience and continued encouragement during the PhD period.

TABLE OF CONTENTS

SUMMARY

The objective of this thesis was to develop a numerical method to couple the flow in porous/fluid domains with a stress jump interfacial condition, and to investigate the effects of porous media on heat and mass transfer. A two-domain method was implemented which was based on finite volume method together with body-fitted grids and multi-block approach. For the fluid part, the governing equation used was Navier-Stokes equation; for the porous medium region, the generalized Darcy-Brinkman-Forchheimer extended model was used. The Ochoa-Tapia and Whitaker's stress jump interfacial condition (1998b) was used with a continuity of normal stress. The thermal or mass interfacial boundary conditions were continuities of temperature/mass and heat/mass flux. Such thermal and mass interfacial conditions have not been combined with stress jump condition in previous studies.

The developed numerical technique was applied to several cases in heat and mass transfer: a) unsteady external flows past a porous square or trapezoidal cylinder, b) natural convective heat-transfer in a porous wavy cavity, c) forced convective heat-transfer after a backward facing step with a porous insert or with a porous floor segment, d) mass transfer in a microchannel reactor with a porous wall. The implementations of the numerical technique are different from those of previous studies which were mainly based on one-domain method with either Darcy's law or Brinkman's equations for the porous medium.

For unsteady flow past a porous square or trapezoidal cylinder, the flow penetrated into the porous bodies; and the resulting flow pattern may be steady or unsteady depending not just on Reynolds number but also on Darcy number. It was

found that the body shape and stress jump parameters can also play an important role for the flow patterns. For natural convection in a porous wavy cavity, the results were shown with a wider range of Rayleigh and Darcy numbers than previous studies; and slightly negative Nusselt numbers were found with small aspect ratio and large waviness values. For forced convection after the backward facing step, heat transfer was enhanced globally with a porous insert or enhanced locally with a porous floor segment. The stress jump parameter effects on heat transfer were more noticeable for the case with the porous floor segment.

The concentration results of the microchannel reactor with a porous wall are found to be well correlated by the use of a reaction-convection distance parameter which incorporates the effects of axial distance, substrate consumption and convection. Another important parameter is the porous Damkohler number (ratio of substrates consumption to diffusion). The reactor efficiency reduces with reaction-convection distance parameter because of reduced reaction (or flux) and smaller local effectiveness factor, due to the lower concentration in Michaelis-Menten type reactions. The reactor is more effective and hence more efficient with smaller porous Damkohler number. When the reaction approaches first-order, increased fluid convection improves the efficiency but it is limited by the diffusion in the fluid region.

The present thesis contributed a numerical implementation for problems involving porous-medium and homogeneous-fluid domains. It can address problems in which the flow and thermal or mass interfacial conditions need to be considered in detail. The technique is also suitable for complex geometries as it implements body-fitted grids and multi-block approach.

NOMENCLATURE

A	discretization coefficients using SIMPLEC method
a	amplitude of wave in a wavy cavity
c	mass concentration, $mol\ m^{-3}$
C	dimensionless mass concentration
C_d , C_D	drag coefficient
C_F	Forchheimer coefficient
C_l , C_L	lift coefficient
D	depth of the porous segment, *m;* mass diffusivity in fluid part, $m^2\ s^{-1}$
Dam	Damkohler number
D_{eff}	effective mass diffusivity in porous part, $m^2\ s^{-1}$
Da	Darcy number
e	the basic number of natural logarithmic function
e_x	unit vector along x-axis
e_y	unit vector along y-axis
F	overall flux
h	porous depth in reactor
H	side length of the square cylinder; height of the channel after the step; the higher height of the trapezoidal cylinder, *m*
K	permeability of porous medium, m^2
K_m	dimensionless Michaelis-Menten constant or substrate concentration at which the SUR is half-maximal
k_m	Michaelis-Menten constant or substrate concentration at which the SUR is half-maximal
k_f	fluid thermal conductivity, $W\ m^{-1}\ K^{-1}$
k_{eff}	effective thermal conductivity of porous media, $W\ m^{-1}\ K^{-1}$

K_m	dimensionless Michaelis-Menten constant or dimensionless substrate concentration at which the SUR is half-maximal
l	integrated length for average Nusselt number, *m*
L	cavity height; length of the porous segment, *m*
Nu	local Nusselt number
Nu_a	average Nusselt number
Nu_{av}	average Nusselt number
n	unit vector along normal direction of the interface
Pr	fluid Prandtl number
$p,\ p_f$	local average and intrinsic average pressure, *Pa*
P, P^*	dimensionless average and intrinsic average pressure
Ra	clear fluid Rayleigh number
Ra^*	Darcy-Rayleigh number (=*Ra Da*)
Re	Reynolds number
R_k	ratio of thermal conductivity in porous and fluid regions
S	surface vector; source term
T	fluid temperature; dimensionless time
T_c	temperature of cold wavy-wall (left), *K*
T_h	temperature of the hot wavy -wall (right), *K*
T_0	characteristic temperature of porous medium $=T_C$, *K*
T_w	temperature of bottom wall
T_∞	temperature of the incoming flow
t	unit vector along tangential direction to the interface, time
U	incoming flow velocity
U_∞	dimensionless incoming flow velocity
u, v	velocity components along x- and y- axes, respectively
V_m	the maximal substrate uptake rate (SUR) per cell, $mol\ s^{-1}$

W	average width of cavity
x, y	Cartesian coordinates

Greek symbols

α	thermal diffusivity, $m^2\ s^{-1}$
β	stress jump parameter related to viscous effect; coefficient of volumetric thermal expansion
β_1	stress jump parameter related to inertia effect
ε	porosity
ε_c	convergence error
ξ	concentration flux reaction parameter
κ	effective distance parameter
γ	kinematic viscosity, $m^2\ s^{-1}$; the cell volume density, m^{-3}
λ	surface waviness in a wavy cavity
μ	dynamic viscosity, $N\ s\ m^{-2}$
λ	interpolation factor
ρ	fluid density, $kg\ m^{-3}$
ϕ	heat flux jump
φ	general dependent variable
$\Delta\Omega$	finite volume of the control cell

Subscripts

av	average value
bot	bottom line in reactor
B	buoyancy source term
D	Darcy term
e	east
eff	effective value for porous media

F	Forchheimer term
f	fluid
fluid	fluid part
i, j	grid node number in x and y directions
in	inlet
int	interface line in reactor
interface	interface value
l	east, west, north, and south point of control volume
n	north
w	west
p	control volume center point; porous part
porous	porous part
ref	reference
s	south
t	tangential direction to the interface

Superscripts

*	non-dimensional quantities
c	convection effect
d	diffusion effect
m	iteration time step
n	iteration step for each time level
-	average value

List of Figures

List of Tables

Chapter 1

Introduction

There have been wide applications for natural and manufactured porous materials in engineering processes, including heat sinks, mechanical energy absorbers, catalytic reactors, heat exchangers, high breaking capacity fuse, cores of nuclear reactors and grain storage. Due to its relatively low permeability and high conductivity, the addition of porous media can help to improve the flow structure, increase or decrease heat transfer. Besides, porous culture medium is also usually used as cell growing environment in bioreactors. Experiments and numerical simulations for flow and transport phenomena in porous media have been attempted since Darcy in the 19th century. Considering the wide applications for porous media, numerical research on heat and mass transfer in porous media, and in porous/fluid coupled domains with complex geometries has been conducted in current work.

This chapter will give a general review of porous media applications, the numerical model development for the flow in porous media, and different interface treatments along the porous/fluid interface. Previous work on the flow around porous bodies, natural and forced heat convection in porous and porous/fluid coupled domains, mass transfer in reactors with porous media will also be reviewed.

1.1 Background

1.1.1 Flow around Porous Bodies

Porous media usually mean materials consisting of a solid matrix with an interconnected void. The interconnection of the void (the pores) allows the flow of one or more fluids through the materials. Examples in nature are beach sand, sandstone, limestone, rye bread, wood and human lung.

Flow past porous bodies occurs in many practical applications and is important in different environmental issues. Examples are the nuclear biological chemical filters allowing flow through a porous cylinder, seepage from streams bounded by porous banks, displacement of oil from sandstones by shalewater influx, and leakage into aquifers.

1.1.2 Heat Transport in Porous Media

Porous materials are used for home and industrial thermal insulation in natural convection system due to their great flow resistance. Natural convection in porous media enclosure has many engineering applications, such as drying process, electronic cooling, ceramic processing, and overland flow during rainfall. In thermal insulation engineering, an appreciable insulating effect is derived by placing porous material in the gap between the cavity walls, and in multishield structures of nuclear reactors between the pressure vessel and the reactor.

In forced convection system, artificial porous materials, e. g. metallic foams with high conductivity, are usually used for heat fins in electronic cooling devices. For forced convection, there have been several studies on the use of porous materials (Vafai, 2001; Kiwan, S. and AI-Nimr, 2001; Bhattacharya and Mahajan, 2002) in order to obtain heat transfer enhancement for convective flow in a duct. Huang and Vafai (1994a) studied flow in a two-dimensional duct with porous blocks placed intermittently on the floor, and in a later study (Huang and Vafai, 1994b) they added porous cavities in the floor between the blocks. The heat transfer was found to be enhanced by the recirculation flows caused by the blocks or the cavities. Fu et al. (1996) continued the study with a porous block placed on one wall.

1.1.3 Mass Transport in Reactors with Porous Media

Porous silicon carrier matrices in micro enzyme reactors are widely used in enzyme coupling for their high surface area for biochemical engineering application. This characteristic can help to avoid lack of long-term stability and yield high reaction effectiveness and improve catalytic efficiency. Optimization of the porous silicon matrix is needed to further improve the reactor performance.

Besides, porous matrix structure is usually used for cell culture in reactors for bioengineering applications. Bioreactors aim to assist the development of new tissue and to provide appropriate stimulation, efficient nutrient delivery and waste removal for the cultured cells. Generally, porous scaffold is used and it should be biocompatible for cell adhesion and growth. Its biodegradation rate should be close to

that of the tissue assembly. Also the scaffold structure should have a high porosity for cell-scaffold interation, cell profileration and extracellular matrix generation. What is more, the scaffold should have high permeability for the purpose of transporting nutrients and metabolites to and from the cells. Among them, the perfusion bioreactor with a porous wall allows essential nutrients to be delivered to cultured cells in a manner very similar to what they are used to within the body.

1.2 Literature Review

1.2.1 Numerical Model Development for Flow in Porous Media

1.2.1.1 Darcy's Law

The velocity in a porous medium is related to the pressure gradient by the Darcy's law (Vafai, 2000):

$$u = -\frac{K}{\mu}\frac{\partial p}{\partial x} \tag{1.1}$$

where p is the interstitial pressure, u is the mean filter velocity, μ is the dynamic viscosity of the fluid, K is the permeability of porous media.

Darcy's law is valid only when the flow is of the seepage type and the fluid is homogeneous. Thus Darcy's law can be considered valid in situations where the flow is of creeping type (Greenkorn, 1981) or when the porous medium is densely packed with small enough permeability (Rudrauah and Balachandra, 1983), so that the pore Reynolds number based on the local volume averaged speed is less than unity.

However, Darcy's law neglects the boundary and inertial effects of the fluid flow due to the small porosity associated with the medium. When the velocity gradient is high, viscous effects cannot be taken into account in this law, especially in the presence of a solid wall, due to its low order accuracy. When the fluid Reynolds number is large enough, it will overpredict the actual fluid motion and the other effects (for example, inertial, viscous and convective effects) cannot be neglected (Vafai and Tien, 1981; Hsu and Cheng, 1990).

1.2.1.2 Non-Darcian Models

Non-Darcian effects have been incorporated to account for the other effects in porous flow. Forchheimer (1901) suggested a modification to the previous models to account for inertia effect. This was due to the rather high speed of the flow in some porous media, which was neglected in Darcy's law. Lapwood (1948) and Yin (1965) added the unsteady term in the Darcy's law to stand for temporal acceleration. Brinkman (1947a, 1947b) introduced a viscous term by examining the flow past a spherical particle to account for the viscous shear stresses that acted on the fluid element. An effective fluid viscosity inside the porous domain was used in his formulation.

1.2.1.3 Darcy-Brinkman-Forchheimer Extended Model

When all the unsteady, inertia and viscous effects are taken into consideration, Vafai and Tien (1981), Hsu and Cheng (1990) derived the generalized Darcy-Brinkman-Forchheimer extended model, as following:

$$\nabla \cdot \vec{u} = 0 \tag{1.2}$$

$$\underbrace{\rho \frac{\partial \vec{u}}{\partial t}}_{\text{Unsteady Term}} + \underbrace{\nabla \cdot \left(\frac{\rho \vec{u}\vec{u}}{\varepsilon} \right)}_{\text{Convective Term}} = - \underbrace{\nabla \left(\varepsilon p^* \right)}_{\text{Pressure Term}} + \underbrace{\mu \nabla^2 \vec{u}}_{\text{Brinkman Term}} - \underbrace{\frac{\mu \varepsilon}{K} \vec{u}}_{\text{Darcy Term}} - \underbrace{\frac{\rho \varepsilon C_F \left| \vec{u} \right|}{\sqrt{K}} \vec{u}}_{\text{Forchheimer Term}} \tag{1.3}$$

where Equation (1.2) is the mass continuity equation; Equation (1.3) is the momentum conservation equation; ε is porosity; K is the permeability; $\vec{u}$ the local average velocity vector (Darcy velocity); t is time; ρ is the fluid density; μ is the fluid dynamic viscosity; p^* is the intrinsic average pressure; and C_F is Forchheimer coefficient. The local average and intrinsic average can be linked by the Dupuit-Forchheimer relationship, for example, $p = \varepsilon p^*$.

Equation (1.2) and (1.3) were derived using local averaging technique. In this approach, a macroscopic variable is defined as an appropriate mean over a sufficiently large representative elementary volume (REV) (Figure 1.1). This operation yields the value of that variable at the centroid of REV (Vafai and Tien, 1981). It is assumed that the result is independent of the size of the REV. The length scale of the REV is much larger than the pore scale, but smaller than the length scale of the macroscopic flow domain.

It should be noted that the above two equations are now the most general equations governing the flow of a viscous fluid in porous media. They can recover the

standard Navier-Stokes equations when the porosity approaches unity and Darcy number goes to infinity. This characteristic makes it easier for those numerical flow problems in porous/fluid coupled domains, as reviewed in Section 1.2.3.

1.2.2 Numerical Model Development for Heat Transfer in Porous Media

There are two kinds of models for heat transfer in porous media. One is the local thermal equilibrium (LTE) model, which is widely accepted and used in various analytical and numerical studies on transport phenomena in porous media. It is assumed that both the fluid and solid phases are at the same temperature (Vafai and Tien, 1981; Hsu and Cheng, 1990; Nithiarasu et al., 1997 and 2002), due to the high conductivity value of the solid parts in porous media. Under the assumption of LTE, many investigators have used one unique set of equation to obtain temperature distributions in a porous medium because an analysis based on the one-equation model is simple and straightforward. The other one is local thermal non-equilibrium (LTNE) model, where two sets of energy equations are used to treat the solid phase and the fluid phase separately (Khashan et al., 2006; Haddad et al., 2007). This model is employed when temperature difference between the two phases is considered as a crucial design parameter.

1.2.3 Interface Treatment for Porous/Fluid Coupled Domains

From the modeling point of view, two different approaches can be used to represent transport phenomena in composite fluid/porous domains: one-domain and two-domain approaches. The detailed comparison of these two approaches has been given out by Goyeau et al. (2003) and here their main differences are discussed.

1.2.3.1 One-domain Approach

In the one-domain approach, the porous region is considered as a pseudo-fluid and the whole regions including fluid and porous domains are treated as a continuum. The transition from the fluid to the porous medium is achieved through a continuous spatial variation of properties such as the abrupt change of permeability and porosity values along the interface. In this case, the problem of explicitly writing the boundary conditions at the interface is avoided, as the matching conditions are automatically implicitly satisfied. Thus this approach has been extensively used in previous numerical computations dealing with natural convection (Bennacer et al., 2003; Gobin et al., 2005), forced convection problems (Zhang and Zhao, 2000; Abu-Hijleh, 1997 and 2000) in composite fluid/porous domains.

However, in the one-domain approach attention should be paid to the abrupt jump of permeability and porosity along the interface which may result in numerical instabilities (Basu and Khalili, 1999). It may be overcome by unphysical numerical techniques (Basu and Khalili, 1999). Thus, its physical representation of momentum conservation at the interfacial region depends on the relevance of the discretization scheme (Goyeau et al., 2003).

1.2.3.2 Two-domain Approach

1.2.3.2.1 Slip and Non-slip Interface Conditions

In the two-domain approach, the fluid and the porous regions are considered separately and the conservation equations in both regions are coupled by appropriate boundary conditions at the fluid/porous interface. For momentum transport, the interfacial conditions depend on the order of the differential equation in the porous region. When Darcy's law is used, the coupling with the Navier-Stokes equation in the fluid region is obtained by using a semi-empirical slip boundary condition (Beavers and Joseph, 1967) involving a slip coefficient which depends on the local microstructure geometry of the interface. This is because Darcy's law is first order and it cannot be coupled with the second order Navier-Stokes equation along the interface.

Alternatively, Brinkman correction to Darcy's law (Brinkman, 1947a, 1947b) can be used to meet the second order requirement in the porous region. Therefore, continuity of both velocity and shear stress can be satisfied at the interface. However, stress jump conditions can also be written in order to account for the heterogeneity of the interfacial region (Ochoa-Tapia and Whitaker, 1995a). Actually, in the two-domain approach, the involved adjustable parameters (slip coefficient, stress jump coefficient) are difficult to predict and need further practical experiments to validate their values (Ochoa-Tapia and Whitaker, 1995b).

The interfacial conditions have to be coupled with the equations for the two regions and additional boundary conditions are applied at the interface. Boundary

conditions for flow and heat transfer at the porous-fluid interface have been proposed previously and summarized in Tables 1.1 and 1.2.

One of the early flow boundary conditions was that of Beavers and Joseph (1967) who proposed the slip-boundary condition, in which the interfacial fluid-shear was related to the interface fluid-velocity and Darcy flow was assumed in the porous region. The interface condition contained a jump in both stress and velocity. However, continuity in both velocity and stress was proposed by Neale and Nader et al. (1974) as well as Vafai and Kim (1990). The continuity of shear stress was also assumed by Vafai and Thiyagaraja (1987) as well as Kim and Choi (1996) but there is non-continuity of velocity gradient, which is satisfied by using an effective viscosity for the porous medium region.

1.2.3.2.2 Stress-jump Interface Conditions

The non-continuity of both velocity gradient and shear stress has been developed by Ochoa-Tapia and Whitaker (1995a, 1995b). The development was based on the non-local form of the volume averaged Stokes' equation. The length-scale constraint was that the radius of the averaging volume is much smaller than the height of the fluid channel. Under these assumptions, the volume-averaged equations in the homogeneous fluid regions are equivalent to the point equations; and the analysis of jump condition is greatly simplified because a single volume-averaged transport equation is used in both fluid and porous regions. The jump condition links the Darcy law, with Brinkman's correction, to the Stokes equation. The analysis

produced a jump in the stress but not in the velocity. The normal component of jump condition simply reduced to continuity of pressure. The function for the jump coefficient indicates dependence on permeability and porosity and was complex to solve. The coefficient was expected to be of order one, and may be either positive or negative. It was noted that the parameter depends on $\sqrt{K}/\delta$ where δ is the thickness of the boundary region.

Subsequently, Ochoa-Tapia and Whitaker (1998b) developed another stress jump condition which includes the inertial effects. Though inertial effects may be negligible in homogeneous regions of channel flow, it is not negligible in the boundary between the porous and fluid regions. Outside the boundary regions, the non-local form of the volume-averaged momentum equation reduces to the Forchheimer equation with Brinkman correction and the Navier Stokes equation. Two coefficients appear in this jump condition: one is associated with an excess viscous stress and the other is related to an excess inertial stress.

The stress jump parameter (associated with an excess viscous stress) was derived by Goyeau et al. (2003) as an explicit function of the effective properties of a transition layer between the fluid and porous regions. The parameter is also related to the variations of the velocity in the transition layer, which is an unknown in the problem. Recently, Chandesris and Jamet (2006) presented a model in which the shear jump is built on fluid stress rather than effective stress. An explicit function for the stress jump coefficient was obtained which only depends on the characteristics of the porous medium (porosity and permeability) in the transition zone.

1.2.3.2.3 Numerical Experiments for Fluid/porous Coupled Flows

Numerical solutions for the coupled viscous and porous flows have been attempted by many researchers with the two-domain approach (Gartling et al., 1996; Costa et al., 2004; Betchen et al., 2006). Costa et al. (2004) proposed a control-volume finite element method to simulate the problems of coupled viscous and porous flows. A continuity of both velocity and stress at the interface was assumed and no special or additional procedure was needed to impose the interfacial boundary conditions. Betchen et al. (2006) developed a finite volume model, also based on continuity of both velocity and stress, but special attention was given to the pressure-velocity coupling at the interface.

The stress jump conditions have been adopted by many researchers. Different types of interfacial conditions between a porous medium and a homogenous fluid have been proposed; and found to have a pronounced effect on the velocity field as shown by Alazmi and Vafai (2001).

The implementation of the numerical methodology for the stress jump condition based on Ochoa-Tapia and Whitaker (1995a, 1995b) can be found in the work of Silva and de Lemos (2003). Although they claimed that their treatment could be applied to complex geometris, their results were based on finite volume method in an orthogonal Cartesian coordinate system and for the case of fully developed flow. In their study, only the jump in shear stress was included and no special treatment on velocity derivatives was mentioned. However, for flow in general, it is necessary to consider how to formulate the velocity derivatives at the interface. Also, for a two-

dimensional problem, the normal stress condition is needed to close the sets of equations.

The main drawback of the stress jump condition is that its parameters are unknown. This closure problem has been investigated by many researchers recently (Goyeau et al., 2003; Chandesris and Jamet, 2006; Valdes-Parada et al., 2007; Chandesris and Jamet, 2007) and derivations have been proposed to evaluate the first stress-jump parameter which is viscous related.

1.2.3.2.4 Heat and Mass Transfer Interface Conditions

For heat transfer interface conditions, usually continuities of temperature and heat flux are required (Neale and Nader, 1974; Vafai and Thiyagaraja, 1987; Ochoa-Tapia and Whitaker, 1997; Jang and Chen, 1992; Kim and Choi, 1996; Kuznetsov, 1999). However, other types of interfacial conditions are also possible. Ochoa-Tapia and Whitaker (1998a) proposed a jump condition for heat flux to account for its production or consumption at the interface. Another hybrid interfacial condition, continuity of heat flux but non-continuity in temperature, was proposed by Sahraoui and Kaviany (1994).

For mass transfer interface conditions, Valencia-Lopez et al. (2003) developed a mass jump condition that representing the excess surface accumulation, convection, diffusion adsorption and a nonequilibrium source, in addition to a term representing the exchange with the surrounding region. Recently, the closure problem has been

derived by Valdes-Parada et al (2006 and 2007b) to predict the jump coefficient as a function of the microstructure of the porous layer.

1.2.4 Unsteady Flow past Porous Cylinders

Flow past bluff bodies, especially cylinders, has been investigated extensively for a long time. Most of the studies concentrated on circular cylinder case under free flow conditions as reviewed by Williamson (1996) and Zdravkovich (1997). However, the research on square cylinder case has not been investigated to the same extent, although it plays a dominant role in many technical applications, such as building aerodynamics, as reported by Davis et al. (1982, 1984), Franke et al. (1990), Klekar and Patankar (1992), and Suzuki et al. (1993). They have provided numerical and experimental data about lift coefficient, drag coefficient, base pressure and Strouhal frequency for a range of Reynolds numbers (*Re*) up to 2800.

Trapezoidal cylinders are also often used in engineering applications, and the flow around them is more complicated. Lee (1998a and 1998b) numerically studied the early stages of an impulsively started unsteady laminar flow past tapered and expanded trapezoidal cylinders, with Re ranging from 25 to 1000. He showed that the flow started with no separation first, then a symmetrical circulation zone developed behind the rear of the cylinder, later with separated flow and separation bubbles. Finally, the vortices merge to form a complex flow regime with its own distinct characteristics. Cheng and Liu (2000) simulated the effects of afterbody shape on flow around prismatic cylinders. The cross-sectional shape of the cylinder varies from

square to trapezoidal and finally to triangular. Later, the laminar vortex shedding from a trapezoidal cylinder with different height ratios was studied by Chung and Kang (2000). They showed that the Strouhal numbers from trapezoidal cylinders with *Re* = 100 and 150, had their minimum values at height ratios of 0.7 and 0.85, respectively; while with Re = 200, they increases to a maximum value at height ratio of 0.7, then decreases with the increase of height ratio. Kahawita and Wang (2002) also numerically investigated the wake flow behind trapezoidal bodies, using the spline method of fractional steps. They found the trapezoidal height was the dominant influence on Strouhal number, compared with the base width.

However, most of the studies focused on flow past impermeable bodies, and flow behind a porous body has not been broadly investigated. For unsteady problems, flow over a circular cylinder with surface suction and blowing was theoretically investigated by Cohen (1991). He derived a model for St-Re relationship by order of magnitude estimation. Ling et al. (1993) numerically verified this model for flow over a square cylinder and obtained a similar trend between Strouhal and Reynolds numbers. These studies on the effects of suction and blowing through the body may help to explain the behaviour of flow past porous bodies.

Jue (2003) simulated vortex shedding behind a porous square cylinder using finite element method. In his study, a general non-Darcy porous media model was applied to describe the flows both inside and outside the cylinder. A harmonic mean was used to treat the sudden change between the fluid and porous medium and no special treatment at the interface was given. He found that Darcy number has more

influence on the flow field than porosity does. Bhattacharyya et al. (2006) simulated the flow around a porous circular cylinder with Reynolds number ranging from 1 to 40. For the interface, the harmonic-mean formulation was also used to handle the abrupt changes of permeability and porosity. Such abrupt changes were a major source of numerical difficulties and the resultant instabilities in the single-domain approach.

1.2.5 Natural Convective Heat Transfer in Complex Porous Domains

There have been many previous studies on natural convection in porous enclosures (Vasseur et al., 1989; Hsiao and Chen, 1994; Nithiarasu, 1996; Bera et al., 1998; Holzbecher, 2004). The non-Darcian effects in natural convection are presented systematically in the works of Lauriat and Prasad (1989), Ettefagh et al. (1991), and Karimi-Fard et al. (1997). Non-Darcian effects represent deviations from the Darcy law, including the viscous and inertial effects, porosity variation effect, and the convective effect. They concluded that Darcy law is only valid when the pore Reynolds number is of order unity; and if the Rayleigh number is large enough, Darcy law will over predict the actual flow motion and the other effects cannot be neglected.

Heat transfer in irregular geometry is also of interest recently. Ratish Kumar et al. (1997 and 1998), Murthy et. al. (1997) and Ratish Kumar and Shalini (2003) have studied natural convection heat transfer in a cavity, enclosing a porous medium, which has one wavy vertical wall. Subsequently Mahmud and Fraser (2004)

considered a wavy cavity, consisting of two wavy-vertical isothermal walls and two horizontal adiabatic walls, which enclosed a viscous and incompressible fluid (clean fluid) inside.

Recently, Misirlioglu et al. (2005) extended the study of natural convection in the wavy cavity by considering that it enclosed a porous medium. However, their numerical results were based on Darcy's law and the stream-function method was used to solve the governing equations. Flow and heat transfer characteristics (isothermal, streamlines and local and average Nusselt numbers) were investigated in their study.

1.2.6 Forced Convective Heat Transfer in Porous-Fluid Coupled Domains

1.2.6.1 Forced Convection over a Backward Facing Step with a Porous Insert

Heat transfer will be enhanced globally if the flow has regions of recirculation and the reduction or elimination of recirculation is highly desirable, as wall temperatures are typically high in these regions. Martin et al. (1998) numerically investigated the heat transfer enhancement with porous inserts behind the backward-facing step, with high porosity above 0.90 and Re = 800. Generally the porous inserts reduce or eliminate the lower wall recirculation zone. They modified the velocity profile and straighten streamlines past the expansion, making the velocity gradient steeper near the floor which thus augmented the heat transfer in the porous region.

Due to the suppression of the recirculation bubble, there is no reattachment point to cause local enhancement of heat transfer at that location.

More recently, Zhang and Zhao (2000) solved the same problem using a high-order upwind finite-volume algorithm. The fluid region was governed by the Navier-Stokes equation and the porous region by the Brinkman-Forchheimer-extended Darcy model. The two equations were unified into one set for both the fluid and porous media regions by introducing a binary parameter which had values one and zero in porous and fluid regions respectively. Thus the matching conditions at the interface were automatically satisfied. However, for such single-domain approach, the physical values at the interface depend on the type of discretization scheme.

1.2.6.2 Forced Convection over a Backward Facing Step with a Porous Floor Segment

Local enhancement of heat transfer was achieved around the reattachment location if a porous segment was embedded in the floor downstream of the backward facing step (Abu-Hijleh, 1997 and 2000). This flow device could serve as a passive heat-control mechanism. The study may also be related to convection in a solid fuel combustion chamber, with an abrupt expansion, in which the fuel particles could be modeled as a porous segment.

Abu-Hijleh's numerical model was based on one-domain approach in which a momentum equation governed the flow in fluid and porous domains. In their equation, a pressure loss coefficient was incorporated to represent the extra pressure drop

through the porous segment. The pressure coefficient takes zero value for fluid domain and a non-zero for porous domain, the value of which depends on the porous materials and arrangements. The local heat transfer was found to be enhanced after the porous segment but the overall heat transfer might be reduced by as much as 16 %.

However, the above study on porous floor segment (Abu-Hijleh, 1997 and 2000) was based on one-domain approach in which continuity of stress was automatically satisfied. In the two-domain approach, there are two sets of equations for the two regions which have to be coupled at the interface. The two-domain approach requires additional boundary conditions to be applied at the interface, as reviewed in Section 1.2.3.2.

1.2.7 Mass Transport in a Reactor with Porous Media

For bioreactors with porous media, experimental research has been conducted before. Dusting et al. (2006) experimentally investigated, using particle image velocimetry technique, the flow field and shear stress outside a scaffold in a spinner-flask bioreactor. It was found that vortex breakdown may still occur and relatively large stresses occur along the edge of scaffold protruding into the boundary of the vortex breakdown region. Drott et al. (1997 and 1999) fabricated a microstructured enzyme reactor with porous silicon along the walls in a channel to yield high enzyme activities. Later, Melander et al. (2006) continued and investigated the effects of flow rate and substrate concentration on the hydrolysis efficiency. A perfusion bioreactor

was designed (Ma et al., 1999; Zhao and Ma, 2005) with fibrous matrix walls in the channels, for tissue engineering of trophoblast and mesenchymal stem cells.

Mathematical modeling and numerical simulations have also been carried out and used to explain experimental results or cast light on research directions for mass transport in reactors with porous media. Porter et al. (2005) applied the lattice-Boltzmann method to simulate the flow of culture media through scaffolds in a bioreactor. Micro-computed tomography imaging was used to define the micro-architecture of the scaffold for the simulations. The local shear stress was estimated from velocity derivatives at various media flow rates. Boschetti et al. (2006) developed a computational fluid dynamic model of the flow through a three dimensional scaffold of homogeneous geometry. The scaffold was idealized as composing of many subunits which were obtained by subtracting a solid sphere from a concentric solid cube. In both of the above two approaches, a large number of elements are needed to describe the microstructure of the scaffolds.

For other researchers, with the use of volume averaging technique (Vafai and Tien, 1981), macroscopic conservation equations for nutrient in the porous scaffold were used. For direct perfusion bioreactor, where the culture media flow was perpendicular to a cellular construct, finite element method was implemented to solve the Navier-Stokes equations for the fluid domain and Brinkman's equation for the porous scaffold domain (Chung et al., 2007). Their model included time-dependent porosity and permeability which varied with cell growth and numerical results showed that cells penetrated to a great extend into the scaffold with a more uniform

distribution. For another kind of perfusion bioreactor, where culture media flow was parallel to the porous scaffold, Lattice-Boltzmann method was used to solve the Stokes' equations in fluid region and the Brinkman's equation in the porous scaffold region (Zhao et al., 2007). However, in the above two references, the details for the bioreactor design (for example, concentration distribution for cell growth, reaction effectiveness and critical reaction length) were not systematically and parametrically investigated.

Recently, from the aspect of design analysis, numerical modeling of a micro-channel flat-plate bioreactor was conducted using the correlation of combined parameters (Zeng et al., 2006, 2007 and 2008). Single-culture (Zeng et al., 2006), co-culture cells (Zeng et al., 2007) and micro-patterning cells (Zeng et al., 2008) were distributed along the bioreactor wall and with the increase in the bioreactor wall length, there existed a critical point after which the cells suffered from hypoxia. The results were presented systematically and parametrically, which may serve as a general guide for the architecture design of a flat-plate bioreactor. However, these work did not involve reactor with porous walls, which is more useful and applicable in practical bioengineering and biochemical problems.

1.3 Objectives of the Study

1.3.1 Motivations

As reviewed above, for numerical simulations of heat and mass transfer in porous/fluid coupled domains, the stress jump interfacial conditions (Ochoa-Tapia

and Whitaker, 1998b) have not been incorporated with heat or mass transfer. There are also limited numerical experiments and systematic results for heat and mass transfer in porous/fluid coupled domains for certain numerical applications. The generalized Darcy-Brinkman-Forchheimer extended model has not been implemented and there is not sufficient work to investigate unsteady flow past porous cylinders, natural convective heat-transfer in porous complex geometries, forced convective heat-transfer in porous/fluid coupled domains and mass transport in a reactor with porous media. The implementation of stress jump interfacial condition has never been attempted before for unsteady problems for flow past porous cylinders. There is also no systematic or parametrical study on a microchannel reactor with a porous wall that examines the influence of flow and geometric parameters on mass transport behavior inside such reactors.

1.3.2 Objectives

The detailed objectives of the current work will be described in the corresponding chapters later and the general objectives are given here as follow:

1. To develop a numerical method for heat and mass transfer in porous/fluid coupled domains with the use of generalized Darcy-Brinkman-Forcheimmer extended model for complex geometries and to implement the numerical technique on several applications related to heat and mass transfer;

2. To implement the Ochoa-Tapia and Whitaker's stress jump conditions for the flow, heat and mass transfer in porous/fluid coupled domains, and to investigate their effects on local and global heat and mass transfer;
3. To implement the numerical method for unsteady flow past porous cylinders, heat transfer in complex geometries and to check the heat transfer enhancement effects with the addition of porous media in porous/fluid coupled domains;
4. To investigate the flow and mass transport in a microchannel reactor with a porous wall; and to develop combined non-dimensional parameters for a systematic and parametrical analysis of the mass concentration.

1.3.3 Scope

Due to the time-consuming mesh generation and high computational effort in complex geometries for three-dimensional problems, the current study only considered two-dimensional cases. The porous medium was considered to be rigid, homogeneous and isotropic; and saturated with the same single-phase fluid as that in the homogenous fluid region. For heat transfer, local thermal equilibrium (LTE) model was assumed. For the shear stress jump parameters, to demonstrate the implementation of current numerical method and to test their effects, they were ranged from -5.0 to +5.0 in the present study. For normal stress, temperature, heat flux, mass and mass flux, the continuity conditions were imposed.

For flow past a porous square or trapezoidal cylinder, Reynolds number up to 250 was considered to avoid the complications from three-dimensional flow. For forced convection after backward facing step with a porous insert or a porous floor segment, the ratio of the effective thermal conductivity of porous medium to fluid conductivity was set to be unity. For the mass transfer in a microchannel reactor with a porous wall, a steady concentration field was assumed.

1.4 Organization of the Thesis

The following chapter will present the details of the numerical method for the flow in porous and porous/fluid coupled domains. It is based on the SIMPLEC method with multi-block technology and body-fitted grids. The grid non-orthogonality is taken into account for complex geometries.

In Chapter 3, a variety of numerical experiments are performed and compared with the benchmark problems for the validation of the present numerical code.

In Chapter 4, unsteady flow past a porous square or trapezoidal cylinder with the stress jump interfacial condition is numerically analyzed.

In Chapter 5, a numerical investigation is carried out for steady, natural convective heat transfer inside a wavy cavity filled with a porous medium.

In Chapter 6, forced convective heat-transfer problems in porous/fluid coupled domains are numerically analyzed. The flow past a backward facing step with the addition of a porous insert or porous floor segment is presented.

In Chapter 7, mass transfer in a mircochannel reactor with a porous wall is considered. The results are correlated with the use of several combined dimensionless parameters; and the reaction effectiveness factor and the reactor efficiency are also investigated.

In Chapter 8, a summary of the main conclusions that can be drawn from this work and the recommendations for future research work are presented.

Table 1.1 Velocity boundary conditions at interface between porous and fluid domains.

Model	Velocity	Velocity Gradient	References
1		$\left.\frac{\partial u_x}{\partial y}\right\|_{\text{fluid}} = \frac{\alpha}{\sqrt{K}}\left(u_x\|_{\text{interface}} - \langle u\rangle_{\infty}\right)$	Beavers and Joseph, 1967.
2	$\langle u\rangle_x\|_{\text{porous}} = u_x\|_{\text{fluid}}$	$\left.\frac{\partial \langle u\rangle_x}{\partial y}\right\|_{\text{porous}} = \left.\frac{\partial u_x}{\partial y}\right\|_{\text{fluid}}$	Neale and Nader et al., 1974; Vafai and Kim, 1990.
3	$\langle u\rangle_x\|_{\text{porous}} = u_x\|_{\text{fluid}}$	$\mu_{eff}\left.\frac{\partial \langle u\rangle_x}{\partial y}\right\|_{\text{porous}} = \mu\left.\frac{\partial u_x}{\partial y}\right\|_{\text{fluid}}$	Vafai and Thiyagaraja,1987; Kim and Choi, 1996.
4	$\langle u\rangle_x\|_{\text{porous}} = u_x\|_{\text{fluid}}$	$\frac{\mu}{\varepsilon}\left.\frac{\partial \langle u\rangle_x}{\partial y}\right\|_{\text{porous}} - \mu\left.\frac{\partial u_x}{\partial y}\right\|_{\text{fluid}} = \beta\frac{\mu}{\sqrt{K}}u_x\|_{\text{interface}}$	Ochoa-Tapia and Whitaker, 1995a, 1995b; Goyeau et al., 2003; Chandesris and Jamet, 2006.
5	$\langle u\rangle_x\|_{\text{porous}} = u_x\|_{\text{fluid}}$	$\frac{\mu}{\varepsilon}\left.\frac{\partial \langle u\rangle_x}{\partial y}\right\|_{\text{porous}} - \mu\left.\frac{\partial u_x}{\partial y}\right\|_{\text{fluid}} = \beta\frac{\mu}{\sqrt{K}}u_x\|_{\text{interface}} + \beta_1\rho u_x^2\|_{\text{interface}}$	Ochoa-Tapia and Whitaker, 1998b.

Table 1.2 Heat transfer boundary conditions at interface between porous and fluid domains.

Model	Temperature	Temperature Gradient	References
1	$\langle T\rangle\|_{\text{porous}} = T\|_{\text{fluid}}$	$k_{eff}\left.\frac{\partial \langle T\rangle}{\partial y}\right\|_{\text{porous}} = k_f\left.\frac{\partial T}{\partial y}\right\|_{\text{fluid}}$	Neale and Nader, 1974; Vafai and Thiyagaraja, 1987; Ochoa-Tapia and Whitaker, 1997; Jang and Chen, 1992; Kim and Choi, 1996; Kuznetsov, 1999.
2	$\langle T\rangle\|_{\text{porous}} = T\|_{\text{fluid}}$	$k_{eff}\left.\frac{\partial \langle T\rangle}{\partial y}\right\|_{\text{porous}} = k_f\left.\frac{\partial T}{\partial y}\right\|_{\text{fluid}} + \phi$	Ochoa-Tapia and Whitaker, 1998a.
3	$\left.\frac{dT}{dy}\right\|_{\text{fluid}} = \frac{\alpha_T}{\lambda}(T\|_{\text{fluid}} - \langle T\rangle\|_{\text{porous}})$	$k_{eff}\left.\frac{\partial \langle T\rangle}{\partial y}\right\|_{\text{porous}} = k_f\left.\frac{\partial T}{\partial y}\right\|_{\text{fluid}}$	Sahraoui and Kaviany, 1994.

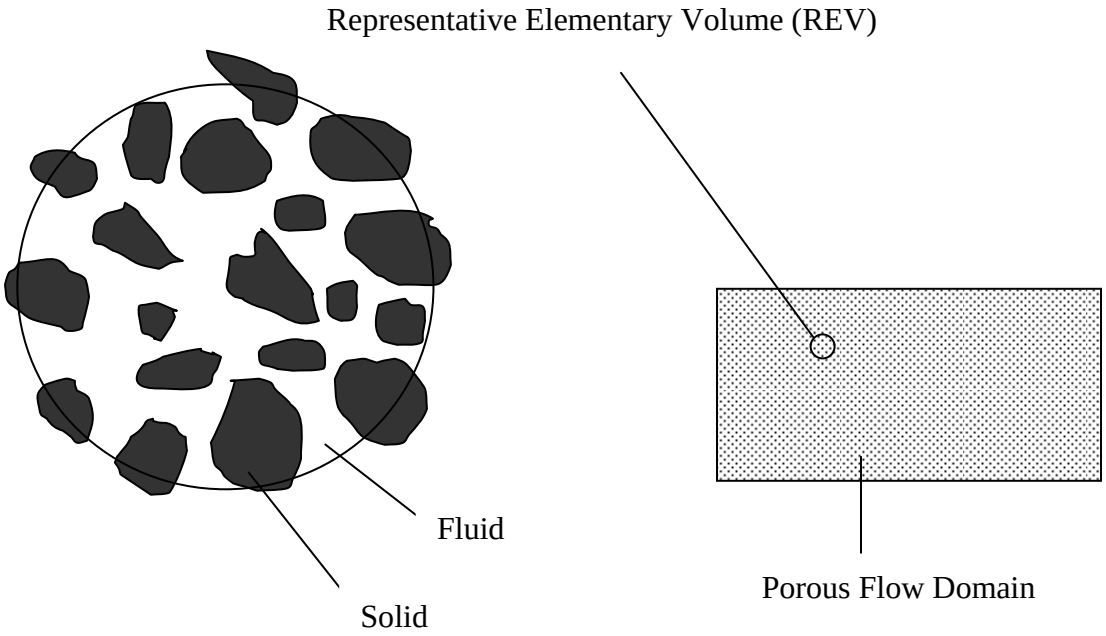

Figure 1.1 The Representative Elementary Volume (REV).

Chapter 2

A Numerical Method for Transport Problems in Porous and Fluid Coupled Domains*

In the present chapter, the development of a finite volume code based on non-orthogonal body-fitted and multi-block grids is described to simulate the coupled flow and heat or mass transport problems in the homogenous flow and porous medium regions. For such problems, previously one-domain approach is widely used, where continuities of velocity, shear stress, pressure, temperature, heat or mass flux are automatically satisfied. However for present method, two-domain approach is used, making it suitable to implement different interfacial conditions. The present code provides a flexible platform for implementing complex interfacial boundary conditions and new porous models. The finite volume method is chosen because it has been well developed and has relatively high computational efficiency. The use of multi-block technique is for convenience because the structured grid is applied.

In the remainder of this chapter, the mathematical equations governing the fluid flow, heat or mass transport in the homogenous flow and porous medium regions for Cartesian coordinates are described, followed by the discretization procedures of the governing equations. The SIMPLEC algorithm is used to couple the

*Parts of this chapter have been published in *International Journal for Numerical Methods in Fluids* (Chen et al., 2008a)

velocity and pressure. Special attention is given to the treatment of the interface between the homogenous flow and porous medium regions. The strongly implicit procedure (SIP) is applied to solve the resultant algebraic equation system.

2.1 Governing Equations in Cartesian Coordinate

2.1.1 Homogenous Fluid Region

For a two-dimensional, incompressible, and viscous flow, the governing equations with primitive variables are:

Continuity equation:

$$\frac{\partial u}{\partial x}+\frac{\partial v}{\partial y}=0 \tag{2.1}$$

X-momentum equation:

$$\rho\frac{\partial u}{\partial t}+\rho(u\frac{\partial u}{\partial x}+v\frac{\partial u}{\partial y})=-\frac{\partial p}{\partial x}+\mu\bullet(\frac{\partial^2 u}{\partial x^2}+\frac{\partial^2 u}{\partial y^2})+\rho S_x \tag{2.2}$$

Y-momentum equation:

$$\rho\frac{\partial v}{\partial t}+\rho(u\frac{\partial v}{\partial x}+v\frac{\partial v}{\partial y})=-\frac{\partial p}{\partial y}+\mu\bullet(\frac{\partial^2 v}{\partial x^2}+\frac{\partial^2 v}{\partial y^2})+\rho S_y \tag{2.3}$$

Heat or mass transfer equation:

$$\rho\frac{\partial \varphi}{\partial t}+\rho u\frac{\partial \varphi}{\partial x}+\rho v\frac{\partial \varphi}{\partial y}=\Gamma_\varphi\bullet(\frac{\partial^2 \varphi}{\partial x^2}+\frac{\partial^2 \varphi}{\partial y^2})+\rho S_\varphi \tag{2.4}$$

where u and v are velocity components in x and y direction respectively; p the pressure; ρ the fluid density; μ the fluid dynamic viscosity; S_x and S_y are the

source terms in *x* and *y* direction respectively. Γ_φ is the diffusivity for the quantity φ; S_φ the source term for the quantity φ.

Equation (2.4) can be regarded as a general form of the governing equations for the Navier-Stokes equations. In the discretization section, the analysis will be carried out from the general conservation equation (Equation 2.4).

2.1.2 Porous Medium Region

The porous medium is considered to be rigid, homogeneous and isotropic; and saturated with the same single-phase fluid as that in the homogenous fluid region. In order to include all the non-Darcian effects, the governing equations for porous region based on a generalized model including both Brinkman and Forchheimer terms as well as the non-linear advection term (Hsu and Cheng, 1990; Gartling et al., 1996; Nithiarasu et al., 2002) can be written as:

Continuity equation:

$$\frac{\partial u}{\partial x}+\frac{\partial v}{\partial y}=0 \tag{2.5}$$

X-momentum equation:

$$\begin{aligned}&\rho\frac{\partial u}{\partial t}+\rho\left\{u\frac{\partial}{\partial x}(\frac{u}{\varepsilon})+v\frac{\partial}{\partial y}(\frac{u}{\varepsilon})\right\}=\\&-\frac{\partial}{\partial x}(\varepsilon p_f)-\frac{\mu\bullet\varepsilon}{K}u-\frac{1.75}{\sqrt{150}}\frac{(u^2+v^2)^{1/2}}{\sqrt{K}}\frac{\rho\bullet u}{\sqrt{\varepsilon}}+\mu\bullet(\frac{\partial^2 u}{\partial x^2}+\frac{\partial^2 u}{\partial y^2})\end{aligned} \tag{2.6}$$

Y-momentum equation:

$$\rho\frac{\partial v}{\partial t}+\rho\left\{u\frac{\partial}{\partial x}(\frac{v}{\varepsilon})+v\frac{\partial}{\partial y}(\frac{v}{\varepsilon})\right\}= \\ -\frac{\partial}{\partial y}(\varepsilon p_f)-\frac{\mu\bullet\varepsilon}{K}v-\frac{1.75}{\sqrt{150}}\frac{(u^2+v^2)^{1/2}}{\sqrt{K}}\frac{\rho\bullet v}{\sqrt{\varepsilon}}+\mu\bullet(\frac{\partial^2 v}{\partial x^2}+\frac{\partial^2 v}{\partial y^2}) \tag{2.7}$$

Heat or mass transfer equation:

$$\rho\frac{\partial\varphi}{\partial t}+\rho u\frac{\partial\varphi}{\partial x}+\rho v\frac{\partial\varphi}{\partial y}=\Gamma_p\bullet(\frac{\partial^2\varphi}{\partial x^2}+\frac{\partial^2\varphi}{\partial y^2})+\rho S_{\varphi_p} \tag{2.8}$$

where u and v are the local average velocity components (Darcy velocity components) in x and y direction respectively; p_f the intrinsic average pressure; ε the porosity; K the permeability; The subscript "f" denotes the intrinsic average. The local average and intrinsic average can be linked by the Dupuit-Forchheimer relationship, for example, u=εu_f . Γ_p and S_{φ_p} are the diffusivity and the source term for the quantity φ in the porous medium respectively.

2.1.3 Interface Boundary Conditions

At the interface between the homogeneous fluid and porous medium regions, additional boundary conditions must be applied to couple the flows in the two domains. The boundary conditions include flow, heat or mass transfer.

For flow interfacial condition, the stress jump condition of Ochoa-Tapia and Whitaker (1998) is applied:

$$\frac{\mu}{\varepsilon}\frac{\partial u_t}{\partial n}\bigg|_{\text{porous}}-\mu\frac{\partial u_t}{\partial n}\bigg|_{\text{fluid}}=\beta\frac{\mu}{\sqrt{K}}u_t\bigg|_{\text{interface}}+\beta_1\rho u_t^2 \tag{2.9}$$

where in the porous medium region, u_t is the Darcy velocity component parallel to the interface aligned with the direction t and normal to the direction n; in the homogenous fluid region u_t is the fluid velocity component parallel to the interface; and β and β_1 are adjustable parameters which account for the stress jump at the interface.

Ochoa-Tapia and Whitaker (1998) derived analytical expressions for parameters β and β_1 which indicate their dependence on permeability and porosity. They concluded that these two parameters are both of order one. Ochoa-Tapia and Whitaker (1995b) experimentally determined that β varies from +0.7 to -1.0 for different materials with permeability varying from 15×10^{-6} to 127×10^{-6} in^2 and average pore size from 0.016 to 0.045 in.

There have been analytical studies which tried to relate the stress jump parameter β to the properties of the porous media. Min and Kim (2005) considered channel flow which has a partial porous-medium with periodic structure (solid and fluid phases repeating in a regular pattern). For the fluid layer the periodic velocity distribution at the interface was expressed as a cosine Fourier series. The control equations for the fluid and porous regions were solved analytically to obtain the shear stress differences at the interface. The values of porosity and pore size were those used in Beavers and Joseph (1967). They found that the stress jump parameter β was of order one and depended on local porosity, Darcy number, pore diameter and thickness of the adjacent fluid layer. Valdes-Parada et al. (2007) proposed a mixed

stress tensor to relate the stress jump coefficient β , which was the sum of the global and Brinkman stress contributions. The porous medium was assumed to be composed of equally spaced spheres or cylinders. Their predicted values of the stress jump coefficient β ranged from 0.96 to 1.25, for pore sizes and porosities used in Beavers and Joseph (1967). From the above two studies, it is noted that the stress jump coefficient β was found to be of order one for two very different types of porous structures.

There is presently no experimental data for β_1. It is not known how much the two parameters may change from one type of interface to another; and it is assumed in this thesis that the changes should be in the same range as those for different types of materials. Thus for the purpose of demonstrating the implementation of the present formulation, both β and β_1 are varied in the range -5.0 to +5.0 in the present study.

In addition to Equation (2.9), the continuity of velocity and normal stress prevailing at the interface is given by:

$$\vec{u}\big|_{\text{fluid}} = \vec{u}\big|_{\text{porous}} = \vec{v}_{\text{interface}} \tag{2.10}$$

$$\frac{1}{\varepsilon}\frac{\partial u_n}{\partial n}\bigg|_{\text{porous}} - \frac{\partial u_n}{\partial n}\bigg|_{\text{fluid}} = 0 \tag{2.11}$$

where in the porous medium region, u_n is the Darcy velocity component normal to the interface; and in the homogenous fluid region, u_n is the fluid velocity component normal to the interface.

For heat or mass transfer interfacial condition, continuities of temperature and heat flux, mass and mass flux are implemented here:

$$\varphi\big|_{\text{fluid}} = \varphi\big|_{\text{porous}} = \varphi_{\text{interface}} \tag{2.12}$$

$$R_k \left.\frac{\partial \varphi}{\partial n}\right|_{\text{porous}} = \left.\frac{\partial \varphi}{\partial n}\right|_{\text{fluid}} \tag{2.13}$$

where R_k is the ratio of thermal conductivities or mass transfer diffusivities between porous and fluid regions.

By combining with the appropriate boundary conditions of the composite regions, Equations (2.1) - (2.13) can be used to simulate the flow and heat or mass transfer in a system composed of a porous medium and a homogenous fluid.

2.2 Discretization Procedures

2.2.1 Homogenous Fluid Region

A typical control volume is shown in Figure 2.1. For a general dependent variable φ, a final discrete form over the control volume can be written as:

$$F_e + F_w + F_n + F_s = S \tag{2.14}$$

where F_e, F_w, F_n and F_s are the overall fluxes (including both convection and diffusion) of φ at faces *e*, *w*, *n*, *s*, which denote *east*, *west*, *north*, and *south* of the control volume; and S is the source term. The detailed numerical methodology for

obtaining the convective flux ($F_e^c, F_w^c, F_n^c,$ and F_s^c) and diffusive flux ($F_e^d, F_w^d, F_n^d,$ and F_s^d) are given by Ferziger and Perić (1999).

With the midpoint rule approximation, the convective flux at face *east* can be calculated as:

$$F_e^c = \int_{S_e} \rho\varphi\vec{u}\cdot\vec{n}dS \approx m_e\varphi_e \tag{2.15}$$

where m_e is the mass flux cross the surface e; S_e is the surface area of face e; and φ_e is the value of φ at the center of the cell face. m_e and S_e can be calculated as:

$$m_e = \rho_e\left(S^x u + S^y v\right)_e, \quad S_e = \sqrt{\left(S_e^x\right)^2 + \left(S_e^y\right)^2} \tag{2.16}$$

where u and v are the velocity components in the x and y directions; S^x and S^y are the surface vector components.

To avoid the non-orthogonal effect, the midpoint rule with the deferred correction term (Muzaferija, 1994) applied to the integrated diffusive flux is given by:

$$F_e^d = \mu_e\left(\frac{\partial\varphi}{\partial \mathrm{n}}\right)_e S_e = \mu_e S_e\left(\frac{\partial\varphi}{\partial\xi}\right)_e + \mu_e S_e\left[\overline{\left(\frac{\partial\varphi}{\partial \mathrm{n}}\right)_e} - \overline{\left(\frac{\partial\varphi}{\partial\xi}\right)_e}\right]^{old} \tag{2.17}$$

If an implicit flux approximation of the term $\left(\frac{\partial\varphi}{\partial\xi}\right)_e$ is applied, the final expression of Equation (2.17) then becomes:

$$F_e^d = \mu_e S_e\frac{\varphi_E - \varphi_P}{L_{PE}} + \mu_e S_e\overline{\left(grad\varphi\right)_e}^{old}\cdot\left(\vec{n} - \vec{i}_\xi\right) \tag{2.18}$$

where L_{PE} stands for the distance between P and E; $\vec{i}_\xi$ is the unit vector in the ξ-direction.

The different methods to approximate the value of φ and its derivative at the cell face result in different interpolation schemes. In the present study, the central difference scheme (CDS) is used. Then the cell-face values of the variables are approximated as:

$$\varphi_e \approx \varphi_{e'} = \lambda_e \varphi_E + (1-\lambda_e)\varphi_P \text{ for face } e \tag{2.19}$$

where the interpolation factor λ_e is defined as:

$$\lambda_e = \frac{|\vec{r}_e - \vec{r}_P|}{|\vec{r}_e - \vec{r}_P| + |\vec{r}_E - \vec{r}_e|} \tag{2.20}$$

where $\vec{r}_e$ is the position vector.

Equation (2.19) is a second-order approximation at the location e' on the straight line connecting nodes P and E (Figure 2.1). If the cell-face center e does not coincide with the location e', a correction term needs to be added in Equation (2.19) to restore the second-order accuracy, which can be expressed as follows:

$$\varphi_e \approx \varphi_{e'} + (grad\varphi)_{e'} \cdot (\vec{r}_e - \vec{r}_{e'}) \tag{2.21}$$

To obtain the deferred derivatives at the cell face, they are calculated first at the control volume centers and then interpolated to the cell faces. By using the Gauss' theorem, the derivative at the CV centers can be approximated by the average value over the cell:

$$\left(\frac{\partial \varphi}{\partial x_i}\right)_P \approx \frac{\int_\Omega \frac{\partial \varphi}{\partial x_i} d\Omega}{\Delta\Omega} = \int_S \varphi \vec{i}_i \cdot \vec{n} dS \approx \sum_c \varphi_c S_c^i, \quad c = e, n, w, s \tag{2.22}$$

Then the cell-center derivatives can also be interpolated to the cell-face centers using the same interpolation as that described by Equation (2.19) to (2.21). It is noted that the derivative at the cell-face center can be directly evaluated by using Gauss theorem if a new control volume whose center is located at the original cell-face center is defined.

The volume integral of the source term is:

$$Q_\varphi = \rho \int_\Omega S_\varphi d\Omega \approx \rho S_\varphi \Delta\Omega \tag{2.23}$$

where Ω is the cell volume. For the unsteady source term, a three-level second order scheme is used:

$$\rho \frac{\partial \varphi}{\partial t} = \frac{\rho(3\varphi_p^n - 4\varphi_p^{n-1} + \varphi_p^{n-2})}{2\Delta t} \tag{2.24}$$

where Δt is the time step, n is the time level. All the steady-state terms in the equations are discretized using the implicit scheme.

The momentum equations contain a contribution from the pressure. The volume integral of the pressure gradient term in *u*-momentum equation can be obtained by:

$$Q_{u,P}^p = \int_\Omega -\left(\frac{\partial p}{\partial x}\right)_P d\Omega \approx -\left(\frac{\delta p}{\delta x}\right)_P \Delta\Omega \tag{2.25}$$

Then the final discrete form of the *u*-momentum equation is:

$$A_P^u u_P + \sum_l A_l^u u_l = Q_{u,P}^* - \left(\frac{\delta p}{\delta x}\right)_P \Delta\Omega \tag{2.26}$$

where P is the index of an arbitrary node; the index l denotes the four neighboring points E, W, S, N; the coefficients A_P^{φ}, A_E^{φ}, A_W^{φ}, A_N^{φ}, A_S^{φ} are those of the resultant algebraic equations; and $Q_{u,P}^{*}$ is the integral of the source term contributed by other forces.

In the present study, SIMPLEC method (van Doormal JP and Raithby, 1984) is applied to couple the velocity and pressure. To avoid oscillations in the pressure or velocity, the interpolation proposed by Rhie and Chow (1983) is adopted:

$$u_e^m = \overline{\left(u^m\right)_e} - \Delta\Omega_e \overline{\left(\frac{1}{A_P^u + \sum_l A_l^u}\right)_e} \left[\left(\frac{\delta p}{\delta x}\right)_e - \overline{\left(\frac{\delta p}{\delta x}\right)_e}\right]^{m-1} \tag{2.27}$$

where m is interation step for each time level.

2.2.2 Porous Medium Region

Equations (2.6) and (2.7) recover the standard Navier-Stokes equations when the porosity approaches unity and permeability goes to be infinity. Thus, the discretizing procedure for porous medium is similar to that for the homogenous fluid as the two sets of governing equations are similar in form. The discretized diffusion flux is similar in form to Equation (2.18). The convective flux at a cell face is similar in form to Equation (2.15) except for a small change:

$$F_e^c = \int_{S_e} \frac{\rho u}{\varepsilon} \vec{u} \cdot \vec{n} dS \approx m_e u_e / \varepsilon_e \tag{2.28}$$

The volume integral of the pressure gradient term (similar in form to Equation 18) is:

$$Q_{u,P}^{p*} = \int_{\Omega} -\left(\frac{\partial \left(\varepsilon p^* \right)}{\partial x} \right)_P d\Omega \approx -\left(\varepsilon \frac{\delta p}{\delta x} \right)_P \Delta\Omega \tag{2.29}$$

For the unsteady source term, a three-level second order scheme is used as shown in Equation (2.24).

For the Darcy term in Equations (2.6) and (2.7), the volume integral can be expressed as:

$$Q_D^u = \int_{\Omega} -\left(\frac{\mu\varepsilon}{K} u \right)_p d\Omega = -\left(\frac{\mu\varepsilon}{K} \right)_p \Delta\Omega \cdot u_p \tag{2.30}$$

For the Forchheimer term, the volume integral is given by:

$$Q_F^u = \int_{\Omega} -\left(\frac{\rho\varepsilon C_F \sqrt{u^2 + v^2}}{\sqrt{K}} u \right)_p d\Omega = -\left(\frac{\rho\varepsilon C_F \sqrt{u^2 + v^2}}{\sqrt{K}} \right)_p \Delta\Omega \cdot u_p \tag{2.31}$$

It is convenient to treat the Darcy and Forchheimer terms as source terms. However, Equations (2.30) and (2.31) indicate that, after integrating, both terms become a product of Darcy velocity component and a coefficient. The two coefficients can be added into the coefficients of the algebraic equation A_p^u, which will accelerate the convergence rate.

The procedure to obtain the pressure correction equation is also similar to that for homogenous fluid (Equation (2.27)), except for a small change:

$$u_e^m = \overline{\left(u^m \right)}_e - \Delta\Omega_e \overline{\left(\frac{1}{A_P^u + \sum_l A_l^u} \right)}_e \left[\left(\frac{\delta \left(\varepsilon p^* \right)}{\delta x} \right)_e - \overline{\left(\frac{\delta \left(\varepsilon p^* \right)}{\delta x} \right)}_e \right]^{m-1} \tag{2.32}$$

2.2.3 Interface Treatment

In some cases, structured grids are difficult, even impossible, to construct for complex geometries. Therefore, in the present study, multi-block grids method is applied to provide a compromise between the simplicity and wide variety of solvers available for structured grids and ability to handle complex geometries that unstructured grids allow.

Figure 2.2 shows details of the interface between two different blocks. Two neighboring control volumes, lying in Block A and Block B respectively, share the interface. The grids in two neighboring blocks match at the interface. Generally, there are three types of interfaces when the block-structured grids method is employed to calculate the flow in the composite region: fluid - fluid interface, porous medium - porous medium interface, and fluid - porous medium interface.

2.2.3.1 Interface between the Same Media

In this case, both blocks A and B (Figure 2.2) represent the same media, either fluid or porous. The method proposed by Lilek *et al.* (1997) is applied to treat the block interface. A special data structure is designed to save the information at the interface, which consists of: the indices of the left (L) and right (R) neighboring cells, the surface vector (pointing from L to R) and the coordinates of cell-surface center (Figure 2.2). The interface cell surface shared by two CVs is treated as a cell surface in the interior of the block. Thus, the convective and diffusive terms at the block interface can be calculated in the same way as that (Section 2.2.2) for the cell faces in

the interior of the block. Then the contributions from the interface cell faces, namely A_L and A_R, can be obtained.

Each interface cell face contributes to the source terms for the neighboring CVs. Thus, if the east side of a CV is a block interface, the coefficient A_E (Equation (2.26)) is set to zero. However, the algebraic equation at node L receives the contribution $A_R\varphi_R$, while at node R, the contribution is $A_L\varphi_L$.

2.2.3.2 Interface between Fluid and Porous Media

2.2.3.2.1 Velocity and Pressure

In this case, blocks A and B (Figure 2.2) represent fluid and porous medium respectively. The velocity vector at the interface is given by $\vec{v}_{\text{interface}}$. It can be written in either the *x*-*y* or *n*-*t* coordinate systems as:

$$\vec{v}_{\text{interface}} = u\vec{e}_x + v\vec{e}_y = u_n\vec{n} + u_t\vec{t} \tag{2.33}$$

where u and v are the components of $\vec{v}_{\text{interface}}$ in the *x* and *y* directions while u_n and u_t are the $\vec{v}_{\text{interface}}$ components along *n* and *t* directions respectively. And the component u_t then can be written as:

$$u_t = u\vec{e}_x \cdot \vec{t} + v\vec{e}_y \cdot \vec{t} \tag{2.34}$$

By combining Equations (2.9), (2.11) and (2.33):

$$\frac{\mu}{\varepsilon}\frac{\partial \vec{v}_{\text{interface}}}{\partial n}\bigg|_{\text{porous}} - \mu\frac{\partial \vec{v}_{\text{interface}}}{\partial n}\bigg|_{\text{fluid}} = \beta\frac{\mu}{\sqrt{K}}u_t\vec{t} + \beta_1\rho u_t^2\vec{t} \tag{2.35}$$

The unit vector ($\vec{t}$) parallel to the interface (Figure 2) is calculated from:

$$\vec{t} = \frac{\left(x_{ne} - x_{se}\right)\vec{e}_x + \left(y_{ne} - y_{se}\right)\vec{e}_y}{\sqrt{\left(x_{ne} - x_{se}\right)^2 + \left(y_{ne} - y_{se}\right)^2}} = \frac{\Delta x_e \vec{e}_x + \Delta y_e \vec{e}_y}{l_e} \tag{2.36}$$

By substituting the components of $\vec{v}_{\text{interface}}$ in the *x* and *y* directions, the Equation (2.35) becomes:

$$\frac{\mu}{\varepsilon}\frac{\partial u}{\partial n}\bigg|_{\text{porous}} - \mu\frac{\partial u}{\partial n}\bigg|_{\text{fluid}} = \beta\frac{\mu}{\sqrt{K}}\frac{u\Delta x_e\Delta x_e + v\Delta y_e\Delta x_e}{l_e^2} + \beta_1\rho\frac{\Delta x_e\left(u\Delta x_e + v\Delta y_e\right)^2}{l_e^3} \tag{2.37}$$

$$\frac{\mu}{\varepsilon}\frac{\partial v}{\partial n}\bigg|_{\text{porous}} - \mu\frac{\partial v}{\partial n}\bigg|_{\text{fluid}} = \beta\frac{\mu}{\sqrt{K}}\frac{u\Delta x_e\Delta y_e + v\Delta y_e\Delta y_e}{l_e^2} + \beta_1\rho\frac{\Delta y_e\left(u\Delta x_e + v\Delta y_e\right)^2}{l_e^3} \tag{2.38}$$

The derivatives at the interface are calculated from the values at auxiliary nodes L' and R'; these nodes lie at the intersection of the cell face normal n and straight lines connecting nodes *L* and *N* or *R* and *NR*, respectively, as shown in Figure 2.2. The normal gradients at the interface can be calculated by using the first order difference approximation:

$$\frac{\partial u}{\partial n}\bigg|_{\text{porous}} = \frac{u\big|_{R'} - u\big|_e}{L_{eR'}},\ \frac{\partial v}{\partial n}\bigg|_{\text{porous}} = \frac{v\big|_{R'} - v\big|_e}{L_{eR'}} \tag{2.39}$$

$$\frac{\partial v}{\partial n}\bigg|_{\text{fluid}} = \frac{v\big|_e - v\big|_{L'}}{L_{L'e}},\ \frac{\partial v}{\partial n}\bigg|_{\text{fluid}} = \frac{v\big|_e - v\big|_{L'}}{L_{L'e}} \tag{2.40}$$

The Cartesian velocity components at L' and R' can be calculated by using bilinear interpolation or by using the gradient at the control volume center:

$$u\big|_{L'} = u\big|_L + \left(gradu\right)_L \cdot \overrightarrow{L'L} \tag{2.41}$$

To obtain higher order approximation of the derivatives, the velocity components at more auxiliary nodes may be needed. Alternatively, the shape

functions may be used, which produces a kind of combined Finite Element/Finite Volume method for calculating the higher order approximations.

By using Equations (2.37) to (2.41) and explicitly calculating the terms at the right hand sides of Equations (2.37) and (2.38), the Cartesian velocity components u and v at the interface are obtained. Then the convective fluxes at the interface can be calculated. The diffusive fluxes are calculated from Equations (2.39) - (2.41). Then the coefficients A_L and A_R can be obtained.

To close the algebra equation system, the pressure at the interface must be determined. However, the pressure gradient at the interface may not be continuous due to the rather large Darcy and Forchheimer terms (Equations (2.6) and (2.7)), which may result in a rapid pressure drop at the porous side (Betchen et al., 2006)). This discontinuity of the pressure gradient becomes more severe at higher Reynolds number and lower Darcy number. Thus it requires special treatment to estimate the interface pressure from that of the vicinity at either side. A simplistic pressure estimation may give unrealistic, oscillatory velocity profile. The coupling issue of pressure-velocity at the interface was described in a recent paper by Betchen et al. (2006) who proposed a solution that enables stable calculations. The pressure is extrapolated in the fluid side to a location at a small distance near the interface. From this location, a momentum balance is then used to estimate the interface pressure. This estimate is then averaged with the pressure extrapolated from the porous side to obtain the interface pressure. In the present paper, a less complex treatment was adopted. Extrapolations from the fluid and porous sides give two different estimates

of the interface pressure. The average of the two estimates is used as the interface pressure. A small number of iterations is required for accuracy.

2.2.3.2.2 Temperature or Mass

The heat or mass transfer interface conditions are defined by Equations (2.12) and (2.13). Following the discretization procedure for the velocity above, the discreticized equations at the interface are:

$$R_k \left.\frac{\partial \varphi}{\partial n}\right|_{\text{porous}} - \left.\frac{\partial \varphi}{\partial n}\right|_{\text{fluid}} = 0 \tag{2.42}$$

$$\left.\frac{\partial \varphi}{\partial n}\right|_{\text{porous}} = \frac{\varphi|_{R'} - \varphi|_{e}}{L_{eR'}} \tag{2.43}$$

$$\left.\frac{\partial \varphi}{\partial n}\right|_{\text{fluid}} = \frac{\varphi|_{e} - \varphi|_{L'}}{L_{L'e}} \tag{2.44}$$

$$\varphi|_{L'} = \varphi|_{L} + \left(grad\,\varphi\right)_{L} \cdot \overrightarrow{L'L} \tag{2.45}$$

The temperature or mass values at the interface can be obtained. The coefficients A_L and A_R for the energy or mass transfer equations can be used for the discretization along the interface control volume.

2.3 Solution Algorithm

The SIMPLEC algorithm based on Multi-block grids and a SIP solver is described as follows:

1. Estimate the initial flow and pressure fields in each block;

2. Assemble the elements of matrix A and the source term Q in each block, ignoring the contributions of the block interfaces;

3. Loop over the list of interface cell faces, updating A_p and Q_p at nodes L and R, and calculate the matrix elements stored at the cell face, A_L and A_R;

4. Assemble and solve the momentum equations to obtain u^{m*} and v^{m*}; then assemble and solve the pressure-correction equation to obtain p'; Calculate the residuals in each block using the regular part of the matrix A. Loop over the list of interface cell faces and update the residuals at nodes L and R by adding the products of $A_{R\varphi R}$ and $A_{L\varphi L}$, where φ denotes u, v or p';

5. Correct the velocities and pressure to obtain the velocities u^m and v^m, which satisfy the continuity equation, and the new pressure *pm* in each blocks;

6. Return to step 2 and repeat, using u^m, v^m and p^m as improved estimates for the next iteration, until all corrections are negligibly small.

2.4 Conclusions

A numerical method was presented for the transport phenomena in porous/fluid coupled domains. Non-orthogonal body-fitted and multi-block grids were used for the discretization of the governing equations in the homogenous flow and porous medium regions. The special attentions to the treatment of the interface between them were given in detail. A stress jump interfacial boundary condition was implemented, which included both viscous and inertia effects. For interface heat or

mass transport, continuities of temperature, heat flux, mass and mass flux are implemented. The SIMPLEC algorithm is used to couple the velocity and pressure. The strongly implicit procedure (SIP) is applied to solve the resultant algebraic equation system.

The main computational code is programmed with the use of C++ language and the grids are generated with the use of Fortran language. Both the convective and diffusive fluxes are approximated using central difference scheme, which is second order accurate. Linear interpolation and numerical differentiation are used to express the cell-face value of the variables and their derivatives through the nodal values. Discretized momentum equations lead to an algebraic equation system for velocity component u and v where pressure and other fluid properties are taken from the previous iteration except the first iteration where initial conditions are applied. These linear equation system are solved iteratively (inner iteration) to obtain improved estimate of velocity. The improved velocity field is then used to estimate new mass fluxes, which satisfy the continuity equation. Pressure-correction equation is then solved using the same linear equation solver and to the same tolerance. Heat or mass transfer equation is then solved in the same manner to obtain the estimate of new solutions.

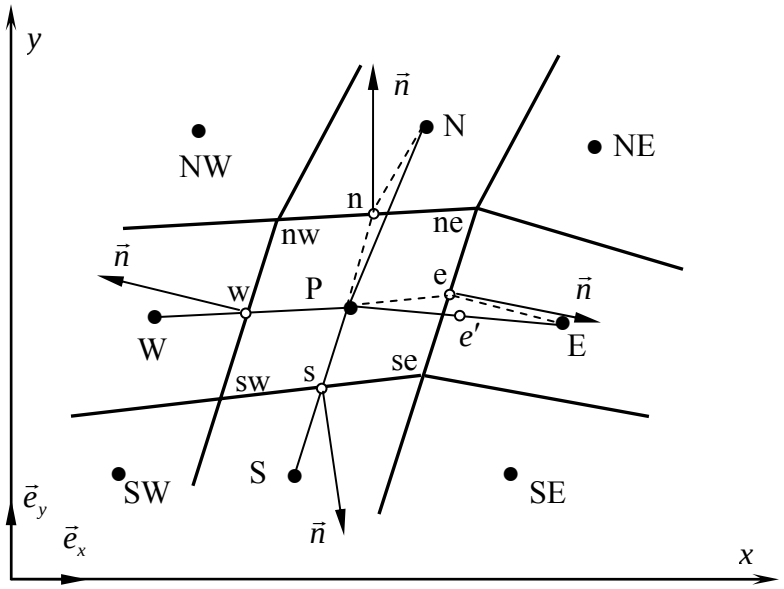

Figure 2.1 A typical two-dimensional control volume.

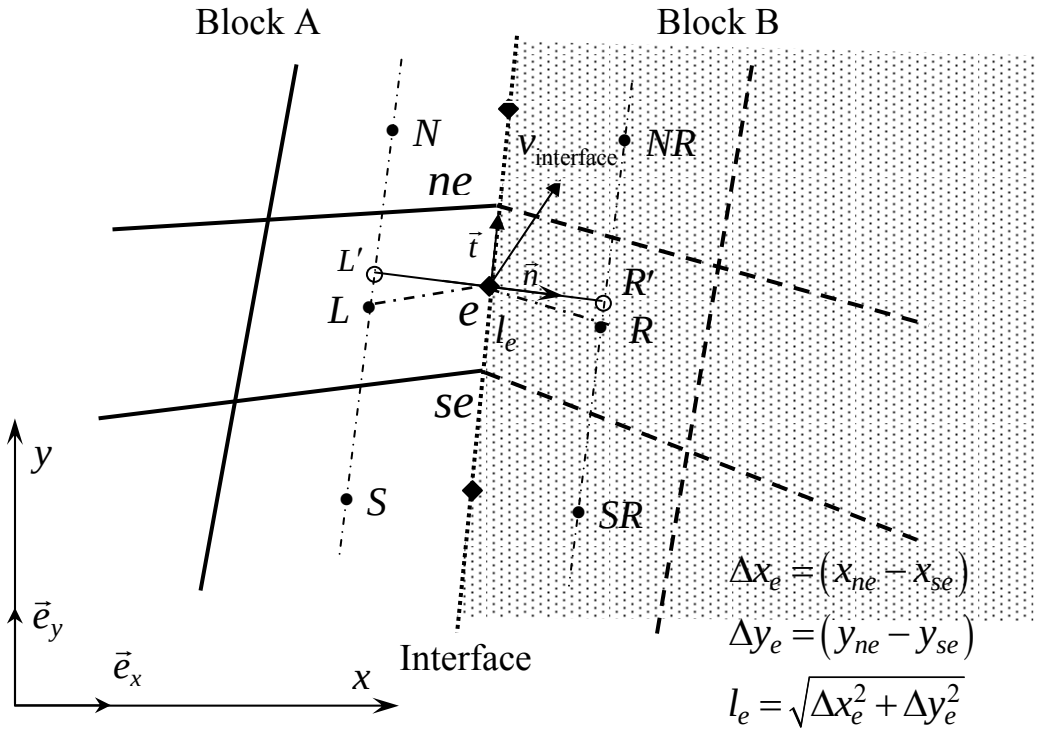

Figure 2.2 Interface between two blocks with matching grids.

Chapter 3

Validation of Numerical Method

In this chapter, in order to validate the adopted numerical method, it is applied to several benchmark problems. Firstly, flows in homogeneous fluid region are investigated, which include: 1) lid driven flow in a square cavity; 2) flow around a circular cylinder; 3) natural convection in a square cavity; 4) forced convection over a backward-facing step. Secondly, flow problems in porous medium region are conducted, which include: 1) flow in a fluid-saturated porous medium channel; 2) natural convection in a fluid saturated porous medium cavity. Finally, the coupled flows in porous and homogenous domains are considered, which include: 1) flow in a channel partially filled with a layer of a porous medium; 2) flow around a porous square cylinder. The computational results are compared with published benchmark solutions to prove the accuracy of the present numerical method.

3.1 Flow in Homogeneous Fluid Region

3.1.1 Lid Driven Flow

Lid driven flow in a square cavity is often used for validating numerical methods based on orthogonal grids because of the simple geometry and the complex developed flow field with multiple regions of recirculation near the corners (Figure 3.1). For such kind of flow, the dimensionless governing equations are as follows:

$$\frac{\partial u}{\partial x}+\frac{\partial v}{\partial y}=0 \tag{3.1}$$

$$\frac{\partial u}{\partial t}+u\frac{\partial u}{\partial x}+v\frac{\partial u}{\partial y}=-\frac{\partial p}{\partial x}+\frac{1}{Re}\bullet(\frac{\partial^2 u}{\partial x^2}+\frac{\partial^2 u}{\partial y^2}) \tag{3.2}$$

$$\frac{\partial v}{\partial t}+u\frac{\partial v}{\partial x}+v\frac{\partial v}{\partial y}=-\frac{\partial p}{\partial y}+\frac{1}{Re}\bullet(\frac{\partial^2 v}{\partial x^2}+\frac{\partial^2 v}{\partial y^2}) \tag{3.3}$$

where Reynolds number is defined as:

$$Re=\frac{U_{lid}L\rho}{\mu} \tag{3.4}$$

where L is the cavity height, U_{lid} is the top wall velocity. The other walls are kept static and with non-slip boundary conditions.

The numerical results are obtained with 62x62 grids. Figure 3.2 shows the streamline contour of a lid driven flow in a square cavity at *Re* = 400. The detailed comparisons between the present results and the numerical results for *Re* = 400 and *Re* = 1000 by Ghia et al. (1982) are shown in Figure 3.3. The horizontal U velocity component on the vertical centerline of the cavity and the vertical V velocity component on the horizontal centerline of the cavity show good agreement with bench mark solution of Ghia et al. (1982).

3.1.2 Flow around a Circular Cylinder

The governing equations are the same with Equations (3.1) to (3.3). The flow with an average velocity U_∞ is coming uniformly around a circular cylinder. Non-slip

boundary condition is imposed at the cylinder surface. The Reynolds number here is defined as:

$$Re = \frac{U_\infty D \rho}{\mu} \tag{3.5}$$

where U_∞ is free stream velocity and D is the diameter of the cylinder.

The drag and lift coefficients are defined as,

$$C_D = \frac{F_x}{\frac{1}{2}\rho U_\infty^2 D} \tag{3.6}$$

$$C_L = \frac{F_y}{\frac{1}{2}\rho U_\infty^2 D} \tag{3.7}$$

where the drag and lift force can be computed from the force along the cylinder interface as,

$$F_x = -\int_\tau f_x ds \tag{3.8}$$

$$F_y = -\int_\tau f_y ds \tag{3.9}$$

where f_x and f_y are the x and y components of the singular force respectively.

The numerical results are obtained with 360x160 grids. For steady flow, numerical results of the length of the recirculation zone, angle of separation and drag coefficient for Re = 20 and Re = 40 are compared with those previous studies (Russel and Wang, 2003; Ye et al. 1999; Dennis and Chang, 1970; Calhoun, 2002). Good agreement is obtained as shown in Table 3.1.

For unsteady flow, the drag and lift coefficients for the flow around a circular cylinder are compared with those in previous studies (Braza et al., 1986;, Liu et al., 1998; Calhoun, 2002). Figure 3.4 shows the drag and lift coefficient development histories for *Re* = 200. The results shown in Table 3.2 agree well with the benchmark studies, which indicate that the present code is valid for the simulation of unsteady flow problems. Figure 3.5 shows instantaneous streamlines for flow around a circular cylinder with *Re* =40 and 200.

3.1.3 Natural Convection in a Square Cavity

Natural convection in a square cavity is a benchmark problem for heat transfer, as shown in Figure 3.6. The dimensionless governing equations are as follows:

$$\frac{\partial u}{\partial x}+\frac{\partial v}{\partial y}=0 \tag{3.10}$$

$$\frac{\partial u}{\partial t}+u\frac{\partial u}{\partial x}+v\frac{\partial u}{\partial y}=-\frac{\partial p}{\partial x}+Pr\bullet(\frac{\partial^2 u}{\partial x^2}+\frac{\partial^2 u}{\partial y^2}) \tag{3.11}$$

$$\frac{\partial v}{\partial t}+u\frac{\partial v}{\partial x}+v\frac{\partial v}{\partial y}=-\frac{\partial p}{\partial y}+Pr\bullet(\frac{\partial^2 v}{\partial x^2}+\frac{\partial^2 v}{\partial y^2})+Pr\bullet Ra\bullet T \tag{3.12}$$

$$\frac{\partial T}{\partial t}+u\frac{\partial T}{\partial x}+v\frac{\partial T}{\partial y}=\frac{\partial^2 T}{\partial x^2}+\frac{\partial^2 T}{\partial y^2} \tag{3.13}$$

where the following scales have been used for non-dimensionalisation,

$$x^*=\frac{x}{L_{ref}},\ y^*=\frac{y}{L_{ref}},\ u^*=\frac{u}{\alpha/L_{ref}},\ v^*=\frac{v}{\alpha/L_{ref}}$$

$$p^*=\frac{p}{\rho\alpha^2/L_{ref}^2},\ T^*=\frac{t-T_0}{T_H-T_C} \tag{3.14}$$

$$Ra = \frac{g\beta\Delta TL_{ref}^3}{\nu\alpha},\ Pr = \frac{\gamma}{\alpha}$$

where γ is the fluid kinematic viscosity, β is the coefficient of the thermal expansion, $T_0 = T_C$ is the characteristic temperature, α is the effective thermal diffusivity, L_{ref} is the characteristic dimension, $\Delta T = T_H - T_C$, T_H and T_C are the hot and cold wall temperatures, respectively.

Note that the asterisks have been omitted from the dimensionless governing equations for the sake of convenience.

The average Nusselt number is defined as,

$$\mathrm{Nu}_{av} = \frac{1}{S}\int_0^s \mathrm{Nu}ds \tag{3.15}$$

Here S is the wall where local Nusselt number is located,

$$\mathrm{Nu} = \frac{\partial T}{\partial n}|_{wall} \tag{3.16}$$

The cases (Pr=0.72) with $Ra = 10^3$, 10^4, 10^5 and 10^6 are compared with those in de Vahl Davis (1983) and Nithiarasu et al. (1997). The numerical results are obtained based on a 82x82 mesh. Figure 3.7 shows temperature and streamline contours with $Ra = 10^5$. Table 3.3 shows that the average Nusselt number along the cold wall agrees well with the benchmark solutions.

3.1.4 Forced Convection over a Backward-facing Step

For convection heat transfer, a benchmark problem is forced convection over a backward-facing step, as shown in Figure 3.8a. The inlet flow (fully-developed) and step wall temperature are set to T_i; the upper and bottom walls supply a constant heat flux q.

The dimensionless governing equations are as follows:

$$\frac{\partial u}{\partial x}+\frac{\partial v}{\partial y}=0 \tag{3.17}$$

$$\frac{\partial u}{\partial t}+u\frac{\partial u}{\partial x}+v\frac{\partial u}{\partial y}=-\frac{\partial p}{\partial x}+\frac{1}{Re}\bullet(\frac{\partial^2 u}{\partial x^2}+\frac{\partial^2 u}{\partial y^2}) \tag{3.18}$$

$$\frac{\partial v}{\partial t}+u\frac{\partial v}{\partial x}+v\frac{\partial v}{\partial y}=-\frac{\partial p}{\partial y}+\frac{1}{Re}\bullet(\frac{\partial^2 v}{\partial x^2}+\frac{\partial^2 v}{\partial y^2}) \tag{3.19}$$

$$\frac{\partial T}{\partial t}+u\frac{\partial T}{\partial x}+v\frac{\partial T}{\partial y}=\frac{1}{Pr\bullet Re}(\frac{\partial^2 T}{\partial x^2}+\frac{\partial^2 T}{\partial y^2}) \tag{3.20}$$

where the following scales have been used for non-dimensionalisation,

$$x^*=\frac{x}{H},\ y^*=\frac{y}{H},\ u^*=\frac{u}{U_{av}},\ v^*=\frac{v}{U_{av}}$$

$$p^*=\frac{p-p_0}{\rho U_{av}^2},\ T^*=\frac{t-T_i}{qH/k_f} \tag{3.21}$$

$$Re=\frac{U_{av}H}{\gamma},\ Pr=\frac{\gamma}{\alpha}$$

Here H is the channel height, U_{av} is the average incoming flow velocity at the inlet, p_0 is the reference pressure, k_f is the fluid conductivity inside.

Note that the asterisks have been omitted from the dimensionless governing equations for the sake of convenience.

The local Nusselt number along the bottom wall is defined as,

$$Nu = \frac{qH}{(T_w - T_i)k_f} \tag{3.22}$$

where T_w is the bottom wall temperature.

In the computation, non-uniform, body-fitted and orthogonal meshes are employed, where the density of meshes over the step back is higher than those in areas far downstream, as shown in Figure 3.8b. A mesh made of 380x100 grids for the flow field is used. Figure 3.9 shows the streamline plot with *Re* = 800, and comparison of velocity profiles with those in benchmark (Gartling, 1990; Martin et al., 1998; Zhang and Zhao, 2000). There is a good agreement for the velocity profiles. For the Nusselt number the agreement is good at small x/H, which is near the inlet. Further away, at large x/H there is good agreement with Zhang and Zhao (2000) but deviation from Martin et al. (1998). The discrepancy is due to the different reference temperatures in the definition of Nusselt number (Equation 3.22). In the present study and that of Zhang and Zhao (2000) the reference temperature is the incoming flow temperature T_i, unlike that of Martin et al. (1998) who used the bulk temperature, which is an average value over the cross section. The bulk temperature would differ more from the inlet temperature at distances further, which thus explains the larger deviation at large x/H.

3.2 Flow in Porous Medium Region

3.2.1 Flow in a Fluid Saturated Porous Medium Channel

The problem under consideration for flow in a fluid saturated porous medium channel is shown in Figure 3.10. For fully developed flow, the dimensionless governing equation is simplified as:

$$\frac{1}{\varepsilon}\frac{\partial^2 \mathrm{U}}{\partial Y^2} - \frac{\mathrm{U}}{Da} - F\mathrm{U}^2 + 1 = 0 \tag{3.23}$$

where Darcy number $Da = \frac{K}{H^2}$, Forchheimer number $F = \frac{C_F \rho G H^4}{K^{1/2}\mu^2}$, $\mathrm{Y} = \frac{y}{H}$, $\mathrm{U} = \frac{\mu u}{GH^2}$. Here G is a constant applied gradient $G = -\frac{dp^*}{dx}$. The analytical solution of (3.23) has been obtained by Nield et al. (1996), which gives:

$$\left(\frac{2F\varepsilon}{3}\right)^{0.5} = \int_0^{b_2} \left[P(t)\right]^{-0.5} dt \tag{3.24}$$

$$\left(\frac{2F\varepsilon}{3}\right)^{0.5} \mathrm{Y} = \int_{\mathrm{U}}^{b_2} \left[P(t)\right]^{-0.5} dt \tag{3.25}$$

where $P(U) = (U - b_1)(U - b_2)(U - b_3)$, $b_2 = U(0)$, $b_1 < b_2 < b_3$ and

$$(b_1, b_3) = \frac{1}{4F}\left\{-\frac{3}{Da} - 2Fb_2 \mp \left[\frac{9}{Da^2} + 48F - \frac{12F^2 b_2}{Da} - 12Fb_2^{\,2}\right]^{1/2}\right\}.$$

The Equations (3.24) and (3.25) can be solved by numerical quadrature.

In the computation, a mesh of 502x52 grids was used. Periodic boundary conditions were assumed at the inlet and outlet. The constant applied pressure gradient was converted to incoming flow Reynolds number. The comparisons of analytical solution and numerical solutions are shown in Figure 3.11, where good agreement between them is obtained.

3.2.2 Natural Convection in a Fluid Saturated Porous Medium

Cavity

Steady natural convection in a porous square cavity is a benchmark problem for heat transfer, as shown in Figure 3.12. The dimensionless governing equations are as follows:

$$\frac{\partial u}{\partial x}+\frac{\partial v}{\partial y}=0 \tag{3.26}$$

$$\begin{aligned}&\frac{1}{\varepsilon}\{u\frac{\partial}{\partial x}(\frac{u}{\varepsilon})+v\frac{\partial}{\partial y}(\frac{u}{\varepsilon})\}=\\&-\frac{1}{\varepsilon}\frac{\partial}{\partial x}(\varepsilon p_f)-\frac{Pr}{Da}u-\frac{1.75}{\sqrt{150}}\frac{(u^2+v^2)^{1/2}}{\sqrt{Da}}\frac{u}{\varepsilon^{3/2}}+\frac{Pr}{\varepsilon}(\frac{\partial^2 u}{\partial x^2}+\frac{\partial^2 u}{\partial y^2})\end{aligned} \tag{3.27}$$

$$\begin{aligned}&\frac{1}{\varepsilon}\{u\frac{\partial}{\partial x}(\frac{v}{\varepsilon})+v\frac{\partial}{\partial y}(\frac{v}{\varepsilon})\}=\\&-\frac{1}{\varepsilon}\frac{\partial}{\partial y}(\varepsilon p_f)-\frac{Pr}{Da}v-\frac{1.75}{\sqrt{150}}\frac{(u^2+v^2)^{1/2}}{\sqrt{Da}}\frac{v}{\varepsilon^{3/2}}+\frac{Pr}{\varepsilon}(\frac{\partial^2 v}{\partial x^2}+\frac{\partial^2 v}{\partial y^2})+RaPrT\end{aligned} \tag{3.28}$$

$$u\frac{\partial T}{\partial x}+v\frac{\partial T}{\partial y}=\frac{\partial^2 T}{\partial x^2}+\frac{\partial^2 T}{\partial y^2} \tag{3.29}$$

where the dimensionless parameter are the same as those in (3.14). The local and average Nusselt numbers are defined as the same as those in (3.15) and (3.16).

In the computation, a mesh made of 80x80 grids for the flow field is used. In Table 3.4, our results for $\varepsilon = 0.4$, 0.6, 0.9 with different Rayleigh numbers and Darcy numbers are compared with the general porous model (Nithiarasu et al., 1997). It is seen that the present values of Nu_{av} are in very good agreement with those obtained by previous authors, which validates the present numerical code.

3.3 Coupled Flow in Porous and Homogenous Domains

3.3.1 Flow in a Channel Partially Filled with a Layer of a Porous Medium

The physical domain is shown schematically in Figure 3.13. It consists of a planar channel which is horizontally divided into a homogenous fluid region with height H_1 above and a fluid-saturated porous region with height H_2 below. The case of height ratio $H_2 / H_1 = 1$ is considered.

The flow is assumed laminar and fully developed. The original governing equations are simplified as follows:

$$\frac{d^2u}{dy^2} = \frac{1}{\mu}\frac{dp}{dx} \qquad \text{for the homogenous fluid} \tag{3.30}$$

$$\frac{d}{dy}\left(\frac{\mu}{\varepsilon}\frac{du}{dy}\right) = \frac{1}{\varepsilon}\frac{d\left(\varepsilon p_f\right)}{dx} + \frac{\mu}{K}u + \frac{\rho C_F}{\sqrt{K}}u^2 \quad \text{for porous medium region} \tag{3.31}$$

with introducing the dimensionless variables

$$\mathrm{U} = \frac{\mu u}{G H_1^{\,2}} \text{ and } \mathrm{Y} = \frac{y}{H_1}, \text{ where } \mathrm{G} = -\frac{dp_f}{dx} \tag{3.32}$$

Equations (3.30) and (3.31) can be rewritten as:

$$\frac{d^2\mathrm{U}}{d\mathrm{Y}^2} = -1 \qquad \text{for the homogenous fluid} \tag{3.33}$$

$$\frac{1}{\varepsilon}\frac{d^2\mathrm{U}}{d\mathrm{Y}^2} = -1 + \frac{1}{Da}\mathrm{U} + F\mathrm{U}^2 \quad \text{for porous medium region} \tag{3.34}$$

where Darcy number $Da = \frac{K}{H_1^2}$ and Forchheimer number $F = \frac{C_F \rho G H_1^4}{K^{1/2} \mu^2}$. The boundary conditions are:

$$\mathrm{U} = 0 \text{ at } \mathrm{Y} = 1 \text{ and } \mathrm{U} = 0 \text{ at } \mathrm{Y} = -H_2 / H_1 \tag{3.35}$$

$$\frac{1}{\varepsilon}\frac{d\mathrm{U}}{d\mathrm{Y}}\bigg|_{\text{porous}} - \frac{d\mathrm{U}}{d\mathrm{Y}}\bigg|_{\text{fluid}} = \frac{\beta}{\sqrt{Da}}\mathrm{U}_{\text{interface}} \text{ at } \mathrm{Y} = 0 \tag{3.36}$$

Following the proposal of Nield et al. (1996), Equations (3.33) to (3.36) can be solved analytically as shown in Yu et al. (2007). Both numerical and analytical solutions are presented for validation of the present numerical implementation.

For the following computations, a mesh of 60 × 60 grids was used. Figure 3.14 shows the *u* velocity profile under different flow conditions. It is seen that the numerical and analytical results for different Darcy numbers, porosity values, and Forchheimer numbers are in good agreement.

3.3.2 Steady Flow around a Porous Square Cylinder

The problem is shown in Figure 3.15a. The governing equations for the fluid domain outside are the same as Equations (3.1) to (3.3). For the porous square domains, the dimensionless governing equations are as follows:

$$\frac{\partial u}{\partial x} + \frac{\partial v}{\partial y} = 0 \tag{3.37}$$

$$\begin{aligned} &\frac{1}{\varepsilon}\{u\frac{\partial}{\partial x}(\frac{u}{\varepsilon}) + v\frac{\partial}{\partial y}(\frac{u}{\varepsilon})\} = \\ &-\frac{1}{\varepsilon}\frac{\partial}{\partial x}(\varepsilon p_f) - \frac{1}{Da \bullet Re}u - \frac{1.75}{\sqrt{150}}\frac{(u^2+v^2)^{1/2}}{\sqrt{Da}}\frac{u}{\varepsilon^{3/2}} + \frac{1}{\varepsilon \bullet Re}(\frac{\partial^2 u}{\partial x^2} + \frac{\partial^2 u}{\partial y^2}) \end{aligned} \tag{3.38}$$

$$\frac{1}{\varepsilon}\{u\frac{\partial}{\partial x}(\frac{v}{\varepsilon})+v\frac{\partial}{\partial y}(\frac{v}{\varepsilon})\}= \\ -\frac{1}{\varepsilon}\frac{\partial}{\partial y}(\varepsilon p_f)-\frac{1}{Da\bullet Re}v-\frac{1.75}{\sqrt{150}}\frac{(u^2+v^2)^{1/2}}{\sqrt{Da}}\frac{v}{\varepsilon^{3/2}}+\frac{1}{\varepsilon\bullet Re}(\frac{\partial^2 v}{\partial x^2}+\frac{\partial^2 v}{\partial y^2}) \tag{3.39}$$

where the dimensionless parameters are the same as those in (3.14).

The Reynolds number here is defined as:

$$Re=\frac{U_\infty H\rho}{\mu} \tag{3.40}$$

where U_∞ is free stream velocity and H is the height of the cylinder.

Figure 3.15b shows an illustration of the body-fitted mesh example around the porous square cylinder. For the computation, grid independency test shows that 240x120 grids for the fluid region and 62x62 grids for the porous region are sufficient.

Figure 3.16 shows the instantaneous streamline contours for different Darcy numbers. It can be seen that when $Da = 10^{-2}$, there is no vortex formation behind the cylinder. When Da decreases from 10^{-3} to 10^{-5}, as less fluid flows through the cylinder, the vortex is formed and its recirculation length is increased. The flow filed resembles that around a solid cylinder, when Da approaches zero.

As shown in Figure 3.17, the circulation length becomes longer with decrease in the Darcy number. However, the recirculation length approaches to a constant value at low Darcy number as the porous cylinder tends to a solid one. The recirculation length at $Da = 10^{-7}$ is about 1.32 (Figure 3.17), which is rather close to the value of around 1.34 for the solid cylinder (Sharma and Eswaran, 2004). This validates current numerical method accuracy for flow around porous bodies.

3.4 Conclusions

A finite volume code has been developed to predict the flow, heat or mass transport in homogenous fluid region, in porous region and in conjugate fluid and porous regions. As detailed in Chapter 2, the present numerical method was based on nonorthogonal, body fitted, and multi-block structured grids, which are effective for problems with complex geometries. The SIMPLEC algorithm was used to couple the velocity and pressure. The strongly implicit procedure (SIP) was applied to solve the resultant algebraic equation system.

For the pure fluid problems, the block interface was treated as the interior cell faces rather than boundaries, which were proposed by Lilek et al. (1997). A variety of numerical experiments are performed to test the validity of the present code. The agreements between the present numerical results and the bench mark results indicate that the present code can be used to predict 2D, incompressible, steady or unsteady, laminar flow, heat and mass transfer problems in Cartesian coordinates.

For the porous flow problems, the governing equations were based on a generalized model including Brinkman and Forchheimer terms as well as non-linear advection term (Hsu and Cheng, 1990; Gartling et al., 1996; Nithiarasu et al., 2002), which recovers the Naver-Stokes equations when the porosity approaches unity. The block interface was also treated as the interior cell faces. Several computed results on the flow and heat transfer in porous media are presented to validate the present method. Comparisons between the present numerical results and analytical solutions, or computational results provided by other researchers confirm that the present code

is a reliable and efficient tool for the steady or unsteady, laminar flow problems in porous media.

For the flow problems with a homogenous fluid and porous medium interface, the main novelty of this study is a numerical method for the theory developed by Ochoa-Tapia and Whitaker (1998b) to model the momentum jump condition at the interface, which includes both viscous and inertial jump parameters β and β_1. A distinctive feature of the present method is the use of multi-block grids which, together with body-fitted grids, makes it more suitable for handling complex geometries. The shear stress jump condition affects both the convective and diffusive fluxes. The normal stress condition, assumed continuous at the interface, is also needed in order to close the two sets of equations.

The numerical results obtained by the present code were consistent with the results reported from the literature, demonstrating that the present method can solve such problems effectively and accurately. The numerical simulation of flow past a porous square cylinder demonstrates the use of multi-block body-fitted grid for coupled fluid-porous flows involving complex geometries.

Table 3.1 Length of the recirculation zone, angle of separation and drag coefficient for Re = 20 and Re = 40.

	Re=20			Re=40		
	L/d	θ	C_D	L/d	θ	C_D
Russel and Wang (2003)	0.94	43.3°	2.13	2.29	53.1°	1.60
Ye et al. (1999)	0.92	-	2.03	2.27	-	1.52
Dennis and Chang (1970)	0.94	43.7°	2.05	2.35	53.8°	1.52
Calhoun (2002)	0.91	45.5°	2.19	2.18	54.2	1.62
Present	0.92	42.3°	2.03	2.21	53.2°	1.52

Table 3.2 Comparison of drag and lift coefficients with previous studies.

	Re=100		Re=200	
	C_D	C_L	C_D	C_L
Braza et al. (1986)	1.36 ± 0.015	± 0.250	1.40 ± 0.050	± 0.75
Liu et al. (1998)	1.35 ± 0.012	± 0.339	1.31 ± 0.049	± 0.69
Calhoun (2002)	1.33 ± 0.014	± 0.298	1.17 ± 0.058	± 0.67
Present	1.38 ± 0.009	± 0.335	1.36 ± 0.050	± 0.73

Table 3.3 Comparison of present results with single phase fluid results in Nithiarasu et al. (1997) and de Vahl Davis (1983) (Pr=0.72).

Rayleigh number	Nusselt number (de Vahl Davis, 1983)	Nusselt number (Nithiarasu et al., 1997)	Present
10^3	1.116	1.127	1.117
10^4	2.238	2.245	2.248
10^5	4.509	4.521	4.531
10^6	8.817	8.800	8.877

Table 3.4 Comparison of Nusselt number along the cold wall (*Pr*=1.0) with Nithiarasu et al. (1997).

Darcy Number	Rayleigh number	$\varepsilon = 0.4$		$\varepsilon = 0.6$		$\varepsilon = 0.9$	
		Nithiarasu et al. (1997)	Present	Nithiarasu et al. (1997)	Present	Nithiarasu et al. (1997)	Present
10^{-2}	10^{3}	1.01	1.01	1.015	1.012	1.023	1.020
	10^{4}	1.408	1.362	1.530	1.500	1.64	1.63
	10^{5}	2.983	2.990	3.555	3.445	3.91	3.92
10^{-4}	10^{5}	1.067	1.064	1.071	1.070	1.072	1.071
	10^{6}	2.55	2.60	2.725	2.714	2.740	2.801
	10^{7}	7.81	7.86	8.183	8.648	9.202	9.49
10^{-6}	10^{7}	1.079	1.078	1.079	1.078	1.08	1.08
	10^{8}	2.97	3.05	2.997	3.081	3.00	3.08
	10^{9}	11.46	12.39	11.79	12.98	12.01	13.30

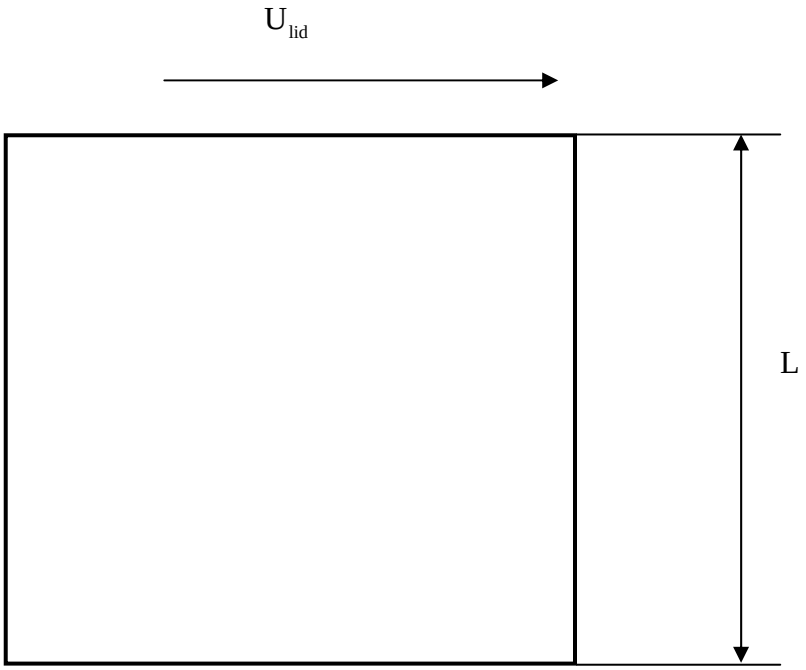

Figure 3.1 Schematic of a lid driven flow in a square cavity.

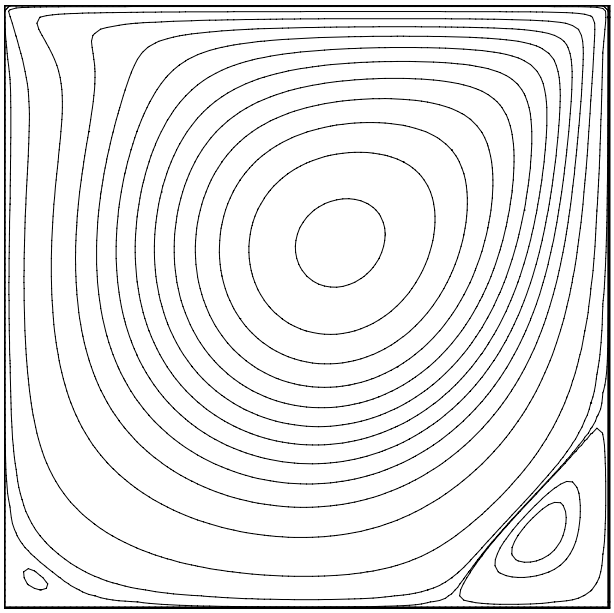

Figure 3.2 Streamline contour of a lid driven flow in a square cavity at *Re* = 400.

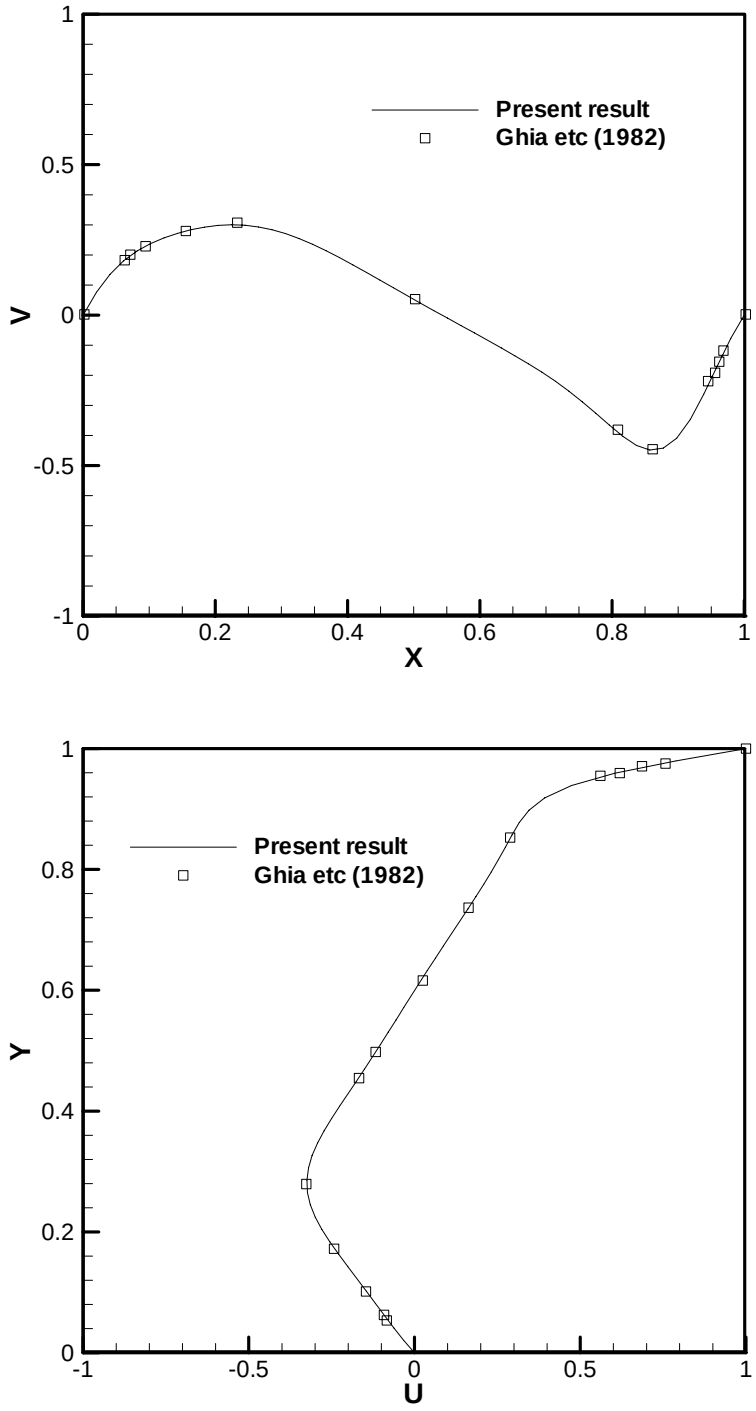

Figure 3.3a

Figure 3.3 Distributions of V (top) and U (bottom) velocity components along the central lines: (a) *Re* =400; (b) *Re* =1000.

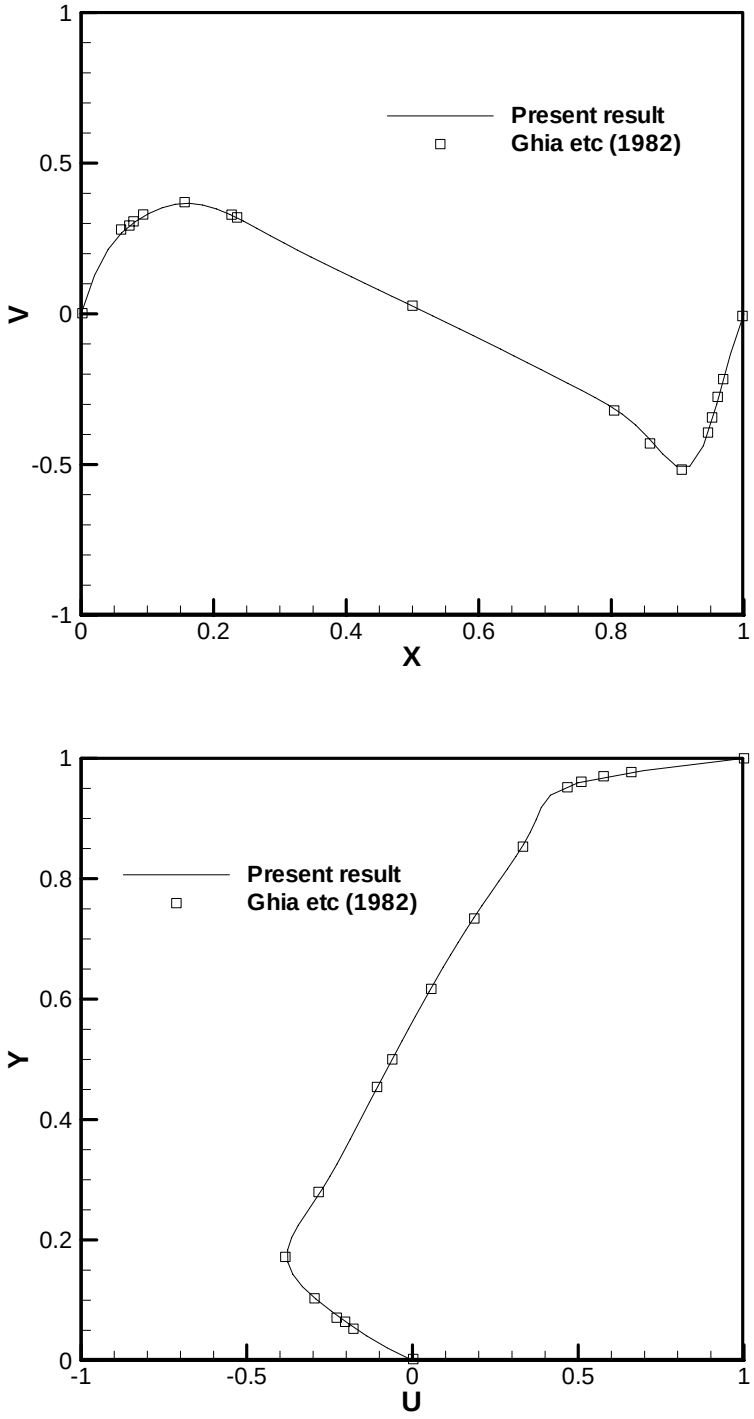

Figure 3.3b

Figure 3.3 Distributions of V (top) and U (bottom) velocity components along the central lines: (a) *Re* =400; (b) *Re* =1000.

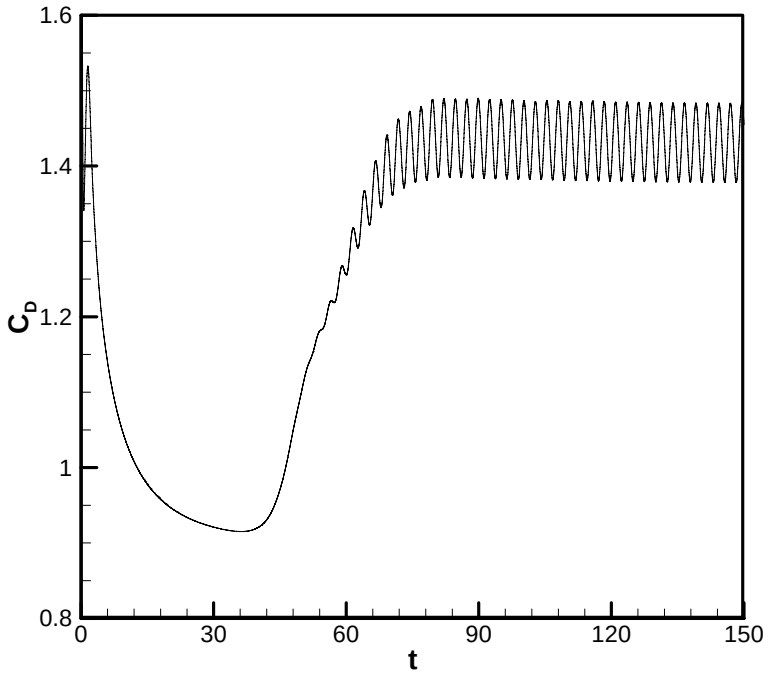

(a)

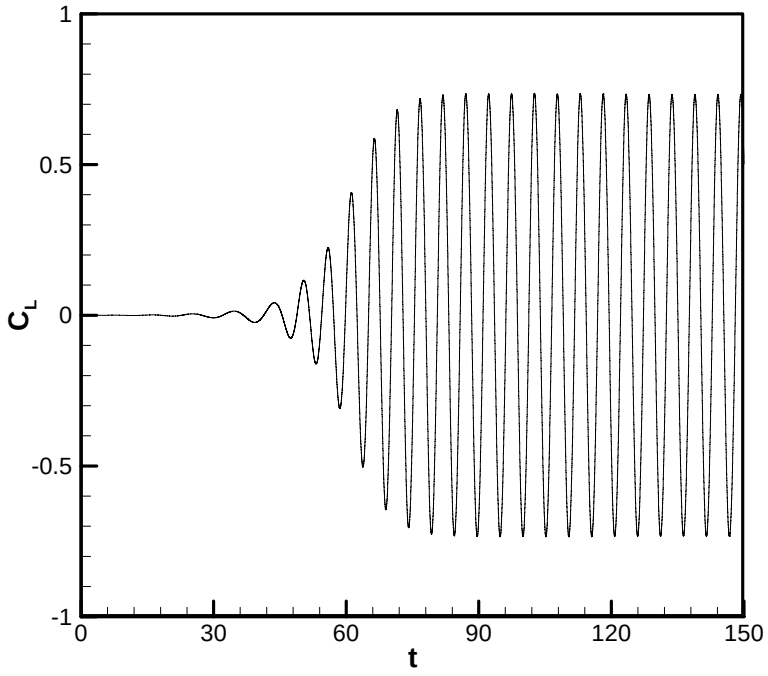

(b)

Figure 3.4 (a) Drag and (b) lift coefficients development histories for *Re* = 200.

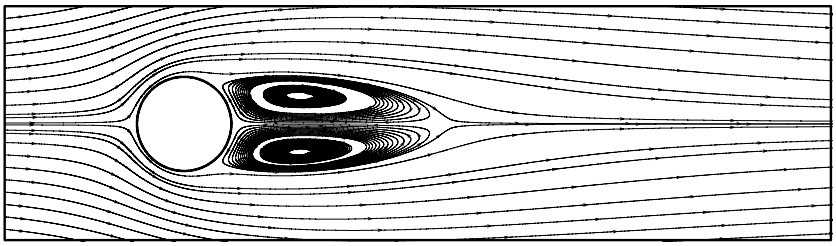

(a)

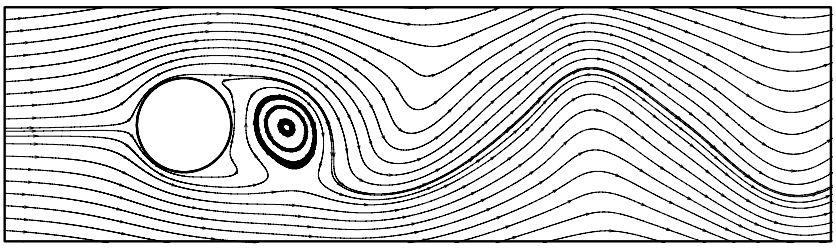

(b)

Figure 3.5 Instantaneous streamlines for flow around a circular cylinder: (a) $Re = 40$; (b) $Re = 200$.

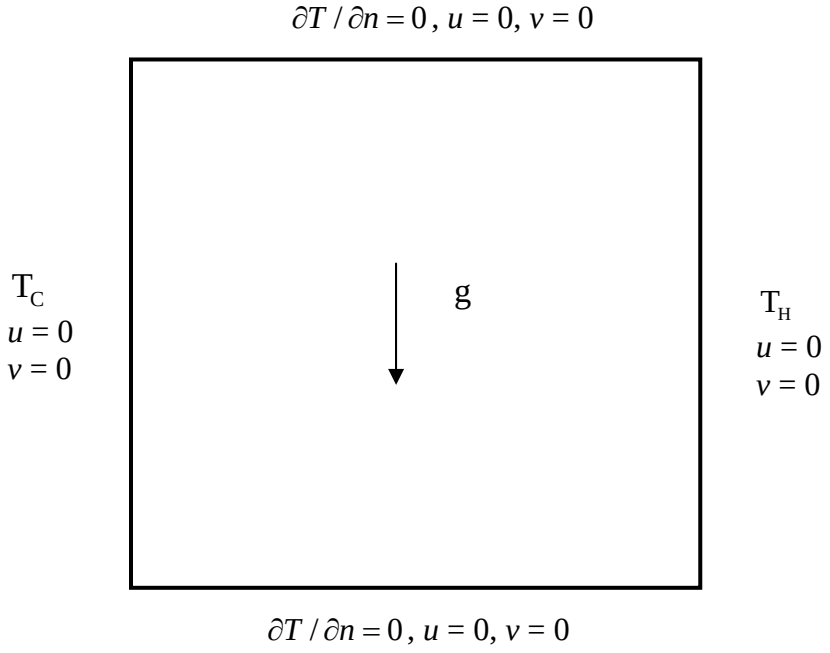

Figure 3.6 Schematic of natural convection in a square cavity.

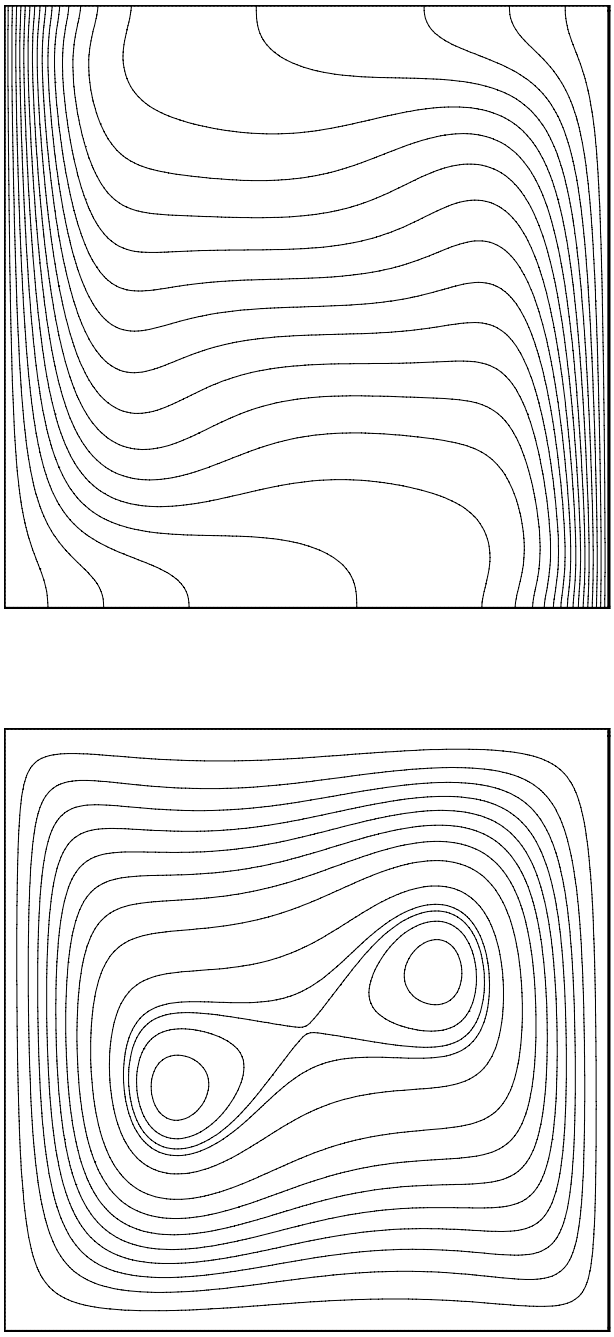

Figure 3.7 Temperature (top) and streamline (bottom) contours with $Ra = 10^5$.

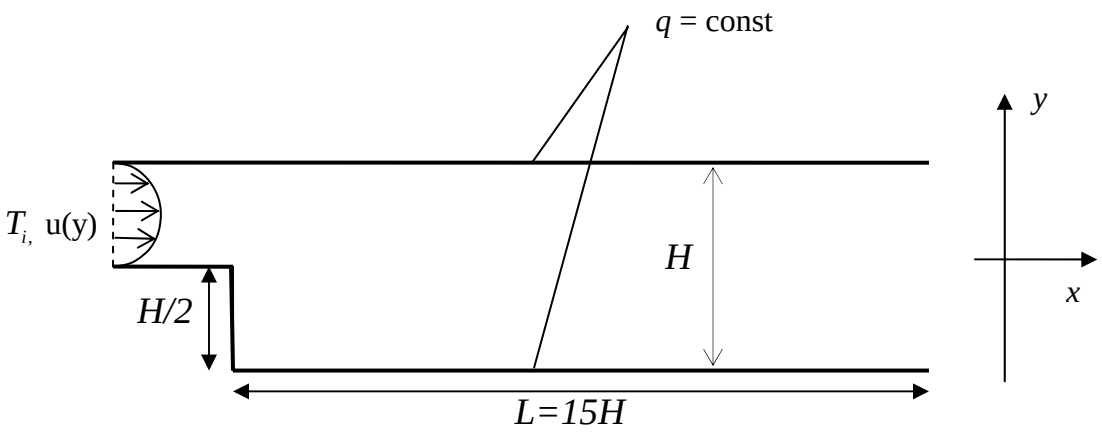

(a)

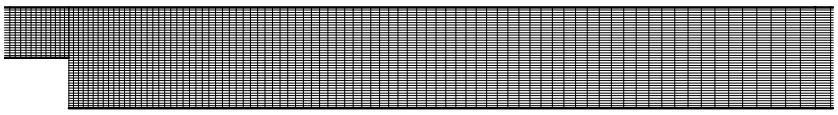

(b)

Figure 3.8 Forced convection over a backward facing step:
(a) Schematic of the problem; (b) Mesh illustration.

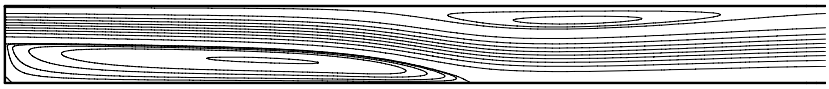

(a)

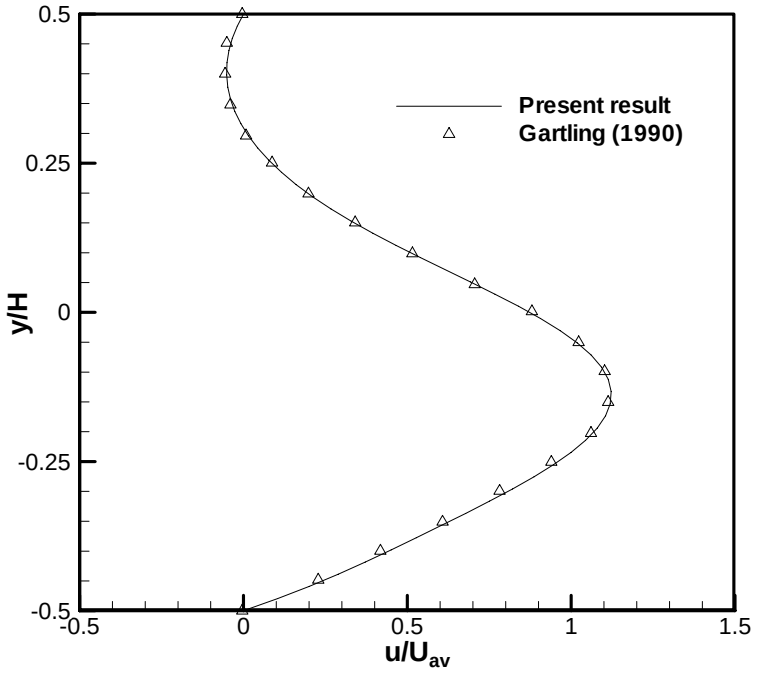

(b)

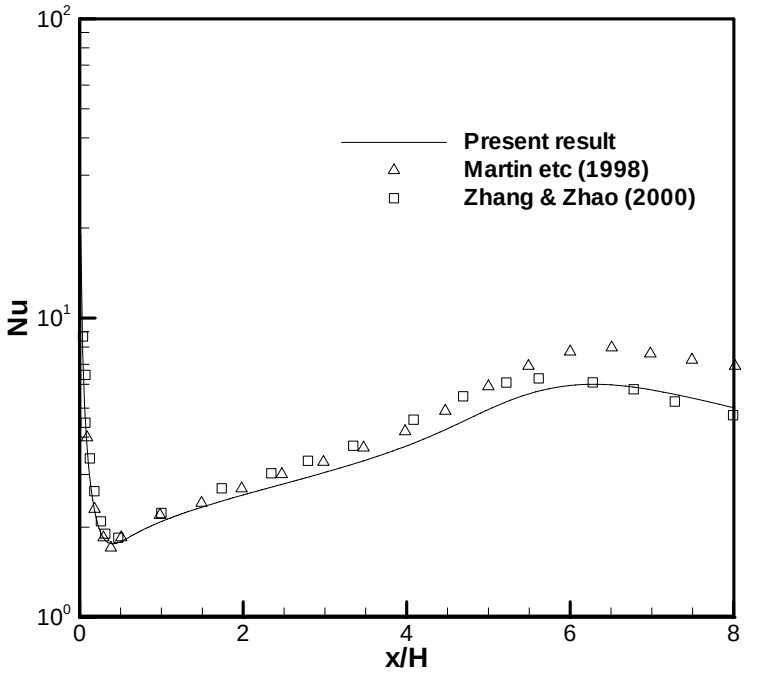

(c)

Figure 3.9 Forced convection past backward-facing step at *Re* = 800: (a) streamline plot; (b) streamwise velocity profile at x/H=7.0; (c) lower wall Nusselt number versus axial location.

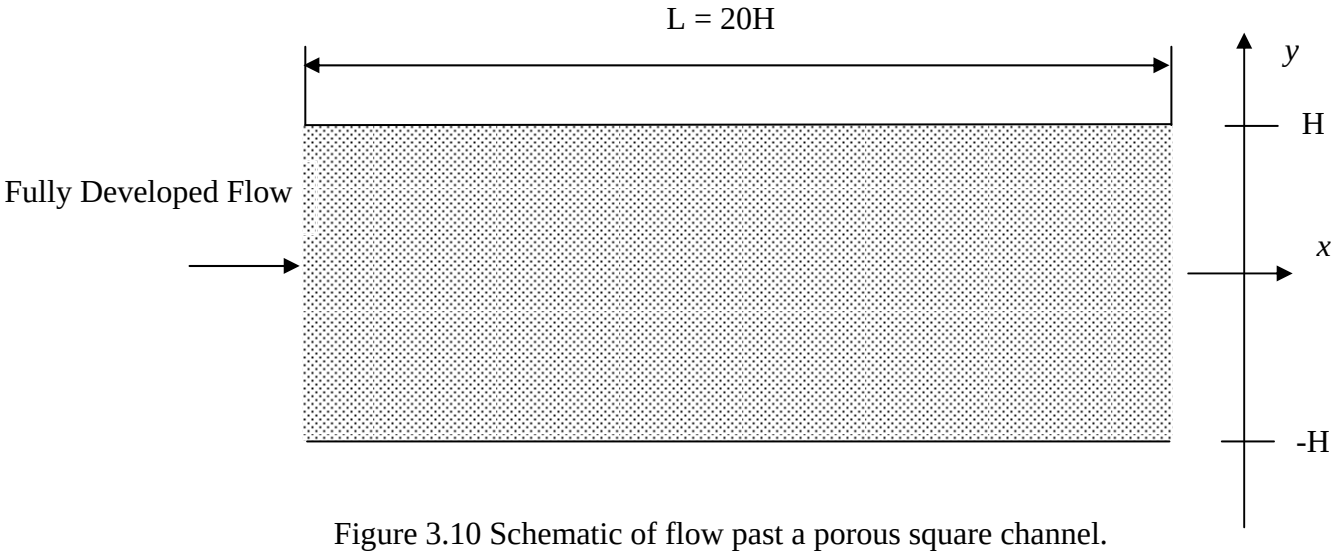

Figure 3.10 Schematic of flow past a porous square channel.

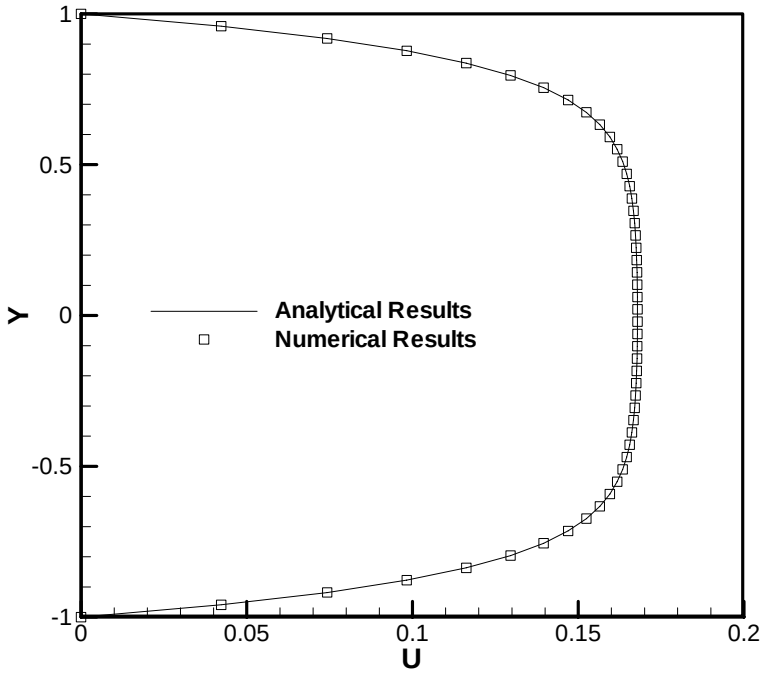

(a)

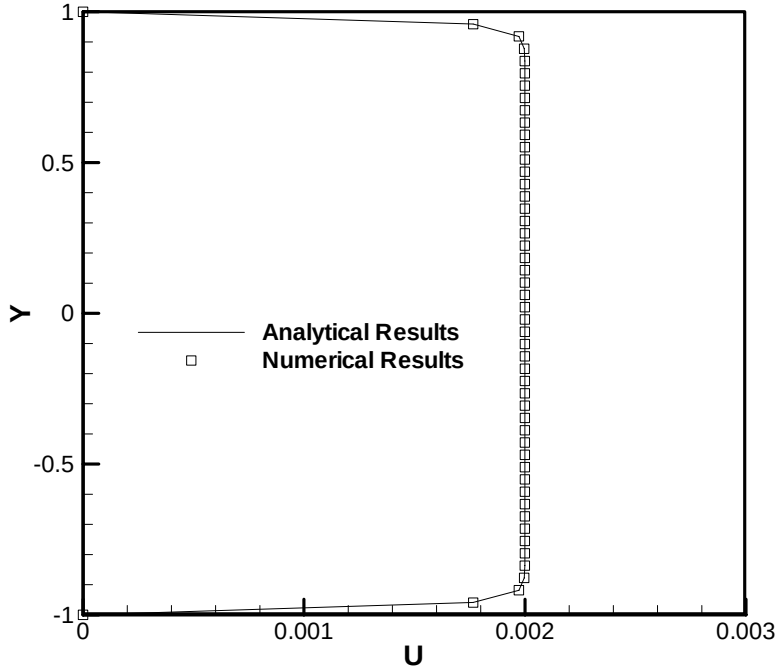

(b)

Figure 3.11 Comparisons of velocity profiles in the porous square channel with $\varepsilon = 0.4$, Re = 20: (a) $Da = 10^{-2}$; (b) $Da = 10^{-4}$.

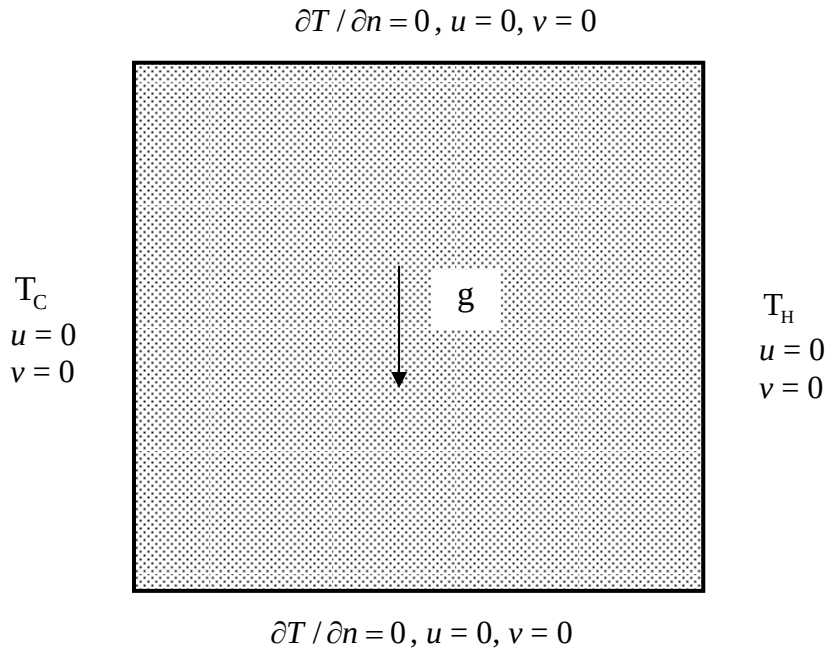

Figure 3.12 Schematic of natural convection in a porous square cavity.

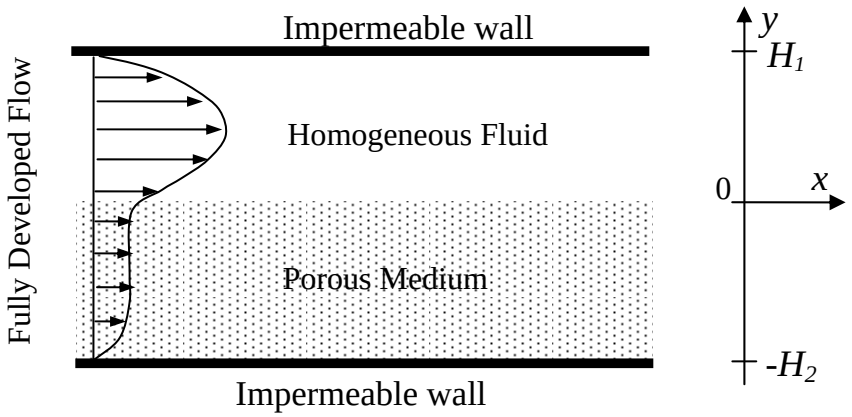

Figure 3.13 Schematic of flow in a channel partially filled with saturated porous medium.

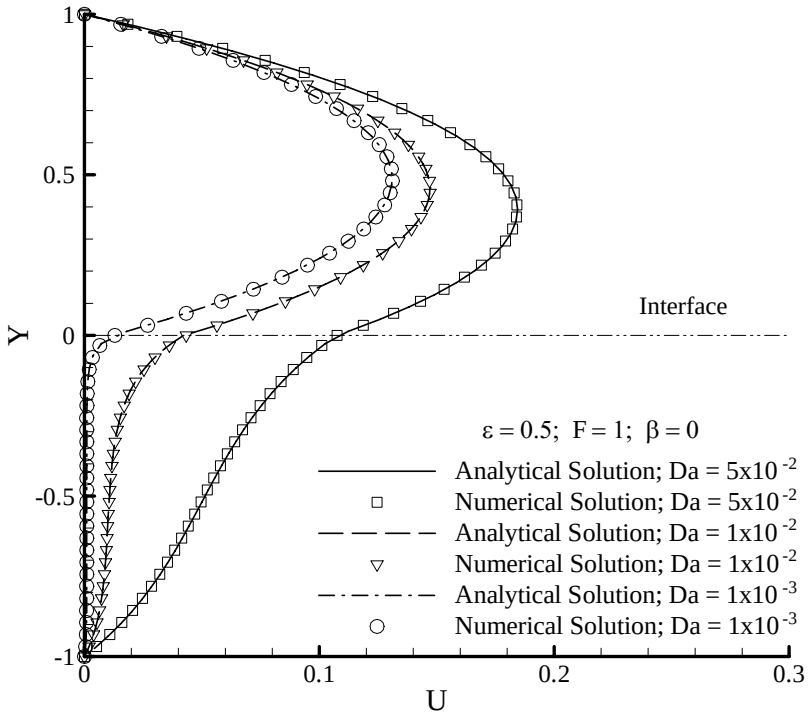

(a)

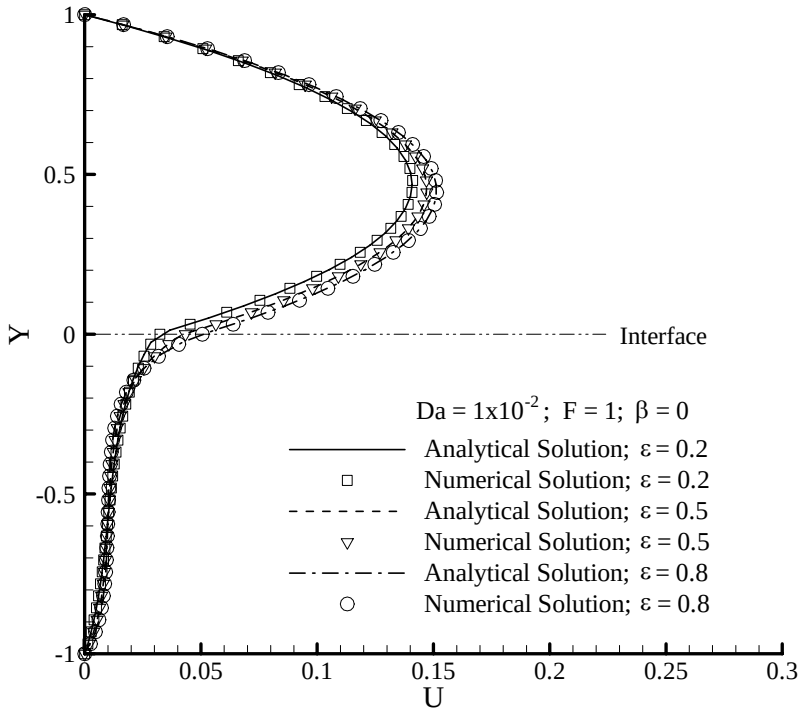

(b)

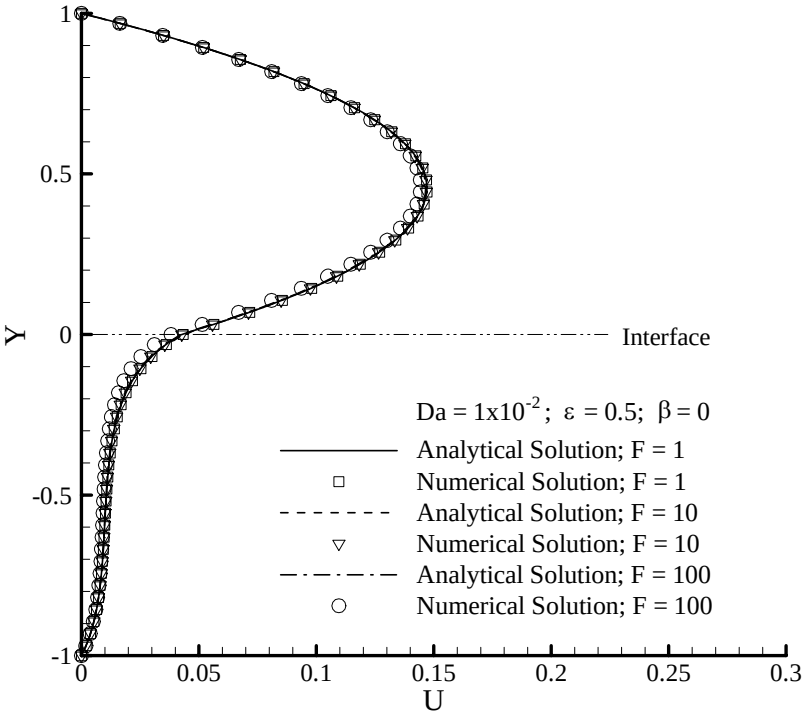

(c)

Figure 3.14 The U velocity profile under different flow conditions: (a) Darcy number effect; (b) Porosity effect; (c) Forchheimer number effect.

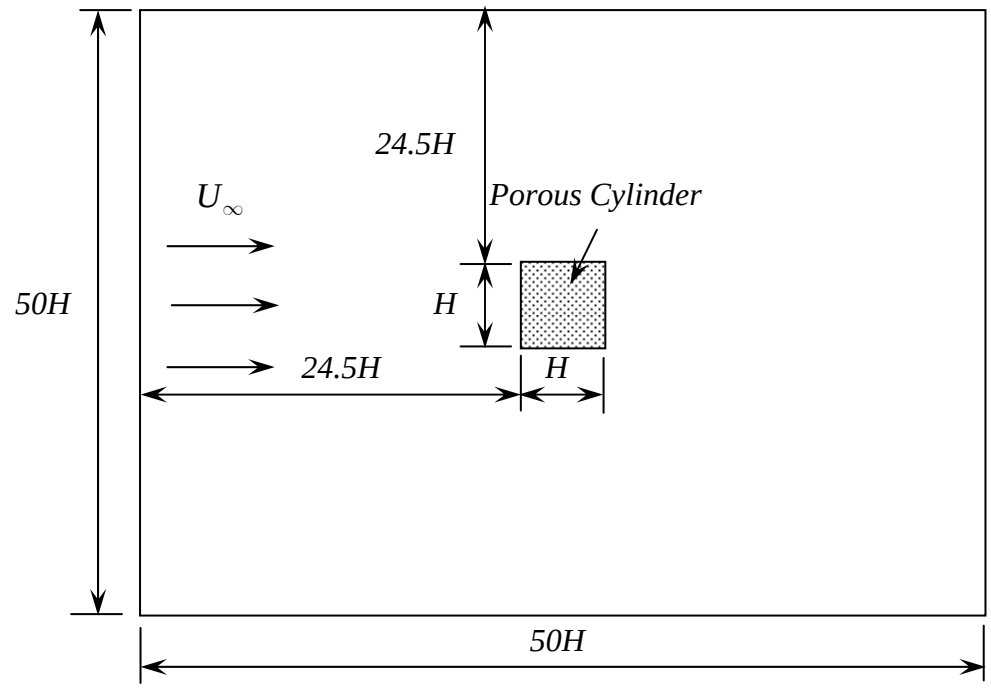

(a)

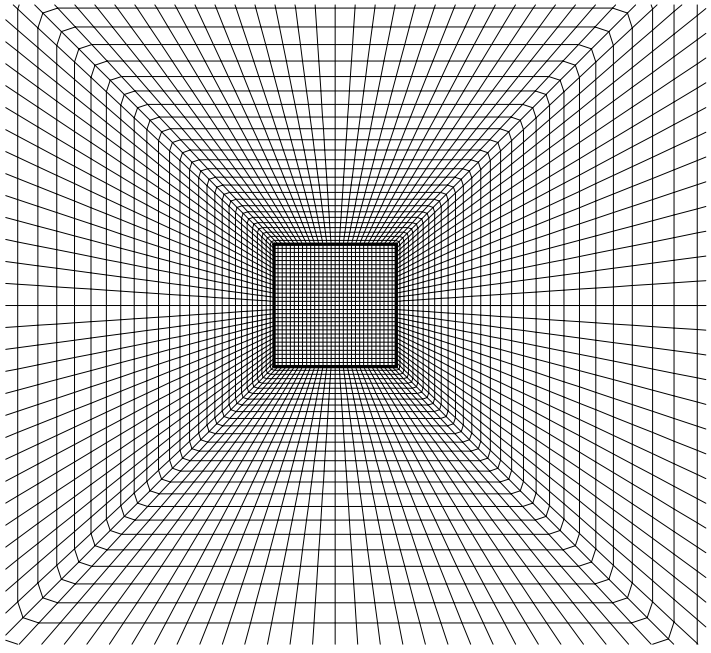

(b)

Figure 3.15 Schematic of flow past a porous square cylinder:
(a) Computational domain; (b) Mesh illustration.

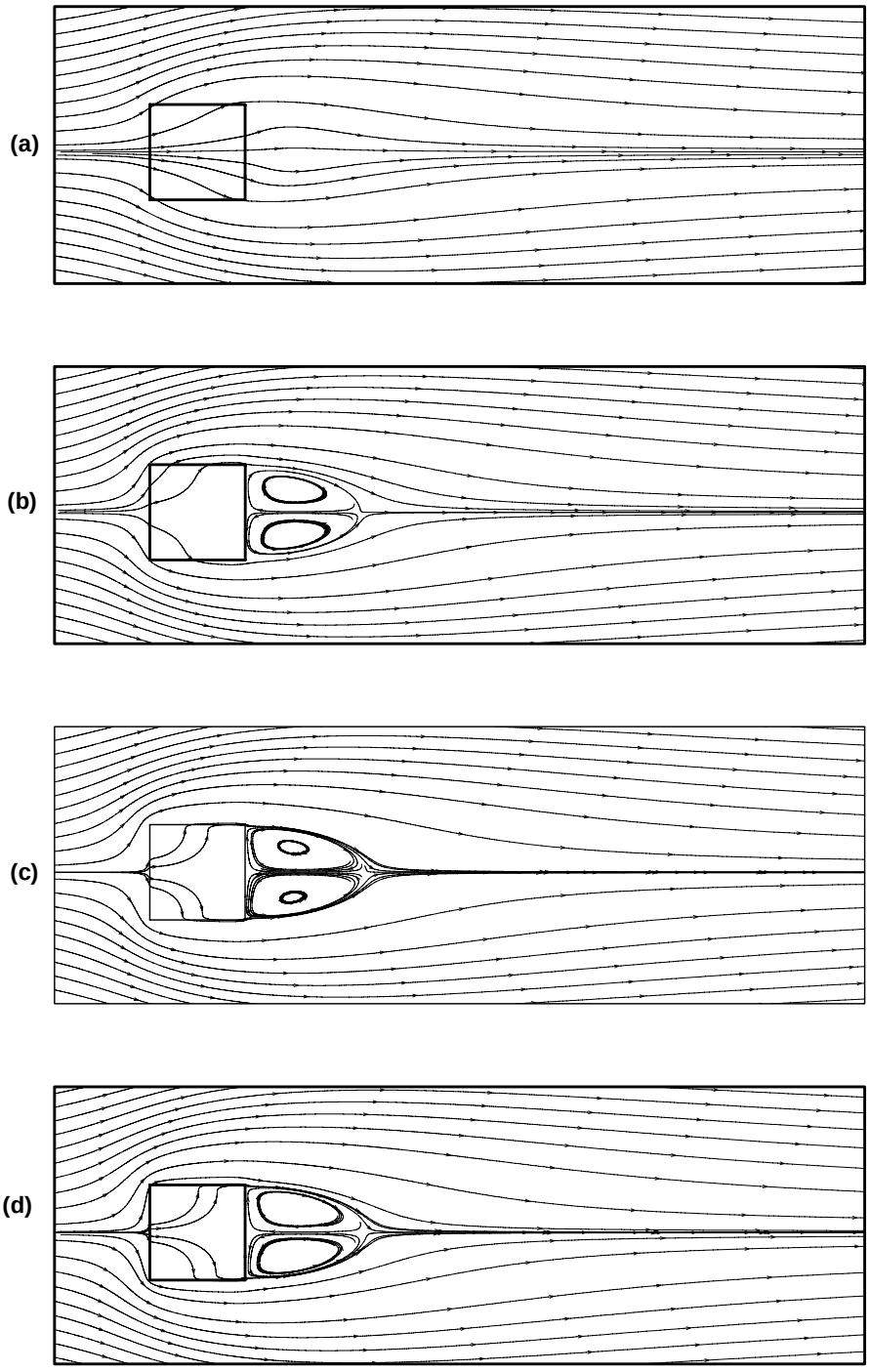

Figure 3.16 Instantaneous streamline contours at $\varepsilon = 0.4$, Re = 20 and $\beta = 0$, $\beta_1 = 0$: (a) Da=10^{-2} (b) Da=10^{-3} (c) Da=10^{-4} (d) Da=10^{-5}.

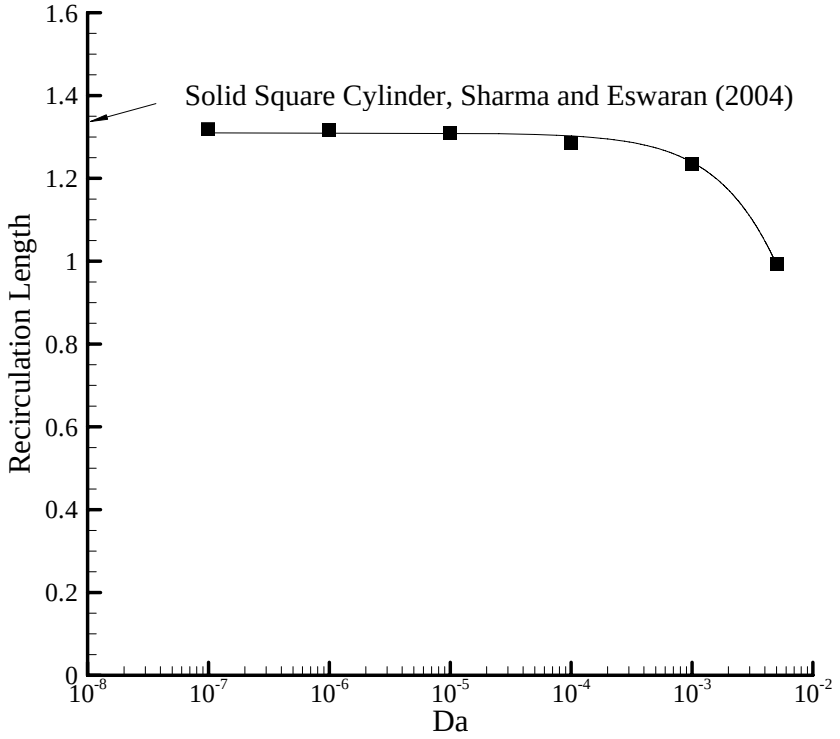

Figure 3.17 Variation of recirculation length with the Darcy number at $\varepsilon = 0.4$, Re = 20 and $\beta = 0$, $\beta_1 = 0$.

Chapter 4

Unsteady Flow around Porous Bodies *

The flow past solid cylinders under free flow conditions has been a hot topic previously as reviewed by Williamson (1996) and Zdravkovich (1997). However, there has been little research work on unsteady flow past porous bodies. Jue (2003) simulated unsteady vortex shedding behind a porous square cylinder using finite element method. However, one-domain approach was used in his model. In his study, a general non-Darcy porous media model was applied to describe the flows both inside and outside the cylinder. A harmonic mean was used to treat the sudden change between the fluid and porous medium and no special treatment at the interface was given. The drawback of one-domain approach is thoroughly reviewed as in Chapter 1.

In this chapter, different from the steady flow past a porous cylinder in Section 3.3.2, unsteady flow past porous bodies is numerically analyzed. The two-domain numerical method as described in Chapter 2, was used. At the interface between fluid and porous parts, a shear stress jump that includes the inertial effect was imposed, together with a continuity of normal stress. Two cases are investigated, one around a porous square cylinder and the other around a porous trapezoidal cylinder. Results are presented with flow configurations for different Darcy and

*Parts of this chapter have been published in *International Journal of Numerical Methods for Heat & Fluid Flow* (Chen et al., 2008c and 2009)

Reynolds numbers. The effects of the porosity, Darcy and Reynolds numbers, stress jump parameters on lift and drag coefficients, and the length of circulation zone or shedding period are studied.

4.1 Problem Statement

The problem under consideration is the same as in Section 3.3.2, as shown in Figure 3.15. The governing equations for the fluid domain outside are the same with (3.1) to (3.3). For the porous domains inside, the governing equations are:

$$\frac{\partial u}{\partial x}+\frac{\partial v}{\partial y}=0 \tag{4.1}$$

$$\begin{aligned}&\frac{\partial u}{\partial t}+\frac{1}{\varepsilon}\{u\frac{\partial}{\partial x}(\frac{u}{\varepsilon})+v\frac{\partial}{\partial y}(\frac{u}{\varepsilon})\}=\\&-\frac{1}{\varepsilon}\frac{\partial}{\partial x}(\varepsilon p_f)-\frac{1}{Da\bullet Re}u-\frac{1.75}{\sqrt{150}}\frac{(u^2+v^2)^{1/2}}{\sqrt{Da}}\frac{u}{\varepsilon^{3/2}}+\frac{1}{\varepsilon\bullet Re}(\frac{\partial^2 u}{\partial x^2}+\frac{\partial^2 u}{\partial y^2})\end{aligned} \tag{4.2}$$

$$\begin{aligned}&\frac{\partial v}{\partial t}+\frac{1}{\varepsilon}\{u\frac{\partial}{\partial x}(\frac{v}{\varepsilon})+v\frac{\partial}{\partial y}(\frac{v}{\varepsilon})\}=\\&-\frac{1}{\varepsilon}\frac{\partial}{\partial y}(\varepsilon p_f)-\frac{1}{Da\bullet Re}v-\frac{1.75}{\sqrt{150}}\frac{(u^2+v^2)^{1/2}}{\sqrt{Da}}\frac{v}{\varepsilon^{3/2}}+\frac{1}{\varepsilon\bullet Re}(\frac{\partial^2 v}{\partial x^2}+\frac{\partial^2 v}{\partial y^2})\end{aligned} \tag{4.3}$$

where the dimensionless parameters are the same with those in Section 3.3.2.

The interface coupling conditions are the same with those Equations (2.9)-(2.11). At the left boundary, the incoming flow is uniform, and at the other three boundaries, $\partial U/\partial n=0$. The initial conditions for the computation were either uniform flow at the inlet U_∞ = 1.0, or the results of a previous calculation, often at different Reynolds number, Darcy number or porosity values. The time step is set

equal to10^{-2}. The mesh distribution is the same as those described in Section 3.3.2, shown as in Figure 3.15b.

4. 2 Results and Discussion

4.2.1 Flow past a Porous Square Cylinder

4.2.1.1 Effect of Reynolds Number

Figure 4.1 shows the instantaneous streamlines for different Reynolds numbers, at constant porosity $\varepsilon = 0.4$, Darcy number $Da = 10^{-4}$, jump coefficients $\beta = 0$ and $\beta_1 = 0$. The flow phenomenon of this case is like those of the non-porous one. At *Re*=20, a closed steady recirculation region consisting of twin symmetric vortices forms behind the cylinder. This recirculation region increases in size with the increase in Reynolds number, shown as *Re* = 40. When the Reynolds number becomes larger, the flow becomes unsteady; the vortices in the separation zone start to separate alternatively from the trailing edge of the square cylinder and move downstream, which is the vortex shedding phenomena. Due to the permeability of the porous media, the shedding intensity would be less than that for a solid case, and the critical Reynolds number, where the flow changes to unsteady from steady, would also be lower.

Figure 4.2 shows the drag and lift coefficient history development, for *Re*=200, $\varepsilon = 0.4$, $Da = 10^{-4}$ and $\beta = 0$, $\beta_1 = 0$. It shows that the unsteady vortex shedding becomes periodic, and the frequency of lift coefficient is twice of drag

coefficient, which are consistent with those of solid ones (Davis, 1982). Figure 4.3 shows this periodic characteristic streamline contour in one period. It is shown that, different from the solid one, the wake flow coming backwards may penetrate into the porous cylinder. However, at *Re* = 250, for the drag coefficient shown in Figure 4.4, it is not a simple sine wave and there seems to be a small modulation in shedding frequency. This kind of phenomena was also found for the solid case by Davis (1982), which is out of the scope of the present study. So in the following study, the Re ranges from 20 to 200.

4.2.1.2 Effect of Stress Jump Parameters

Table 4.1 shows the influence of the stress jump parameters β and β_1 at the lower Reynolds numbers *Re* = 20 and 40, with $\varepsilon = 0.4$ and $Da=10^{-4}$. When *Re*=20, the β effect is noticeable, whereas β_1 has less effect. From Equation (2.9), if the permeability *K* is small, that is Darcy number is small, the viscous term $\beta \frac{\mu}{\sqrt{K}} u_t$ is large. An interesting phenomenon is that when *Re*=40, for different combinations of β and β_1, the flow would become steady or unsteady. The instability at low *Re* is unexpected and may be caused by the sudden large stress jump at the interface. Figure 4.5 shows the instantaneous stream contours for these stress jump interface conditions. By checking the stream contours in one periodic time, it is found that the two vortices are not shed from the cylinder, but its size alternate periodically from small to large. This observation shows the importance of the stress jump boundary

conditions. The stress jump parameters β and β_1 are empirical inputs dependent on the porous medium properties as discussed in Chapter 2. In the numerical model these boundary parameters will determine the flow of fluid into as well as out of the porous medium; and the differences in bleed flow may have caused the changes in the vortex formation. Note that β and β_1 are not numerical stability parameters which need to be optimized.

Table 4.2 shows the influence of the stress jump parameters β and β_1 at the higher Reynolds numbers *Re*=100, and 200, with $\varepsilon = 0.4$ and *Da*=10^{-4}. It can be seen that for the same Reynolds number, β effect is still more obvious than β_1. Yu et al. (2007) showed that the viscous term $\beta \frac{\mu}{\sqrt{k}} u_t$ effect dominates for *Re*=20, and suggested that the inertial term $\beta_1 \rho u_t^2$, in Equation (2.9), may be important at high Reynolds number. However, the Reynolds number in the present study was not increased above 200 to avoid the complications from three dimensional flow and the frequency modulation noted above.

Table 4.2 also shows in greater detail the effect of β and β_1 for Re = 200, respectively. It can be seen that when β increases from -0.7 to 0.7, the average drag coefficient, and the amplitude of both lift and drag coefficients shows a decreasing trend; but for the shedding period, there is no consistent trend. When β_1 increases

from -0.7 to 0.7, the change is not large. This shows that in Equation (2.9), the viscous term $\beta \frac{\mu}{\sqrt{k}} u_t$ is more important than the inertial term $\beta_1 \rho u_t^2$.

4.2.1.3 Effect of Darcy Number

The instantaneous streamline contours for different Darcy number at $\varepsilon = 0.4$, *Re*=20 and $\beta = 0$, $\beta_1 = 0$ have been shown in Section 3.3.2.

Table 4.3 shows the influence of Darcy number. For the steady cases, Re = 20 and 40, the drag coefficient and length of recirculation zone decreases when the Darcy number increases. This is due to more porous flow. It can be seen that the results for $Da = 10^{-4}$ and 10^{-5} changes little, as for $Da \le 10^{-4}$, the flow inside the porous media is rather small, called Darcy flow conventionally. For Re = 100, it is interesting to find that the flow is still steady when $Da = 10^{-2}$. For the unsteady cases, *Re* = 100 and 200, there is no clear trend arising from Darcy number. The flow is more complicated because the porous flow may affect the location of the streamline separation near the back edge of the square cylinder (see instantaneous streamlines in Figures 4.1 and 4.3).

4.2.1.4 Effect of Porosity Value

Table 4.4 shows that at higher porosity, there is decrease of drag coefficient (average for unsteady cases). For the unsteady cases the lift amplitude is smaller at higher porosity. This behavior may be explained by the effect of more porous flow

through the cylinder. There are not much effect of porosity on recirculation length and shedding period. However the effect of porosity is smaller than that of Darcy number which is consistent with the observation of Jue (2003).

4.2.2 Flow past a Porous Trapezoidal Cylinder

The problem under consideration is shown in Figure 4.6a. Non-uniform, body-fitted and non-orthogonal meshes are employed, where the mesh density around the cylinder is higher than those areas far away (Figure 4.6b). A grid independency test was conducted for $Re = 200, \varepsilon = 0.4$, $Da=10^{-4}$ and $\beta = 0, \beta_1 = 0$. It shows that when the grid number in the porous domain was kept at 62x62 constant, increasing the grid number in the fluid domain outside from 320x140 to 360x160 resulted in 3% change for shedding period, lift and drag coefficients. Further increasing the grid number larger than 360x160 did not change them more than 1%. Thus, considering the computational cost and accuracy, a 360x160 mesh for the fluid domain with 62x62 mesh for the porous domain is enough for use in subsequent computations.

4.2.2.1 Early Stage Development of Steady Flow Pattern

Figure 4.7 shows the early stage development of streamline patterns for Re=40, $\varepsilon = 0.4$, $Da=10^{-4}$ and $\beta = 0, \beta_1 = 0$. There is no visible separation flow downstream of the cylinder for $T \leq 0.1$. After a short lapse of time, the flow separates from the rear surface of the cylinder forming a recirculation zone which has two symmetrical

eddies. After a certain lapse of time, the size of these two eddies become larger and finally they reach a constant shape at steady state flow (T=6.0).

4.2.2.2 Early Stage Development of Unsteady Flow Pattern

Figure 4.8 shows the flow development history at a higher *Re*=200. Compared with the previous *Re*=40, the flow also starts with no separation. However, subsequently the twin eddies after the cylinder develop faster and bigger. When T=75.0, one eddy breaks into two and tends to separate from the cylinder far away. Vortex shedding phenomena happens at T=95.0, and finally the flow has a periodic pattern (T=115.0). Figure 4.9 shows the drag and lift coefficient history developments. The results show that the vortex shedding becomes periodic, and the frequency of the lift coefficient is twice that of the drag coefficient, which are consistent with those of solid ones (Davis, 1982).

4.2.2.3 Effect of Reynolds Number

Figure 4.10 shows the instantaneous streamlines for different Reynolds number, at dimensionless time T = 150.0, constant porosity $\varepsilon = 0.4$, Darcy number $Da=10^{-4}$, jump coefficients $\beta = 0$ and $\beta_1 = 0$. The flow phenomenon of this case is similar with those described as in Section 4.2.1.1.

4.2.2.4 Effect of Darcy Number

Figure 4.11 shows the variation of recirculation length with Darcy number. As shown, the recirculation length becomes longer when Darcy number is lower, because there is less porous flow through the cylinder. At very low Darcy number, there is very little porous flow and thus the recirculation length approaches to an asymptotic value near to that of a solid one. At $Da = 10^{-2}$, there is no recirculation length as there is no vortex formation behind the cylinder.

Figure 4.12 shows the instantaneous streamline contours for different Darcy number at higher $Re = 100$. It can be seen that when $Da = 10^{-2}$, there is no vortex formation behind the cylinder. And when $Da = 10^{-3}$, the flow show steady characteristic with two vortices after the cylinder. When Da decreases from 10^{-4} to 10^{-5}, with less porous flow through the cylinder, the flow pattern becomes unsteady, and the vortex begins to separate.

Table 4.5 shows the influence of Darcy number. For the steady cases, Re=20 and 40, the drag coefficient and length of recirculation zone behave like those in Section 4.2.1.3. Differently, for Re=100 and Re=200, it is interesting to find that the flow is still steady when Da=10^{-2}. For the unsteady cases, Re=100 and 200, while Da decreases from 10^{-3} to 10^{-5}, the average drag coefficient, and the amplitude of both lift and drag coefficients, show increasing trends, whereas for the shedding period, there is no obvious trend.

4.2.2.5 Vortex Shedding

Figure 4.13 shows this vortex contour in one period. It is shown that, different from the solid one, the vortex formulation extends to the porous part. The two main vortex after the cylinder interact with each other to generate negative or positive lift forces.

4.2.2.6 Effect of Stress Jump Parameters

Table 4.6 shows the influence of the stress jump parameters β and β_1 at the lower Reynolds numbers *Re* = 20 and 40, with $\varepsilon = 0.4$ and *Da* =10^{-4}. Similar with those in Section 4.2.1.2, the β effect is noticeable, especially for negative values, whereas β_1 has less effect. However, it is noted in Table 4.6 that the recirculation lengths are not much affected by the stress jump parameters. That is, these parameters do not affect the flow patterns at these lower Reynolds numbers of 20 and 40. This observation is different from the study in Section 4.2.1.2 on porous square cylinders where the parameters tend to make the flow more unstable.

Table 4.7 shows the influence of the stress jump parameters β and β_1 on the vortex shedding period τ_p, lift and drag coefficients C_L, C_D at the higher Reynolds numbers *Re* = 100, and 200, with $\varepsilon = 0.4$ and *Da* =10^{-4}. It can be seen that for the same Reynolds number, β effect is still more obvious than β_1. It can also be seen that when β increases from -1.0 to +1.0, the average drag coefficient, and the amplitude of both lift and drag coefficients, and the shedding period show increasing trends. When β_1 increases from -1.0 to +1.0, the change is not large. This shows that in

Equation (2.9), the viscous term $\beta \frac{\mu}{\sqrt{k}} u_t$ is more important than the inertial term $\beta_1 \rho u_t^2$.

4.2.2.7 Effect of Porosity Values

Table 4.8 shows that at higher porosity, there is decrease of drag coefficient (average for unsteady cases). Similar with those in Section 4.2.1.4, for the unsteady cases the lift amplitude is smaller at higher porosity.

4.3 Conclusions

Two-dimensional flow around a porous square or trapezoidal cylinder has been carried out using numerical method as described in Chapter 2. To couple the flows at the interface, the shear-stress jump condition is implemented.

The flow range considered varied from steady state to unsteady Reynolds number of 200, and different porosities, Darcy numbers and stress jump parameters were considered. With a larger Darcy number, the Reynolds number has to be higher before the vortex shedding phenomena occurs. The effects of the stress jump parameters are given for the flow condition from *Re* = 20 to 200. The first coefficient β has a more noticeable effect whereas the second coefficient β_1 has small effect, even for *Re* = 200. The results also show that the interface stress jump parameters play an important role in the stability of the flow around a porous cylinder, which is different for porous square and trapezoidal cylinders. The Darcy number effect

becomes smaller when $Da \le 10^{-4}$; at larger Darcy number, the fluctuation-amplitude of drag coefficient decreases. Generally, a larger porosity cylinder results in a smaller drag coefficient and lift amplitude.

Table 4.1 Drag coefficient and length of the recirculation zone, for low Re, with $\varepsilon = 0.4$ and Da=10^{-4} for flow past a porous square cylinder.

Re	β	β_1	C_D	L/H	Re	β	β_1	C_D	L/H
20	-0.7	0	1.991	1.23	40	-0.7	0	1.448-1.463	-
	0	0	2.411	1.26		0	0	1.611	2.77
	0.7	0	2.550	1.27		0.7	0	1.534-1.568	-
	0	-0.7	2.376	1.26		0	-0.7	1.502-1.539	-
	0	0	2.411	1.26		0	0	1.611	2.77
	0	0.7	2.371	1.26		0	0.7	1.611	2.76

Table 4.2 Drag, lift and period for high Re with unsteady vortex shedding, with $\varepsilon = 0.4$ and Da=10^{-4} for flow past a porous square cylinder.

Re	β	β_1	τ_p	C_L	C_D (Amplitude)
100	0	0.7	6.97	-0.265-0.265	1.432-1.447 (0.015)
	0	0	6.94	-0.269-0.269	1.433-1.448 (0.015)
	0	-0.7	7.08	-0.266-0.266	1.431-1.447 (0.016)
	0.7	0	6.93	-0.264-0.264	1.441-1.457 (0.016)
	0	0	6.94	-0.269-0.269	1.433-1.448 (0.015)
	-0.7	0	7.02	-0.270-0.270	1.417-1.432 (0.015)
200	0	0.7	6.63	-0.788-0.788	1.585-1.730 (0.145)
	0	0.5	6.59	-0.783-0.783	1.584-1.726 (0.142)
	0	0.3	6.60	-0.782-0.782	1.583-1.725 (0.142)
	0	0	6.60	-0.782-0.782	1.581-1.722 (0.141)
	0	-0.3	6.61	-0.783-0.783	1.581-1.724 (0.143)
	0	-0.5	6.66	-0.785-0.785	1.582-1.726 (0.144)
	0	-0.7	6.63	-0.787-0.787	1.584-1.731 (0.147)
	0.7	0	6.62	-0.759-0.759	1.568-1.706 (0.138)
	0.5	0	6.64	-0.765-0.765	1.571-1.710 (0.139)
	0.3	0	6.62	-0.770-0.770	1574-1.714 (0.140)
	0	0	6.60	-0.782-0.782	1.581-1.722 (0.141)
	-0.3	0	6.60	-0.799-0.799	1.593-1.736 (0.143)
	-0.5	0	6.67	-0.816-0.816	1.604-1.750 (0.146)
	-0.7	0	6.53	-0.840-0.840	1.621-1.771 (0.150)

Table 4.3 Effect of Darcy number with $\varepsilon = 0.4$, $\beta = 0$ and $\beta_1 = 0$ for flow past a porous square cylinder.

Re	Da	τ_p	C_L	C_D (amplitude)	L/H
20	10^{-5}	-	0	2.413	1.32
	10^{-4}	-	0	2.411	1.26
	10^{-3}	-	0	2.143	1.21
	10^{-2}	-	0	1.974	-
40	10^{-5}	-	0	1.616	2.81
	10^{-4}	-	0	1.611	2.77
	10^{-3}	-	0	1.535	2.66
	10^{-2}	-	0	1.472	-
100	10^{-5}	7.15	-0.225-0.225	1.284-1.293 (0.009)	-
	10^{-4}	6.94	-0.269-0.269	1.433-1.448 (0.015)	-
	10^{-3}	7.10	-0.262-0.262	1.638-1.658 (0.020)	-
	10^{-2}	-	0	1.096	-
200	10^{-5}	6.43	-0.546-0.546	1.343-1.418 (0.075)	-
	10^{-4}	6.60	-0.782-0.782	1.581-1.722 (0.141)	-
	10^{-3}	6.23	-0.310-0.310	1.634-1.816 (0.182)	-
	10^{-2}	6.52	-0.212-0.212	1.064-1.288 (0.224)	-

Table 4.4 Effect of porosity with Da=10^{-4} and $\beta = 0, \beta_1 = 0$ for flow past a porous square cylinder.

Re	ε	τ_p	C_L	C_D (amplitude)	L/H
20	0.4	-	0	2.411	1.26
	0.6	-	0	2.105	1.24
	0.8	-	0	2.049	1.25
40	0.4	-	0	1.611	2.73
	0.6	-	0	1.584	2.69
	0.8	-	0	1.537	2.71
100	0.4	6.94	-0.269-0.269	1.433-1.448 (0.015)	-
	0.6	7.06	-0.261-0.261	1.419-1.433 (0.014)	-
	0.8	7.02	-0.257-0.257	1.407-1.420 (0.013)	-
200	0.4	6.60	-0.782-0.782	1.581-1.722 (0.141)	-
	0.6	6.55	-0.772-0.772	1.575-1.715 (0.140)	-
	0.8	6.49	-0.750-0.750	1.563-1.698 (0.135)	-

Table 4.5 Effect of Darcy number with $\varepsilon = 0.4$, $\beta = 0$ and $\beta_1 = 0$ for flow past a porous trapezoidal cylinder.

Re	*Da*	τ_p	C_L	C_D (amplitude)	L/H
20	10^{-5}	-	0	1.838	1.14
	10^{-4}	-	0	1.826	1.12
	10^{-3}	-	0	1.805	0.95
	10^{-2}	-	0	1.610	-
40	10^{-5}	-	0	1.353	2.22
	10^{-4}	-	0	1.345	2.13
	10^{-3}	-	0	1.330	1.94
	10^{-2}	-	0	1.210	-
100	10^{-5}	5.46	-0.235-0.235	1.294-1.329 (0.035)	-
	10^{-4}	5.41	-0.206-0.206	1.199-1.228 (0.028)	-
	10^{-3}	5.52	-0.116-0.116	1.164-1.171 (0.007)	-
	10^{-2}	-	0	0.895	-
200	10^{-5}	4.58	-0.552-0.552	1.356-1.570 (0.214)	-
	10^{-4}	4.42	-0.460-0.460	1.275-1.409 (0.134)	-
	10^{-3}	4.62	-0.175-0.175	1.125-1.147 (0.022)	-
	10^{-2}	-	0	0.772	-

Table 4.6 Drag coefficient and length of the recirculation zone, for low *Re*, with $\varepsilon = 0.4$ and $Da = 10^{-4}$ for flow past a porous trapezoidal cylinder.

Re	β	β_1	C_D	L/H	*Re*	β	β_1	C_D	L/H
20	-1.0	0	1.602	1.06	40	-1.0	0	1.192	2.01
	0	0	1.826	1.12		0	0	1.345	2.13
	1.0	0	1.877	1.14		1.0	0	1.375	2.14
	0	-1.0	1.816	1.12		0	-1.0	1.342	2.13
	0	0	1.826	1.12		0	0	1.345	2.13
	0	1.0	1.826	1.12		0	1.0	1.346	2.13

Table 4.7 Drag, lift and shedding period for high Re with unsteady vortex shedding, with $\varepsilon = 0.4$ and $Da = 10^{-4}$ for flow past a porous trapezoidal cylinder.

Re	β	β_1	τ_p	C_L	C_D (Amplitude)
100	0	1.0	5.47	-0.207-0.207	1.199-1.224 (0.025)
	0	0	5.41	-0.206-0.206	1.199-1.228 (0.028)
	0	-1.0	5.48	-0.207-0.207	1.198-1.225 (0.027)
	1.0	0	5.51	-0.211-0.211	1.222-1.249 (0.027)
	0	0	5.41	-0.206-0.206	1.199-1.228 (0.028)
	-1.0	0	5.37	-0.192-0.192	1.099-1.122 (0.023)
200	0	1.0	4.50	-0.451-0.451	1.258-1.395 (0.137)
	0	0	4.42	-0.460-0.460	1.275-1.409 (0.134)
	0	-1.0	4.63	-0.487-0.487	1.284-1.431 (0.147)
	1.0	0	4.53	-0.472-0.472	1.296-1.432 (0.136)
	0	0	4.42	-0.460-0.460	1.275-1.409 (0.134)
	-1.0	0	4.36	-0.431-0.431	1.189-1.311 (0.122)

Table 4.8 Effect of porosity with $Da = 10^{-4}$ and $\beta = 0, \beta_1 = 0$ for flow past a porous trapezoidal cylinder.

Re	ε	τ_p	C_L	C_D (amplitude)	L/H
20	0.4	-	0	1.826	1.12
	0.6	-	0	1.768	1.12
	0.8	-	0	1.713	1.11
40	0.4	-	0	1.345	2.13
	0.6	-	0	1.314	2.12
	0.8	-	0	1.281	2.12
100	0.4	5.41	-0.206-0.206	1.199-1.228 (0.028)	-
	0.6	5.47	-0.207-0.207	1.178-1.205 (0.027)	-
	0.8	5.53	-0.208-0.208	1.158-1.184 (0.026)	-
200	0.4	4.42	-0.460-0.460	1.275-1.409 (0.134)	-
	0.6	4.46	-0.462-0.462	1.257-1.389 (0.132)	-
	0.8	4.49	-0.464-0.464	1.243-1.373 (0.130)	-

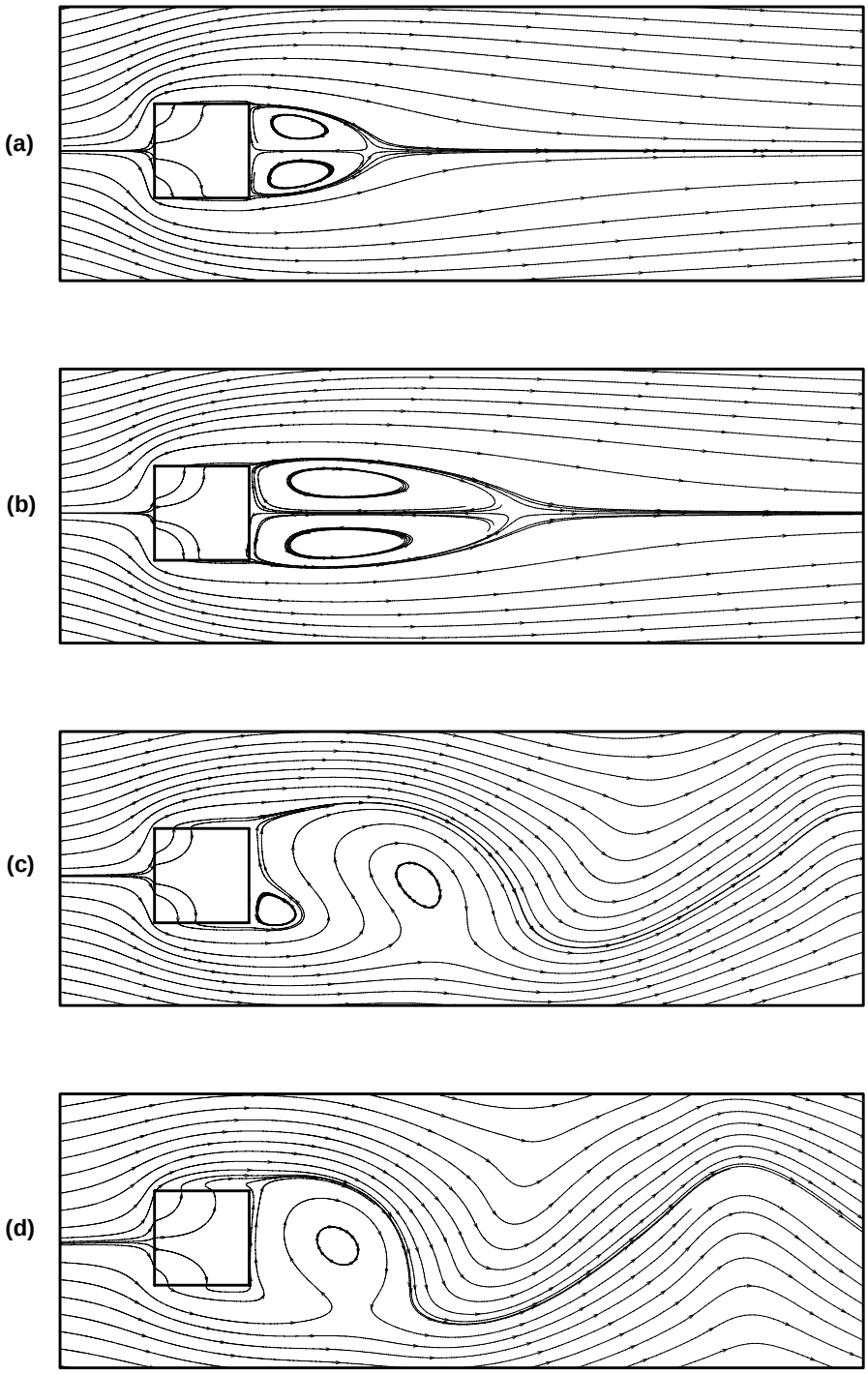

Figure 4.1 Instantaneous streamline contours at $\varepsilon = 0.4$, Da=10^{-4} and $\beta = 0$, $\beta_1 = 0$: (a)Re=20; (b)Re=40; (c)Re=100; (d)Re=200.

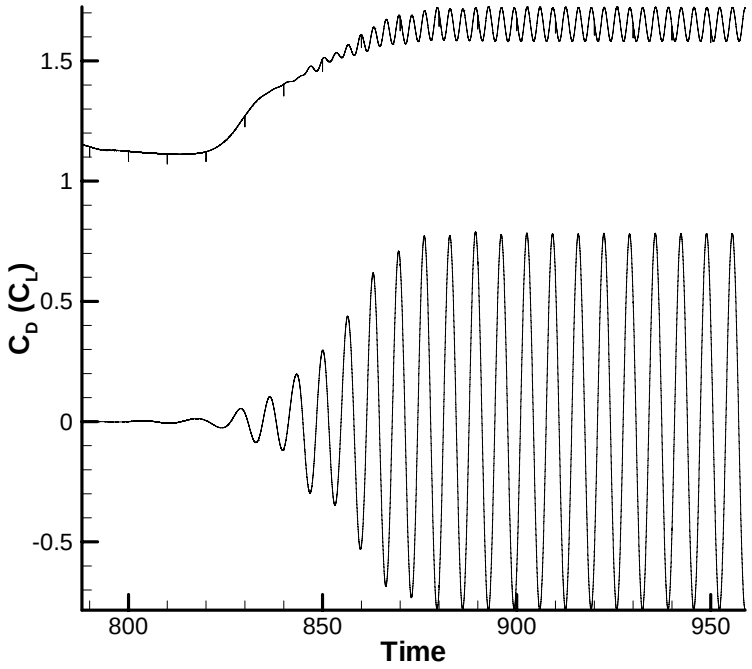

Figure 4.2 Drag (up) and lift (down) coefficient histories, at Re=200, $\varepsilon = 0.4$, Da=10^{-4} and $\beta = 0$, $\beta_1 = 0$.

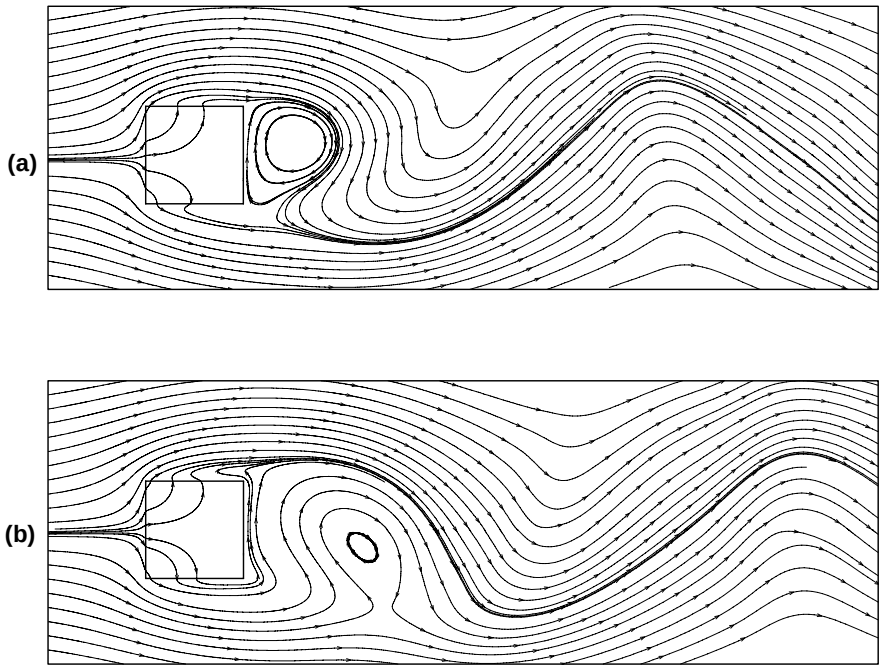

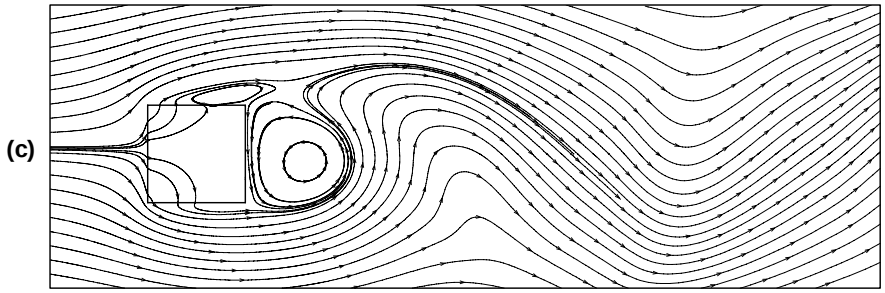

Figure 4.3 Streamline contours at Re=200, $\varepsilon = 0.4$, Da=10^{-4} and $\beta = 0$, $\beta_1 = 0$: (a) $C_L = \max$; (b) $C_L = 0$; (c) $C_L = \min$.

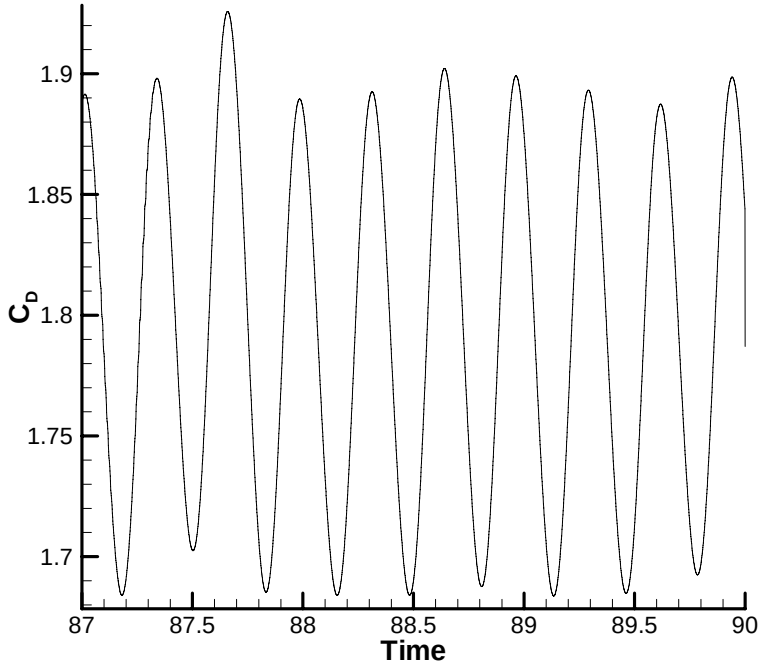

Figure 4.4 Periodic drag coefficient histories, at *Re* = 250, $\varepsilon = 0.4$, *Da* =10^{-4} and $\beta = 0.7$, $\beta_1 = 0$.

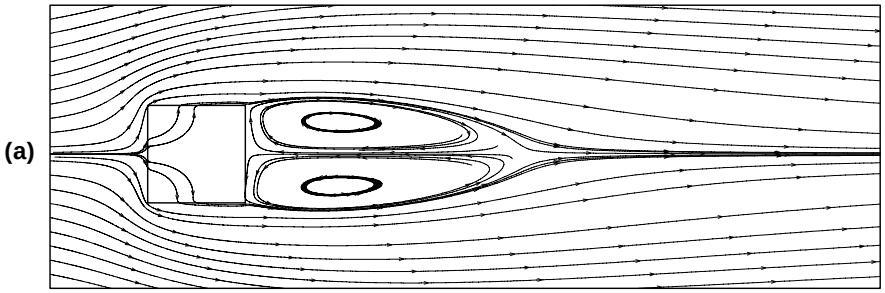

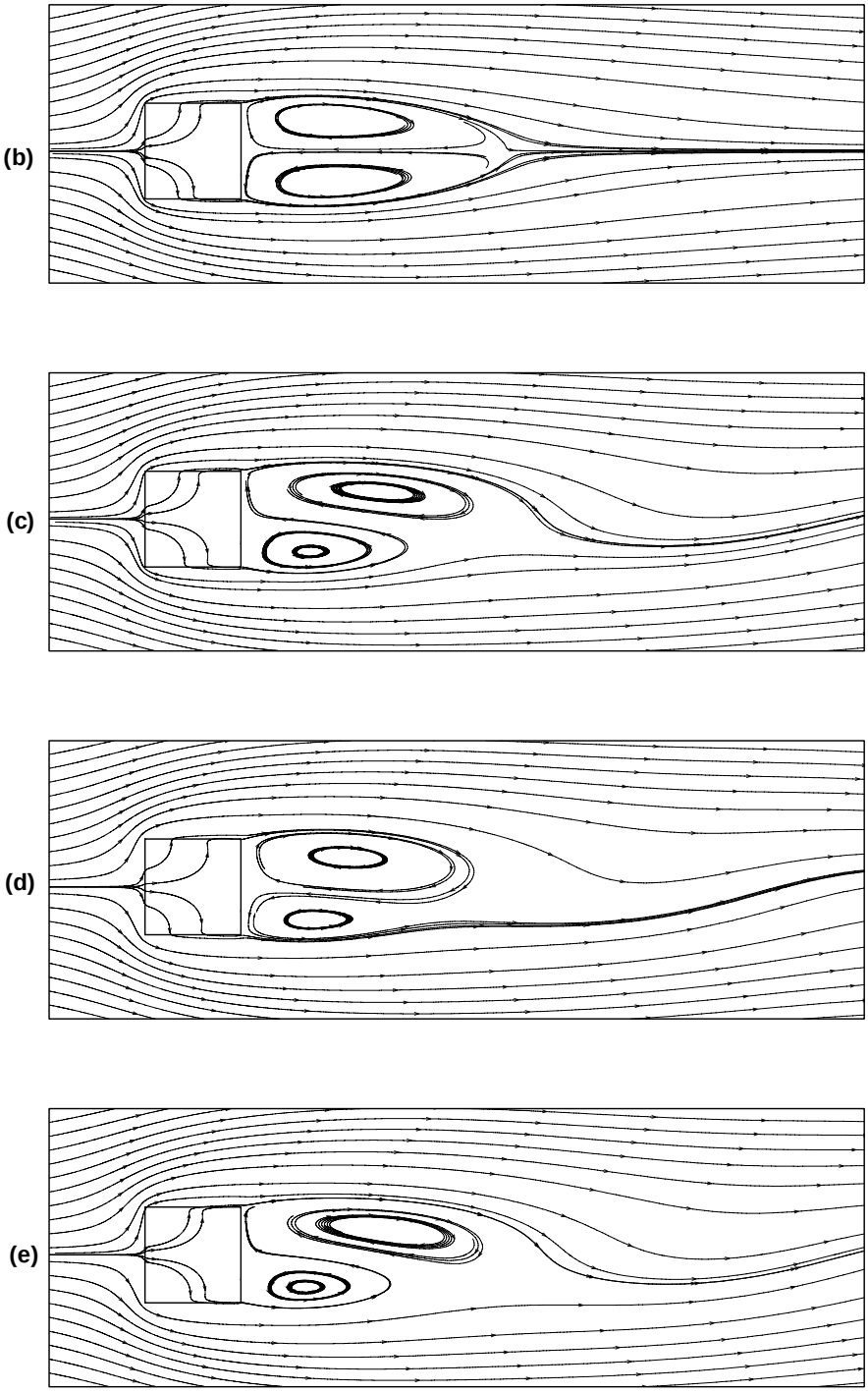

Figure 4.5 Instantaneous streamline contours at Re = 40, $\varepsilon = 0.4$, $Da = 10^{-4}$: (a) $\beta = 0$, $\beta_1 = 0$; (b) $\beta = 0$, $\beta_1 = 0.7$; (c) $\beta = 0$, $\beta_1 = -0.7$; (d) $\beta = 0.7$, $\beta_1 = 0$; (e) $\beta = -0.7$, $\beta_1 = 0$.

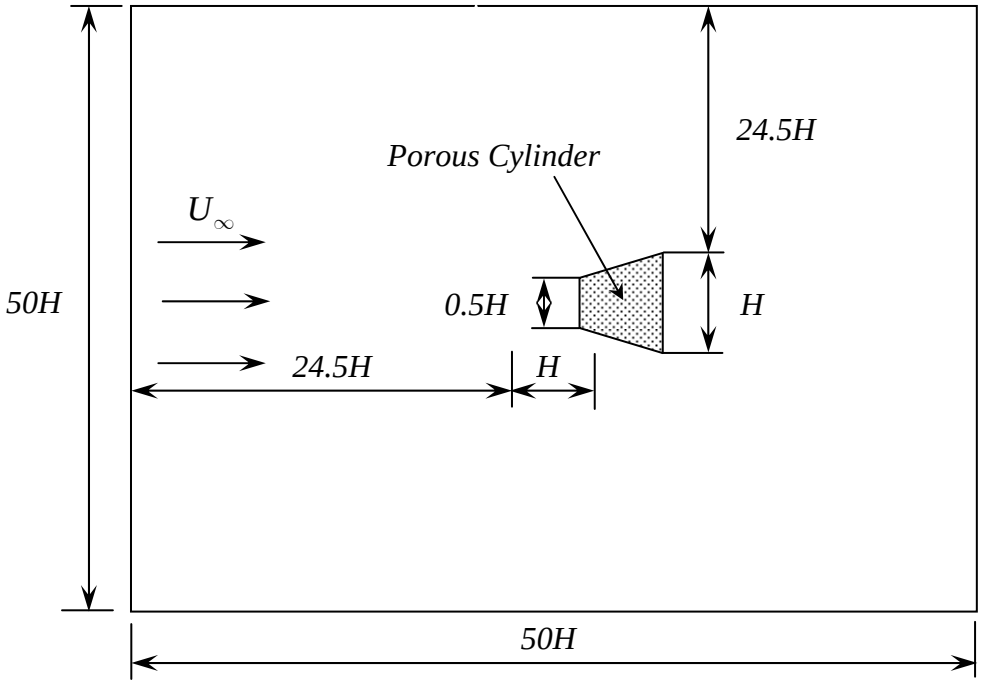

(a)

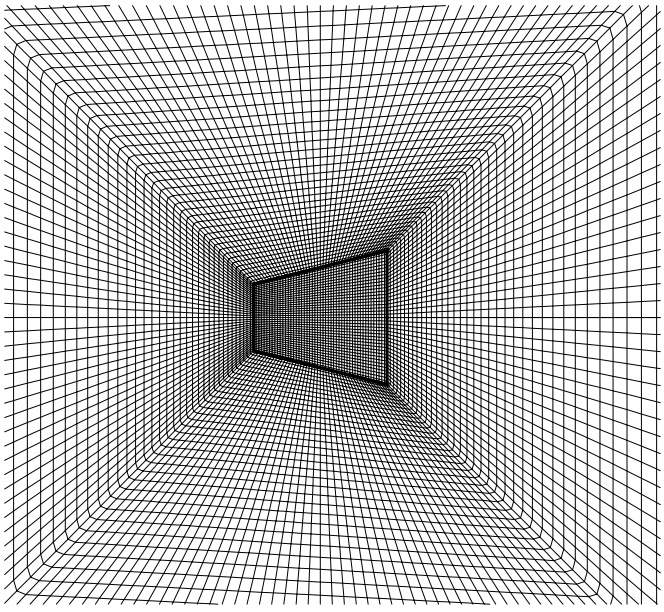

(b)

Figure 4.6 Schematic of flow past a porous expanded trapezoidal cylinder: (a) Computational domain; (b) Mesh illustration.

T=0.1

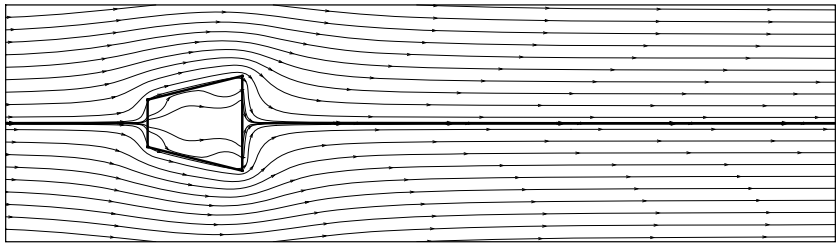

T=0.5

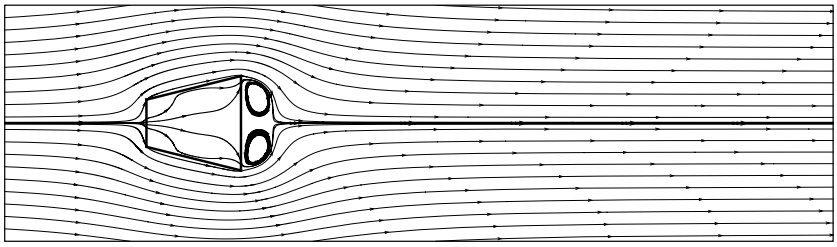

T=1.0

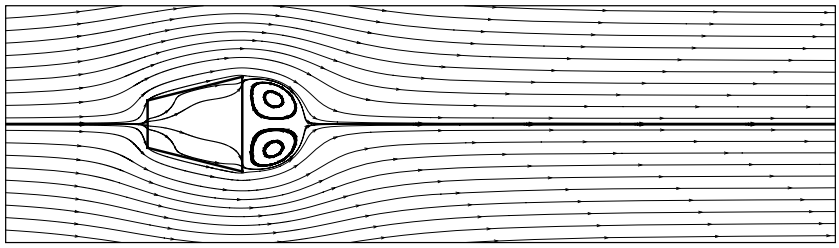

T=2.0

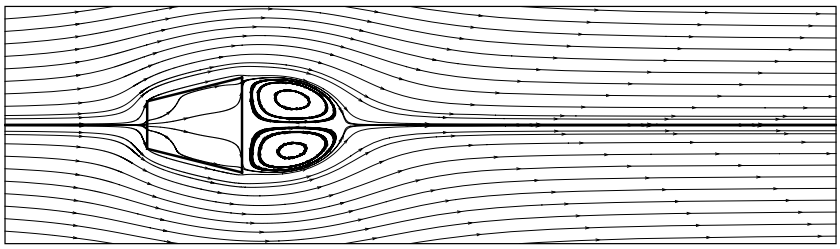

T=3.0

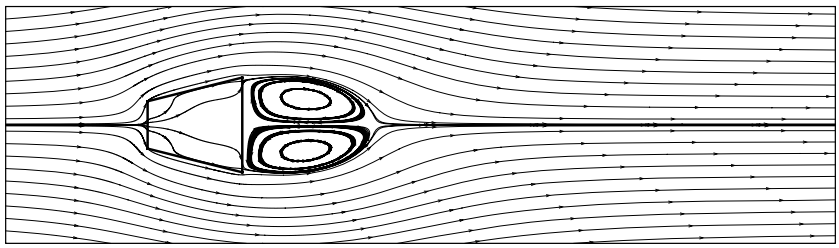

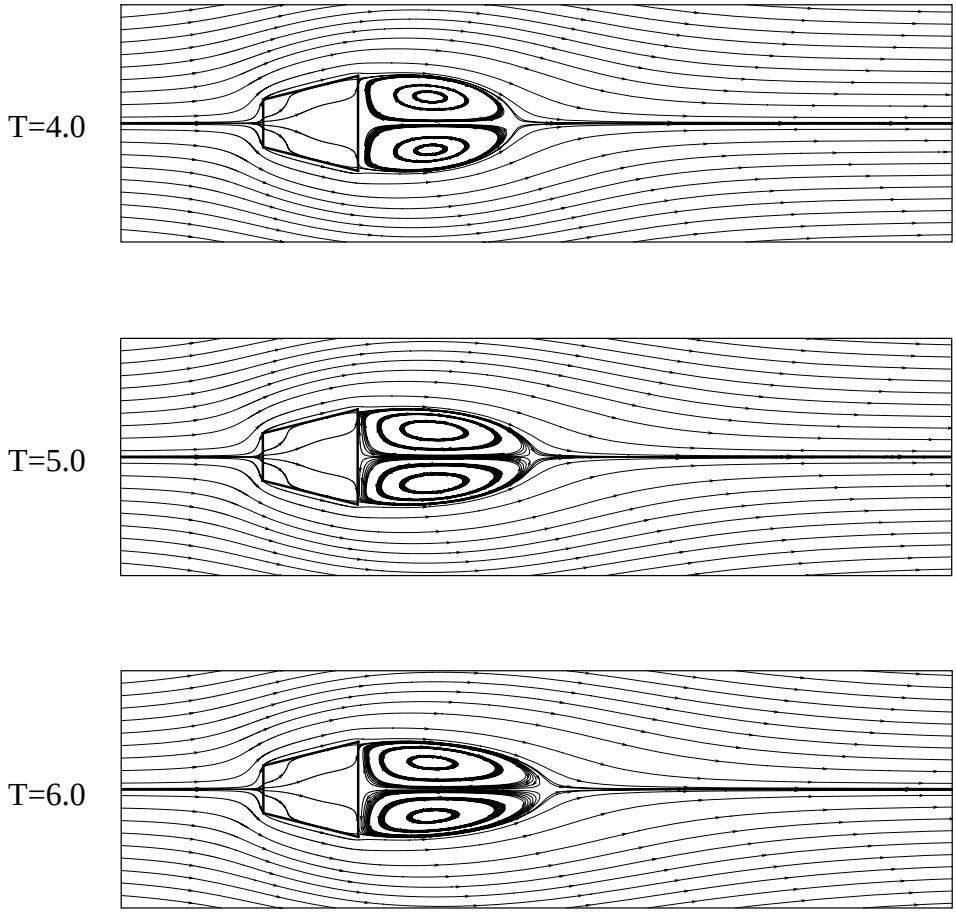

Figure 4.7 Instantaneous streamline pattern for *Re* = 40 at various times, with $\varepsilon = 0.4$, $Da = 10^{-4}$ and $\beta = 0$, $\beta_1 = 0$.

T=0.1

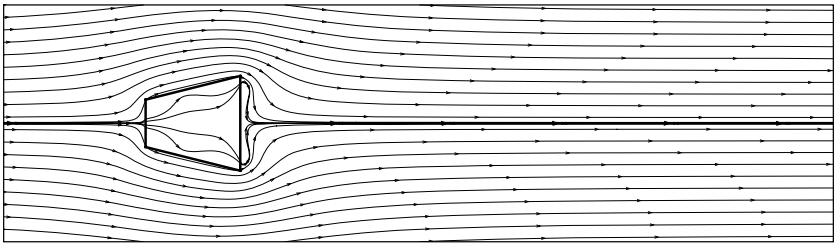

T=0.5

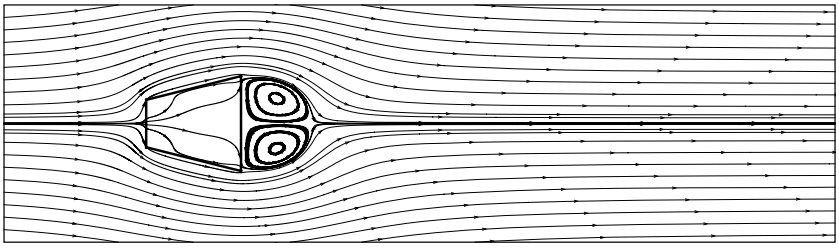

T=1.0

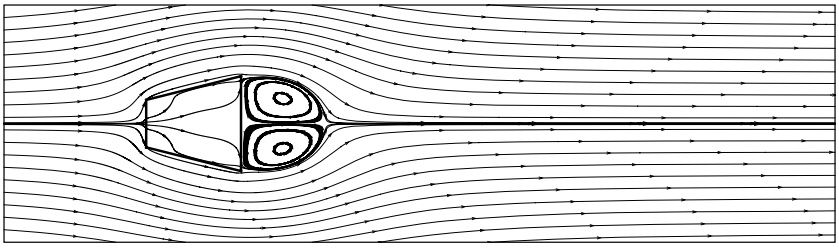

T=5.0

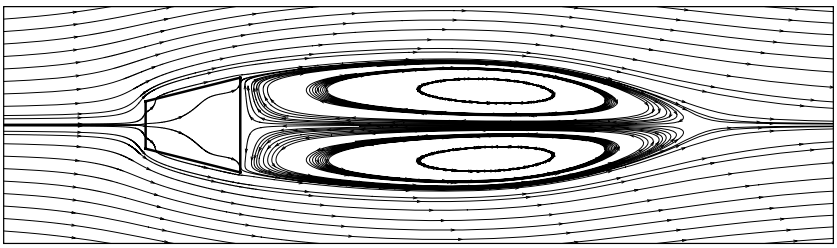

T=25.0

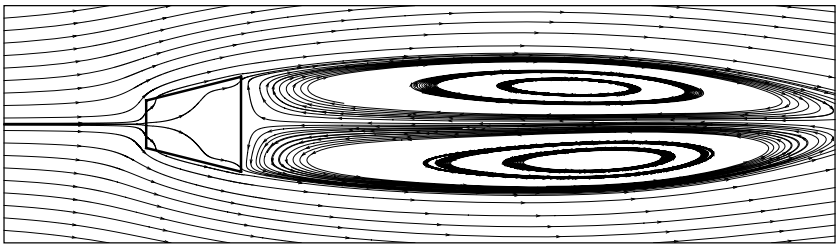

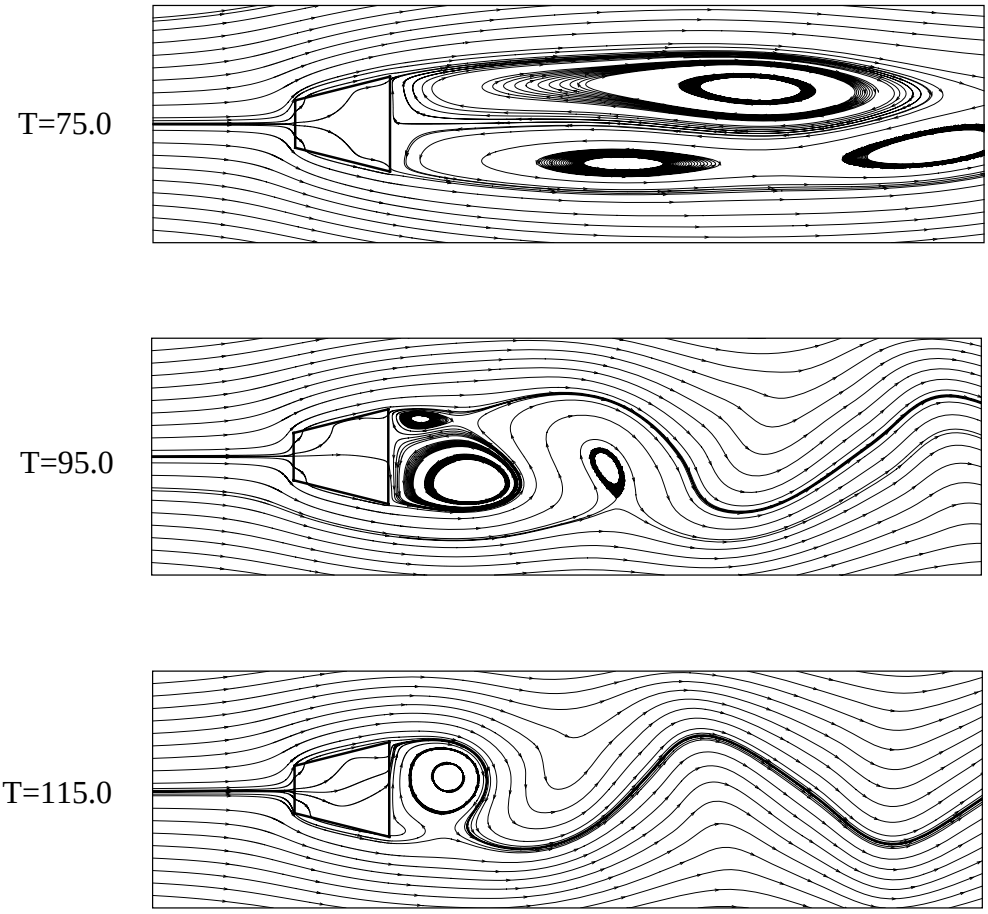

Figure 4.8 Instantaneous streamline pattern for *Re* = 200 at various times, with $\varepsilon = 0.4$, $Da = 10^{-4}$ and $\beta = 0$, $\beta_1 = 0$.

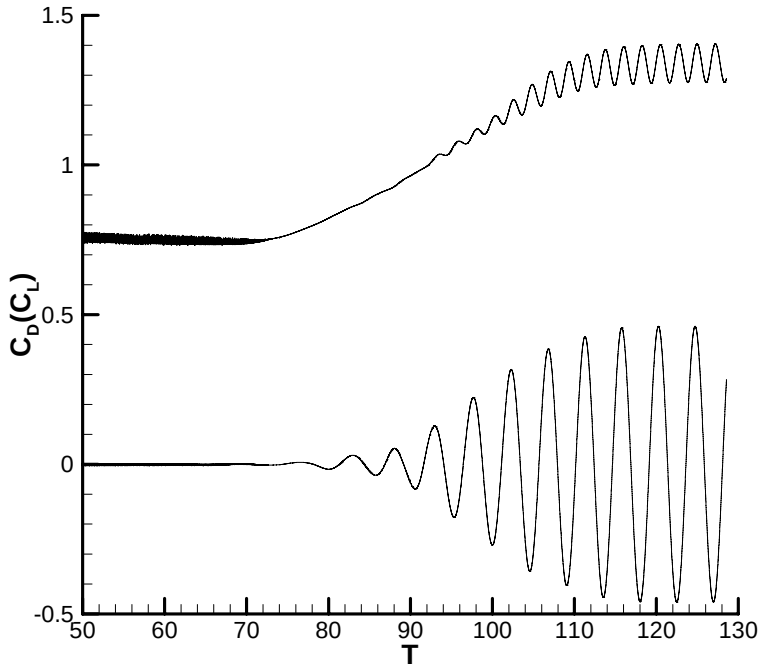

Figure 4.9 Drag (up) and lift (down) coefficient histories, at *Re* = 200, $\varepsilon = 0.4$, *Da* $=10^{-4}$ and $\beta = 0$, $\beta_1 = 0$.

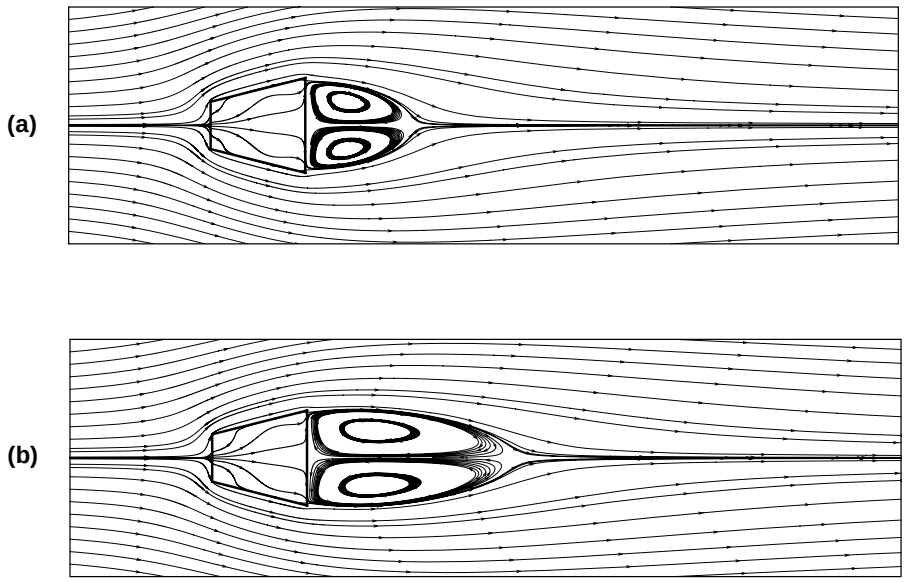

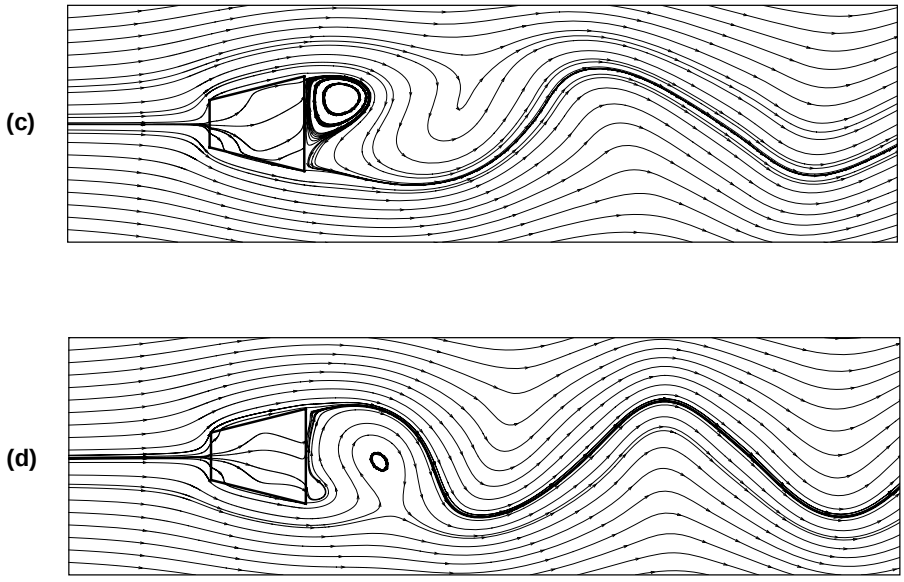

Figure 4.10 Instantaneous streamline contours at T = 150.0, $\varepsilon = 0.4$, $Da = 10^{-4}$ and $\beta = 0$, $\beta_1 = 0$: (a)Re = 20; (b)Re = 40; (c)Re = 100; (d)Re = 200.

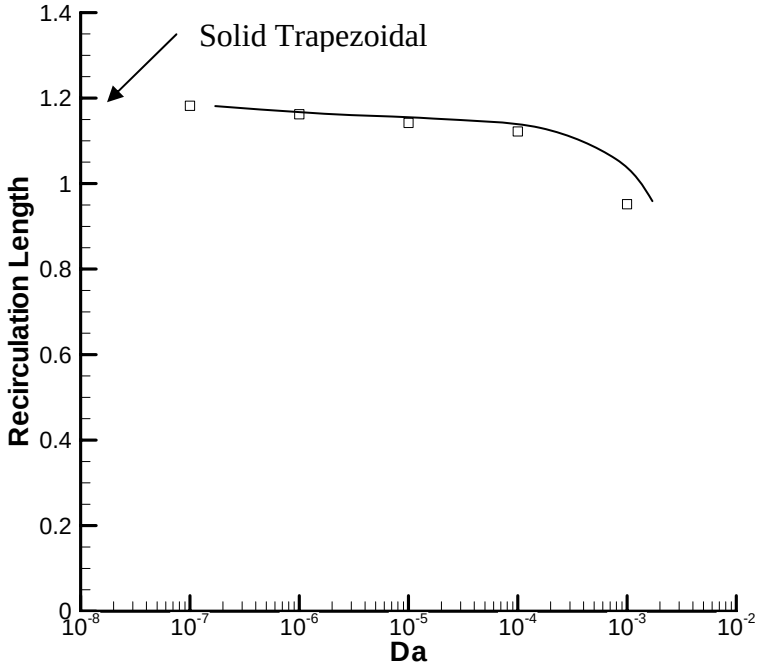

Figure 4.11 Variation of recirculation length with Darcy number at $\varepsilon = 0.4$, Re = 20 and $\beta = 0$, $\beta_1 = 0$.

.

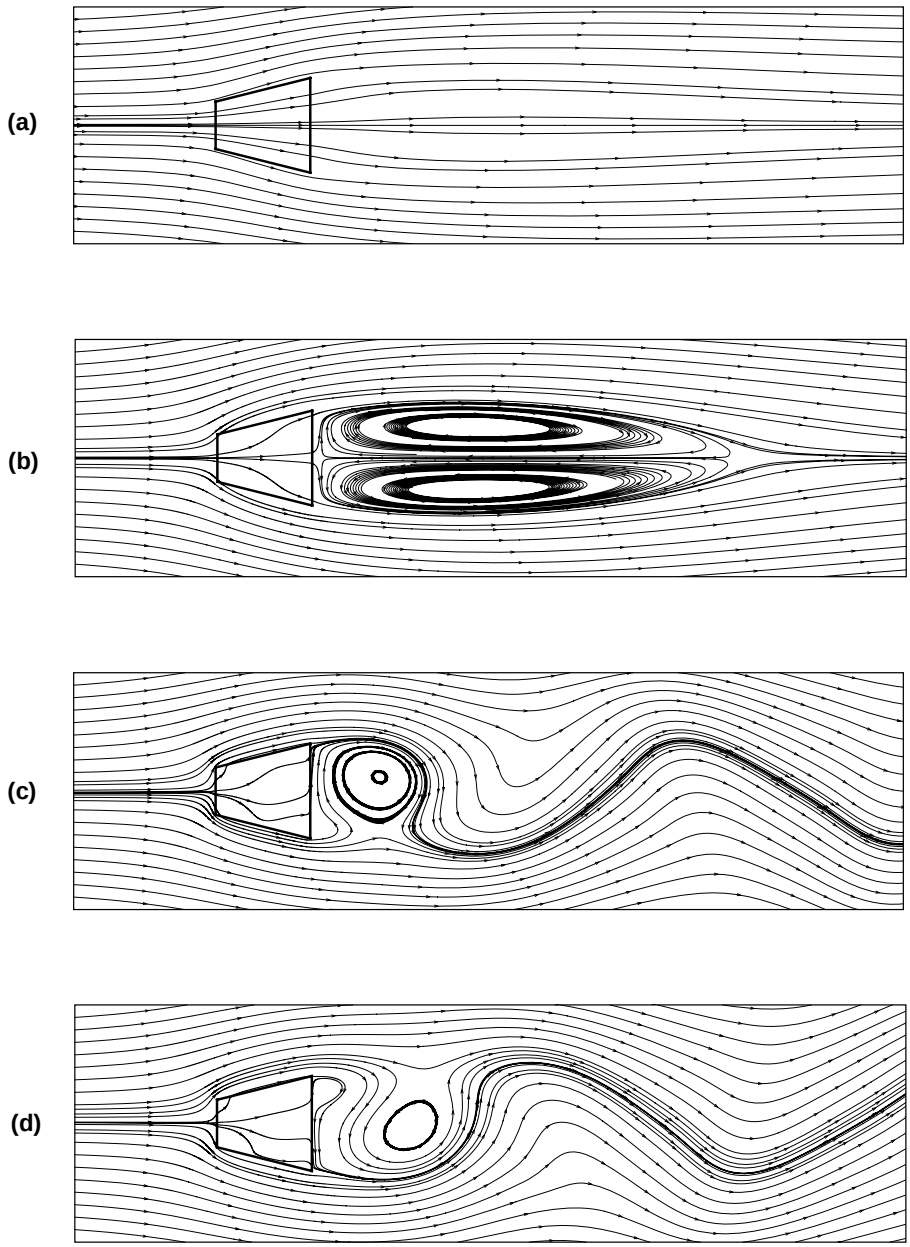

Figure 4.12 Instantaneous streamline contours at T = 120.0, $\varepsilon = 0.4$, Re = 100 and $\beta = 0$, $\beta_1 = 0$:

(a) $Da = 10^{-2}$; (b) $Da = 10^{-3}$; (c) $Da = 10^{-4}$; (d) $Da = 10^{-5}$.

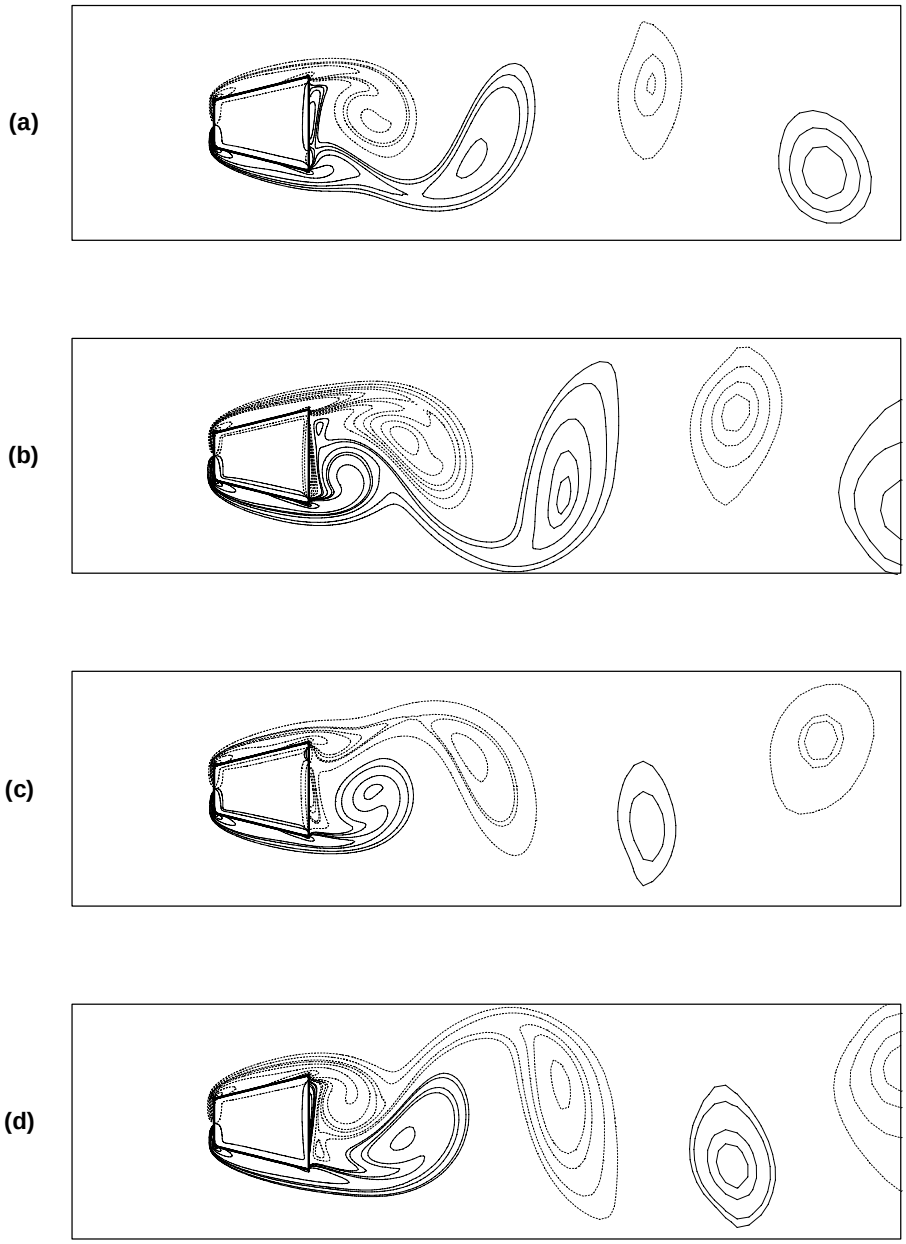

Figure 4.13 Vorticity contours in a period τ_p =4.42 from T = 125.0 at Re = 200, $\varepsilon = 0.4$, $Da = 10^{-4}$ and $\beta = 0$, $\beta_1 = 0$:

(a) $C_L = 0$, from positive to negative; (b) $C_L = C_{L\min} = -0.460$; (c) $C_L = 0$, from negative to positive;. (d) $C_L = C_{L\max} = +0.460$.

Chapter 5

Natural Convection in a Porous Wavy Cavity*

Natural convection in porous media cavity is of great interest in the references (Vasseur et al., 1989; Hsiao and Chen, 1994; Nithiarasu, 1996; Bera et al., 1998; Holzbecher, 2004). In practice, the cavity wall may be roughened or have protrusions attached to it to enhance the heat transfer process. Thus it is of interest to study the effects of surface undulations or waviness in porous cavities. Misirlioglu et al. (2005) investigated natural convection in a wavy cavity by considering that it enclosed a porous medium. Their numerical results were based on Darcy's law and the stream-function method was used to solve the governing equations. However, as reviewed in Section 1.2.1, Darcy's law can not predict the flow well when the Reynolds or Rayleigh numbers are large, as it neglects viscous, inertia, and convective effects.

Current chapter makes use of Darcy-Brinkman-Forchheimer extended model to depict the flow inside the porous region more generally by including the non-Darcian effects, which enables studies at higher Reynolds and Rayleigh numbers. The results are shown in terms of local and average Nusselt numbers, isotherms and streamlines at various aspect ratios, surface wavinesses and porosity values. A wider range of Rayleigh number and Darcy number is considered.

*Parts of this chapter have been published in *Numerical Heat Transfer A: Applications* (Chen et al., 2007)

5.1 Problem Statement

The flow and heat transfer characteristics inside a wavy cavity made of two straight horizontal adiabatic walls and two bent vertical isothermal walls are considered here, as shown in Figure 5.1. The height is L, interval spacing is W, and amplitude of the wavy bent wall is a. The porous medium temperature is initially T_0. The cavity is heated by the right wall at temperature T_H and cooled by the left wall at temperature T_C.

The porous medium is assumed to be rigid, homogeneous and isotropic; and saturated with the same single-phase fluid. The governing equations have been described in Equations (3.26-3.29) in Chapter 3, and the non-dimensional parameters have also been shown as in Equations (3.14).

For natural convection in porous media, another important parameter is the Darcy-Rayleigh number (Karimi-Fard et al., 1997), defined as,

$$Ra^* = Ra\ Da = \frac{gK\beta\Delta TL_{ref}}{\alpha\gamma} \tag{5.1}$$

The boundary conditions are as follows,

$$\frac{\partial T}{\partial n} = 0,\ \text{on y=0},\ 0 \le x \le W$$

$$\frac{\partial T}{\partial n} = 0,\ \text{on y=L},\ 0 \le x \le W \tag{5.2}$$

$$T\text{=0, on } 0 \le y \le L,\ x = \lambda[1-\cos(2\pi y/L)]$$

$$T\text{=1.0, on } 0 \le y \le L,\ x = 1+\lambda[1-\cos(2\pi y/L)]$$

where $\lambda = a/W$ is the surface waviness of the wavy cavity. The aspect ratio of the wavy cavity is A = *L*/*W*.

The definitions of local Nusselt number and average Nusselt number have been shown as those in Equations (3.15-3.16). Various computations were carried out for the following ranges of parameters: Darcy-Rayleigh number from 10 to 10^5, aspect ratio A from 1 to 5, and surface waviness λ from 0 to 1.8. During the computation, a non-orthogonal, non-uniform and non-staggered grid system was implemented (Figure 5.1). Considering the computational cost and accuracy, a grid independence survey (detail not given here) shows that it is adequate to use a mesh composed of 3200 control volumes and 3444 nodes, with 40 control volumes along the width of the cavity and 80 control volumes along the height.

5.2 Results and Discussion

5.2.1 Streamlines and Isotherms

5.2.1.1 Effect of Aspect Ratio

Figures 5.2a shows the typical isotherm and flow streamline for aspect ratio A = 1 and the Rayleigh-Darcy number is varied from Ra^* = 10 to 10^5. It can be seen that hot fluid moves up along the hot wall (right wall) and turns to the left at the top adiabatic wall, then move down along the cold wall. This causes the circulation inside the cavity. Figures 5.2b and 5.2c show results for other aspect ratios of 3 and 5 respectively, also from Ra^* = 10 to 10^5. The other parameters are fixed at $\lambda = 0.5$,

$\varepsilon = 0.4$, and $Da = 10^{-2}$. Note that the present Darcy number is much higher than those which assumed Darcy law, which is valid for $Da \leq 10^{-4}$ (Karimi-Fard et al., 1997; Aydin et al., 2005).

At low Darcy-Rayleigh number (Figure 5.2a), the flow circulation is very weak, which means a conduction-dominant flow and heat transfer. The result shows similar behaviours with those in a previous study (Misirlioglu et al., 2005). However, some differences also exist especially near top and bottom regions at the right hand side. The present streamlines do not have so large curvatures as those based on Darcy law especially at $Ra^* = 10^5$. This is because Darcy model does not consider the convective, inertia, and viscous terms and thus the flow is able to turn abruptly at the corners, especially those at the right hand side of the cavity.

At higher aspect ratio A=3 (Figures 5.2b), it is interesting that there is a main recirculating flow near the central region and two smaller recirculations near the top and bottom regions. The flow near the axial region is unable to recirculate to the top or bottom regions, due to the viscous effect. Had Darcy law, which has no viscous term, been assumed then there will just be a single main recirculation. It is noted that near the walls, where the natural convection is strong enough, the fluid is able to recirculate to the top unlike those near the axis. When the *Ra** reaches 10^3 (Figure 5.2b middle), the convective effect is strong enough for the whole flow domain to have a single recirculation.

At large $Ra^* = 10^5$ (Figures 5.2a, 5.2b and 5.2c, streamline diagrams on right) there are two recirculation loops at the middle region, instead of just one. The

convection caused by the hot and cold walls is so large that each wall generates a recirculation flow. It is noted that near the middle region, along the *x* direction from cold to hot walls, the temperature gradient is negative near the axis. This is different from those at lower *Ra** in which the temperature gradient is positive throughout the region from cold to hot walls. This explains the distortion of the recirculation streamline at the middle region.

5.2.1.2 Effect of Surface Waviness

Figure 5.3 show the surface waviness effect on the flow and thermal fields at Darcy-Rayleigh number of $Ra^* = 10$ to 10^5. At low Darcy-Rayleigh number (Figure 5.3a), there is one main recirculation region if the cavity is less wavy (see streamline diagram on left).; however at large waviness value $\lambda = 0.6$ there are smaller recirculation regions at the top and bottom in addition to the main one at the middle region The flow near the axial region is unable to recirculate to the top or bottom regions, due to the viscous effect. However, the fluid near the walls is able to recirculate to the top, as the natural convection near the walls is stronger than those near the axis. When the *Ra** reaches 10^5 (Figures 5.3a, b and c, streamline diagrams on right), the convective effect is strong enough for the whole flow domain to have a single recirculation.

The effect of waviness seems to be similar to that caused by aspect ratio which has been discussed earlier. Both waviness and aspect ratio increase the length of the cavity and hence the viscous effect. However when the Darcy-Rayleigh

number becomes large, it dominates over the viscous effect, so that the recirculation flow from the middle region is able to reach the top and bottom. The natural convection at large Darcy-Rayleigh number becomes so strong that it generates two recirculation regions at the middle as discussed earlier.

5.2.2 Local and Average Nusselt Numbers

5.2.2.1 Effect of Darcy Number

To examine the dependence on Darcy number, the local Nusselt number along the cold wall is presented in Figures 5.4a and 5.4b. It is seen that for low Darcy-Rayleigh number (Figures 5.4a), the local Nusselt number has negligible dependence on Darcy number which is thus not needed to be specified as another independent parameter. However at large Darcy-Rayleigh number ($Ra^*=10^3$ in Figures 5.4b) there is a strong dependence on Darcy number. The Darcy number characterizes the permeability effect and Rayleigh number characterizes the natural convection effect. However the combined effects are not characterized by the Darcy-Rayleigh number when it is of large values. In addition to the Darcy-Rayleigh number, the Darcy number is needed as another independent parameter.

It is seen that the Darcy number seems to change the local Nusselt number greatly, around an order of magnitude. This is because when Darcy number is changed, the Rayleigh number also changes in order to keep the Darcy-Rayleigh number constant. That is, the effects of permeability and natural convection are not isolated in Figure 5.4b.

To see the real effects of Darcy number, instead of setting the Darcy-Rayleigh number constant, the Rayleigh number is made constant in Figures 5.5a and 5.5b. it is seen that at low *Ra* of 10^3 the effect of *Da* is negligible. However at high *Ra* of 10^5 there is obvious effect of *Da*. At larger *Da*, or larger permeability, there is smaller flow resistance through the porous medium, leading to larger flow convection and heat transfer. Thus the local Nusselt number increases with *Da*. However, when *Da* is less than10^{-4}, the Nu changes little with *Da* (see Figure 5.5b). This range of low Darcy number less than 10^{-4} is called the Darcy flow region (Karimi-Fard et al., 1997; Misirlioglu et al., 2005).

5.2.2.2 Effect of Porosity Value

The effect of porosity is examined next, as presented in Figures 5.6a and 5.6b. At larger porosity, with permeability constant, there is larger flow through the porous medium, leading to larger flow convection and heat transfer. Thus the local Nusselt number increases with porosity. The dependence is rather similar to that of Darcy number considered above. There is negligible dependence on porosity at low Darcy-Rayleigh number (Figure 5.6a) but when *Ra** becomes large the dependence is noticeable (Figure 5.6b). The porosity, like Darcy number, is needed as another independent parameter.

The dependence on Darcy number and porosity can be seen from the generalized momentum Equation (3.27). The Darcy number is present in the Darcy and inertia terms; and the porosity is in the convective, inertia and viscous terms. However, when

the Darcy equation is assumed, there is no dependence on Darcy number and porosity; also, the effect of Darcy number is included in the Darcy-Rayleigh number.

5.2.2.3 Effect of Aspect Ratio and Surface Waviness

In Figure 5.7 the effect of aspect ratio on local Nusselt number is shown. For the case shown, a larger aspect ratio reduces the local Nusselt number. When the aspect ratio is small, A=1, the local Nusselt number along the middle region approaches zero, which indicates that the temperature gradient there is small (see Figure 5.2a isotherm) due to the shape effect.

The near-zero Nusselt number is more obvious in Figure 5.8a in which the shape effect is more pronounced, with A=0.5 and λ up to 1.8. It is interesting that at λ =1.4, slightly negative Nusselt numbers are found, which indicates negative temperature gradient. Negative Nusselt numbers were also observed by Misirlioglu et al. (2005). However positive Nusselt number is always found at another aspect ratio, A = 4 (Figure 5.8b) in which the temperature gradient is large (see Figure 5.3b isotherm).

The values of the average Nusselt number Nu_{av} at the cold wall (left) are shown in Table 5.1 for different Darcy-Rayleigh number *Ra**, aspect ratio A and wave amplitude λ. In general, Nu_{av} increases with Darcy-Rayleigh number due to stronger natural convection. For each Darcy-Rayleigh number, the aspect ratio or wave amplitude has effect on the Nusselt number. Whether the Nusselt number increases or decreases may be due to the different flow regimes inside the cavity as

explained by Mahmut and Fraser (2004). There may be an optimum aspect ratio or wave amplitude to achieve a peak Nusselt number which enhances the heat transfer.

5.3 Conclusions

The steady natural convection inside a porous cavity, with wavy vertical walls, is numerically studied with the Darcy-Brinkman-Forchheimer extended model. Isotherms and streamlines are presented at different aspect ratio, waviness, and Darcy-Rayleigh number. The present results show some interesting differences as compared with the Darcy's law results due to its over prediction of the velocity field. The present flow field does not have so large curvature near the top and bottom regions. At low Darcy-Rayleigh number another recirculation zone may appear at both the top and bottom regions, which are additional to the main recirculation at the middle. At large Darcy-Rayleigh number, the top and bottom recirculations vanished and the middle recirculation was distorted into two. The results of local Nusselt number show that the dependence on Darcy number and porosity is not small at large Darcy-Rayleigh number.

Table 5.1 Average Nusselt number at the cold wall for different aspect ratios and wave amplitudes (Da=0.01, $\varepsilon = 0.4$).

		Nusselt number for cold wall		
		$Ra^* = 10^1$	$Ra^* = 10^3$	$Ra^* = 10^5$
A=4	$\lambda = 0$	1.000	1.614	4.920
	$\lambda = 0.3$	1.038	1.561	5.468
	$\lambda = 0.4$	1.068	1.526	5.358
	$\lambda = 0.5$	1.107	1.498	5.229
	$\lambda = 0.6$	1.155	1.487	5.091
$\lambda = 0.5$	A=1	1.274	1.659	6.796
	A=2	1.219	1.768	6.001
	A=3	1.153	1.645	5.292
	A=4	1.107	1.498	5.229
	A=5	1.077	1.377	4.333

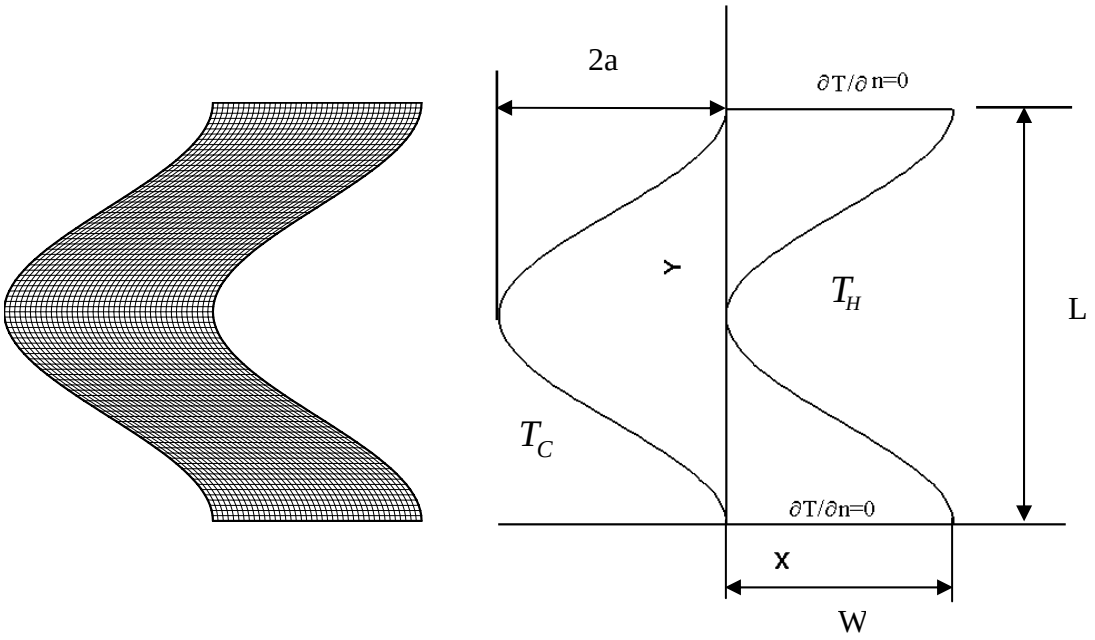

Figure 5.1 Schematic diagram of the porous cavity.

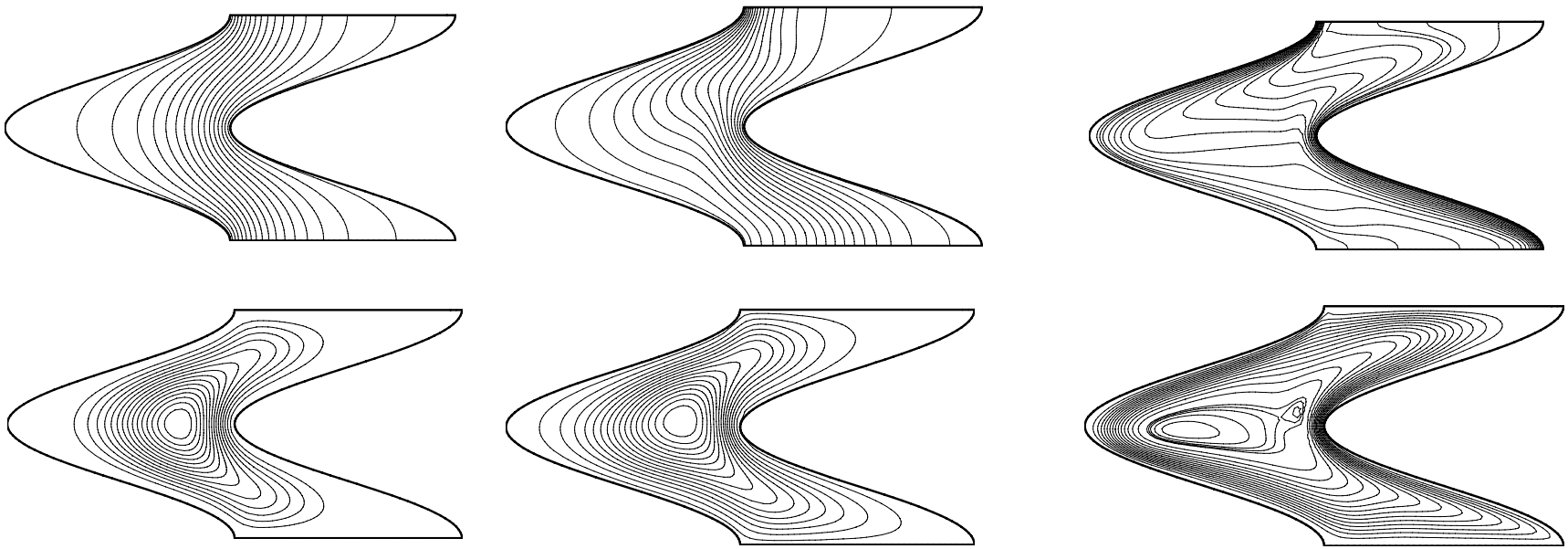

Figure 5.2a

Figure 5.2 Isotherms (top) and streamlines (bottom) at different Darcy-Rayleigh number $Ra^* = 10$, 10^3, 10^5 (left to right); with $\lambda = 0.5$, Da = 0.01, $\varepsilon = 0.4$; at (a) A = 1; (b) A = 3; (c) A =5.

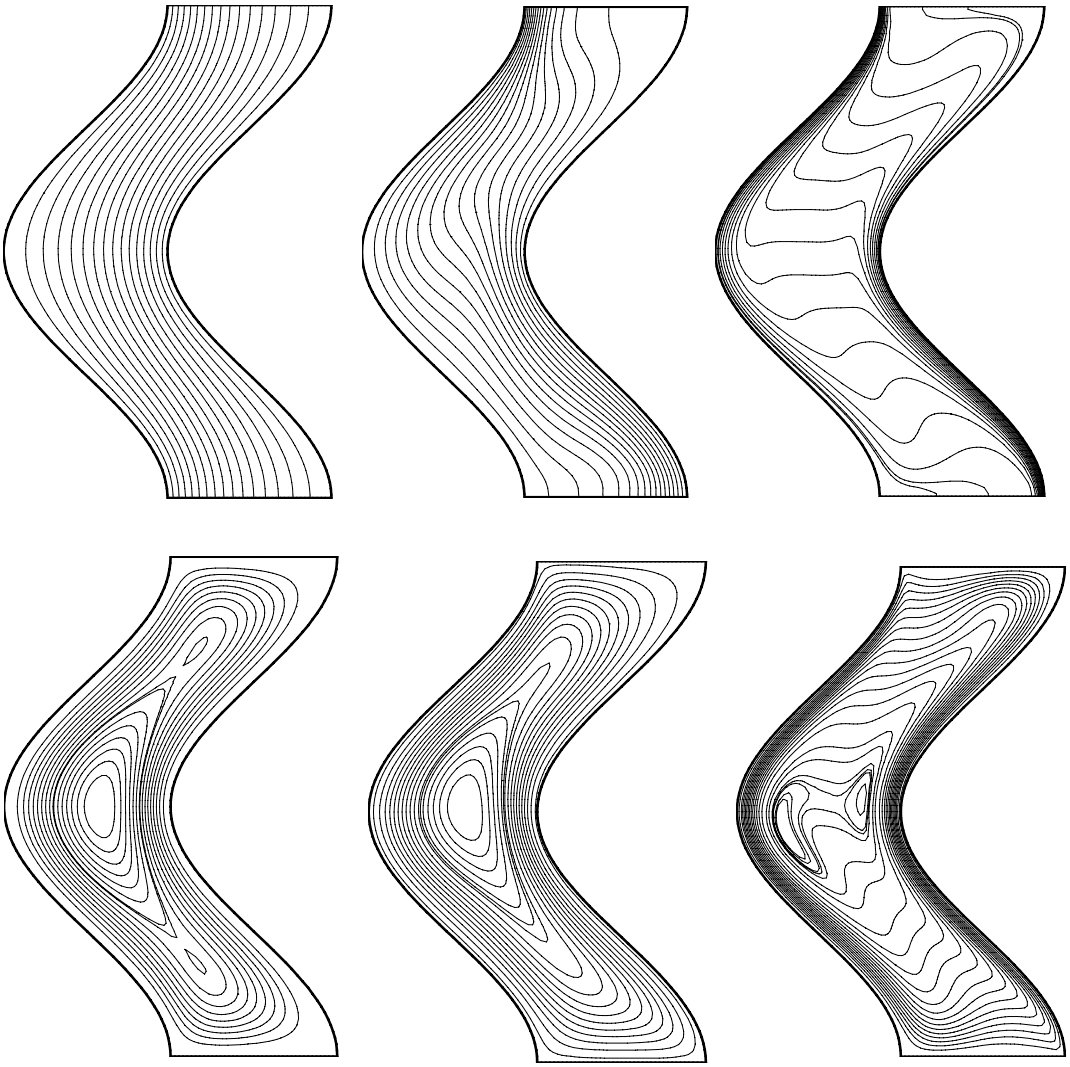

Figure 5.2b

Figure 5.2 Isotherms (top) and streamlines (bottom) at different Darcy-Rayleigh number $\mathrm{Ra}^* = 10$, 10^3, 10^5 (left to right); with $\lambda = 0.5$, Da = 0.01, $\varepsilon = 0.4$; at (a) A = 1; (b) A = 3; (c) A =5.

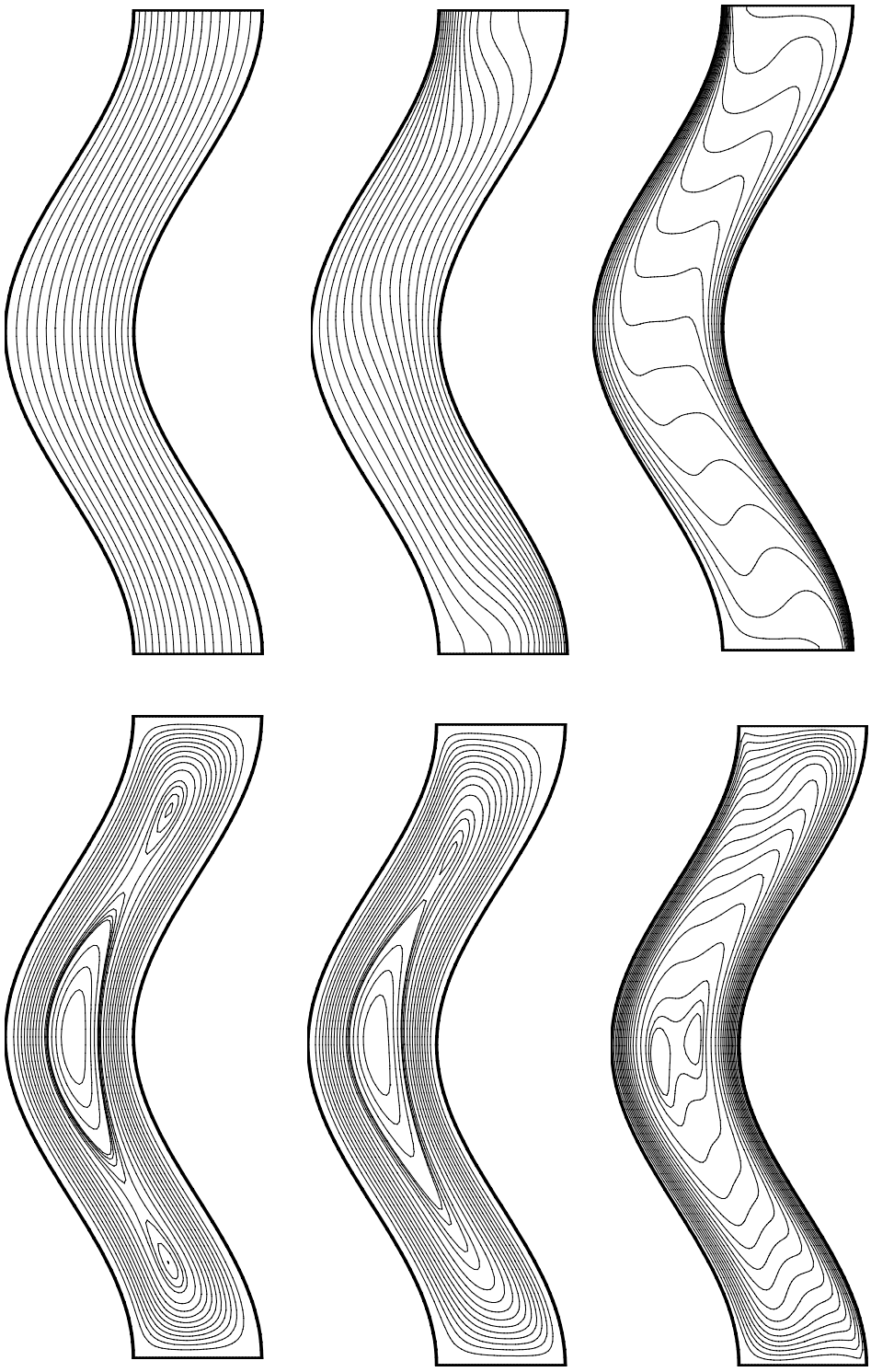

Figure 5.2c

Figure 5.2 Isotherms (top) and streamlines (bottom) at different Darcy-Rayleigh number $\mathrm{Ra}^* = 10$, 10^3, 10^5 (left to right); with $\lambda = 0.5$, Da = 0.01, $\varepsilon = 0.4$; at (a) A = 1; (b) A = 3; (c) A =5.

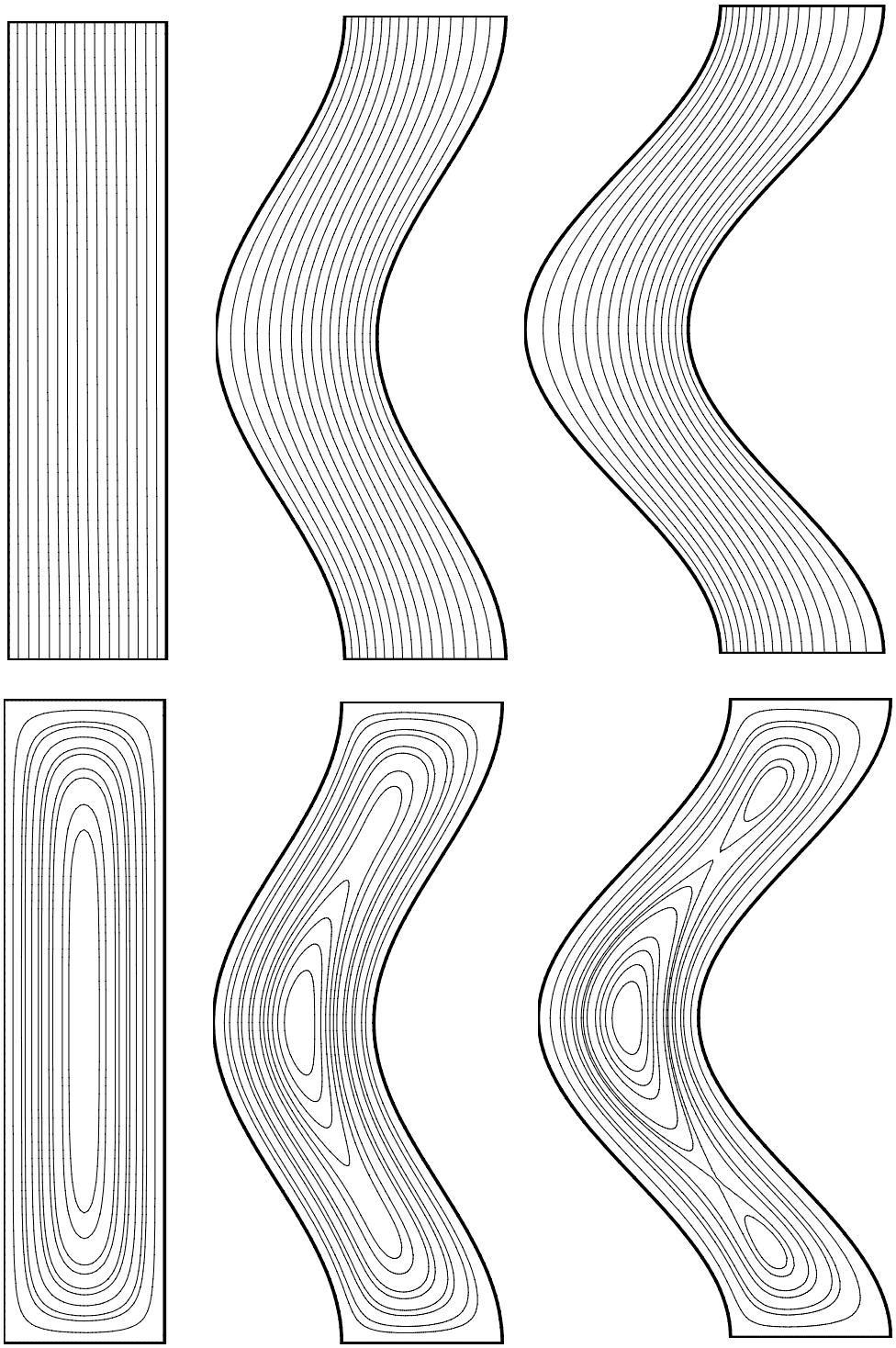

Figure 5.3a

Figure 5.3 Isotherms (top) and streamlines (bottom) at different waviness ratio $\lambda = 0,\ 0.4,\ 0.6$ (left to right); with A = 4, Da = 0.01, $\varepsilon = 0.4$;

at (a) $\mathrm{Ra}^* = 10$; (b) $\mathrm{Ra}^* = 10^3$; (c) $\mathrm{Ra}^* = 10^5$.

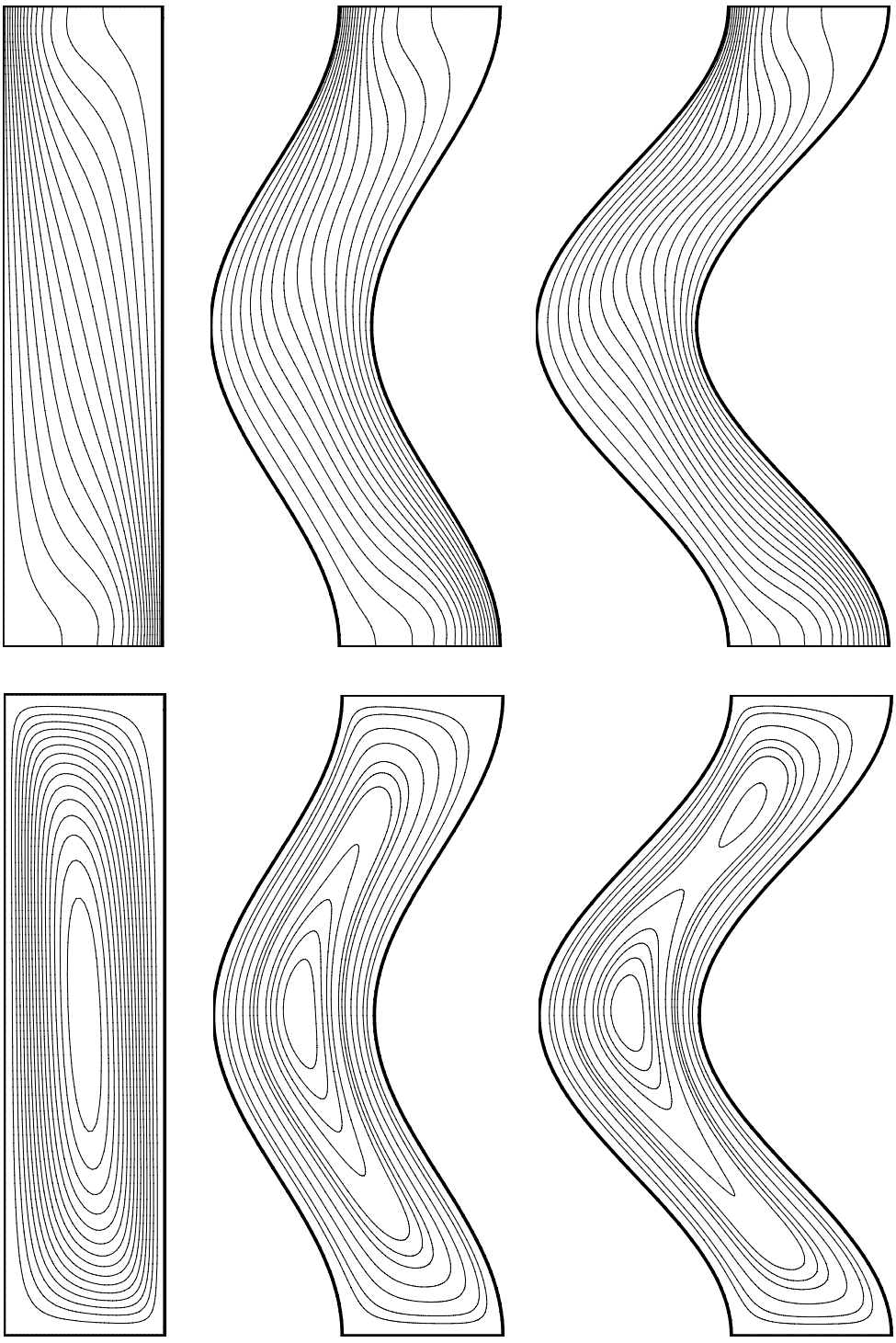

Figure 5.3b

Figure 5.3 Isotherms (top) and streamlines (bottom) at different waviness ratio $\lambda = 0,\ 0.4,\ 0.6$ (left to right); with A = 4, Da = 0.01, $\varepsilon = 0.4$;

at (a) $\mathrm{Ra}^* = 10$; (b) $\mathrm{Ra}^* = 10^3$; (c) $\mathrm{Ra}^* = 10^5$.

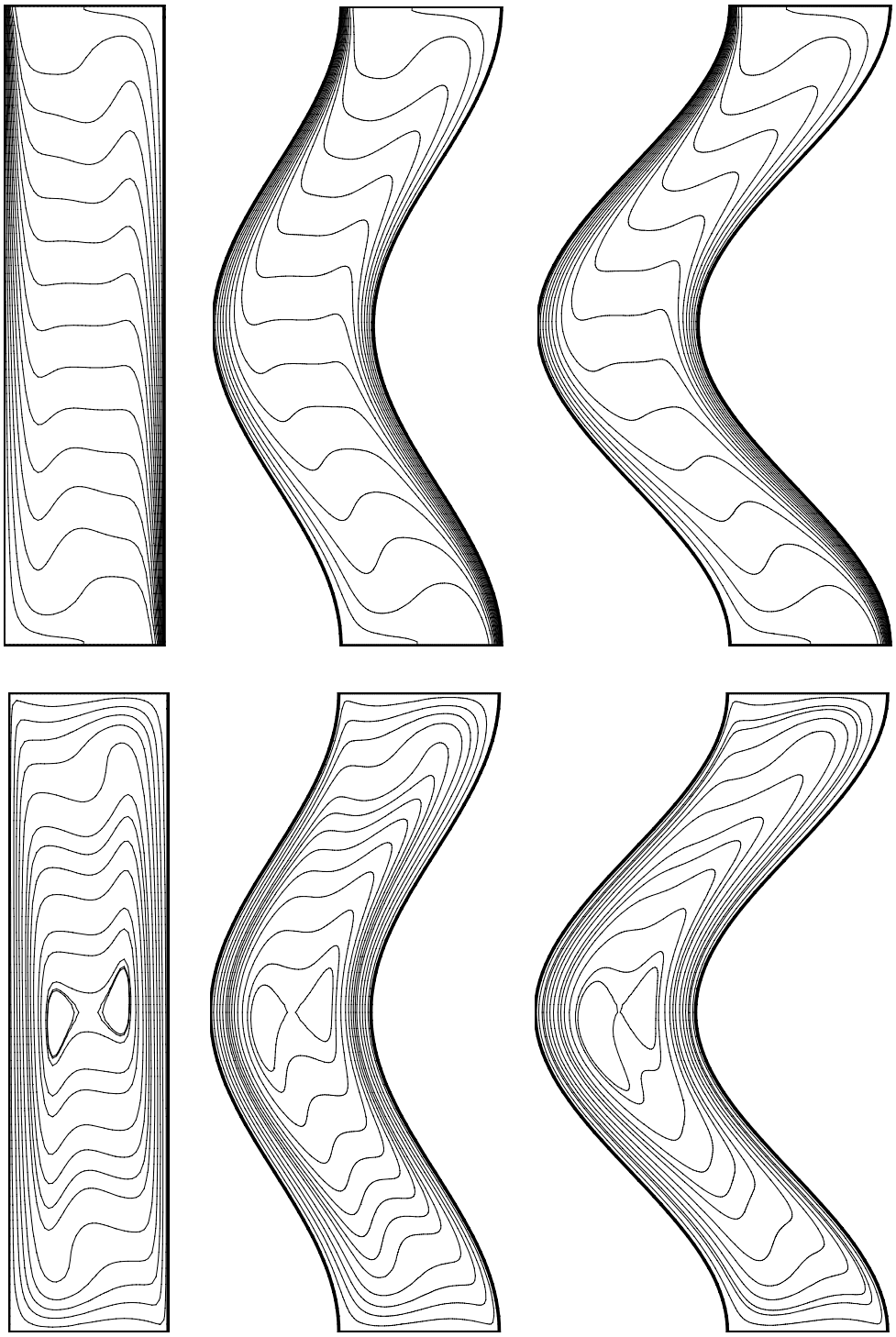

Figure 5.3c

Figure 5.3 Isotherms (top) and streamlines (bottom) at different waviness ratio $\lambda = 0,\ 0.4,\ 0.6$ (left to right); with A = 4, Da = 0.01, $\varepsilon = 0.4$;

at (a) $\mathrm{Ra}^* = 10$; (b) $\mathrm{Ra}^* = 10^3$; (c) $\mathrm{Ra}^* = 10^5$.

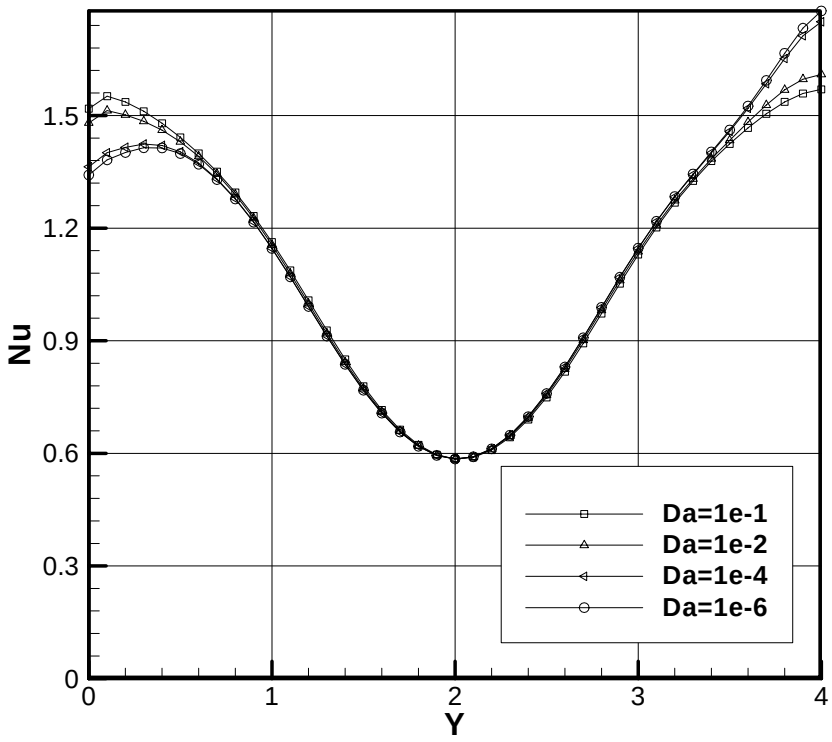

(a)

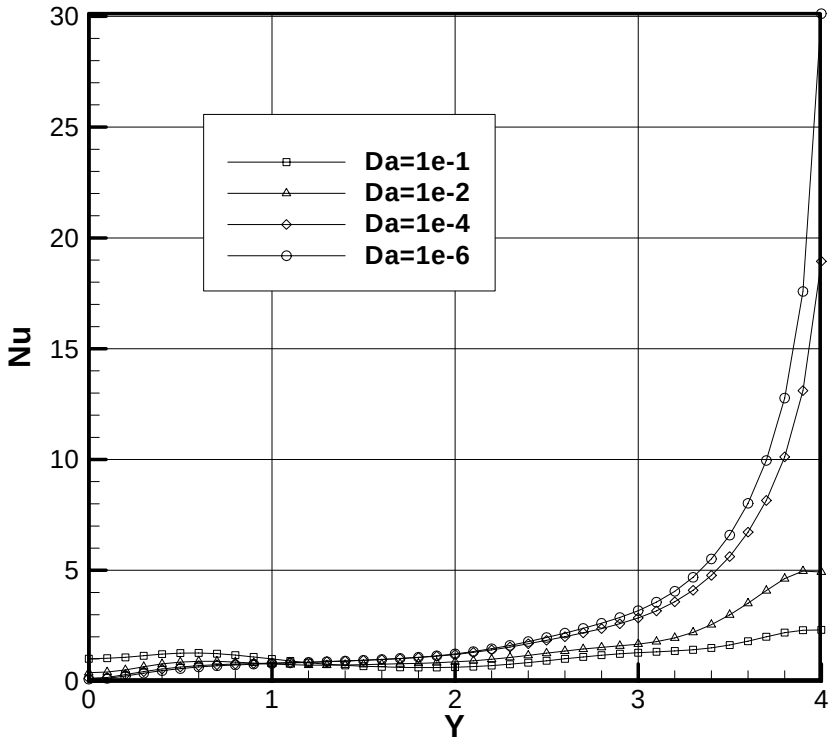

(b)

Figure 5.4 Local Nusselt number along the cold wall and its dependence on Darcy number at (a) $Ra^* = 10$; (b) $Ra^* = 10^3$; other parameters are $\varepsilon = 0.4$, A=4, $\lambda = 0.5$.

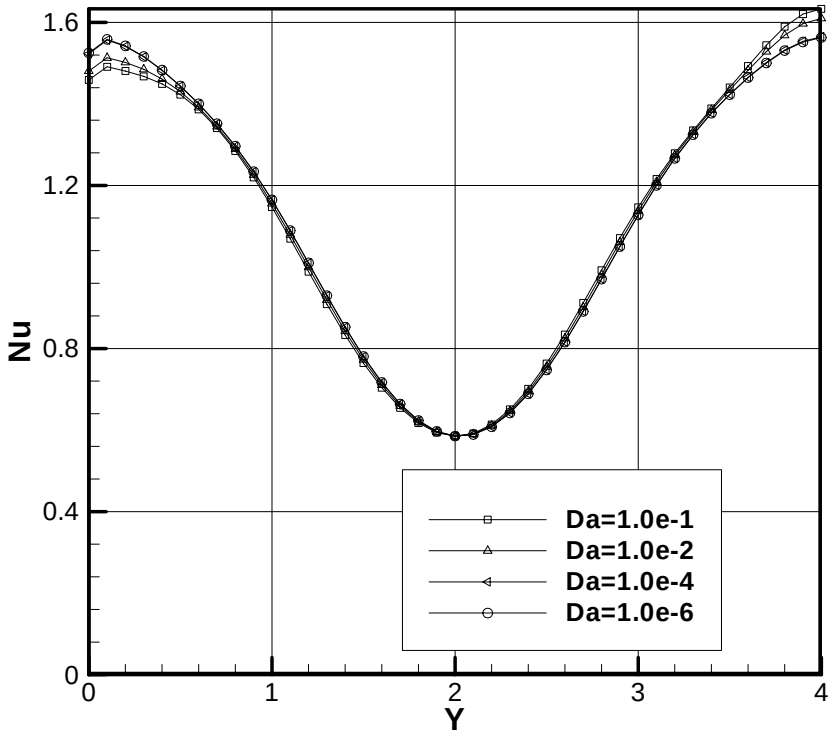

(a)

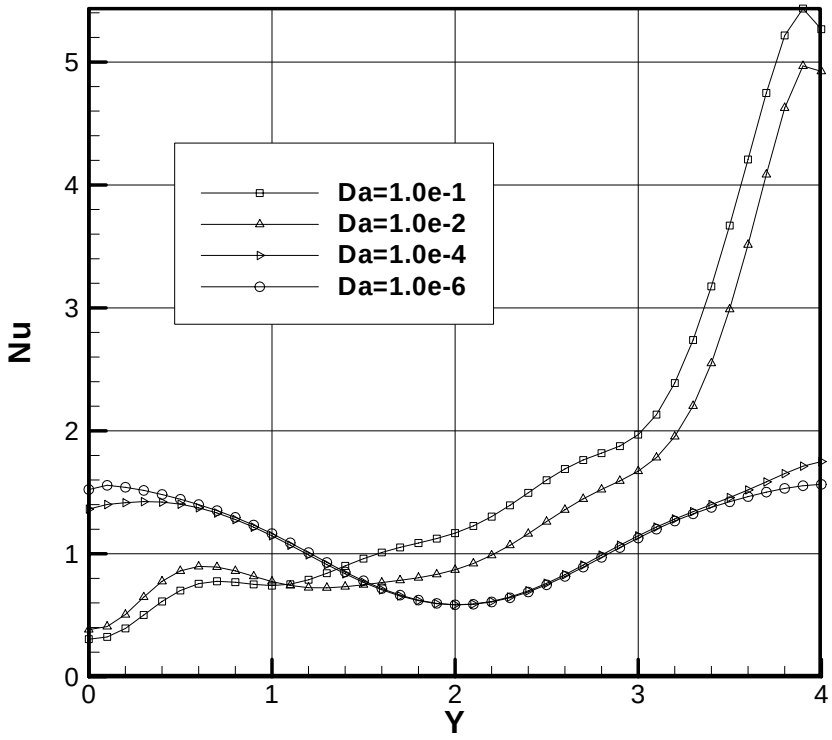

(b)

Figure 5.5 Local Nusselt number along the cold wall and its dependence on Darcy number at (a) $Ra=10^3$; (b) $Ra=10^5$; other parameters are $\varepsilon = 0.4$, A=4, $\lambda = 0.5$.

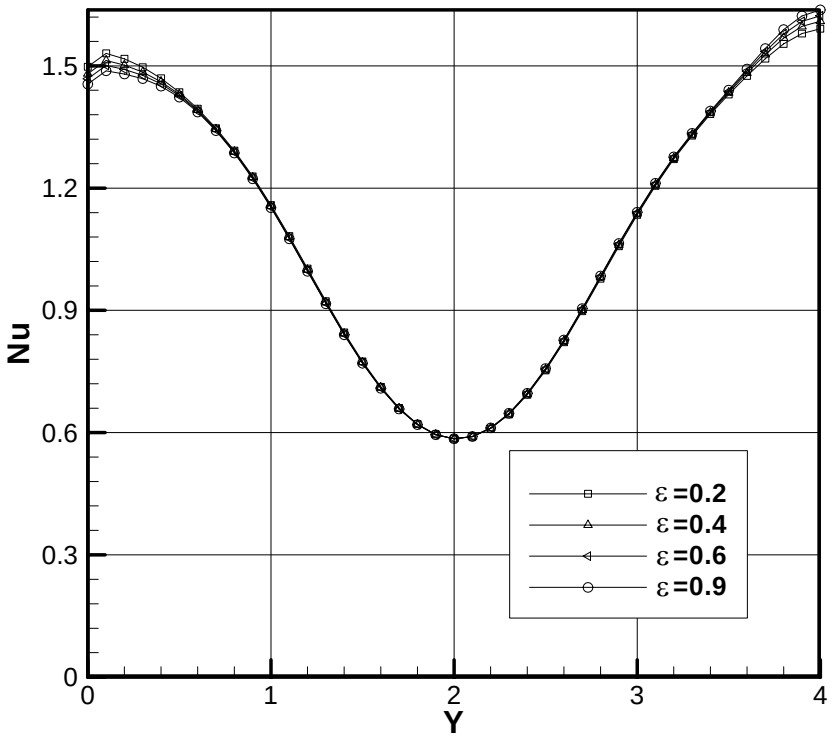

(a)

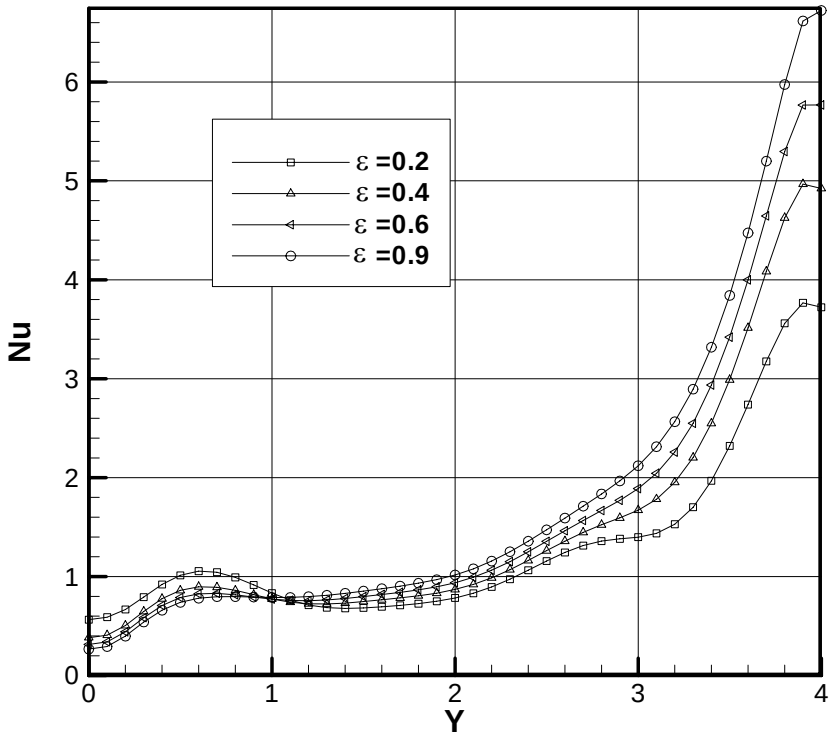

(b)

Figure 5.6 Local Nusselt number along the cold wall and its dependence on porosity at (a) $Ra^{*}=10$; (b) $Ra^{*}=10^{3}$; other parameters are fixed at Da=10^{-2}, A=4, $\lambda=0.5$.

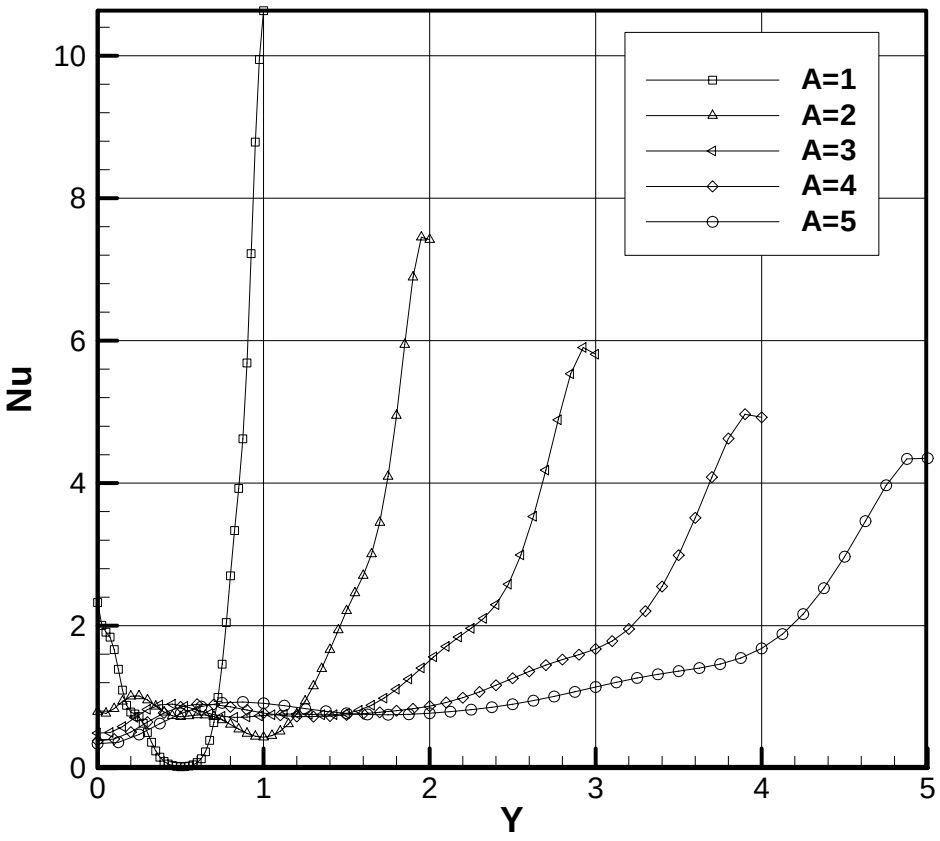

Figure 5.7 Effect of different values of aspect ratio local Nusselt number along the cold walls; at $Ra^{*}=10^{3}$, $Da=10^{-2}$, $\varepsilon = 0.4$, $\lambda = 0.5$.

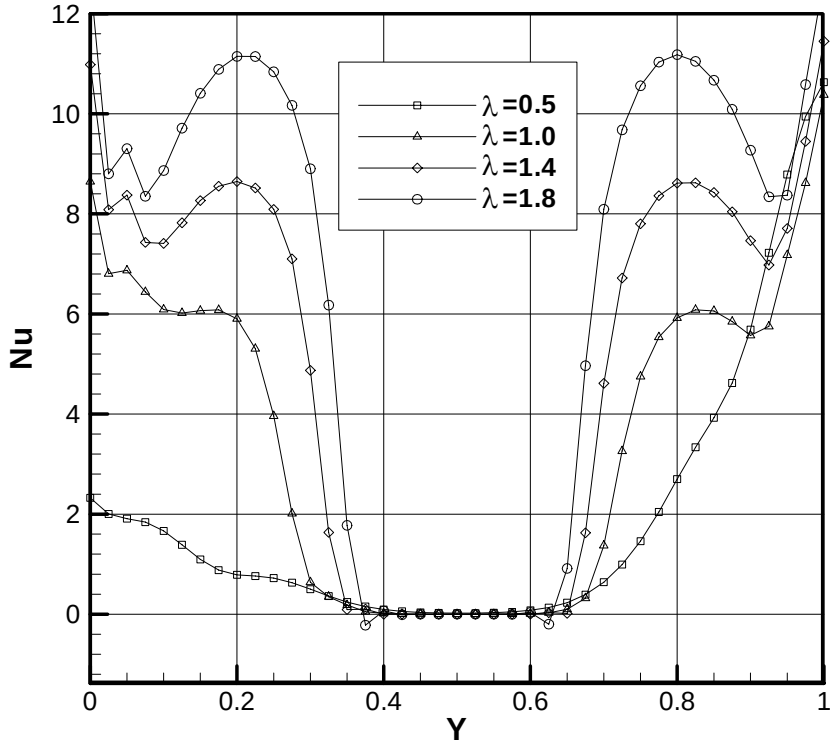

(a)

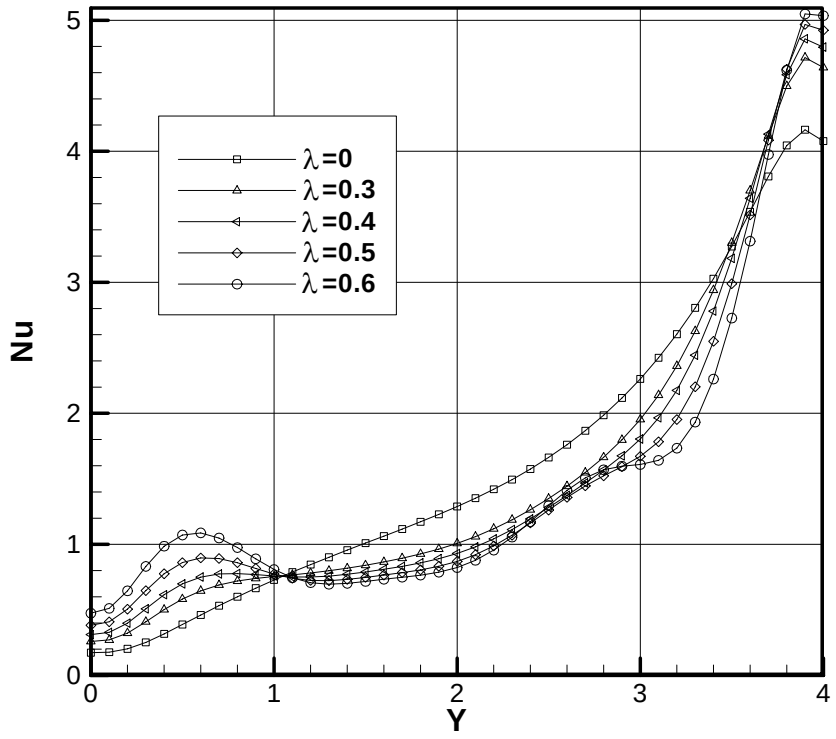

(b)

Figure 5.8 Effect of waviness on local Nusselt number along the cold walls; at $Ra^* = 10^3$, Da=10^{-2}, $\varepsilon = 0.4$; (a) A=0.5; (b)A=4.

Chapter 6

Forced Convection in Porous/fluid Coupled Domains*

Heat transfer enhancement is usually required in engineering situations, for example, heat sink, electronic cooling, drying technology and packed-bed chemical reactors. Forced convection heat transfer can be enhanced with the addition of porous media (Huang and Vafai, 1994a and b; Vafai, 2001; Kiwan and AI-Nimr, 2001; Bhattacharya and Mahajan, 2002). Different from those natural convection problems in Chapter 5, the fluid flow is caused by an external agent unrelated to the heating effect. Thus heat transfer effect is mainly influenced by the incoming flow properties. Numerical simulations show that heat transfer can be increased globally with a porous media insert after backward facing step (Martin et al., 1998; Zhang and Zhao, 2000) or locally with the addition of a porous floor segment (Abu-Hijleh, 1997 and 2000). However, their numerical methods were based on one-domain approach, and the interface conditions between the porous and fluid domains were not carefully treated.

In this chapter, a two-domain approach is implemented to solve these forced convection problems in porous/fluid coupled domains. At its interface, the flow boundary condition imposed is a shear stress jump, which includes viscous and inertial effects, together with a continuity of normal stress. The thermal boundary

*Parts of this chapter have been published in *International Journal for Numerical Methods in Fluids* (Chen et al., 2008a), and *Numerical Heat Transfer A: Applications* (Chen et al., 2008b)

condition is continuity of temperature and heat flux. Two kinds of flow over a backward facing step are investigated. One is set with a porous insert after the step, which can eliminate the regions of recirculation. This can enhance the global heat transfer along the bottom wall. The other one is set with a porous floor segment, which can elongate the regions of recirculation. This can increase the local heat transfer after the segment along the bottom wall. The results were presented with the streamlines and local Nusselt number for different geometry lengths, Darcy numbers, porosity values. The local and average Nusselt numbers dependency on the stress jump parameters was also investigated.

6.1 Backward Facing Step with a Porous Insert

6.1.1 Problem Statement

Steady, two-dimensional, laminar and incompressible flow over a backward-facing step is considered here (Figure 6.1). The porous insert is located after the step. The inlet flow velocity is specified as a parallel flow with a parabolic horizontal component given by u(y) = 24y(0.5-y) for $0 \le y \le 0.5$. This produces an average inflow velocity of $u_{av} = 1.0$ which is taken as the reference velocity. The inlet flow and step wall temperature are set to T_i; the upper and bottom walls supply a constant heat flux q; and the outlet condition is adiabatic.

The dimensionless governing equations for porous regions are the same with Equations (3.37) to (3.39). The dimensionless heat transfer equation is as following:

$$u\frac{\partial T}{\partial x}+v\frac{\partial T}{\partial y}=R_k\bullet\frac{1}{Pr\bullet Re}(\frac{\partial^2 T}{\partial x^2}+\frac{\partial^2 T}{\partial y^2}) \tag{6.1}$$

where the dimensionless parameters are the same as those in Equation (3.21) in Chapter 3. R_k is the ratio of thermal conductivity in porous and fluid regions; *Pr* is the Prandtl number of the fluid; *Re* is the Reynolds number defined as following:

$$R_k=\frac{k_{eff}}{k_f}, Pr=\frac{\mu}{\rho\alpha}, Re=\frac{\mathrm{U}_{av}\mathrm{H}\rho}{\mu} \tag{6.2}$$

where α is the fluid thermal diffusivity; k_f is the fluid thermal conductivity, k_{eff} is effective thermal conductivity of porous media.

For the homogeneous fluid part, the dimensionless governing equations are the same with Equations (3.17) to (3.20).

At the interface between the homogeneous fluid and porous medium regions, additional boundary conditions must be applied to couple the flows in the two domains. The boundary conditions include flow and heat transfer.

The interface coupling conditions for flow are the same with those Equations (2.9) to (2.11) and they are non-dimensionlized as:

$$\frac{1}{\varepsilon}\frac{\partial u_t}{\partial n}\bigg|_{\text{porous}}-\frac{\partial u_t}{\partial n}\bigg|_{\text{fluid}}=\beta\frac{1}{\sqrt{Da}}u_t\bigg|_{\text{interface}}+\beta_1\bullet Re\bullet u_t^2 \tag{6.3}$$

$$\vec{u}\big|_{\text{fluid}}=\vec{u}\big|_{\text{porous}}=\vec{v}_{\text{interface}} \tag{6.4}$$

$$\frac{1}{\varepsilon}\frac{\partial u_n}{\partial n}\bigg|_{\text{porous}}-\frac{\partial u_n}{\partial n}\bigg|_{\text{fluid}}=0 \tag{6.5}$$

For heat transfer interfacial condition, continuities of temperature and heat flux are implemented here (Neale and Nader, 1974; Vafai and Thiyagaraja, 1987; Ochoa-Tapia and Whitaker, 1997; Jang and Chen, 1992; Kim and Choi, 1996; Kuznetsov, 1999),

$$T\big|_{\text{fluid}} = T\big|_{\text{porous}} = T_{\text{interface}} \tag{6.6}$$

$$R_k \left.\frac{\partial T}{\partial n}\right|_{\text{porous}} = \left.\frac{\partial T}{\partial n}\right|_{\text{fluid}} \tag{6.7}$$

The local and average Nusselt number and frictional loss (Zhang and Zhao, 2000; Beavers and Joseph, 1967) are defined as:

$$Nu = \frac{qH}{(T_w - T_i)k_f} \tag{6.8}$$

$$Nu_{av} = \frac{1}{L}\int_l Nu dx \tag{6.9}$$

$$h_l = \left(\frac{\overline{p}_i}{\rho_f} + \alpha_i \frac{U_i^2}{2}\right) - \left(\frac{\overline{p}_o}{\rho_f} + \alpha_o \frac{U_o^2}{2}\right) \tag{6.10}$$

where $\overline{p}_i$ and $\overline{p}_o$ are the average inlet and outlet pressures, and α_i and α_o are the kinetic coefficients, defined as:

$$\alpha_{i,o} = \frac{\int_{A_{i,o}} u^3 dA}{\left(\int_{A_{i,o}} u dA\right)^3} \tag{6.11}$$

In the present study, non-uniform, body-fitted and orthogonal meshes are employed, where the density of meshes over the step back is larger than those in areas far downstream. The initial conditions for the computation were either a uniform flow

at the inlet or the results of a previous calculation, often at different Reynolds number, Darcy number or porosity values. For simplicity, the ratio of the effective thermal conductivity of porous medium to fluid conductivity, R_k is set to be 1; the heat transfer would be more enhanced if the ratio is larger. The Prandtl number is set as Pr = 0.72, which is the value for air.

Considering the computational cost and accuracy, the grid independency survey (details not given here) shows that a total 380x100 mesh, for both porous and fluid domains, is adequate.

6.1.2 Results and Discussion

6.1.2.1 Effect of Reynolds Number

Figure 6.2 shows the stream contours of the flow for different Reynolds number from 10 to 800, at $Da = 10^{-2}$. It is observed that increasing the Reynolds number would increase the recirculation length, which is the distance from the back of the step to the vortex reattachment point. The flow field affects the heat transfer and this is shown in Figure 6.3 for the same Darcy number, in the form of axial distribution of lower wall Nusselt number. In the recirculation region, the heat transfer is first reduced. Then it increases towards the attachment point, after which the Nusselt number gradually decreases toward the fully developed state. However for low Re = 10, the recirculation region is so small that it does not cause much effect on the Nusselt number which shows decrease with distance from the step. Higher Reynolds number gives higher Nusselt number as expected.

When the Darcy number is small, $Da=10^{-4}$ (details not shown here), the flow after the step is different as there is no recirculation region even with the *Re*=800. There is no flow separation due to the small porous flow. The lower wall Nusselt number keep decreasing (Figure 6.4) with distance from the step. As *Re* increases to 800, the main heat transfer is convection. In the following computation to study mainly the convective mode, the *Re* is set to 800.

6.1.2.2 Effect of Darcy Number

The Darcy number effect is shown in Figure 6.5, with the same parameters as Zhang and Zhao (2000), for the flow field at *Re* = 800. When the insert has high permeability, the recirculation length is still long (Figure 6.5a). With a lower permeability ($Da = 10^{-3}$ in Figure 6.5b), the insert breaks up the recirculation region into a small vortex in the region porous and a recirculation region in the fluid domain. With even lower Darcy number ($Da = 10^{-4}$ and 10^{-5} in Figures 6.5c and d respectively) the recirculation has disappeared. The effect on heat transfer is shown in Figure 6.6. Note that the scale is larger for ease of comparison later with results of Zhang and Zhao (2000). In the region downstream of the step, there is pronounced heat-transfer enhancement with lower Darcy numbers (high Nusselt number at $Da = 10^{-4}$). There is enhanced heat transfer due to elimination of the recirculation region. After the recirculation region has been suppressed, there is no further enhancement of heat transfer when Darcy number is lowered to10^{-5}; the Nusselt number drops due to

lower convection in the porous insert. So for this Re = 800, there is an optimal Da between 10^{-4} and 10^{-5}.

A comparison with the one-domain results of Zhang and Zhao (2000) is also shown in Figure 6.6. The main difference in the two methods is the treatment of the interface pressure and velocity as discussed in Section 2.2, Chapter 2. Note that the present stress jump parameters were set to zero to permit comparison with the one-domain model. As compared with the one-domain results, there is little discrepancy of the Nusselt numbers in the regions inside the porous insert and far downstream. Some discrepancies are found in the region just downstream of the porous insert. However the discrepancies are small for $Da = 10^{-4}$ (see Figure 6.6). At this small Da, there is no recirculation region (Figure 6.5) which may explain why the interface treatment seems to have less effect. The unseparated gross-flow downstream of the porous inserts, being mainly determined by the channel height, would be relatively less sensitive to the interface pressure. At larger Darcy numbers (10^{-2} and 10^{-3}), the discrepancies are significant which is attributed to the presence of the recirculation regions (see streamline Figures 6.5a and b). It is noted that the recirculation lengths computed here are longer than those of Zhang and Zhao (2000). The comparison indicates that the interface pressure has greater effects on the downstream flow, and hence the local Nusselt number, when there is a recirculation region. Thus a careful treatment of the interface pressure would be advantageous when the flow pattern is complex.

6.1.2.3 Effect of Porous Insert Length

Figure 6.7 shows the effect of the porous insert length on the flow field with $Da = 10^{-2}$. With insert length of zero or small, there are two recirculation regions. A longer insert length of a/H=0.2 suppresses the upper recirculation region. Longer insert also reduces the length of the lower recirculation region. However, there is little difference in Nusselt numbers (details not shown here) as the insert length does not suppress the bottom recirculation. It is not suppressed, even with a longer insert, because there is insufficient flow resistance with a large Darcy number.

Figure 6.8 shows the effect of the porous insert length on the flow field with a smaller $Da = 10^{-4}$. With longer insert, the recirculation regions are completely suppressed (Figures 6.8c and d). Figure 6.9 shows the corresponding axial distribution of lower wall Nusselt number. The longer inserts give more enhanced heat transfer behind the step due to the elimination of recirculation region.

Figures 6.10a and b show velocity profiles behind the step (x/H = 0.5) for a short and long inserts respectively. With a short insert (Figure 6.10a), there are negative or small velocities near the lower wall due to the recirculation regions there (see Figures 6.7b and 6.8b). With a long insert (Figure 6.10b), the velocity profiles are greatly affected by the Darcy number. With large $Da \geq 10^{-2}$, there are negative velocities near the lower wall due to the recirculation region there (see Figure 6.7d). When Da decreases to 10^{-3} or less, there is forward velocity near the bottom wall as the bottom recirculation region has been eliminated (see Figure 6.8d for $Da = 10^{-4}$). The velocity profiles explain the enhancement of the local heat convection in the

bottom region behind the step. However, there is no additional enhancement below $Da = 10^{-4}$. Once the recirculation has been suppressed, a further decrease of the Darcy number to 10^{-5} will give lower velocity (compared to that of $Da = 10^{-4}$ as shown in Figure 6.10b). Thus there is an optimal Darcy number to achieve enhanced heat transfer at the lower wall as mentioned earlier (shown in Figure 6.6).

In Figure 6.11, the dimensionless channel head loss (normalized by that with no porous insert) is shown as a function of insert length and Darcy number. The head loss is higher with longer insert length or smaller Darcy number, as expected. To achieve optimal enhancement of heat transfer, it is necessary to avoid excessive frictional losses. Thus a combination of medium Darcy number and insert length is preferred.

6.1.2.4 Effect of Porosity Values

Figure 6.12 gives out the porosity effect on the axial distribution of lower wall Nusselt number with $Da = 10^{-4}$. A smaller porosity gives higher Nusselt number behind the step, as expected. However, the porosity effect is rather small.

6.1.2.5 Effect of Stress Jump Parameters

The stress jump parameters were varied from -1 to +1 and its effect on the average lower wall Nusselt number is presented in Table 6.1 for $Re = 800$. It can be seen that for the larger Darcy number $Da = 10^{-2}$, there is little effect; the insert is too porous to affect the recirculation region as discussed earlier. For the smaller Darcy

number $Da = 10^{-4}$, the difference is more noticeable but still not large, about 4% when both β and β_1 are varied from -1 to 1. It is not surprising that the jump coefficients have little effect on average values like the wall Nusselt number in Table 6.1. In the literature, it is possible to find studies (Valencia-Lopez and Ochoa-Tapia, 2001) which show that even the type of formulation have almost no effect on global coefficients.

The importance of a numerical method that considers properly the effect of the jump coefficients or the formulation of the boundary conditions should be assessed by analyzing local variable predictions in the neighborhood of the interface fluid-porous medium. The effect of the stress jump parameters on the local Nusselt number is shown in Figure 6.13. Their effects on the local velocity and temperature profiles at x/H=3.0 are shown respectively in Figures 6.14 and 6.15. It is noted that there are some effects of β and β_1 when they are varied from -1 to +1. Positive parameters give a larger peak velocity and smaller velocity near the wall. Thus the temperatures there are smaller and hence the Nusselt numbers are larger.

The effect of stress jump parameters is small in the present case because the dominant flow direction is near normal to the interface. In parallel flow past a porous-fluid interface (Alazmi and Vafai, 2001), in which the porous medium partially fills the channel, it was found that the velocity profile was very sensitive to the stress parameters. It is expected that the stress parameters will have greater effect on the heat transfer, if the porous-insert was designed to partially fill the channel in order to avoid high friction losses.

6.2 Backward Facing Step with a Porous Floor Segment

6.2.1 Problem Statement

As shown in Figure 6.16a, the porous floor segment is located after the step. The inlet flow velocity is specified as that in section 6.1.1. The inlet flow temperature is set to T_∞; the upper, step walls and left wall of the porous segment are adiabatic, while the bottom wall temperature is T_w.

The governing equations for porous and fluid regions, interface coupling conditions and dimensionless parameters are the same with those Equations (3.17) to (3.20), (3.37) to (3.39) and (6.1) to (6.7).

The local and average Nusselt numbers (Abu-Hijleh, 1997 and 2000) are defined as:

$$Nu(x) = \frac{-H \left.\dfrac{\partial T(x,y)}{\partial y}\right|_{y=floor}}{(T_w - T_\infty)} \tag{6.12}$$

$$Nu_{av} = \frac{1}{l}\int_l Nu(x)dx \tag{6.13}$$

Non-uniform, body-fitted and orthogonal meshes are employed, where the density of meshes over the step back is larger than those in areas far downstream, shown as in Figure 6.16b. The initial conditions for the computation were either a uniform flow or the results of a previous calculation, often at different Reynolds number, Darcy number or porosity values. For simplicity, the ratio of the effective thermal conductivity of porous medium to fluid conductivity, R_k is set to be 1; the

heat transfer effect would be more enhanced if the ratio is larger. The Prandtl number is set as Pr = 0.72, which is the value for air.

The mesh size was varied to obtain a mesh independent solution, which served as a check on the consistency of the numerical scheme. For the longest or deepest porous floor cases considered in the study, a mesh made of 360x100 grids for the pure flow field. For the porous field, a mesh composed of 80x25 to 300x25 (depending on the floor lengths) or 200x10 to 200x100 (depending on the floor depths) was found to be sufficient. Further increase of the grid numbers was found to cause less than 1% change in the reattachment length and maximum Nusselt number. Thus considering the computational cost and accuracy, a total grid range from 38000 to 56000, for both porous and fluid domains was adequate for the various cases of different segment lengths and depths.

6.2.2 Results and Discussion

6.2.2.1 Effect of Reynolds Number

Figures 6.17 shows the stream contours of the flow for different Reynolds numbers from 100 to 800; with $Da = 10^{-2}$, segment length L/H = 3.3 and depth D/H = 0.25, porosity $\varepsilon = 0.4$, jump parameters $\beta = 0$ and $\beta_1 = 0$. Generally, increasing the Reynolds number would increase the distance from the step to the recirculation reattachment point. At higher Reynolds number, the shear layer needs a longer distance to entrain fluid before reattaching to the lower wall. At small Re of 100 the

reattachment point is inside the porous segment. When the *Re* is large (above 400), the reattachment is outside. At *Re* of 800 there is another recirculation bubble in the upper wall region.

Figure 6.18 shows the axial distribution of lower wall Nusselt number for the cases in Figure 6.17. The Nusselt number is small in the porous segment due to the small convective flow there. There is a step increase in Nusselt number at the end of the porous segment. The step increase is due to the discontinuous lower wall which gives rise to a new boundary layer after the end of the porous segment. Downstream of the porous segment, the Nusselt number shows peak value for *Re* of 400 and 800. By referring to the streamlines in Figures 6.17c and d, it is seen that the locations of the peak *Nu* are around the reattachment points due to greater convection there, which is consistent with previous studies without porous floor (Kondoh et al., 1993). After the flow reattaches, the Nusselt number reaches an equilibrium value at the fully developed flow further downstream. The equilibrium *Nu* is higher at larger *Re* as expected. As for the *Re* of 200, the reattachment point is around the end of the porous segment (see Figure 6.17b). Thus the effects of the lower-wall discontinuity and the reattachment points give rise to significant enhancement of the Nusselt number just after the porous segment. The reattachment location for the low *Re* = 100 lies inside the porous segment, giving a small peak in *Nu* there, but it does not help to enhance the *Nu* downstream of the porous segment. It may be concluded that the reattachment location should be around the lower-wall discontinuity to obtain heat transfer enhancement due to both factors.

6.2.2.2 Effect of Segment Length

Figure 6.19 shows how the flow field is affected by the length of the porous-segment, with *Re*=200. The porous floor does not eliminate the recirculation flow, as those suppressed bubbles (Martin et al, 1998; Zhang and Zhao, 2000; Assato, et al, 2005). On the contrary, the recirculation length increases if the porous segment is longer. When there is a porous floor, the shear layer needs a longer distance to entrain fluid before reattaching to the lower wall because the porous medium hampers the fluid returning from the reattachment point. The reattachment length approximately matches the porous length at L/H=3.3 (Figure 6.19c). At longer porous length the reattachment point is inside the porous segment (Figure 6.19d).

Figure 6.20 shows the local Nusselt number for the cases in Figure 6.19. It is noted that there is a jump in *Nu* due to the discontinuity in lower wall as discussed earlier. As compared the case without porous floor, there is not much *Nu* enhancement at the downstream region if the porous floor is too short (L/H=1.1). On the other hand, a long porous floor (L/H = 5.5) will result in a long region of low *Nu* due to the small convective flow there. To obtain high local heat transfer effect after the porous segment, its length should be around the recirculation length as discussed earlier. The matching of porous and recirculation length depends on Reynolds number. At *Re*=280 the matched length is L/H=3.3 for heat enhancement effect.

6.2.2.3 Effect of Segment Depth

Figures 6.21 and 6.22 show how the flow and heat transfer are affected by the depth of the porous segment at *Re* =280. The porous floor causes the recirculation length to be longer as compared with solid one. However, a deeper porous floor does not cause further increase of the recirculation length. Even though the porous floor is deeper, the fluid returning from the reattachment point moves mainly at a height around that of the channel floor; thus the entrainment of fluid by the shear layer is not hampered more if the porous medium is deeper. There is a noticeable increase for the local Nusselt number after the segment and it increases with increasing depths. This is attributed to the discontinuity of the lower wall. However the deeper floor causes the *Nu* in the porous region to be lower (Figure 6.22), due to the low convective flow. Thus it is not advantageous to have a porous floor with greater depth.

6.2.2.4 Effect of Darcy Number

Figure 6.23 shows the Darcy number effect on the flow field with *Re*=280. The case of *Da* = 0 represents that with no porous floor segment. When *Da* is larger, the recirculation length is seen to be slightly longer as more fluid goes into the porous medium and thus a longer length is needed for entrainment by the shear layer before reattachment.

Figure 6.24 shows the local Nusselt number for different Darcy numbers. It can be seen that there is small heat convection in the porous medium due to small flow convection. After the step there is a jump in the local Nusselt number, which is bigger at larger Darcy number because the reattachment point is shifted a little further

downstream (see Figure 6.23). Just before the segment end the *Nu* shows a peak for $Da = 10^{-1}$ because of the recirculation flow there.

Since the *Nu* is reduced along the permeable wall (Figure 6.24 and also previous Figures 6.20 and 6.22) there may be little or negative heat enhancement if the entire wall length is considered; that is, if the overall (integrated) Nusselt number along the entire bottom wall is considered. However, the overall heat transfer can be increased by using higher conductivity materials for the porous medium (Huang and Vafai, 1994a; Kiwan and AI-Nimr, 2001). For example, the conductivity ratio between metal foam and air is about 10^3 to 10^4 whereas the present computation uses a ratio of one.

It was found (results not shown) that the head loss from inlet to outlet increased by less than 1% if a porous floor segment was embedded as compared with that of no porous segment; the case considered was for $Da = 10^{-1}$, $\varepsilon = 0.4$, *Re* = 280, L/H = 3.3, D/H = 0.25, $\beta = 0$ and $\beta_1 = 0$. However, for a backward facing step with a porous insert (Martin et al, 1998; Zhang and Zhao), the head loss increases with decreasing Darcy number and at $Da = 10^{-4}$ it becomes six times larger than that with the porous floor; the case considered was for porous insert length a/H = 0.2 and the other parameters are the same as that with the porous floor. The comparison indicates that for the purpose of heat transfer enhancement using high conductivity porous material, it may be advantageous to embed it along the wall to avoid incurring high head loss.

6.2.2.5 Effect of Porosity Values

The Darcy number defines the permeability which determines the flow through the porous medium and thus affects the heat transfer. As for porosity it is a geometry parameter related to the fraction of void space, and is not expected to affect the flow very much. This is confirmed in Figure 6.25 which shows little change in *Nu* for different porosities at a fixed $Da = 10^{-2}$.

6.2.2.6 Effect of Stress Jump Parameters

Table 6.2 shows the effect of stress jump parameters (varied from -5 to +5) on the average and maximum Nusselt number at lower wall. It can be seen for the larger $Da=10^{-2}$, there are some effects of β and β_1. But the effects are insignificant at smaller $Da=10^{-4}$ as the porous flow is small, which is consistent with the case for the flow past a parallel porous interface (Alazmi and Vafai, 2001).

The effects of the stress jump parameters β and β_1 on the local Nusselt number are shown in Figures 6.26a and 6.27a respectively. Also presented are their effects on the velocity profiles (Figures 6.26b and 6.27b) and temperature profiles (Figures 6.26c and 6.27c) at a location x/H=3.8. It is noted that the parameters have some effects, especially for the second parameter β_1. The parameters affect the velocity profile which thus influences the temperature gradients at the wall and hence the heat transfer is affected.

Note that the second stress jump parameter β_1 was varied in the present study by a wide range of -5 to + 5 as it was expected to be of order one by Ochoa-Tapia and Whitaker (1998b). This inertia-related parameter is usually negligible for parallel flows but may be relevant in the vicinity of the reattachment point. For the flow there, a large negative β_1 may not be realistic. Outside the porous medium, the velocity gradients around the reattachment point are not expected to be large. Thus, unless the porosity is very small, the stress jump is not expected to be a large negative value (see Equation 6.3). For positive β_1 variation from 0 to +5, it is interesting that the results are not very sensitive.

6.3 Conclusions

The forced convection after a backward facing-step, with a porous insert or porous floor segment after the step, has been numerically investigated using the numerical method described in Chapter 2. To couple the flows at the interface, the shear-stress jump condition is used as developed by Ochoa-Tapia and Whitaker (1998b). For the temperature and heat flux at the interface, the continuity condition is imposed.

For the forced convection through a porous insert behind a backward-facing step, results are presented with flow configurations for different Darcy number from 10^{-2} to 10^{-5}, porosity from 0.2 to 0.8, and Reynolds number from 10 to 800, and ratio of insert length to channel height from 0.1 to 0.3. The Darcy number, Reynolds

number and insert length influence the recirculation regions and hence the heat transfer, but the porosity effect is small. To achieve an optimal heat transfer effect, without excessive frictional loss, it is preferable to use a medium insert length with flow at medium Darcy number and large Reynolds number. The stress jump parameters have small effects on the average lower wall Nusselt number. For the smaller Darcy number $Da = 10^{-4}$, the difference in *Nu* is about 4%, when both β and β_1 are varied from -1 to 1. The effects are more discernible on the local velocity and temperature profiles.

For the forced convection with a porous floor segment after a backward-facing step, the porous floor does not eliminate the recirculation flow which forms after the step. On the contrary, the recirculation length increases if the porous segment is longer or more permeable. This is attributed to the longer distance for the shear layer to entrain fluid before reattaching to the lower wall. The Nusselt number is reduced at the lower wall within the porous segment but this may be offset by using a porous medium of high conductivity. After the porous segment the *Nu* is enhanced, more so at higher Darcy number. It is concluded that the heat transfer enhancement is high if the recirculation length is matched with the porous segment length. It is interesting that the depth of the porous floor has little effect on heat enhancement. The two stress jump parameters β and β_1 (from -5 to +5) show some effects on the Nusselt numbers if the *Da* is large.

The second case is very different from the first case, which considered a porous insert that completely filled the duct directly behind the step. Its flow is more

complex at the porous-fluid interface due to the existence of recirculation region and reattachment point. Also a larger range of the jump parameters were used; -5 to +5 as compared to the first case -1 to +1. The flow complexity and larger stress jumps were found to cause convergent problems which have to be carefully handled in the numerical implementation.

Table 6.1 Average Nusselt number for lower wall with different stress jump parameters at *Re*=800, $\varepsilon = 0.4$, a/H=0.2.

Da	β	β_1	Nu_{av}	*Da*	β	β_1	Nu_{av}
10^{-2}	0	-1	3.276	10^{-4}	0	-1	3.855
	0	0	3.273		0	0	3.826
	0	1	3.273		0	1	3.785
	-1	0	3.272		-1	0	3.844
	0	0	3.273		0	0	3.826
	1	0	3.275		1	0	3.807
	1	1	3.275		1	1	3.741
	-1	-1	3.273		-1	-1	3.902

Table 6.2 Average and maximum Nusselt number for lower wall with different stress jump parameters at *Re* = 280, $\varepsilon = 0.4$, L/H = 3.3, D/H = 0.25.

Da	β	β_1	Nu_{av}	$Nu_{\max}$	*Da*	β	β_1	Nu_{av}	$Nu_{\max}$
10^{-2}	0	-5	2.48	21.04	10^{-4}	0	-5	2.25	10.98
	0	0	2.27	13.45		0	0	2.25	11.00
	0	5	2.26	12.81		0	5	2.25	11.02
	-5	0	2.43	19.21		-5	0	2.21	10.94
	0	0	2.27	13.45		0	0	2.25	11.00
	5	0	2.25	12.78		5	0	2.25	11.04

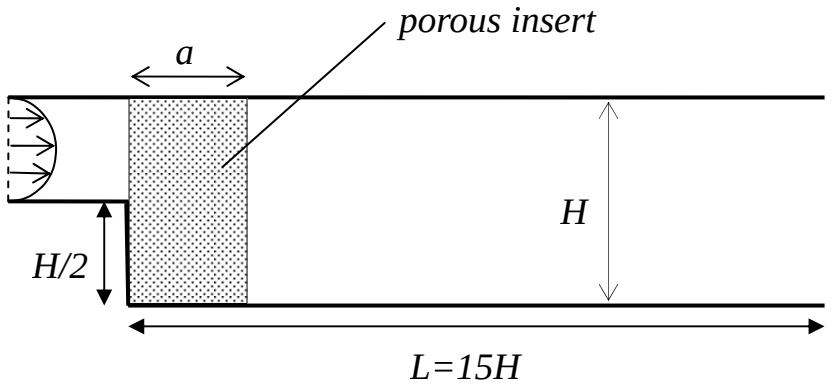

Figure 6.1 Schematic of the flow model.

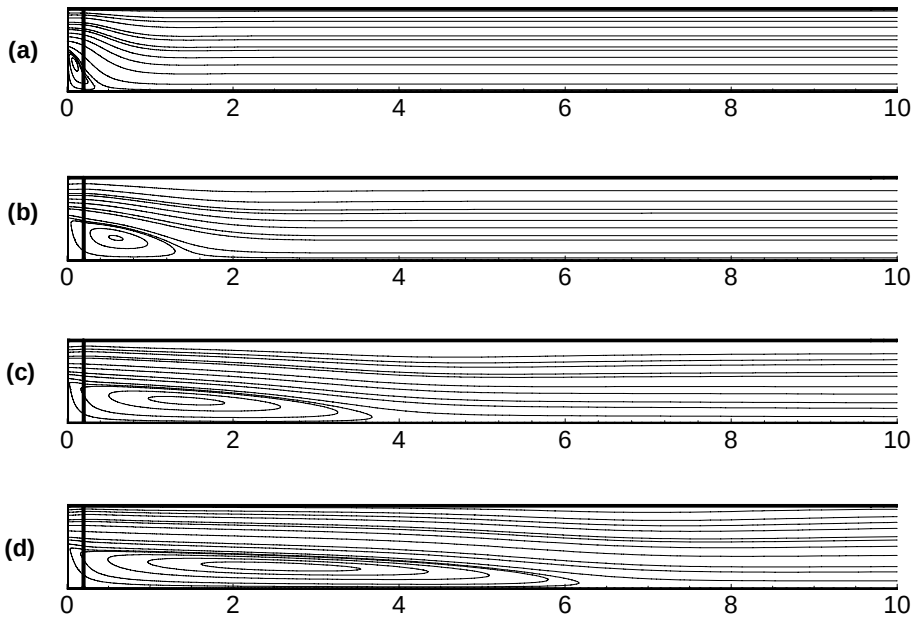

Figure 6.2 Streamline plots at Darcy number $Da = 10^{-2}$, inset length a/H = 0.2, porosity $\varepsilon = 0.4$, jump parameters $\beta = 0$ and $\beta_1 = 0$:
(a) *Re*=10; (b) *Re*=100; (c) *Re*=400; (d) *Re*=800.

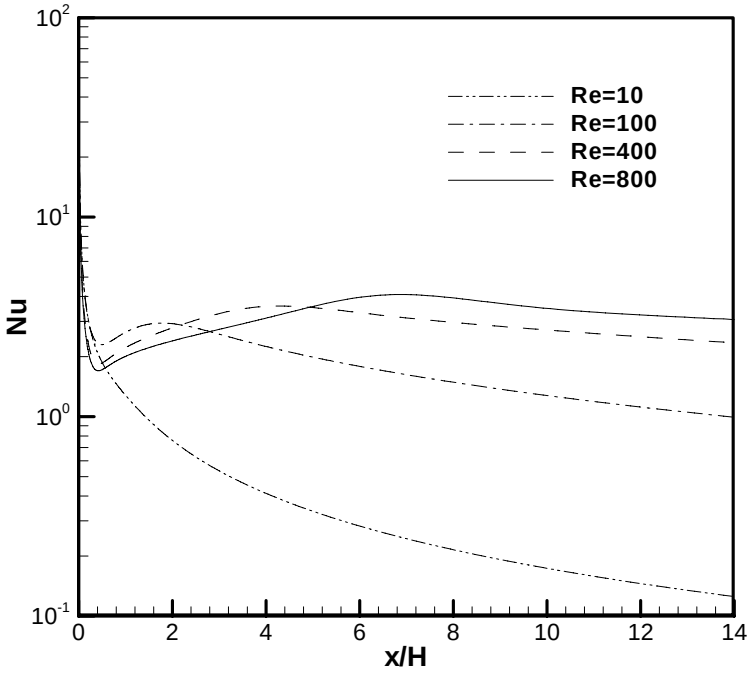

Figure 6.3 Axial distribution of lower wall Nusselt number at $Da=10^{-2}$, a/H=0.2, $\varepsilon = 0.4$, $\beta = 0$ and $\beta_1 = 0$.

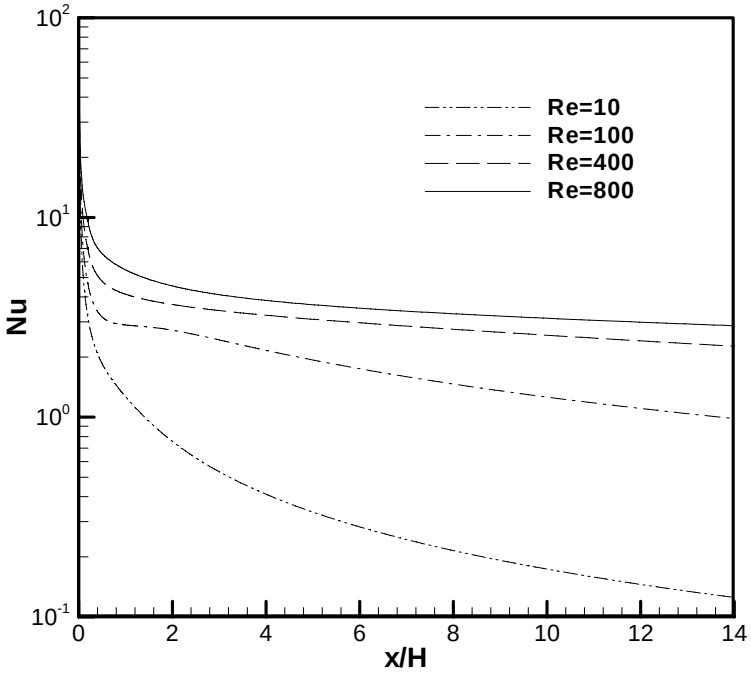

Figure 6.4 Axial distribution of lower wall Nusselt number at $Da=10^{-4}$, a/H=0.2, $\varepsilon = 0.4$, $\beta = 0$ and $\beta_1 = 0$.

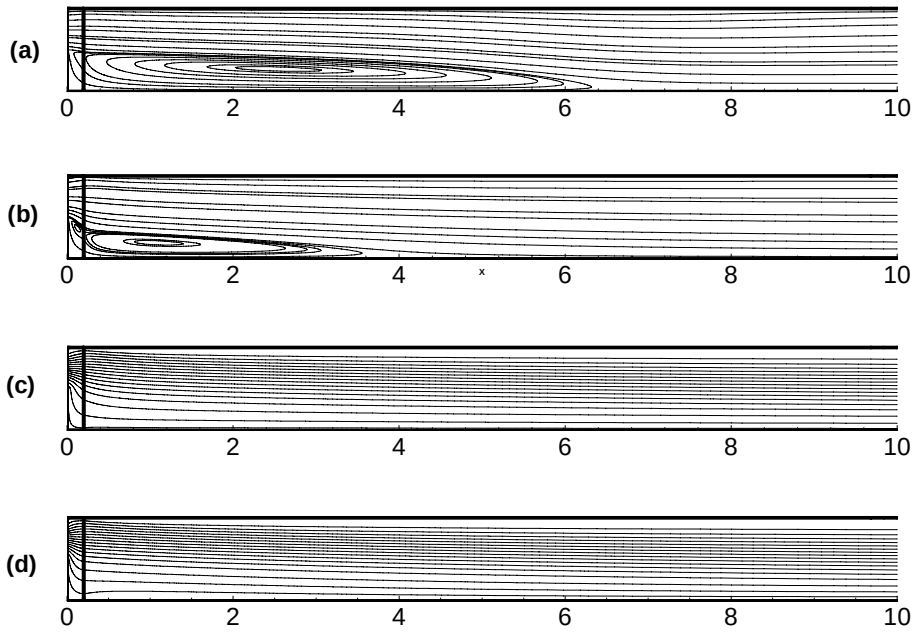

Figure 6.5 Streamline plots at *Re*=800, a/H=0.2, $\varepsilon = 0.99$, $\beta = 0$ and $\beta_1 = 0$ with various Darcy numbers:
(a) $Da=10^{-2}$; (b) $Da=10^{-3}$; (c) $Da=10^{-4}$; (d) $Da=10^{-5}$.

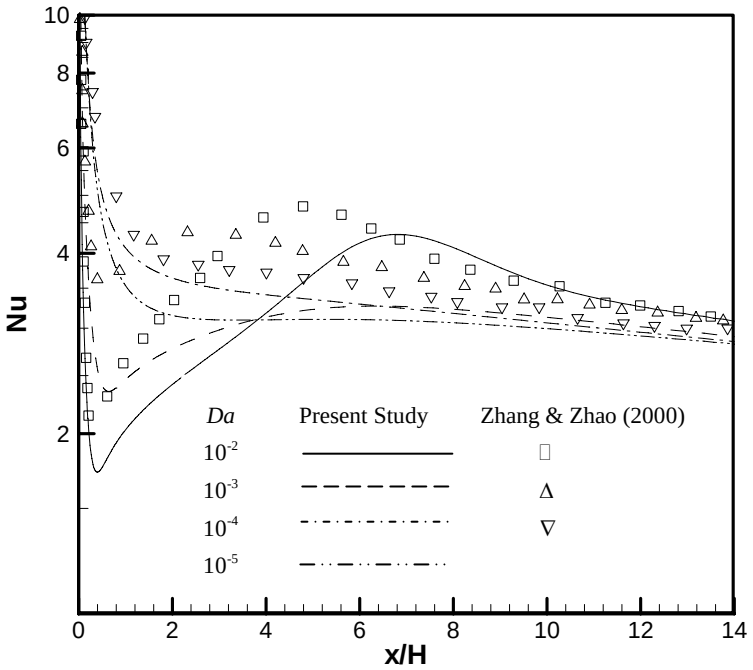

Figure 6.6 Axial distribution of lower wall Nusselt number at *Re*=800, a/H=0.2, $\varepsilon = 0.99$, $\beta = 0$ and $\beta_1 = 0$ with various Darcy numbers.

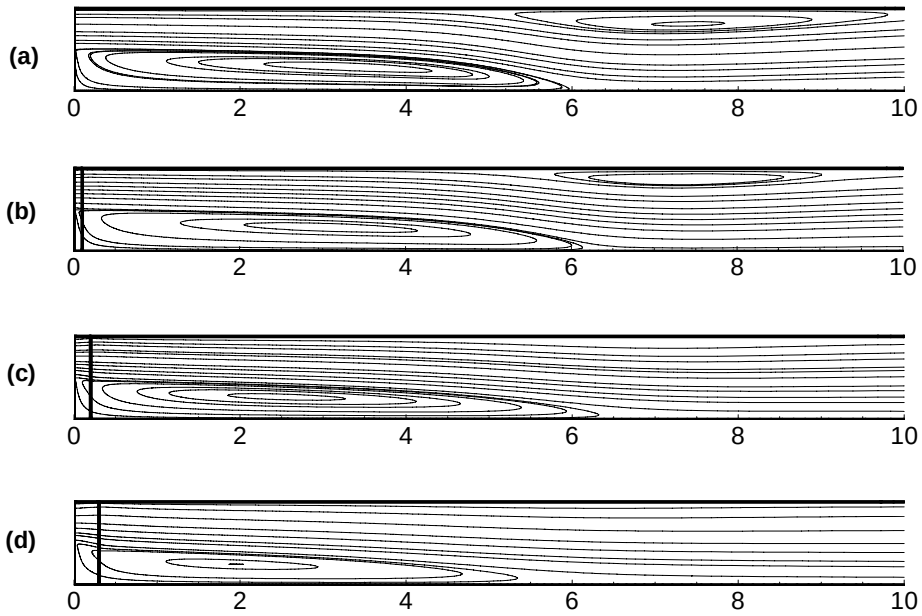

Figure 6.7 Streamline plots at *Re*=800, $Da=10^{-2}$, $\varepsilon = 0.4$, $\beta = 0$ and $\beta_1 = 0$ with various insert lengths: (a) a/H=0.0; (b) a/H=0.1; (c) a/H=0.2; (d) a/H=0.3.

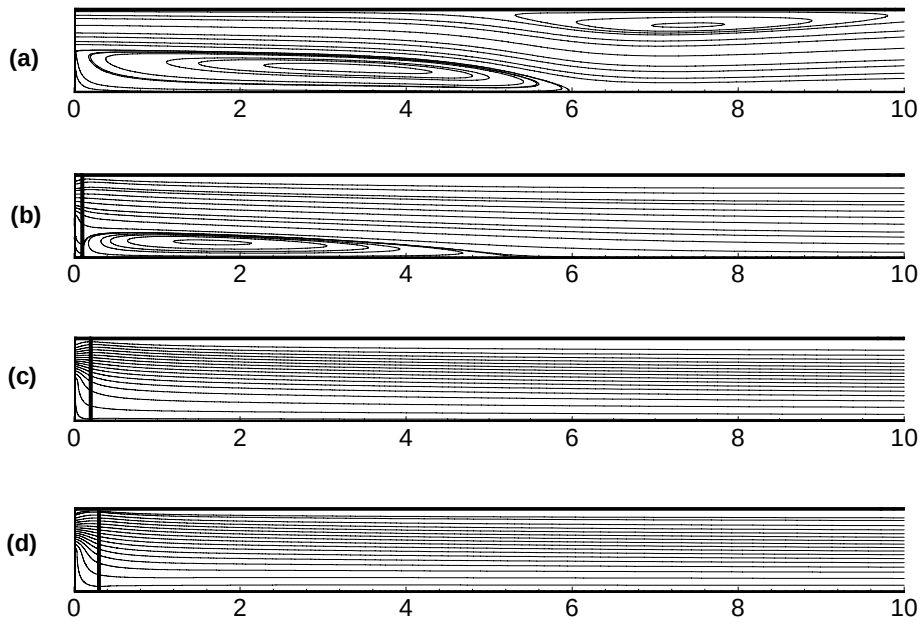

Figure 6.8 Streamline plots at *Re*=800, $Da=10^{-4}$, $\varepsilon = 0.4$, $\beta = 0$ and $\beta_1 = 0$ with various insert lengths: (a) a/H=0.0; (b) a/H=0.1; (c) a/H=0.2; (d) a/H=0.3.

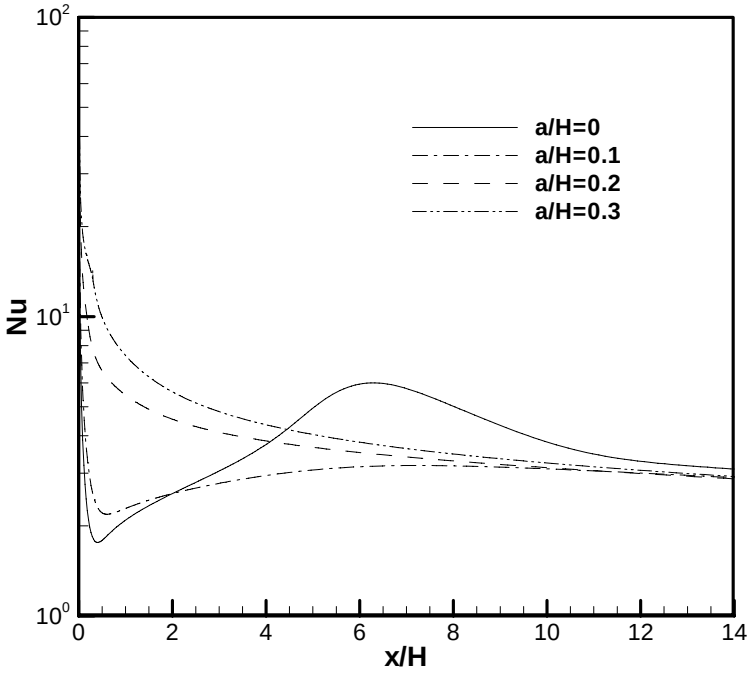

Figure 6.9 Axial distribution of lower wall Nusselt number for $\varepsilon = 0.4$, *Re*=800, $Da=10^{-4}$, $\beta = 0$ and $\beta_1 = 0$.

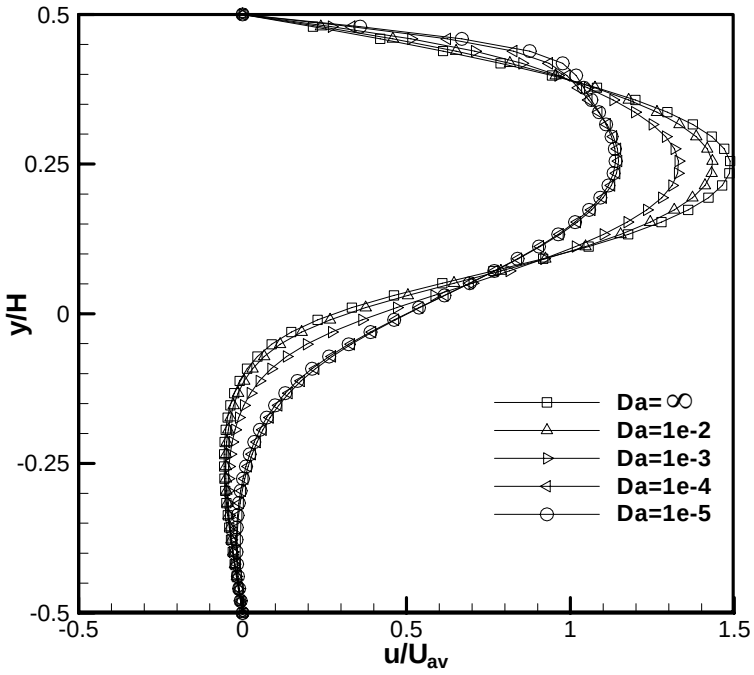

(a)

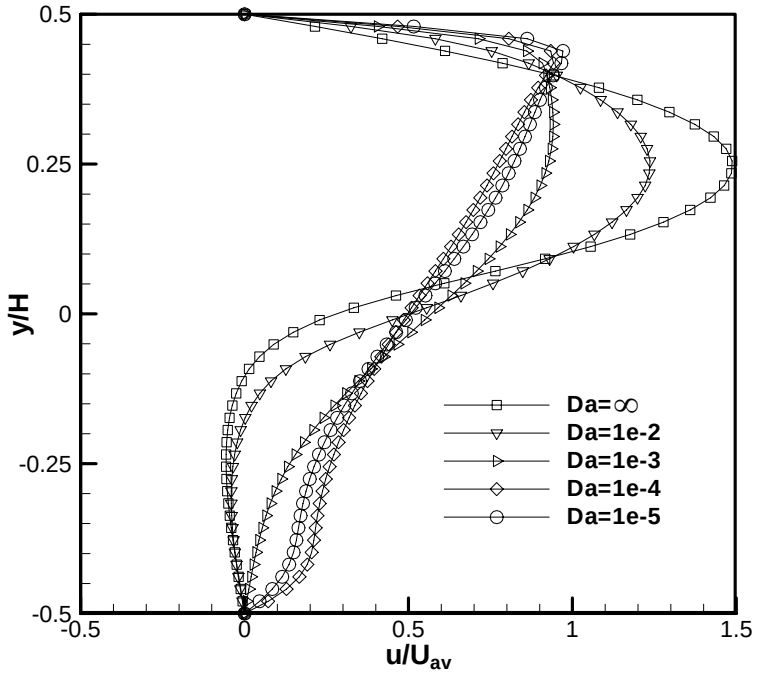

(b)

Figure 6.10 Streamwise velocity profiles at x/H=0.5, with *Re*=800, $\varepsilon = 0.4$, $\beta = 0$ and $\beta_1 = 0$: (a) a/H=0.1; (b) a/H=0.3.

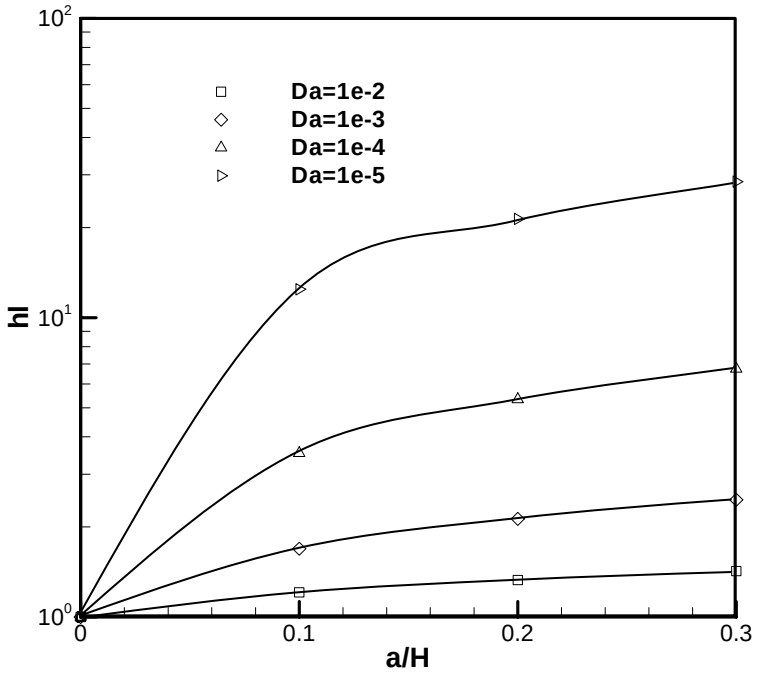

Figure 6.11 Dimensionless channel head loss, with *Re*=800, $\varepsilon = 0.4$, $\beta = 0$ and $\beta_1 = 0$.

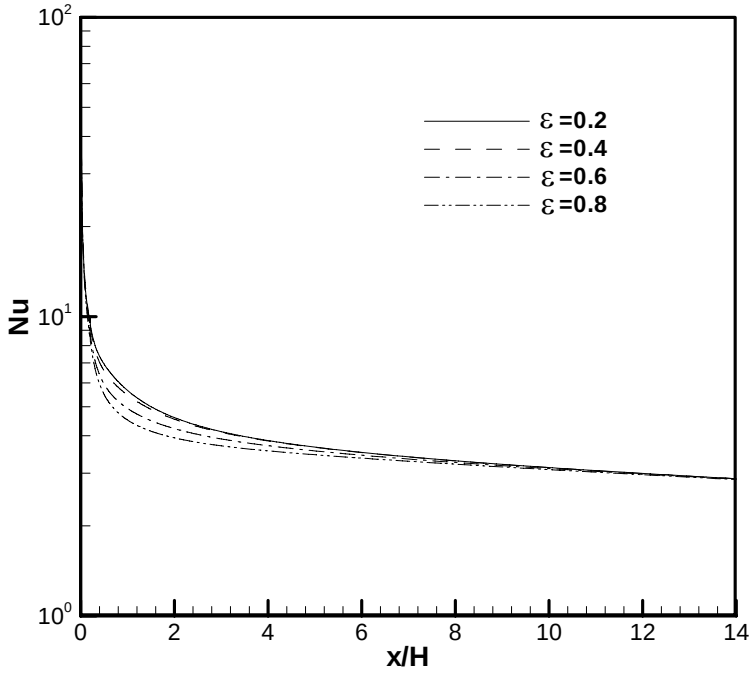

Figure 6.12 Axial distribution of lower wall Nusselt number for a/H=0.2, *Re*=800, $Da=10^{-4}$, $\beta = 0$ and $\beta_1 = 0$.

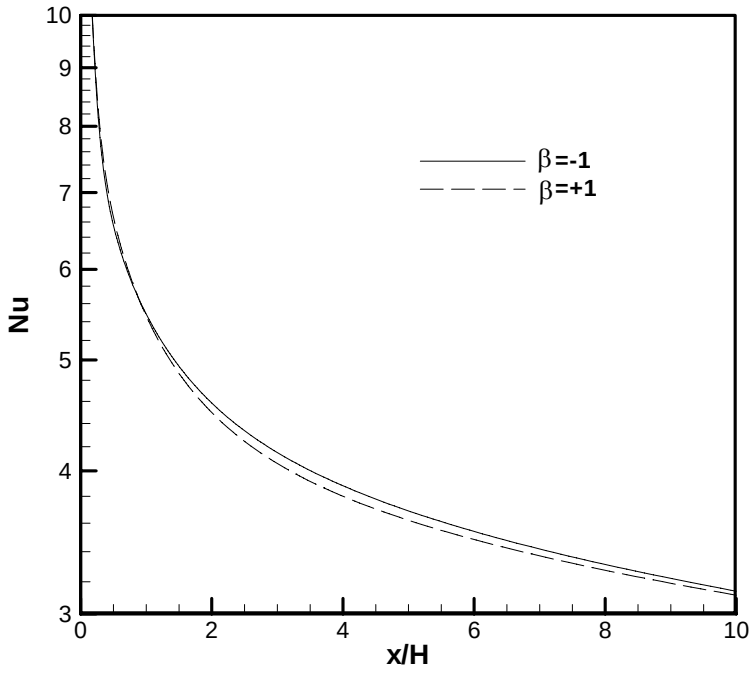

(a)

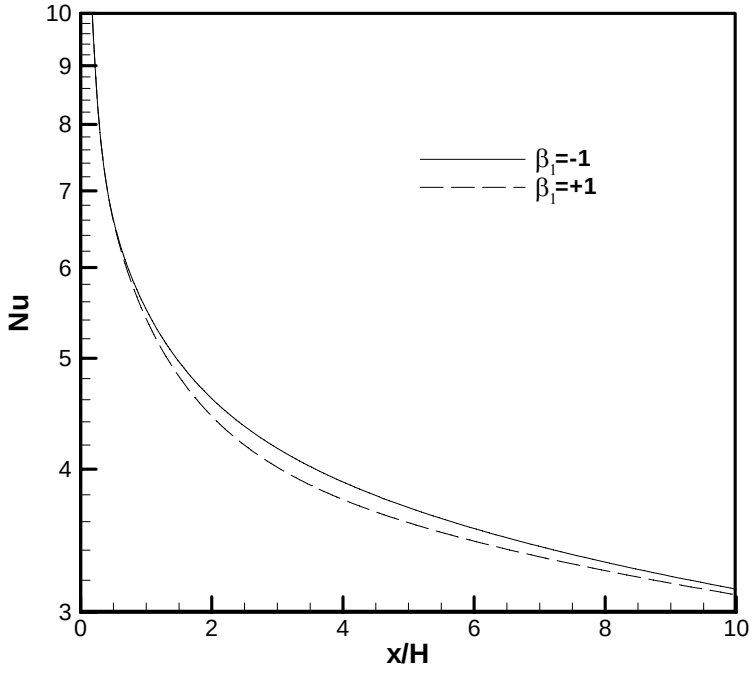

(b)

Figure 6.13 Effect of stress jump parameters on the local Nusselt number with a/H=0.2, Re=800, $\varepsilon = 0.4$, Da=10^{-4}:
(a) β effect with β_1=0 ; (b) β_1 effect with β=0.

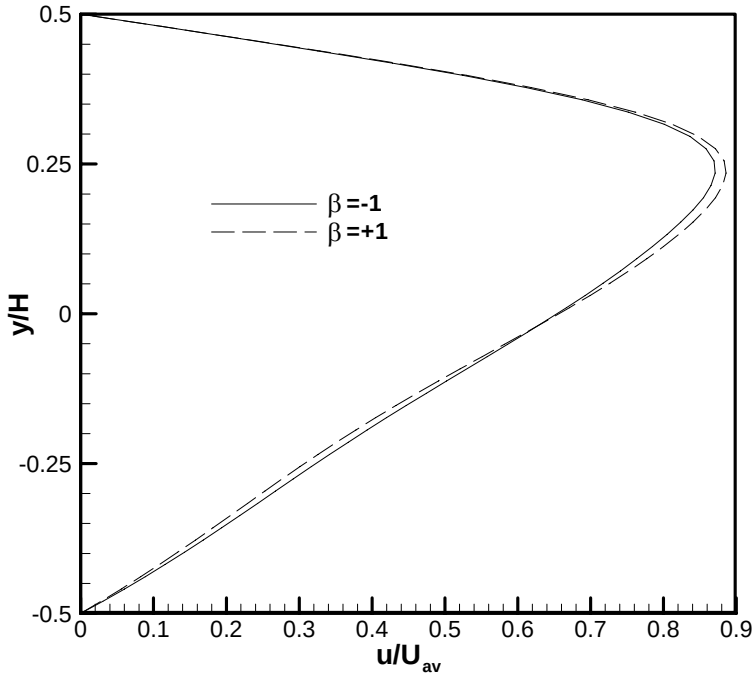

(a)

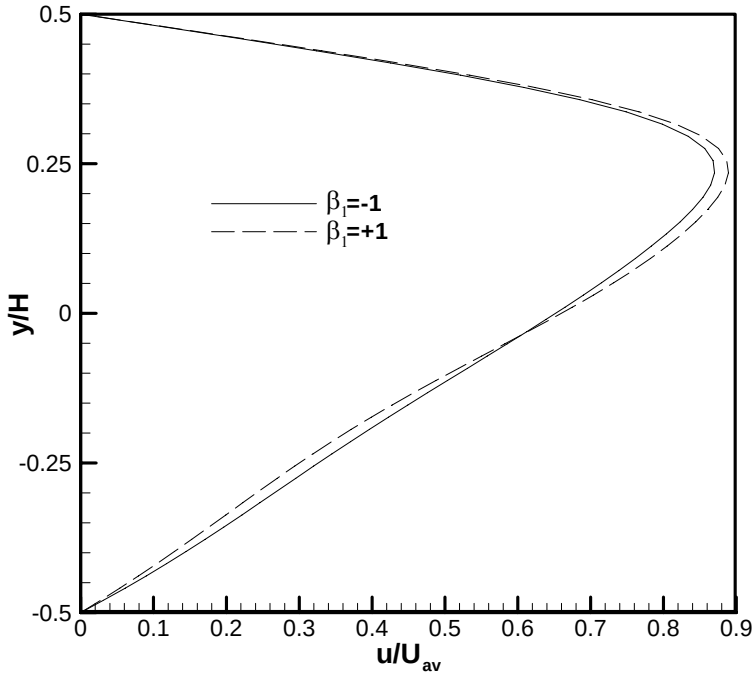

(b)

Figure 6.14 Effect of stress jump parameters on the velocity profile at x/H=3.0 with a/H=0.2, *Re*=800, $\varepsilon = 0.4$, *Da*=10^{-4}:
(a) β effect with β_1=0 ; (b) β_1 effect with β=0.

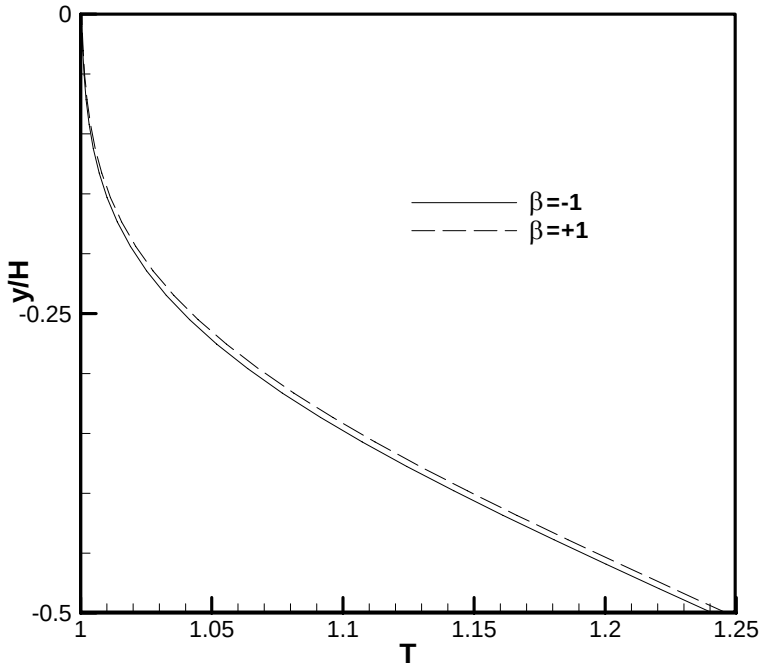

(a)

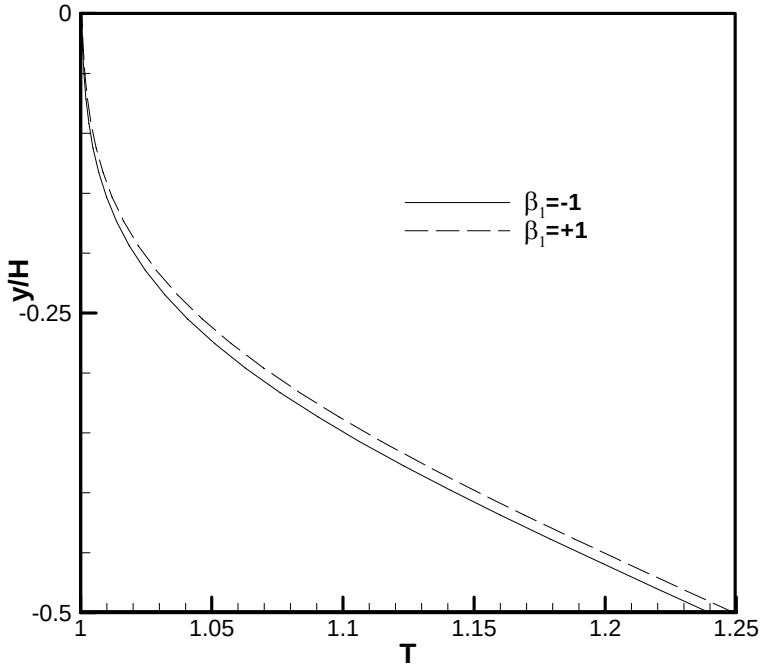

(b)

Figure 6.15 Effect of stress jump parameters on the temperature profile at x/H=3.0 with a/H=0.2, *Re*=800, $\varepsilon = 0.4$, *Da*=10^{-4}:
(a) β effect with β_1=0 ; (b) β_1 effect with β=0.

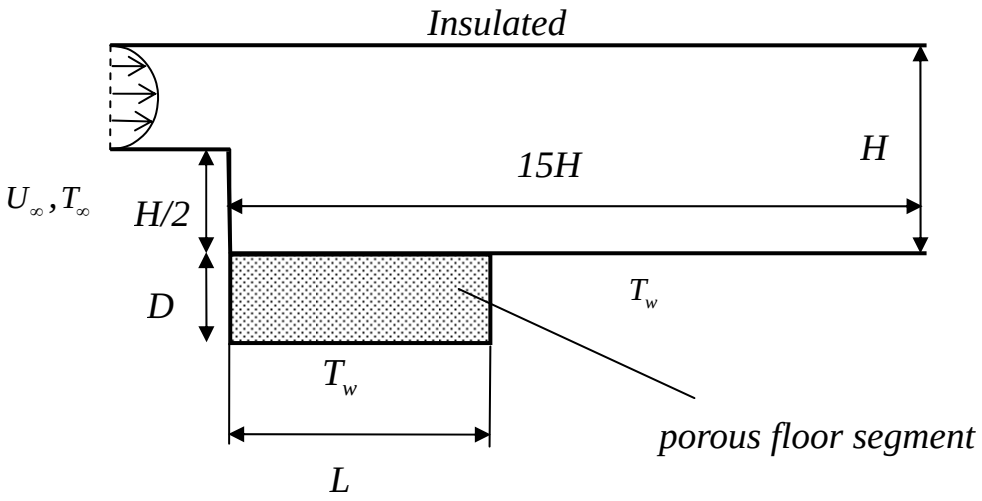

(a)

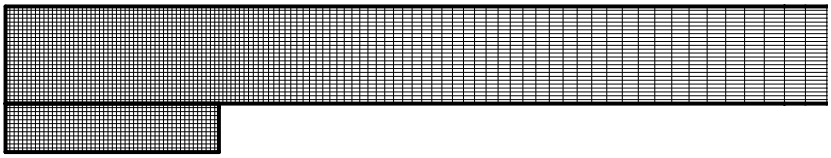

(b)

Figure 6.16 Schematic of the flow model: (a) Computational domain; (b) Mesh illustration with L/H=2.2, D/H=0.5.

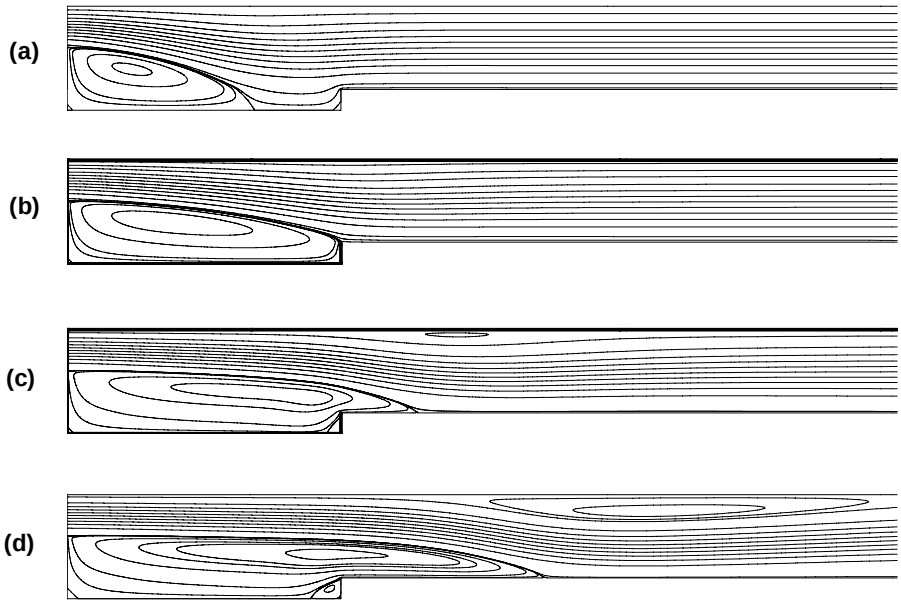

Figure 6.17 Streamline plots at different Reynolds numbers:
(a) *Re* = 100, (b) *Re* = 200, (c) *Re* = 400, (d) *Re* = 800;
$\varepsilon = 0.4$, *Da* = 10^{-2}, L/H = 3.3, D/H = 0.25, $\beta = 0$ and $\beta_1 = 0$.

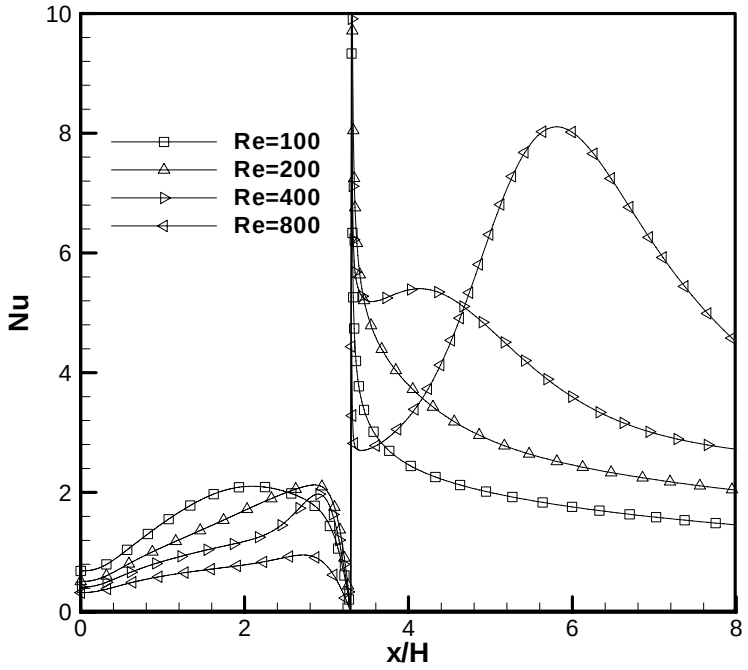

Figure 6.18 Axial distribution of lower wall Nusselt number at different Reynolds numbers; $\varepsilon = 0.4$, $Da = 10^{-2}$, L/H = 3.3, D/H=0.25, $\beta = 0$ and $\beta_1 = 0$.

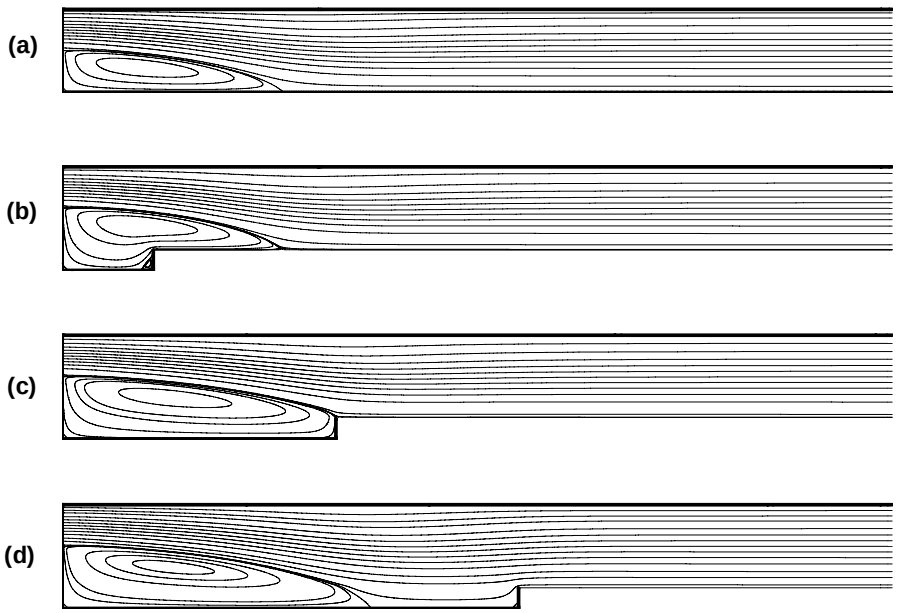

Figure 6.19 Streamline plots with different lengths of porous segment:
(a) L/H = 0, (b) L/H = 1.1, (c) L/H = 3.3, (d) L/H = 5.5;
$\varepsilon = 0.4$, $Da = 10^{-2}$, Re = 200, D/H = 0.25, $\beta = 0$ and $\beta_1 = 0$.

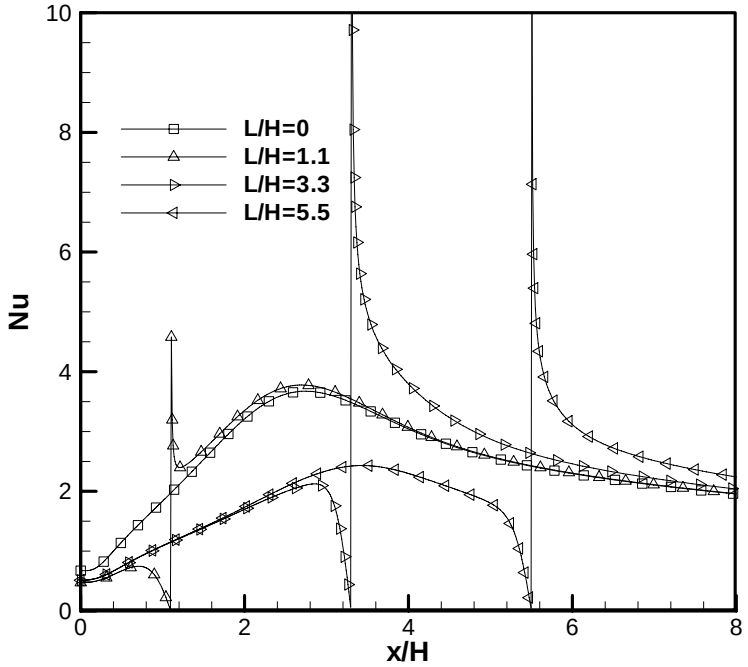

Figure 6.20 Axial distribution of lower wall Nusselt number with different lengths of porous segment;
$\varepsilon = 0.4$, $Da = 10^{-2}$, Re = 200, D/H = 0.25, $\beta = 0$ and $\beta_1 = 0$.

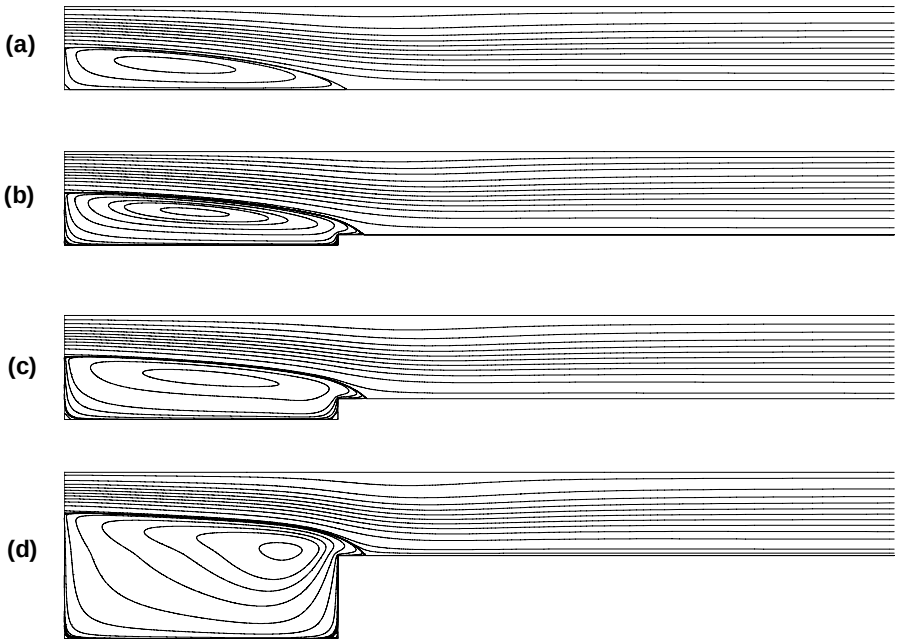

Figure 6.21 Streamline plots with different depths of porous segment:
(a) D/H = 0, (b) D/H = 0.125, (c) D/H = 0.25, (d) D/H = 1.0;
$\varepsilon = 0.4$, $Da = 10^{-2}$, Re = 280, L/H = 3.3, $\beta = 0$ and $\beta_1 = 0$.

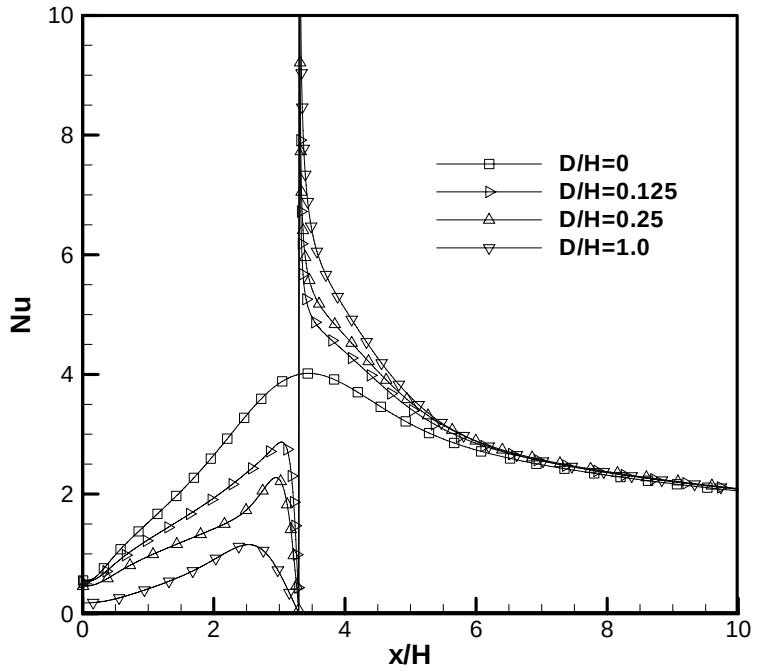

Figure 6.22 Axial distribution of lower wall Nusselt number with different depths of porous segment; $\varepsilon = 0.4$, $Da = 10^{-2}$, Re = 280, L/H = 3.3, $\beta = 0$ and $\beta_1 = 0$.

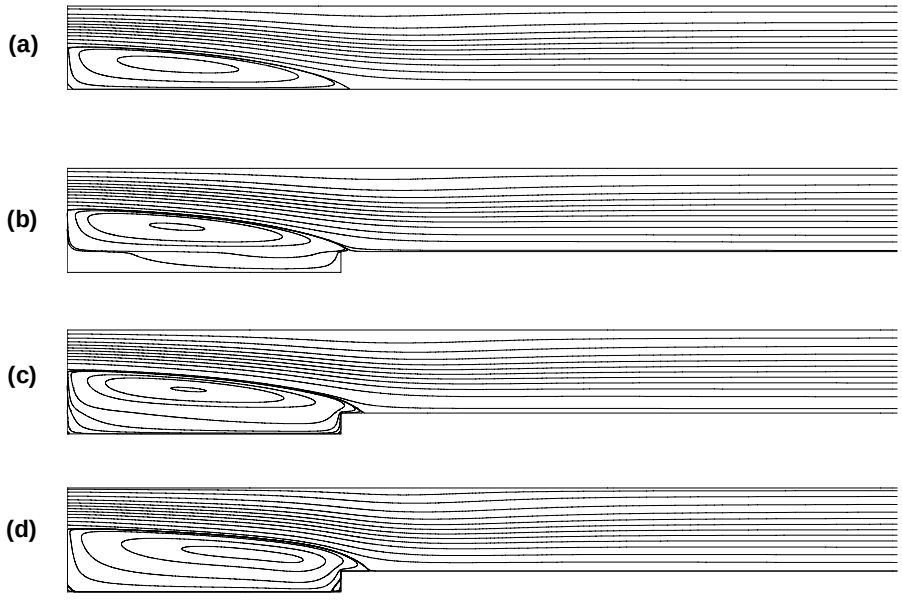

Figure 6.23 Streamline plots at different Darcy numbers:
(a) Da = 0, (b) $Da = 10^{-5}$, (c) $Da = 10^{-3}$, (d) $Da = 10^{-1}$;
$\varepsilon = 0.4$, Re = 280, L/H = 3.3 and D/H = 0.25, $\beta = 0$ and $\beta_1 = 0$.

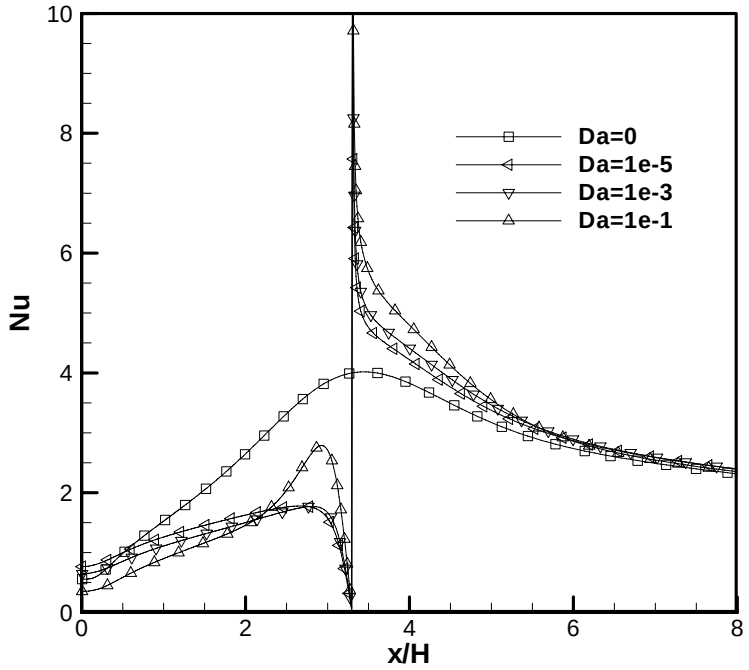

.

Figure 6.24 Axial distribution of lower wall Nusselt number at different Darcy numbers; $\varepsilon = 0.4$, *Re* = 280, L/H = 3.3, D/H = 0.25, $\beta = 0$ and $\beta_1 = 0$.

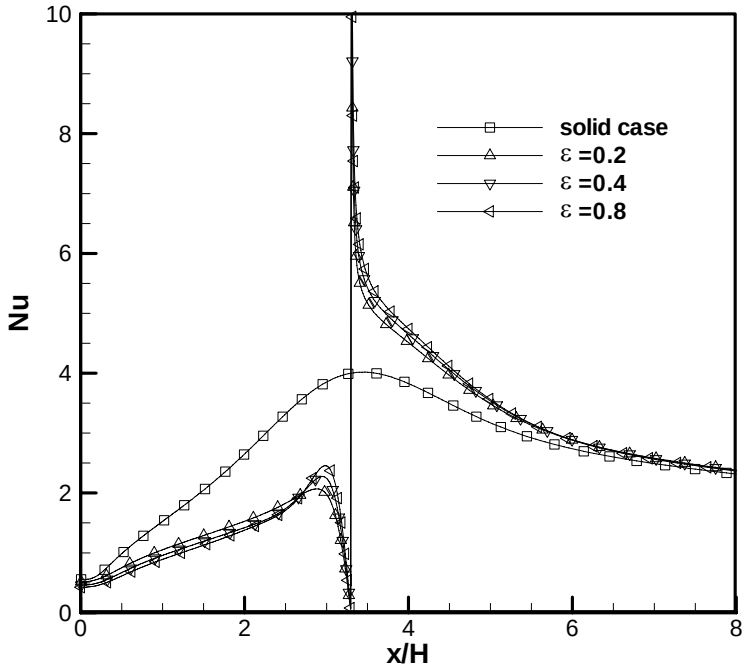

Figure 6.25 Axial distribution of lower wall Nusselt number with different porosities; *Da* = 10^{-2}, *Re* = 280, L/H = 3.3, D/H = 0.25, $\beta = 0$ and $\beta_1 = 0$.

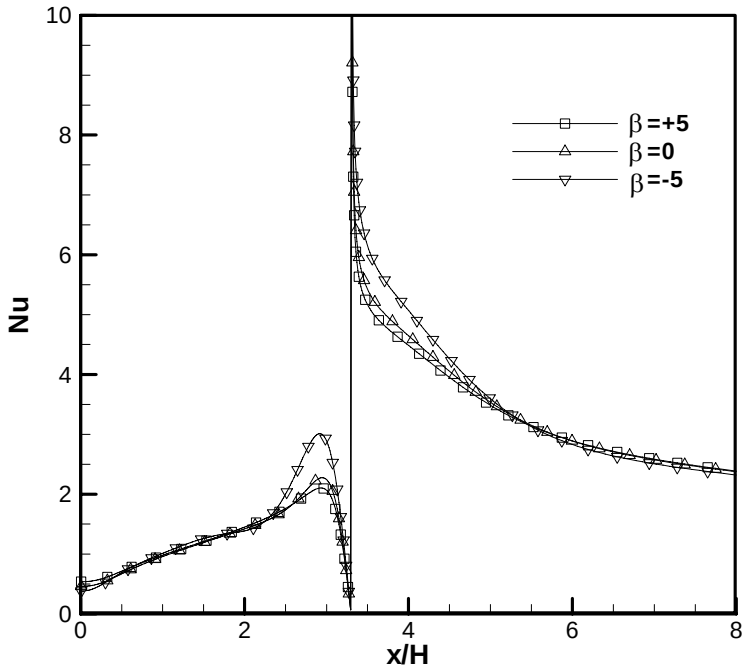

(a)

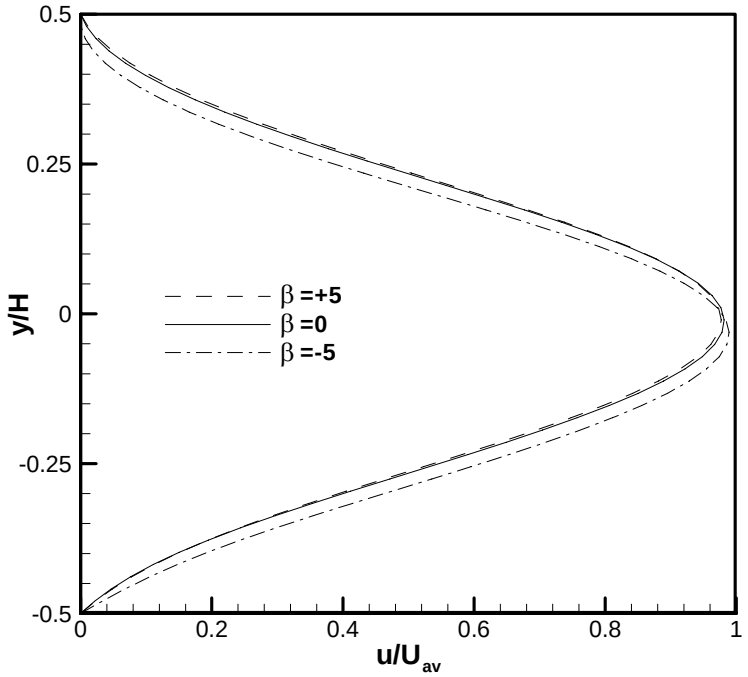

(b)

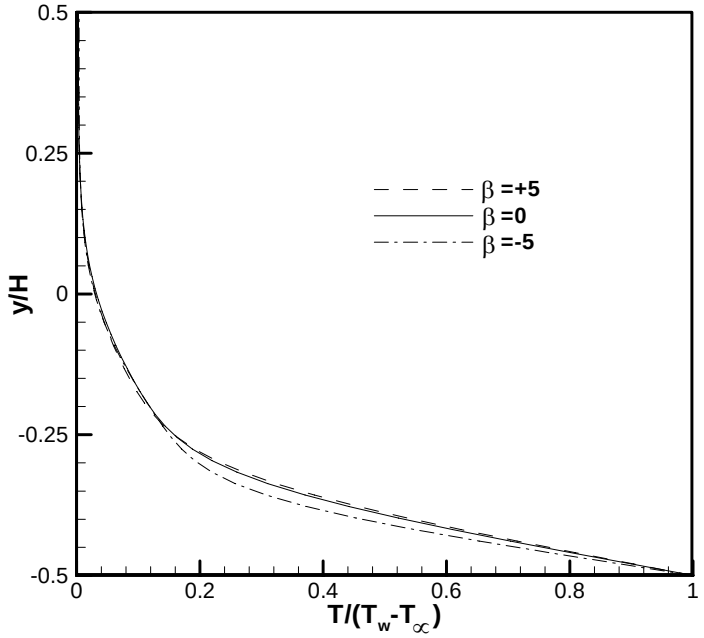

(c)

Figure 6.26 Effect of stress jump parameter β : (a) Local Nusselt number, (b) Velocity profiles at x/H = 3.8, (c) Temperature profiles at x/H = 3.8; β_1 = 0, $\varepsilon = 0.4$, $Da = 10^{-2}$, Re = 280, L/H = 3.3 and D/H = 0.25.

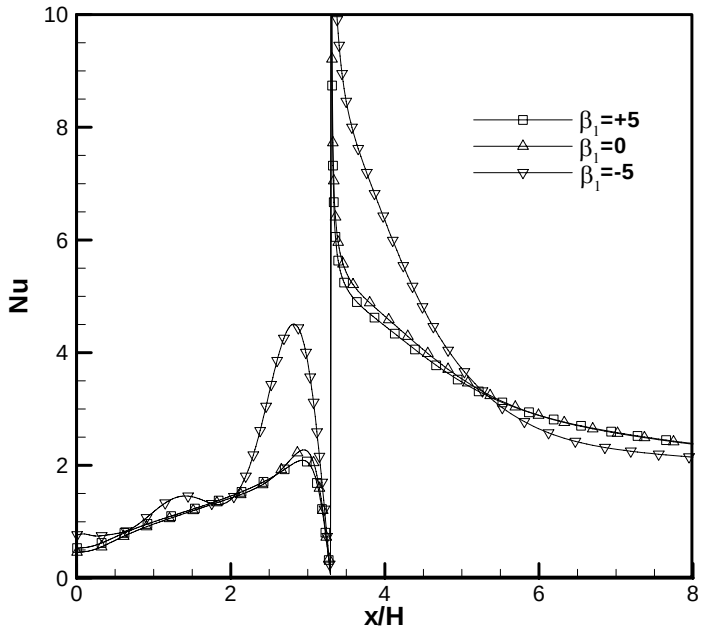

(a)

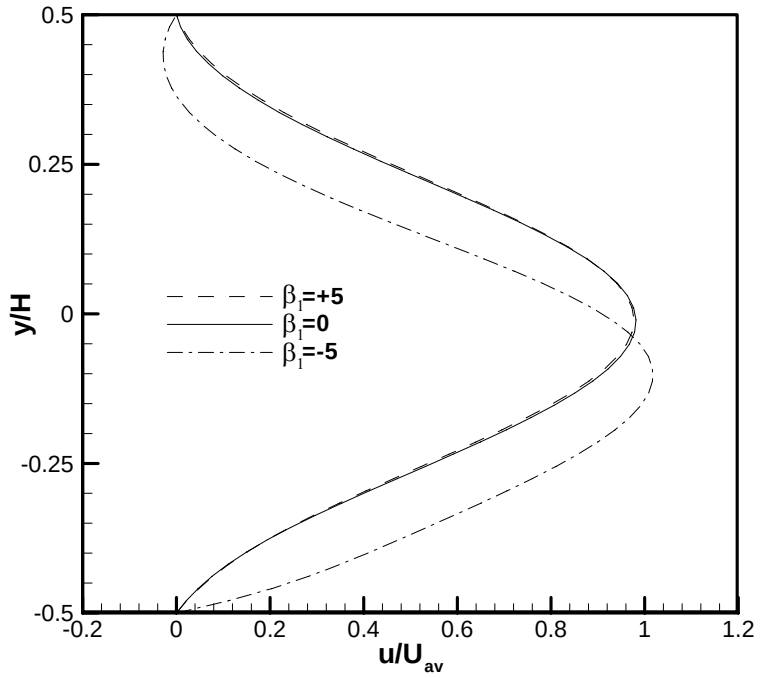

(b)

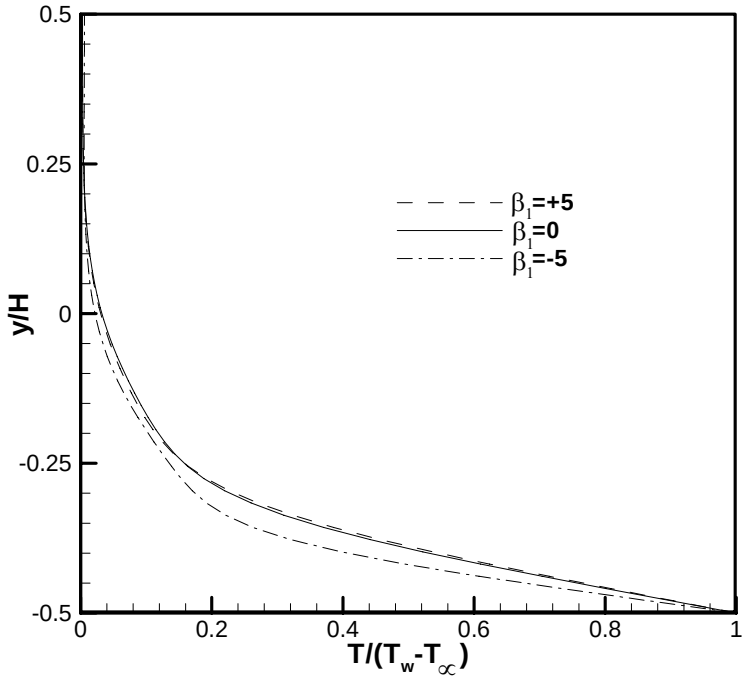

(c)

Figure 6.27 Effect of second stress jump parameter β_1: (a) Local Nusselt number, (b) Velocity profiles at x/H = 3.8, (c) Temperature profiles at x/H = 3.8; β = 0, $\varepsilon = 0.4$, $Da = 10^{-2}$, Re = 280, L/H = 3.3 and D/H = 0.25.

Chapter 7

Mass Transport in a Microchannel Reactor with a Porous Wall*

Besides its applications in heat transfer problems as studied in Chapters 5 and 6, porous structures are also used in reactors for biochemical/bioengineering applications. For reactors with a porous wall, several experimental researches have been conducted, for example, mircochannel enzyme reactors with porous-silicon wall and perfusion bioreactors with porous-matrix wall.

A microstructured enzyme reactor was fabricated by Drott et al. (1997 and 1999) which had porous silicon etched along the walls in the microchannels. Glucose oxidase was immobilized on the porous structure; and the enzyme activity was monitored following a colorimetric assay. A 170-fold increase of catalytic turn-over rate was obtained as compared with a non-porous reactor. Later, Melander et al. (2006) experimentally studied the influence of several parameters on the hydrolysis efficiency of maltodextrins and starch and found that it increased with lower flow rate and lower substrate concentration. As for modeling of the mass transport there are previous studies (Bhatia et al., 2004; Tmej et al., 2005; Horta et al., 2007) on enzyme reactors whose porous matrix fully filled the channel. They analyzed the effects of

*Parts of this chapter have been submitted to *ASME Journal of Biomechanical Engineering* (Chen et al., submitted for publication)

principle operational parameters (for example, reactor channel length, inlet concentration, flow rate, reaction rate and Michaelis-Menten constant) of the reactor system for the optimization of the enzyme reactor performance. Al-Muftah and Abu-Reesh (2005) developed a mathematical model for a packed bed immobilized enzyme reactor. It was concluded that the effectiveness factor was reduced by intraparticle diffusion resistance and external mass transfer resistances. However there has been no modeling for a channel enzyme reactor partially filled with porous walls.

A perfusion bioreactor was designed (Ma et al., 1999; Zhao and Ma, 2005) with fibrous matrix walls in the channels, for tissue engineering of trophoblast and mesenchymal stem cells. The porous matrix provides opportunities for the cells to grow into a three dimensional space and thus maintained their normal functional activities. Zhao et al. (2007) considered the porous matrix useful for tissue engineering of human mesenchymal stem cell (MSC) as the shear stress was significantly lower than those with other perfusion bioreactors, and the MSC differentiation are sensitive to low levels of shear stress.

A model for the mass transport in a bioreactor with a porous matrix wall was given by Pathi et al. (2005) and Zhao et al. (2005). They assumed Poiseuille velocity profile in the fluid domain. In the cell layer, the flow convection was not considered; the substrate continuity equation involved diffusion and consumption terms. The equations were solved by MATLAB to give concentration distribution in the fluid and cell layers for their specific bioreactor. In their recent model (Zhao et al., 2007), the Stokes' equation was used for the fluid region and the Brinkman's equation for the

porous region. Continuities of velocity and shear stress were imposed at the porous-fluid interface. The equations were solved by Lattice-Boltzmann method. Distributions of velocity, shear stress and concentration in the fluid and porous regions were presented for their specific cases of perfusion, bioreactor geometry and cell type (MSC). Pierre et al. (2008) numerically analyzed the influence of construct thickness and media flow rate for engineered cartilage oxygenation in a parallel-plate bioreactor. Poiseuille velocity profile in the fluid domain and negligible flow convection in tissue layer were also assumed. The mass transfer equation was solved using Femlab for four culture conditions with different tissue thicknesses and flow rates. So far, there is no general study which presents the influence of flow and geometric parameters on mass transport behavior in such bioreactors with porous walls. The general results would be useful in design of such bioreactors and its optimization.

In this chapter, the flow and mass transport in a microchannel with a porous wall are studied with a view to applications in enzyme reactors and cell bioreactors. The Navier-Stokes equation in the fluid region and the Brinkman-Forcheimmer extended model in the porous medium are coupled and numerically solved. For porous-fluid interface, the Ochoa-Tapia and Whitaker's stress jump interfacial condition (1998b) is used to investigate its effects on flow and mass transfer. The reaction kinetics are based on first-order, zeroth-order, and Michaelis-Menten types. The numerical results are correlated by non-dimensional parameters for the purpose

of presenting generalized results which can find applications in the design analysis of such microchannel reactors with a porous wall.

7.1 Problem Statement

7.1.1 Microchannel Reactor Model

The reactor modeled in this chapter was a channel with dimensions typically of length 300 mm, 150 μm in depth and width 2.5cm as shown in Figure 7.1. In practice due to its larger value, the width effect is small as shown by Zeng et al. (2006). Thus the numerical model considered here is simplified into a two-dimensional one like Zhao et al. (2005). The porous wall has a depth from 1.5 μm to 150 μm. The porous medium has cells or enzyme uniformly distributed in it, which forms the reactive (consumption) elements.

The incoming flow is a steady, laminar and incompressible one with substrate concentration c_{in} . The inlet velocity is specified as that of a fully-developed flow.

The governing equations for the flow are the same as described in Equations (3.17) to (3.20) and Equations (3.37) to (3.39). For the mass transfer equation in the porous part, the reaction is assumed to follow the Michaelis-Menten model (Michael and Fikret, 1992; Chow et al., 2001a and 2001b):

$$u\frac{\partial c}{\partial x}+v\frac{\partial c}{\partial y}=D_{eff}\left(\frac{\partial^2 c}{\partial x^2}+\frac{\partial^2 c}{\partial y^2}\right)-\frac{\gamma V_m c}{c+k_m} \tag{7.1}$$

where c is volume-averaged concentration, γ is the cell or enzyme volume density, V_m is the maximal substrate uptake rate (SUR), k_m is Michaelis-Menten constant or substrate concentration at which the SUR is half-maximal, D_{eff} is the effective mass diffusivity in porous medium.

The porous medium consists of a matrix structure with either cells or enzymes attached on it, with volume fraction ε_s and ε_c occupied by the matrix and cells/ enzymes respectively. Thus the porosity of the porous medium can be calculated as:

$$\varepsilon = 1 - \varepsilon_s - \varepsilon_c \tag{7.2}$$

Generally, for the matrix without cells, the porosity may vary from 0.6 to 0.95 (Cooper et al., 2005) and the permeability of the porous medium is in the range of 10^{-12} to 10^{-9} (Wang and Tarbell, 2000). The results in Chapter 6 show that porosity makes little effect on flow and heat transfer, compared with permeability; thus for simplicity ε is set to be ε=0.9 in the simulations. As for the permeability, it will be shown to affect the Peclet numbers of the fluid and porous flows which will be discussed later.

The mass transfer equation in fluid part is written as:

$$u\frac{\partial c}{\partial x} + v\frac{\partial c}{\partial y} = D\left(\frac{\partial^2 c}{\partial x^2} + \frac{\partial^2 c}{\partial y^2}\right) \tag{7.3}$$

For the velocity boundary conditions, the non-slip condition was imposed on the solid upper and bottom walls and fully-developed condition for the outlet. For the upper and bottom solid-walls, zero mass flux condition was imposed. At the interface between the homogeneous fluid and porous media regions, the stress-jump interfacial

conditions (Equation 6.3) together with continuities of velocity and normal stress (Equations 6.4 and 6.5) are imposed. Also imposed at the interface are continuities of mass and mass flux (similar with heat transfer Equations 6.6 and 6.7).

Before the computation of results, a grid independency study was investigated for different geometries, which were composed of both upper fluid and bottom porous parts. The grid distribution was similar with those in Figure 6.16 in Chapter 6, where there were more grids near the inlet than further downstream. Considering the computational cost and accuracy, a total number of 1500x200 (for case of largest depth) to 1500x110 (smallest depth) meshes for both porous and fluid domains, were found to be adequate.

7.1.2 Dimensionless Parameters

The non-dimensional substrate concentration is defined as:

$$C = \frac{c}{c_{in}} \tag{7.4}$$

The porous and fluid Peclet numbers for mass transfer are a measure of the relative importance of convection to diffusion in porous or fluid domains. They are defined as follows:

$$Pe_p = \frac{u_{p\_av} h}{D_{eff}} \tag{7.5}$$

$$Pe_f = \frac{u_{f\_av} H}{D} \tag{7.6}$$

where u_{p_av} and u_{f_av} are the incoming mean flow velocities in porous and fluid domains respectively; h and H are the heights of the porous wall and fluid channel respectively.

The fluid and porous Damkohler numbers are defined as:

$$Dam_f = \frac{V_m \gamma h}{u_{f\_av} c_{in}} \tag{7.7}$$

$$Dam_p = \frac{V_m \gamma h^2}{D_{eff} c_{in}} \tag{7.8}$$

Dam_f characterizes the ratio of the time scales of substrate reaction in the porous medium to substrate convection in the upper fluid domain. Dam_p characterizes the ratio of the time scales of substrate reaction to substrate diffusion in the porous medium.

The non-dimensional Michaelis-Menten constant (or non-dimensional concentration at which specific uptake rate is half maximal) is defined as:

$$K_m = \frac{k_m}{c_{in}} \tag{7.9}$$

7.1.3 Simple Analysis for Fluid Region

Consider a microchannel with Michaelis-Menten reaction in the porous medium. It is assumed that the velocity is uniform and the diffusion is in Y-direction. The mass transfer equation in fluid part (Equation 7.3) is simplified as:

$$u_{f\_av}\frac{\partial c}{\partial x}=D\frac{\partial^2 c}{\partial y^2} \tag{7.10}$$

For zeroth-order reaction, the flux normal to the interface (explained later in Section 7.1.4.1) may be approximated as:

$$\left.\frac{\partial C}{\partial Y}\right|_{\text{int}}=\frac{(C_{\text{int}}-C_{bot})H}{h}=\frac{1}{2}\frac{H}{h}Dam_p=\frac{1}{2}Dam_{f\_d} \tag{7.11}$$

where the fluid-diffusion Damkohler number is defined:

$$Dam_{f\_d}=\frac{V_m\gamma hH}{Dc_{in}} \tag{7.12}$$

It characterizes the ratio of the time scales of substrate reaction along the boundary to substrate diffusion in the fluid domain.

Using separation of variables techniques with the above boundary condition, the mass transfer equation can be solved to give the concentration distribution along the interface:

$$\begin{aligned}C_{\text{int}}-1=&-\frac{1}{2}\frac{x\bullet Dam_f}{H}-\frac{1}{6}Dam_{f\_d}\\&+\frac{1}{\pi^2}Dam_{f\_d}\sum_{n=1}^{\infty}\frac{(-1)^n}{n^2}\cos(n\pi)\exp(-n^2\pi^2\frac{x}{H}\frac{1}{Pe_f})\end{aligned} \tag{7.13}$$

Note that for the simplified analyses, the diffusivity D_{eff} in the porous part was assumed to be the same as the diffusivity D of the fluid. Equation (7.13) shows that the interface concentration C_{int} is a function of the parameters $\frac{x}{H}Dam_f$ and Dam_{f_d}.

The third term on the right is at least one order smaller than that of the first two terms; thus the effect of $\frac{x}{H}Pe_f$ may be relatively smaller.

For first-order reaction, the flux along the interface (as explained later in Section 7.1.4.2) may be approximated as:

$$\left.\frac{\partial C}{\partial Y}\right|_{\text{int}} = \frac{(C_{\text{int}} - C_{bot})H}{h} = \frac{1}{2}\frac{H}{h}\frac{Dam_p}{K_m} = \frac{1}{2}\frac{Dam_{f\_d}}{K_m} \tag{7.14}$$

Using similar techniques as that for the zeroth-order reaction, but now using the above boundary condition for first-order reaction, the mass transfer Equation (7.10) can be solved to give the concentration distribution along the interface:

$$\begin{aligned} C_{\text{int}} - 1 &= -\frac{1}{2}\frac{x \bullet Dam_f}{HK_m} - \frac{1}{6}\frac{Dam_{f\_d}}{K_m} \\ &+ \frac{1}{\pi^2}\frac{Dam_{f\_d}}{K_m}\sum_{n=1}^{\infty}\frac{(-1)^n}{n^2}\cos(n\pi)\exp(-n^2\pi^2\frac{x}{H}\frac{1}{Pe_f}) \end{aligned} \tag{7.15}$$

Equation (7.15) shows that the interface concentration C_{int} is a function of the parameters $\frac{x}{H}\frac{Dam_f}{K_m}$ and $\frac{Dam_{f\_d}}{K_m}$. The effect of $\frac{x}{H}Pe_f$ may be relatively smaller as the term is at least one order smaller like before.

The above simplified analyses identified two combined parameters which may be useful for correlating the data:

Reaction-convection distance parameter (zeroth-order) defined as:

$$\kappa = \frac{x \bullet Dam_f}{H} \tag{7.16}$$

Reaction-convection distance parameter (first-order) defined as:

$$\kappa = \frac{x \bullet Dam_f}{K_m \bullet H} \tag{7.17}$$

7.1.4 Simple Analysis for Porous Region

7.1.4.1 Zeroth-order Reaction Type

Due to the relatively higher flow resistance provided by the porous medium, the velocity there is much smaller than that in the fluid part. Since the reactor length is relatively larger than the porous medium depth, the mass transfer by diffusion is dominant in the Y-direction, that is $\frac{\partial C}{\partial y} >> \frac{\partial C}{\partial x}$. Since K_m=0**,** zeroth-order reaction type, Equation (7.1) becomes:

$$\frac{\partial^2 c}{\partial y^2} = \frac{\gamma V_m}{D_{eff}} \tag{7.18}$$

Equation (7.18) can be non-dimensionalized using c_{in}, h:

$$\frac{\partial^2 C}{\partial Y^2} = \frac{\gamma V_m h^2}{D_{eff} c_{in}} = Dam_p \tag{7.19}$$

The boundary conditions are:

$$\text{Y=1, } C = C_{\text{int}} \tag{7.20}$$

$$\text{Y=0, } \frac{\partial C}{\partial Y} = 0 \tag{7.21}$$

Using the above boundary conditions, the solution of Equations (7.19) is:

$$C = \frac{1}{2} Dam_p Y^2 + C_{\text{int}} - \frac{1}{2} Dam_p \tag{7.22}$$

$$C_{bot}\,(\mathrm{Y}=0) = C_{\mathrm{int}} - \frac{1}{2} Dam_p \tag{7.23}$$

$$\frac{C_{\mathrm{int}} - C_{bot}}{Dam_p} = \frac{1}{2} \tag{7.24}$$

Equation (7.24) gives a simple relationship between the concentration difference and porous Damkohler number. This combined parameter may be rearranged as:

$$\xi = \frac{C_{\mathrm{int}} - C_{bot}}{Dam_p} = \frac{\dfrac{D_{eff}\,(c_{\mathrm{int}} - c_{bot})}{h}}{V_m \gamma h} \tag{7.25}$$

which shows that it is a ratio between the concentration flux into the porous medium (Griffith and Swartz, 2006) and the maximum reaction rate. It should be noted for initial part of the reactor, there is also inlet concentration convection in the porous medium, and thus the concentration difference parameter is under-estimated for the initial part. The new combined parameter is proposed in the present study for correlating the data, and it is named as concentration difference parameter.

As defined by Al-Muftah and Abu-Reesh (2005), the effectiveness factor is the ratio of actual reaction rate to that which would be obtained if the enzyme or cells are at the interface (that is without the porous medium); the reaction efficiency is the ratio of actual reaction rate to the maximum amount that could be used at the inlet. For the zeroth-order type reaction, Equation (7.25) may give an indication of the effectiveness factor; when averaged over the reactor length, it may give an indication of the reaction efficiency for the reactor.

For Michaelis-Menten type reactions, the effectiveness factor can be defined as:

$$\xi = \frac{C_{\text{int}} - C_{bot}}{Dam_p \dfrac{C_{\text{int}}}{C_{\text{int}} + K_m}} = \frac{\dfrac{D_{eff}(c_{\text{int}} - c_{bot})}{h}}{V_m \gamma h \dfrac{c_{\text{int}}}{c_{\text{int}} + k_m}} \tag{7.26}$$

The reactor efficiency can be defined as:

$$\eta = \frac{\bar{C}_{\text{int}} - \bar{C}_{bot}}{Dam_p \dfrac{1}{1 + K_m}} = \frac{\dfrac{D_{eff}(\bar{c}_{\text{int}} - \bar{c}_{bot})}{h}}{V_m \gamma h \dfrac{c_{\text{in}}}{c_{\text{in}} + k_m}} \tag{7.27}$$

where $\bar{c}_{\text{int}}$ and $\bar{c}_{bot}$ are the interface and bottom concentrations averaged over the reactor length.

7.1.4.2 First-order Reaction Type

Using similar assumption as in Section 7.1.4.1, except using first-order reaction type, that is small Dam_p / K_m, Equation (7.1) can be simplified as,

$$\frac{\partial^2 c}{\partial y^2} = \frac{\gamma V_m}{D_{eff} k_m} c \tag{7.28}$$

As before, non-dimensionalize the equation using c_{in}, h:

$$\frac{\partial^2 C}{\partial Y^2} = \frac{\gamma V_m h^2}{D_{eff} c_{in} K_m} C = \frac{Dam_p}{K_m} C \tag{7.29}$$

With boundary conditions (7.20) and (7.21), Equation (7.29) can be solved as,

$$C = \frac{C_{\text{int}}}{e^{\sqrt{\frac{Dam_p}{K_m}}} + e^{-\sqrt{\frac{Dam_p}{K_m}}}} \left(e^{\sqrt{\frac{Dam_p}{K_m}} Y} + e^{-\sqrt{\frac{Dam_p}{K_m}} Y}\right) \tag{7.30}$$

So,

$$\frac{C_{bot}}{C_{\text{int}}} = \frac{2}{e^{\sqrt{\frac{Dam_p}{K_m}}} + e^{-\sqrt{\frac{Dam_p}{K_m}}}} \tag{7.31}$$

or $$\frac{C_{bot}}{C_{\text{int}}} a = 1 \tag{7.32}$$

where $a = \frac{e^{\sqrt{\frac{Dam_p}{K_m}}} + e^{-\sqrt{\frac{Dam_p}{K_m}}}}{2}$.

Using series extension for the exponential terms and neglecting higher order terms, assuming a small Dam_p / K_m,

$$a \approx 1 + \frac{1}{2}\frac{Dam_p}{K_m} \tag{7.33}$$

Equation (7.32) can be re-written as,

$$(\frac{C_{\text{int}} - C_{bot}}{C_{\text{int}}}) / \frac{Dam_p}{K_m} = \frac{0.5}{1 + 0.5\frac{Dam_p}{K_m}} \tag{7.34}$$

Equation (7.34) gives a simple relationship between the concentration difference and porous Damkohler number. This combined parameter may be rearranged as:

$$\xi = (\frac{C_{\text{int}} - C_{bot}}{C_{\text{int}}}) / \frac{Dam_p}{K_m} = \frac{\frac{D_{eff}(c_{\text{int}} - c_{bot})}{h}}{\frac{V_m \gamma h}{k_m} c_{\text{int}}} \tag{7.35}$$

which shows that it is a ratio between the concentration flux into the porous medium (Griffith and Swartz, 2006) and the reaction rate based on interface concentration. The new combined parameter is proposed in the present study for correlating the data,

and it is named as concentration difference parameter. It may give an indication of the reaction effectiveness factor for the first-order type reactor (Al-Muftah and Abu-Reesh, 2005).

For first-order reaction, the concentration along the interface C_{int} is close to 1.0, thus concentration difference parameter can be simplifies as:

$$\xi = (C_{\text{int}} - C_{bot}) / \frac{Dam_p}{K_m} \tag{7.36}$$

The concentration difference parameter is a combined parameter related to the ratio between the concentration flux into the porous part and maximum consumption rate inside. When averaged over the reactor length, it may give an indication of the reaction efficiency for the first-order type reactor (Al-Muftah and Abu-Reesh, 2005).

It should be noted that the above analysis in Sections 7.1.4.1 and 7.1.4.2 is meant only for the purpose of developing the combined dimensionless parameters. It is a simplified reaction type which assumes no convection but only diffusion in Y-direction in porous part. It is necessary to evaluate from the numerical results whether the use of the combined parameters listed in Section 7.1.3 and 7.1.4 are able to give good collapse of data.

7.2 Results and Discussion

7.2.1 General Results for Flow and Concentration

7.2.1.1 Concentration and Velocity Fields

Figure 7.2 shows a typical concentration contour field for the fluid and porous regions. There is relatively higher substrate concentration in the fluid region than in the porous medium. The substrate in the fluid is convected to the interface; there the concentration is higher than the bottom due to the consumption in the porous medium. Along the downstream direction, the concentrations at the interface and bottom are decreasing, also due to the consumption.

The downstream decrease of interface concentration is shown in Figure 7.3a. Normal to the interface a typical concentration profile is shown in Figure 7.3b. A typical velocity profile of the fully developed flow is shown in Figure 7.3c. In these concentration and velocity plots, the effects of interfacial boundary conditions are explored with the change of stress jump coefficients. There are some effects of the first stress jump coefficient β especially on the interfacial velocity and the maximum velocity (Figure 7.3c). The second stress jump coefficient β_1 has relatively smaller effect. This is because in the interfacial boundary conditions (Equation 6.3), the term involving β_1 is associated with Reynolds number which is low in present study. But the term involving β, associated with the reciprocal of Darcy number, can become large if *Da* is low. However, both effects are not large compared to the other parameters which will be discussed later. Thus in the following computations, stress and velocity continuities are imposed to couple the two sets of controlling equations in porous and fluid domains.

It is noted that the concentration distribution in the porous medium (Figure 7.3b) behaves approximately linear except near the bottom wall where the mass flux is zero. Thus it is an approximation to assume linear concentration distribution for defining the flux in Equation (7.11) and (7.14).

7.2.1.2 Effects of Porous and Fluid Peclet Numbers

The effects of porous and fluid Peclet numbers are investigated for the interface concentration (Figure 7.4a), bottom concentration (Figure 7.4b) and their difference (Figure 7.4c); with the consumption rate Dam_p constant. The porous Peclet number ranges from 0.025 to 2.5, which is in the diffusion-dominated range (McClelland et al. 2003). The fluid Peclet number ranges from 15 to 150, which is in the convection-dominated range (Zhao et al., 2007).

It is seen that a larger fluid Peclet numbers gives larger values of interface and bottom concentrations (Figure 7.4a and b) and their differences (Figure 7.4c). This is due to the larger convection of substrate in fluid region. In the numerical model of Zhao et al. (2007) for a perfusion bioreactor with a porous wall, the concentration values was also found to increase significantly with fluid Peclet number (15 to 225). They stated that their porous Peclet number, being two orders smaller, had a negligible role for mass transfer. Similarly in the present study, the porous Peclet numbers Pe_p is found to have relatively smaller effect because the convection in the porous medium is small especially for $Pe_p < 0.25$. However the convection in the

porous medium is less negligible at the largest Pe_p of 2.5, as reflected in the slightly higher values of interface and bottom concentrations and slightly lower values of their difference.

To further check the effect of Pe_f, it is studied together with the fluid Damkohler number Dam_f in Figure 7.5a, b and c. It can be seen that when Dam_f is kept constant, a great change of Pe_f from 15.0 to 150.0 does not have much effect on the results. However change of Dam_f has significant effects.

Thus it can be concluded that Dam_f is more important than Pe_f for the interface line concentration. The results show that the parameter relating convection to consumption Dam_f is much more dominant than that relating convection to diffusion Pe_f. The mass transfer is convection-dominated in the fluid region and the diffusion rate in the fluid part is much less important than the consumption rate. The apparent effects of Pe_f described in previous Figure 7.4 actually arises from the changes of Dam_f.

7.2.1.3 Effect of Porous and Fluid Damkohler Numbers

For low reaction rate (close to first-order type), the effects of consumption rates on substrate concentration are presented in Figure 7.6a, b and c. The consumption rates as compared to porous diffusion and fluid convection are

respectively characterized by $\frac{Dam_p}{K_m}$ and $\frac{Dam_f}{K_m}$ as suggested by the simplified analysis (Equation 7.15). It is seen that the interface and bottom concentration (Figure 7.6a and b) is larger when $\frac{Dam_f}{K_m}$ is lower, which is expected as it is associated with smaller consumption relative to fluid convection. There is similar influence on concentration by $\frac{Dam_p}{K_m}$ but its effect is smaller. For the effect on concentration difference (Figure 7.6c) both $\frac{Dam_p}{K_m}$ and $\frac{Dam_f}{K_m}$ are seen to be important parameters. The concentration difference is larger when $\frac{Dam_p}{K_m}$ is larger or when $\frac{Dam_f}{K_m}$ is smaller. As explained earlier, the concentration difference is approximately related to the flux into the porous medium. A larger $\frac{Dam_p}{K_m}$ is associated larger consumption and hence larger flux. A smaller $\frac{Dam_f}{K_m}$ is associated with larger convection (in fluid) relative to consumption and hence larger flux into porous medium.

For middle and high reaction rates (close to zeroth-order and Michaelis-Menten type), the effects of consumption rates on substrate concentration are presented in Figure 7.7a, b and c. The consumption rate as compared to porous diffusion and fluid convection are respectively characterized by Dam_p and Dam_f as

suggested by the simplified analysis (Equation 7.13). Note that the Michaelis-Menten constant K_m is not incorporated, different from that of first-order.

It is seen that the interface and bottom concentration (Figure 7.7a and b) is larger when Dam_f or Dam_p are lower, which is expected as these are associated with smaller consumptions. For the effect on concentration difference (Figure 7.7c) it is larger when Dam_p is larger or when Dam_f is smaller. The explanation is similar to that for the first order case. A larger Dam_p is associated with larger consumption and hence larger flux. The significance of parameter Dam_p in reaction and diffusion has been highlighted by Griffith and Swartz (2006) for porous tissue constructs. As for the smaller Dam_f, it is associated with larger convection (in fluid) relative to consumption and hence larger flux into porous medium.

The present results, for both small to large reaction rates, show that the mass transport is influenced by two consumption parameters: Dam_f and Dam_p (or $\frac{Dam_f}{K_m}$ and $\frac{Dam_p}{K_m}$ for first-order case). The two parameters characterize the consumptions relative to convection and diffusion. In a previous study, Zhao et al. (2007) suggested two parameters: Peclet number Pe_f and Thiele modulus (related to $\frac{V_m \gamma H^2}{Dc_{in}}$). The Thiele modulus was also suggested by Griffith and Swartz (2006), but unlike Zhao et

al (2007), the axial length of the porous tissue was used; the present parameter Dam_p uses the depth of the porous medium.

7.2.2 Correlation of Concentration Results

7.2.2.1 Reactions Close to First-order Type

The interface concentration (Figure 7.6a) at different consumption, convection and distance is plotted as a correlated plot in Figure 7.8 with the use of reaction-convection distance parameter $\frac{x}{H}\frac{Dam_f}{K_m}$ and reaction-diffusion (fluid) parameter $\frac{Dam_{f\_d}}{K_m}$. The data was obtained from various reaction-convection parameter $\frac{Dam_f}{K_m}$. The correlation is for the case near to first-order where $\frac{Dam_{f\_d}}{K_m}$ is close to zero value. It can be seen that the use of the proposed parameters has correlated the results very well. The numerical results show that the interface concentration is mainly a function of the reaction-convection distance parameter $\kappa = \frac{x \bullet Dam_f}{K_m H}$ and the other parameter $\frac{Dam_{f\_d}}{K_m}$ is not significant. It is consistent with the simplified analysis (Equation 7.15) because the second and third terms on the right hand side, associated with $\frac{Dam_{f\_d}}{K_m}$, are not large for first-order reaction.

The concentration difference (Figure 7.6c) at different consumption, convection and distance is plotted as a correlated plot in Figure 7.9; where $(C_{\text{int}} - C_{bot}) / \frac{Dam_p}{K_m}$ is plot against $\frac{x}{H}\frac{Dam_f}{K_m}$ as these two combined parameters are identified by the simplified analysis (Section 7.1.4.2) to be significant for the purpose of correlating the data at different consumption, convection and porous-diffusion.

It is seen (Figure 7.9) that the use of the proposed parameters has generally correlated the data well and collapsed the data obtained from various $\frac{Dam_f}{K_m}$ and $\frac{Dam_p}{K_m}$. The correlation is not good for the case of $\frac{Dam_f}{K_m}$ = 0.38 because it is not close to first order. The general trend of the correlated curve shows that the local concentration difference parameter is decreasing with increase of the reaction-convection distance parameter. This means there is decreasing mass flux into the porous region further downstream, due to smaller consumption locally. This is because in first order reaction, the consumption is proportional to the local concentration which is smaller downstream.

The effectiveness factor is shown in Figure 7.10. It is the ratio of actual reaction rate to that which would be obtained if the enzyme or cells are at the interface (that is without the porous medium). It is seen that there is still effect of $\frac{Dam_f}{K_m}$ even though it is incorporated in $\frac{x}{H}\frac{Dam_f}{K_m}$, but the effect is small except for

the two curves of $\frac{Dam_f}{K_m}$ = 0.38 which are not near first-order reaction. The results shows that effectiveness factor is a function of $\frac{x}{H}\frac{Dam_f}{K_m}$ and $\frac{Dam_p}{K_m}$. Note that $\frac{Dam_p}{K_m}$ was used to define the effectiveness factor but not to normalize the flux into the porous medium. Thus the data at various $\frac{Dam_p}{K_m}$ is not expected to be collapsed although the results show that its effect is small.

It can be seen that the effectiveness factor is small when the reaction-convection distance parameter $\frac{x}{H}\frac{Dam_f}{K_m}$ is small. This is because at large fluid convection, the mass transport is limited by diffusion in the fluid medium. Also the fluid convection there is so large that the effectiveness is not changed much by the present range of changes in porous medium diffusion as reflected in the parameter $\frac{Dam_p}{K_m}$. Further downstream or large $\frac{x}{H}\frac{Dam_f}{K_m}$, the effectiveness factor tends to an asymptotic value of 0.5 as predicted in the simplified analysis (Equation 7.34) for small $\frac{Dam_p}{K_m}$. There, the porous diffusion can affect the effectiveness factor. A smaller $\frac{Dam_p}{K_m}$ (larger porous diffusion) improves the effectiveness, which is consistent with the simplified analysis (see Equation 7.34).

The reactor efficiency is shown in Figure 7.11. It is correlated by the parameter $\frac{x}{H}\frac{Dam_f}{K_m}$ only when it is larger than 5. The efficiency is initially affected by $\frac{Dam_f}{K_m}$ due to diffusion limitation in the porous medium as discussed before for the effectiveness factor; a larger $\frac{Dam_f}{K_m}$ gives lower efficiency. The influence of $\frac{Dam_p}{K_m}$ is small but this is because it cannot be varied greatly in first order reaction. The efficiency is reduced at longer distance or smaller convection, as reflected in the parameter $\frac{x}{H}\frac{Dam_f}{K_m}$; the local concentration there small is small which makes the reaction small, and hence the flux into the porous medium is small.

Drott et al. (1997 and 1999) experimentally studied an enzyme microreactor which consisted of microchannels with porous silicon walls. They found the reaction rate initially increased with porous depth and then leveled off at depth $5\,\mu m$ due to diffusion limitation of the porous matrix. This appears consistent with the present results in Figure 7.11. The reactor efficiency shows a peak and then reduces with larger $\frac{x}{H}\frac{Dam_f}{K_m}$. A larger $\frac{x}{H}\frac{Dam_f}{K_m}$ is associated with bigger porous depth h if other specifications are fixed. The reactor efficiency is the ratio of reaction rate (flux into porous medium) and inlet reaction rate. The flux (which is normalized by *h*

through Dam_p) would not increase with the porous depth *h* (or larger $\frac{x}{H}\frac{Dam_f}{K_m}$) because the efficiency is decreasing. That is the larger *h* increases Dam_f resulting in lower efficiency which offsets the higher flux effect of Dam_p.

For such enzyme microreators, Melander et al. (2006) experimentally found that reactor efficiency decreased with increasing flow rate (due to shorter residence time). Their range of $\frac{x}{H}\frac{Dam_f}{K_m}$ is around 7.0, and for this range, the present results in Figure 7.11 show that reactor efficiency increases with increasing flow rate or decreasing $\frac{x \bullet Dam_f}{HK_m}$. The difference is due to the difference in the definition of efficiency as the present one is based on maximum reaction rate (in Michaelis-Menten reaction) per residence time (Al-Muftah and Abu-Reesh, 2005), whereas Melander et al. (2006) based their efficiency on inlet convection flux. Their efficiency is lower with higher inlet concentration (due to saturation). The saturation effect seems to be present in the present results (Figure 7.11) as the present efficiency, though defined differently, does not increase with higher concentration (or smaller $\frac{Dam_p}{K_m}$).

7.2.2.2 Michaelis-Menten Type Reactions

The interface concentration (Figure 7.7a) at different consumption, convection and distance is plotted as a correlated plot in Figure 7.12 with the use of reaction-convection distance parameter $\frac{x}{H}Dam_f$ and fluid-diffusion Damkohler number Dam_{f_d}. The data were obtained from various fluid Damkohler number Dam_f as listed in the figure. The correlation is for Michaelis-Menten reaction type (K_m is not zero).

It can be seen in Figure 7.12a that the effect of different Dam_f is not much as it has been incorporated into the reaction-convection distance parameter. The effect of Dam_{f_d} is larger in the initial part of $\frac{x}{H}Dam_f$ as the fluid diffusion effect is relatively more dominant than axial convection. Thus larger $Dam_{f\_d} = \frac{V_m \gamma h H}{Dc_{in}}$ (smaller diffusion) gives lower interface concentration initially, leaving more substrate for the region further downstream as seen from the cross-over in interface concentration. There, the effect of diffusion Dam_{f_d} is relatively less dominant compared to the axial convection.

However the above correlation does not involve the Michaelis-Menten constant K_m and the effect is investigated in Figure 7.12b. There is some effect of K_m but relatively smaller than that of Dam_{f_d} in Figure 7.12a. Larger K_m will result in higher interface concentration due to smaller consumption rate using Michaelis-Menten reaction. It may be concluded that the interface concentration is

approximately correlated with the use of combined parameters $\frac{x}{H}Dam_f$ and $Dam_{f\_d} = \frac{V_m \gamma hH}{Dc_{in}}$ which respectively characterizes the ratios of reaction to fluid convection and reaction to fluid diffusion. Better correlation will need the incorporation of Michaelis-Menten constant K_m.

The concentration difference (Figure 7.7c) at different consumption, convection and distance is plotted as a correlated plot in Figure 7.13. The concentration difference parameter $\xi = \frac{C_{\text{int}} - C_{bot}}{Dam_p}$ is plotted as a function of the reaction-convection distance parameter $\frac{x}{H}Dam_f$. The data were obtained from various fluid Damkohler number Dam_f and porous Damkohler number Dam_p as given in the figure. It is seen that Figure 7.13a has correlated the data of Figure 7.7c satisfactorily. The effect of Dam_f is not much after $\frac{x}{H}Dam_f > 0.1$; the fluid convection affects the porous domain indirectly through the interface concentration, which has already been incorporated in the reaction-convection distance parameter $\frac{x}{H}Dam_f$. However, the use of $\frac{C_{\text{int}} - C_{bot}}{Dam_p}$ in Figure 7.13a has reduced the spread of data in Figure 7.7c but not collapse the influence of different Dam_p; when Dam_p is smaller (larger porous diffusion) $\frac{C_{\text{int}} - C_{bot}}{Dam_p}$ is larger. This shows that the concentration difference would not be completely normalized by Dam_p which is

based on various maximum reaction rates. For non-zeroth order reaction of Michaelis-Menten type, the actual reaction is dependent on concentration and thus on concentration difference. However the influence of the other reaction parameter Dam_f has been incorporated in the combined parameter $\frac{x}{H} Dam_f$.

The concentration difference parameter is also larger at smaller K_m as shown in Figure 7.13b. Smaller K_m will result in larger consumption rate, using Michaelis-Menten reaction, and hence larger concentration difference for regions of $\frac{x}{H} Dam_f$ below around 1. But this larger consumption results in earlier depletion of fluid substrate which explains the cross-over at $\frac{x}{H} Dam_f$ around 1.

It may be concluded that the concentration difference parameter $\frac{C_{\text{int}} - C_{bot}}{Dam_p}$ is correlated with the use of combined parameters $\frac{x}{H} Dam_f$, Dam_p and K_m. The concentration difference may be related to the concentration flux into the porous medium if first order finite difference approximation is assumed.

The concentration flux is meaningful as it indicates the mass transfer resistance of the porous medium. To quantify the mass transfer effectiveness of the porous medium, an effectiveness factor is defined. It is the ratio of actual reaction rate to that which would be obtained if the enzyme or cells are at the interface (that is without the porous medium).

The effectiveness factor is shown against $x\frac{Dam_f}{H}$ in Figure 7.14a. It is seen that the effect of Dam_f is very small and only slightly noticeable at small $x\frac{Dam_f}{H} < 0.1$. However the porous Damkholer number Dam_p has large effect on the effectiveness. A smaller Dam_p (larger porous diffusion) improves the effectiveness as would be expected. The reaction effectiveness factor with different K_m is shown in Figure 7.14b. A larger K_m gives smaller reaction at interface, for Michaelis-Menten reaction, especially when the concentration is small like those further downstream, or larger $x\frac{Dam_f}{H}$. With a smaller interface reaction, the local effectiveness, by definition, will be relatively bigger. Note that K_m is incorporated in the effectiveness factor only to define the interface reaction. It was not meant to normalize the flux and thus the effectiveness factor is still dependent on K_m.

The reactor efficiency is presented in Figure 7.15. It is seen that efficiency is satisfactorily correlated by plotting against the parameter $x\frac{Dam_f}{H}$. The efficiency varies from about 0.5 to 0.2. The main effect on efficiency is the Dam_p, which is the ratio of reaction to porous diffusion. Smaller Dam_p gives better efficiency as expected because the porous diffusion is larger. The effect of Dam_f is only noticeable for smaller $x\frac{Dam_f}{H}$ and is not large. The effect of Michaelis-Menten

constant K_m is relatively small (Figure 7.15b). The efficiency is defined with reference to the reaction at inlet where the concentration is largest and thus the K_m effect on reaction, and thus efficiency, is expected to be small.

7.2.3 Applications of Correlated Results

7.2.3.1 Perfusion Bioreactor with Porous Scaffolds

The results may find possible applications in the design of microchannel reactors with a porous wall. In considering the performance of the bioreactor, there are a few criteria. Firstly, there should be adequate substrate concentration for cell growth to avoid hypoxia, that is the concentration should be greater than the critical value. This condition $C_{bot} \geq K_m$ may not be satisfied with a large Dam_p. As shown in Figure 7.13a, the concentration C_{bot} has reached critical K_m at $x\frac{Dam_f}{H} = 0.3$ beyond which it will be subcritical. Secondly, the porous medium should not pose a large resistance to the mass transport. Different from those bioreactors with an impervious wall (Zeng et al., 2006), the present mass transport is affected by the diffusion in the porous medium, as quantified by the effectiveness factor which then affects the reactor efficiency.

To illustrate, consider the perfusion bioreactor system for growth of mesenchymal stem cells and hematopoietic cells (Zhao et al., 2005 and 2007; Pathi et al., 2005). Their flow configuration was similar to the present model (Figure 7.1) except a membrane formed the upper boundary of the flow channel, across which

there was oxygen transport additional to that from medium convection at the inlet. However the oxygen diffusion across the membrane was considered to be around one sixth of that from the medium convection (Pathi et al., 2005). The mass transport is not constant with time due to the increase in cell number. It is assumed here that the change of cell density does not cause transient behavior and can be regarded as a quasi steady change of the reaction parameters Dam_{f_d}, Dam_f and Dam_p.

To ensure adequate substrate concentration for cell growth, it is necessary to estimate the concentration along the interface and bottom of the porous region, especially at the outlet of the bioreactors. In the bioreactor of Zhao et al. (2005, 2007) and Pathi et al. (2005) the geometry, flow and substrate properties are listed in Table 7.1. For instance, at day 20, the MSC density is $3.99 \times 10^6 cells/ml$ (Zhao et al., 2005). The Damkholers parameters are calculated as: Dam_p =0.051, Dam_{f_d} =0.51, Dam_f =0.0123, and the outlet reaction-convection distance parameter is calculated as $\frac{x \bullet Dam_f}{H}$=0.20. Using Figure 7.12a, C_{int} -1 is -0.25, giving C_{int} = 0.75. Using Figure 7.13b, $\frac{C_{\text{int}} - C_{bot}}{Dam_p}$ = 0.4, giving C_{bot} = 0.73. Thus the interface and bottom concentrations at the outlet, even without considering mass diffusion from their upper membrane, were sufficient for cell growth ($C > K_m$). Moreover, from Figures 7.14a and 7.15a, using $\frac{x \bullet Dam_f}{H}$=0.20, the reaction effectiveness factor and the reactor efficiency are both around 0.5.

Another similar bioreactor with porous media has been used for tissue engineering of cartilage oxygenation (Gemmiti and Guldberg 2006; Pierre et al., 2008). Although their bioreactor included an additional lower static chamber, the model is basically similar to the present one when the oxygen flux from the porous construct into the bottom static chamber approached zero at steady state (after 1 to 6 hours). In their third case, Dam_p =7.95x10^{-2}, Dam_f =8.75x10^{-3}, Dam_{f_d} =7.95x10^{-2}, the outlet reaction-convection distance parameter is $\frac{x \bullet Dam_f}{H}$ =0.40. Using Figures 7.12a, C_{int} -1 is -0.65, giving C_{int} = 0.35. Using Figure 7.13a, $\frac{C_{\text{int}} - C_{bot}}{Dam_p}$ = 0.36, giving C_{bot} = 0.38. Thus the bottom substrate shows a wide change from inlet 1 to outlet 0.38. Using Figures 7.14a and 7.15a, the reaction effectiveness factor is close to 0.5, the reactor efficiency is around 0.44.

7.2.3.2 Microchannel Enzyme Reactor with Porous Silicon

The criteria to consider in designing an enzyme bioreactor include the concentration, effectiveness factor and reactor efficiency (Al-Muftah and Abu-Reesh, 2005). From the present results assuming first-order reaction, the interface and bottom concentrations, C_{int} and C_{bot} , can be estimated from Figures 7.8 and 7.9. The effectiveness factor can be estimated from Figure 7.10 and the reactor efficiency from Figure 7.11. From the efficiency, the conversion rate (ratio between substrate converted and fed) can also be determined.

To illustrate the design application, the enzyme micro-bioreactor of Drott et al. (1997 and 1999) is considered. Their geometry and mass properties are as listed in Table 7.1. For their maximum reaction rate of 364 *nmol/min* with K_m of 10, $\frac{Dam_p}{K_m}$ =0.17, $\frac{Dam_{f\_d}}{K_m}$ =0.34, and the largest reaction-convection distance parameter $\kappa = \frac{x \bullet Dam_f}{K_m \bullet H}$ =0.02. Using Figure 7.8, the outlet interface concentration C_{int} is 0.98; and using Figure 7.9, $\xi = (\frac{C_{\text{int}} - C_{bot}}{C_{\text{int}}}) / \frac{Dam_p}{K_m}$ =0.025, so the outlet bottom C_{bot} is 0.97. Thus with their reactor length and maximum reaction rate, the glucose concentration in the porous matrix is adequate for glucolysis by the enzyme.

To obtain higher conversion rate, one option is to make the reaction-convection distance parameter longer which gives lower concentration at outlet. Furthermore with longer reaction-convection distance parameter, the local effectiveness factor (Figure 7.10) increases to be around 0.5. However, reactor efficiency keeps decreasing as shown in Figure 7.11 and more so for $\frac{x \bullet Dam_f}{K_m \bullet H}$ larger than 4, because of the low concentration which makes the flux small (for near first order reaction). That is, although the reactor is locally more effective, the benefit is offset by the lower concentration. To avoid the efficiency dropping by more than 20% in attempting to maximize the conversion rate, the parameter $\frac{x \bullet Dam_f}{K_m \bullet H}$ should not be increased beyond 5.

Recently, for the same enzyme reactor geometry, Melander et al. (2006) investigated the effect of flow rate on the hydrolysis efficiency. In their experiment, the flow rate is 0.5 to 2 $\mu l \min^{-1}$, giving Dam_f / K_m of 0.015 to 0.004. Thus their reaction-convection distance parameter $\kappa = \frac{x \bullet Dam_f}{K_m \bullet H}$ varies from around 4 to 16. The present results show that the efficiency was increased by at least 50% when their flow rate was increased. Besides using higher flow rate to obtain higher efficiency, the present results of Figure 7.11 show that other options include: shorter reactor length, smaller porous depth, larger channel height, and larger inlet concentration.

7.3 Conclusions

The velocity and concentration fields have been computed in a microchannel reactor with a porous wall. Two parameters are defined to characterize the mass transports in the fluid and porous regions. The porous Damkohler number Dam_p is the ratio of consumption to diffusion of the substrates in the porous medium. The fluid Damkohler number Dam_f is the ratio of substrate consumption in the porous medium to substrate convection in the fluid region. It is shown that the apparent effect of the conventionally used fluid Peclet number Pe_f is actually due to the change of Dam_f. As the consumption is considered over an axial distance, and Dam_f relates to consumption per unit length, the combined parameter $\frac{x \bullet Dam_f}{H}$ is

defined from a simplified analysis for Michaelis-Menten reaction. Another parameter is the fluid-diffusion Damkohler number Dam_{f_d} which is the ratio of substrate consumption in the porous medium and substrate diffusion in the fluid region. The concentration difference between the interface and base of the porous medium are normalized to form a concentration difference parameter $\frac{C_{\text{int}} - C_{bot}}{Dam_p}$. The numerical results are found to be well correlated by the use of these parameters.

The interface concentration C_{int} is found to be a function of the reaction-convection distance parameter $\frac{x \bullet Dam_f}{H}$ and the fluid-diffusion Damkohler number Dam_{f_d} whose influence is relatively smaller at $\frac{x \bullet Dam_f}{H}$ >1. The concentration difference parameter $\frac{C_{\text{int}} - C_{bot}}{Dam_p}$ is not completely normalized by Dam_p which is based on various maximum values of the Michaelis–Menten reactions. For reactions close to first-order type, similar parameters are involved except all the Damkohler numbers are divided by the Michaelis-Menten constant K_m. The influence of $\frac{Dam_{f\_d}}{K_m}$ and $\frac{Dam_p}{K_m}$ are small as they could not be varied much for reactions close to first-order type.

The effectiveness factor is the ratio of local reaction rate to that which would be obtained if the enzyme or cells are at the interface. The reactor efficiency is the ratio of overall reaction rate to the maximum reaction rate based on the inlet

concentration. For Michaelis-Menten type reactions, the reactor efficiency reduces with $\frac{x \bullet Dam_f}{H}$ due to the lower reaction (or flux) because of the low concentration; furthermore the local effectiveness factor becomes lower. The effectiveness drops because the concentration in the porous medium is low which gives small Michaelis-Menten reaction. A larger Dam_p (smaller diffusion) also gives smaller reactor efficiency. For reactions close to first-order type, the reactor efficiency reduces with $\frac{x}{H}\frac{Dam_f}{K_m}$ because of the reduced reaction (or flux) due to low concentration. Although increased fluid convection (smaller $\frac{Dam_f}{K_m}$) does increase the efficiency, the effect is not large. There is no advantage in reducing $\frac{Dam_f}{K_m}$ below 0.02 because the effectiveness is poor due to the diffusion limitation in the fluid region.

The correlated plots could be applied in the design of microchannel reactors with porous walls. From the plots, the concentration in the porous medium could be predicted for a given reactor geometry. The critical length to avoid concentration insufficiency could also be determined. The flow and geometry conditions could be designed to achieve high reactor efficiency.

Table 7.1 List of parameter values for model predictions.

Type of Applications	Parameters		References
Perfusion Bioreactor (oxygen)		Assumed Values	
	L	100 *mm*	Zhao et al., 2005 and 2007; Pathi et al., 2005.
	H	6 *mm*	
	h	0.6 *mm*	
	C_{in}	$2.2 \times 10^{-7}\ mol/ml$	
	k_m	$1.1 \times 10^{-8}\ mol/ml$	
	D_{eff}	$1.59 \times 10^{-9}\ m^2/s$	
	D	$3.29 \times 10^{-9}\ m^2/s$	
	V_m	$1.25 \times 10^{-17}\ mol/cell/s$	
	γ	$5.40 \times 10^{5} \sim 3.60 \times 10^{7}\ cells/ml$	Zhao et al., 2005; Pathi et al., 2005.
		Computed Values	
	K_m	5.0×10^{-2}	
	Pe_f	15 ~225	
	Pe_p	$5.60 \times 10^{-7} \sim 8.40 \times 10^{-6}$	
	Dam_p	$6.94 \times 10^{-3} \sim 0.463$	
	Dam_f	$1.66 \times 10^{-4} \sim 0.111$	
Micro-Enzyme Reactor (glucose)		Assumed Values	
	L	11 *mm*	Drott et al., 1997 and 1999.
	H	$32.5\ \mu m$	
	h	$\leq 15\ \mu m$	
	C_{in}	0.5, 1.2, 5 $mmol/L$	
	k_m	3~10 $mmol/L$	
	D_{eff}	$5.4 \times 10^{-10}\ m^2/s$	Ye et al., 2006.
	D	$5.4 \times 10^{-10}\ m^2/s$	
	$V_m\ \gamma$ h	$\leq 3.05 \times 10^{-5}\ mol/m^2/s$	Drott et al., 1997 and 1999.
		Computed Values	
	K_m	0.6~20	
	Pe_f	3.24×10^{3}	
	Pe_p	3.53×10^{-9}	Lysenko et al., 2004.
	Dam_p	≤ 1.60	
	Dam_f	$\leq 6.1 \times 10^{-4}$	

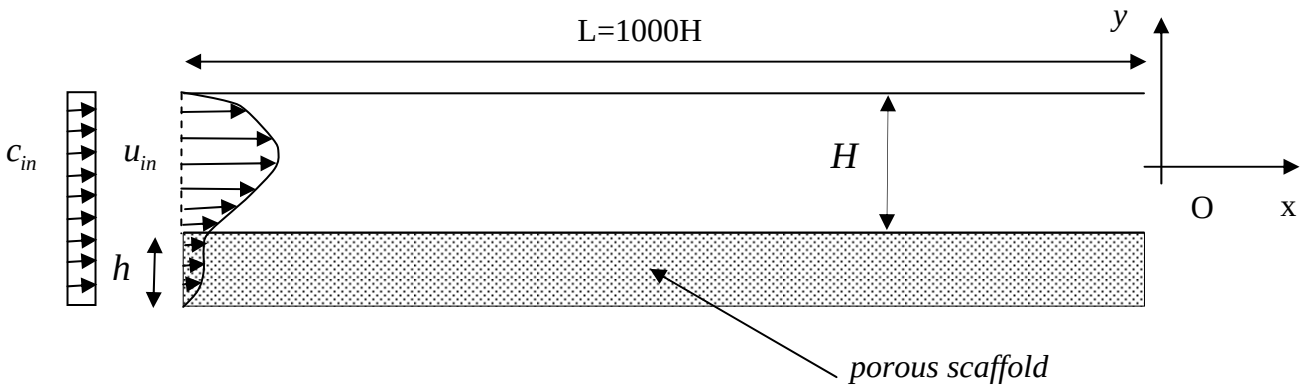

Figure 7.1 Schematic of the bioreactor model (not to scale).

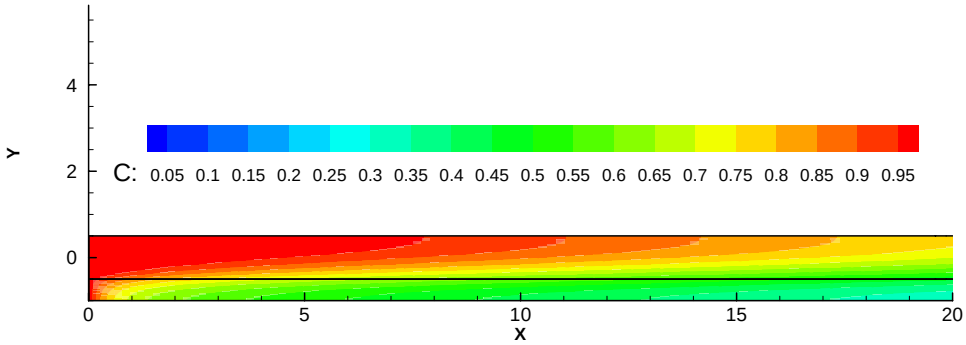

Figure 7.2 Contour of concentration field with Pe_p=0.25, Dam_p=0.5, Dam_f=0.025, h/H=0.5, K_m=0.260, $\varepsilon = 0.9$, $\beta = 0$ and $\beta_1 = 0$.

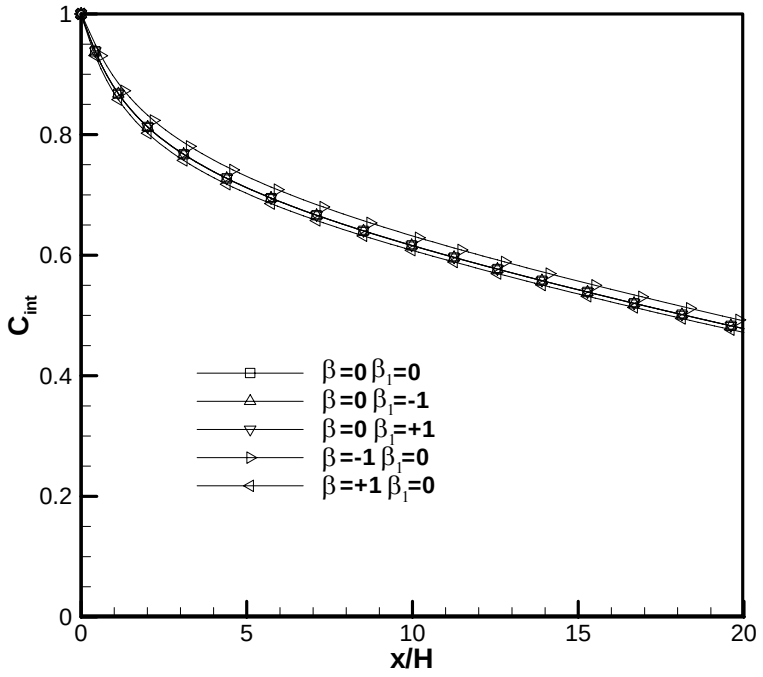
1
0.8
0.6
0.4
0.2
0
0
5
10
15
20
C_int
x/H
β=0 β_l=0
β=0 β_l=-1
β=0 β_l=+1
β=-1 β_l=0
β=+1 β_l=0

(a)

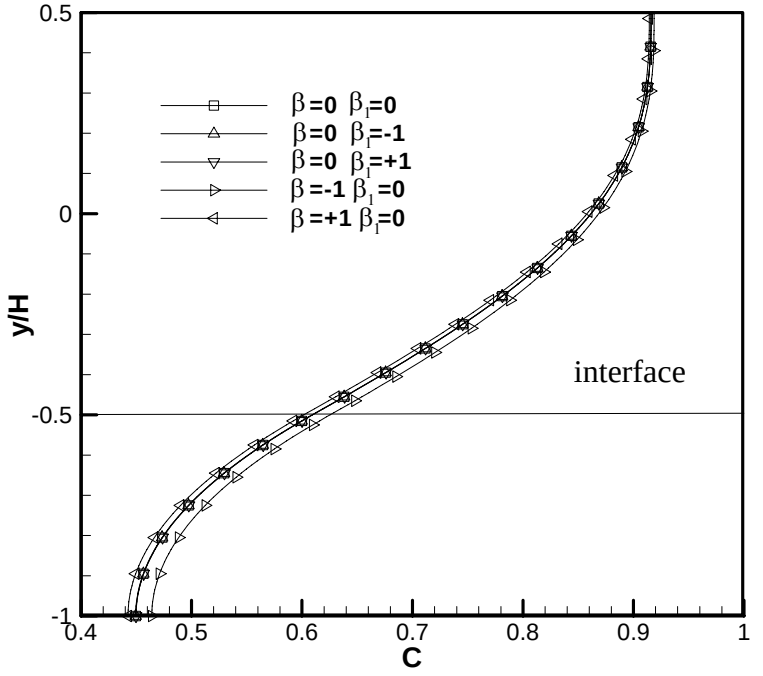
0.5
0
-0.5
-1
0.4
0.5
0.6
0.7
0.8
0.9
1
y/H
C
β=0 β_l=0
β=0 β_l=-1
β=0 β_l=+1
β=-1 β_l=0
β=+1 β_l=0
interface

(b)

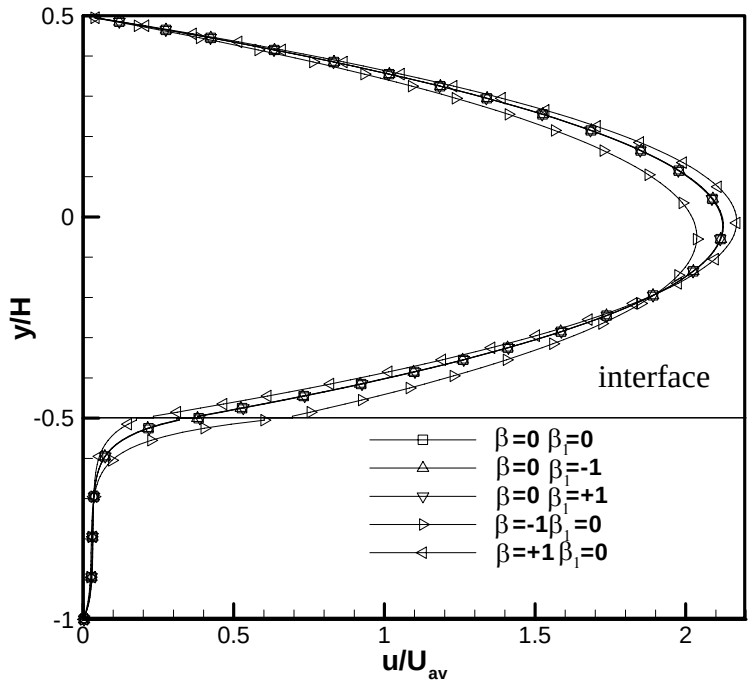

(c)

Figure 7.3 Effects of different stress jump coefficients; Pe_p =0.25, Dam_p =0.5, Dam_f =0.025, h/H=0.5, K_m =0.260, $\varepsilon = 0.9$, $\beta = 0$ and $\beta_1 = 0$:
(a) Concentration distribution along interface; (b) Concentration profiles normal to interface at x/H=10.0; (c) Velocity profiles.

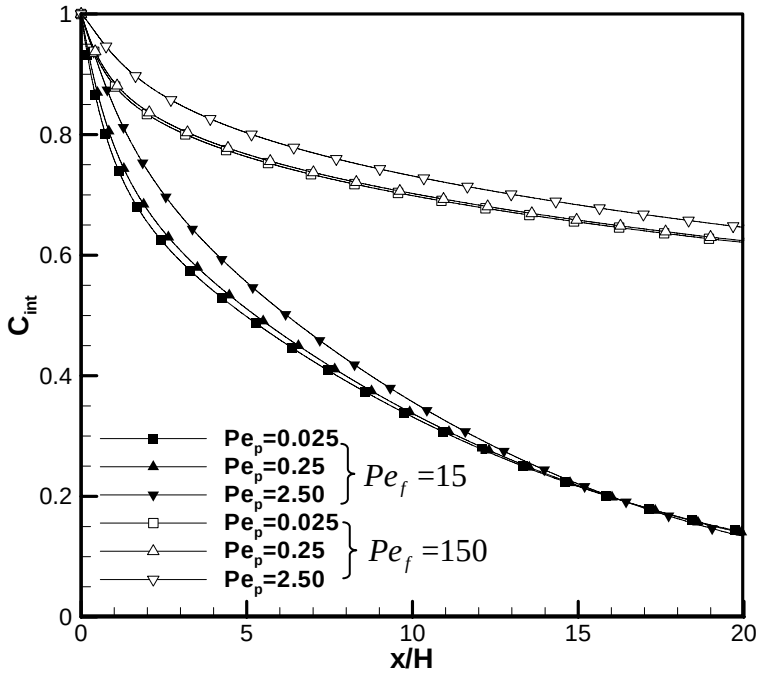
C_int
x/H
Pe_p=0.025
Pe_p=0.25
Pe_p=2.50
Pe_f =15
Pe_p=0.025
Pe_p=0.25
Pe_p=2.50
Pe_f =150

(a)

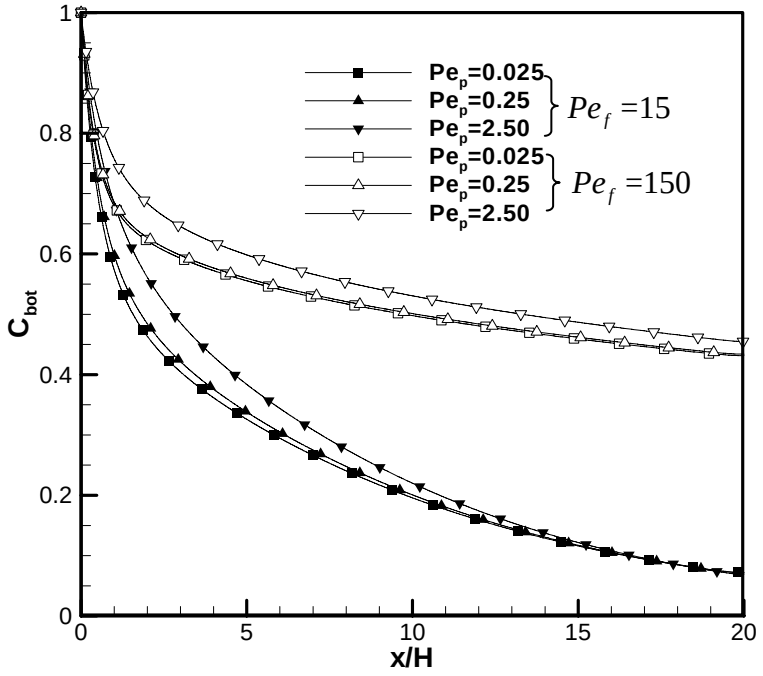
C_bot
x/H
Pe_p=0.025
Pe_p=0.25
Pe_p=2.50
Pe_f =15
Pe_p=0.025
Pe_p=0.25
Pe_p=2.50
Pe_f =150

(b)

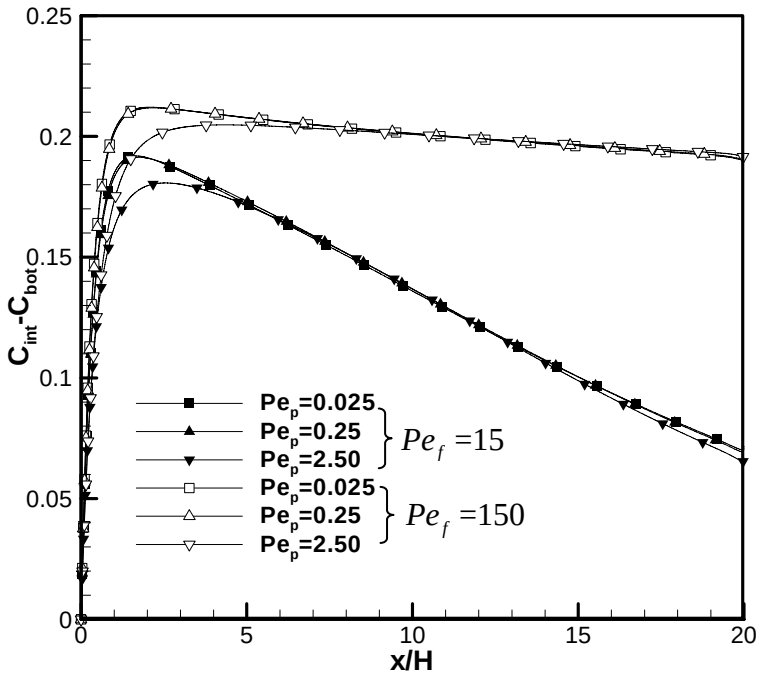

(c)

Figure 7.4 Effects of different Pe_p and Pe_f; Dam_p =0.6, h/H=0.5, K_m =0.260, $\varepsilon = 0.9$, $\beta = 0$ and $\beta_1 = 0$: (a) Interface line concentration; (b) Bottom line concentration; (c) Concentration difference.

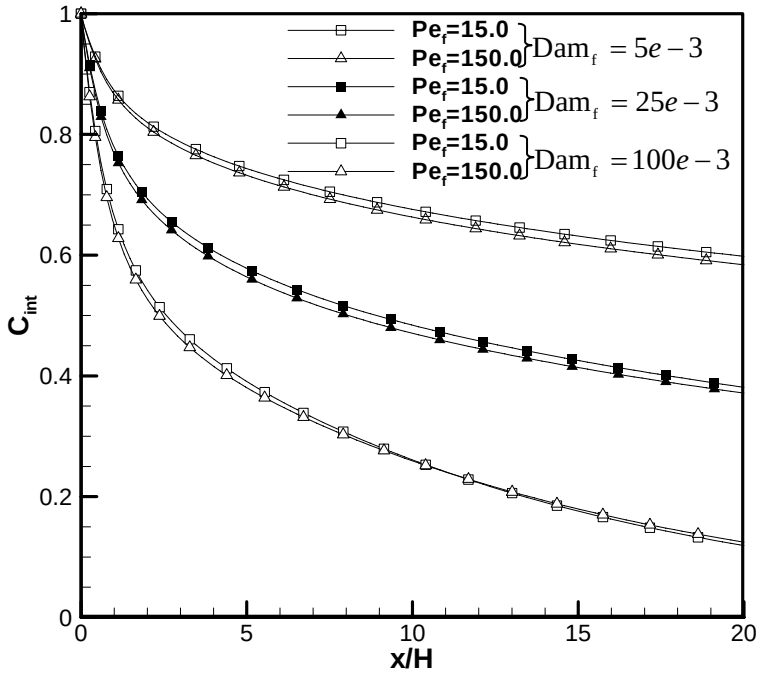
Pe_f=15.0
Pe_f=150.0
Dam_f = 5e−3
Pe_f=15.0
Pe_f=150.0
Dam_f = 25e−3
Pe_f=15.0
Pe_f=150.0
Dam_f = 100e−3
C_int
x/H
0
0.2
0.4
0.6
0.8
1
0
5
10
15
20

(a)

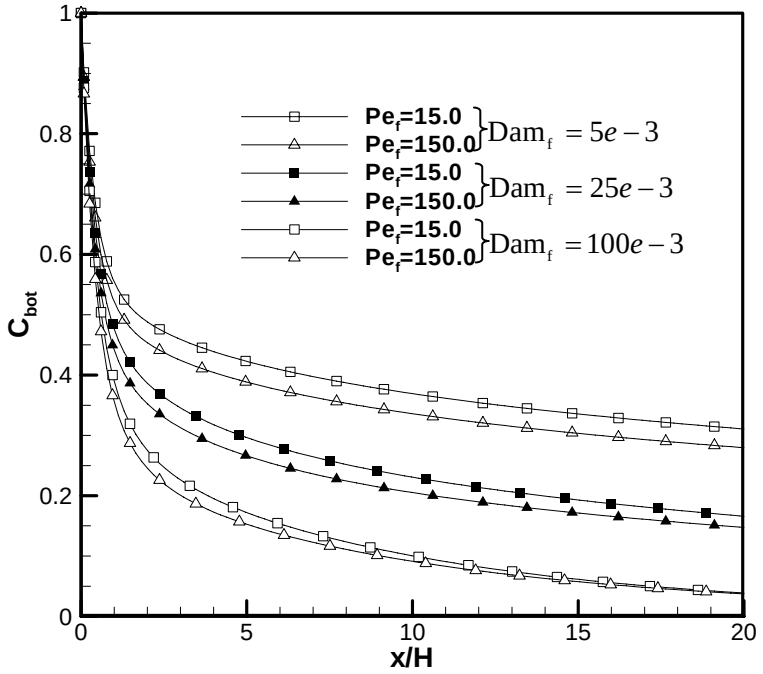
Pe_f=15.0
Pe_f=150.0
Dam_f = 5e−3
Pe_f=15.0
Pe_f=150.0
Dam_f = 25e−3
Pe_f=15.0
Pe_f=150.0
Dam_f = 100e−3
C_bot
x/H
0
0.2
0.4
0.6
0.8
1
0
5
10
15
20

(b)

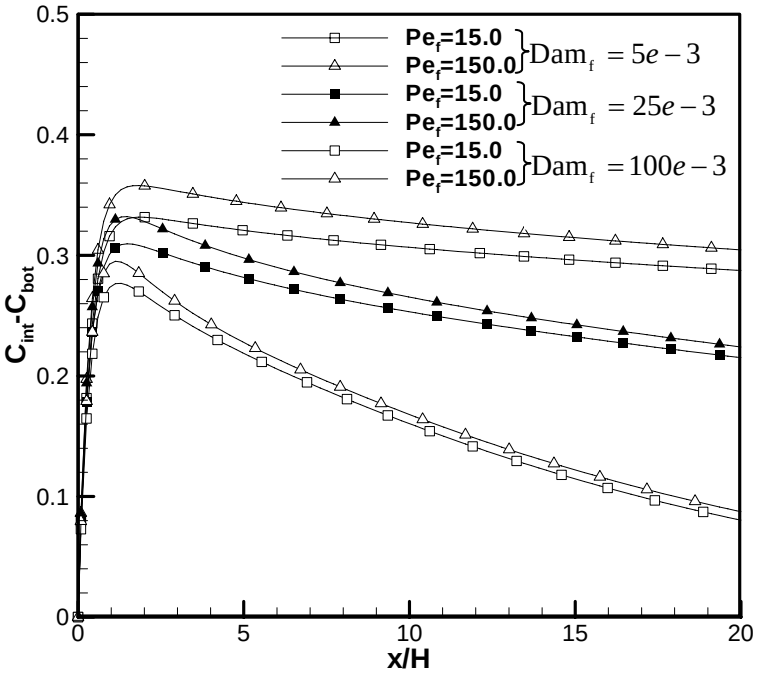

(c)

Figure 7.5 Effects of different Dam_f and Pe_f ; Dam_p =1.0, K_m =0.260, h/H=0.5, $\varepsilon = 0.9$, $\beta = 0$ and $\beta_1 = 0$: (a) Interface line concentration; (b) Bottom line concentration; (c) Concentration difference.

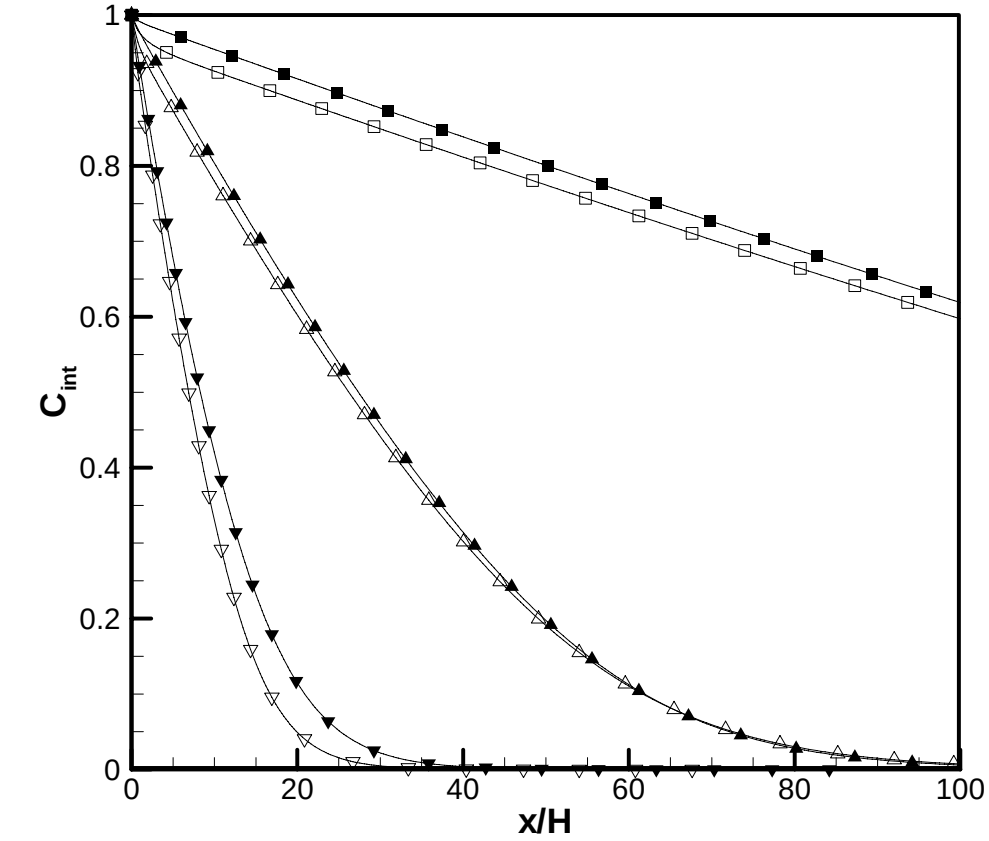

Figure 7.6a

Figure 7.6 Effects of different $\frac{Dam_p}{K_m}$ and $\frac{Dam_f}{K_m}$ for low reaction rate; h/H=0.5, $\varepsilon = 0.9$, $\beta = 0$ and $\beta_1 = 0$:

(a) Interface line concentration; (b) Bottom line concentration; (c) Concentration difference.

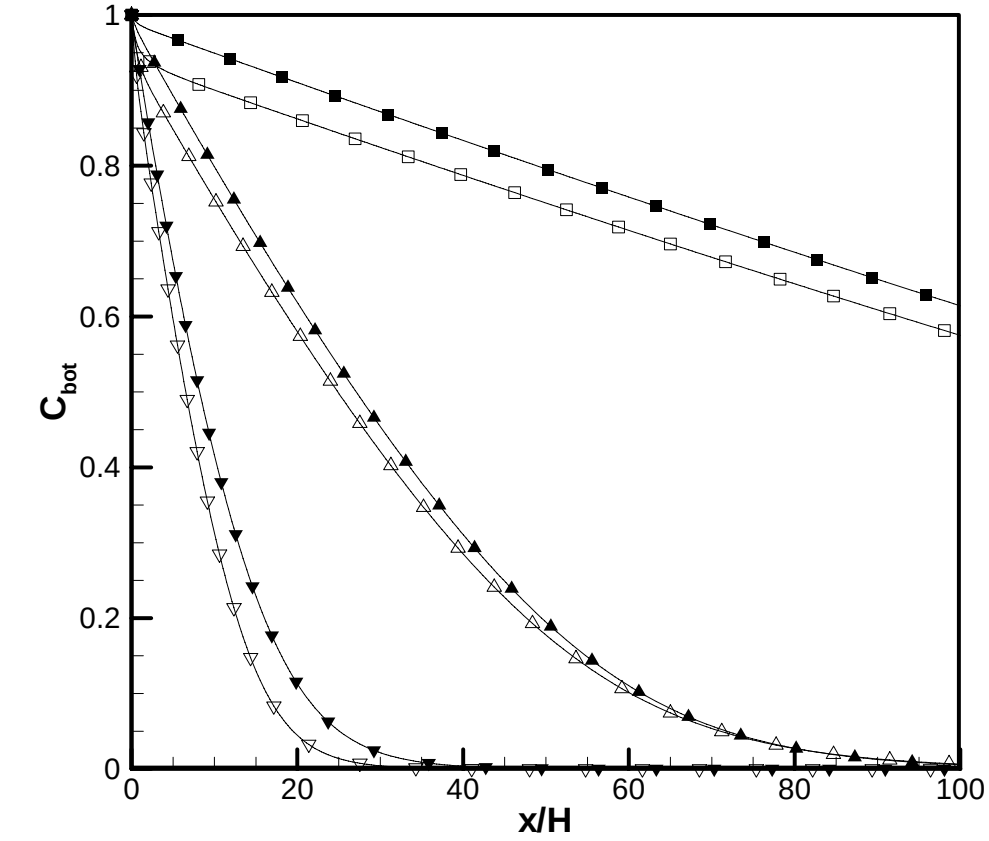

Figure 7.6b

Figure 7.6 Effects of different $\frac{Dam_p}{K_m}$ and $\frac{Dam_f}{K_m}$ for low reaction rate; h/H=0.5, $\varepsilon = 0.9$, $\beta = 0$ and $\beta_1 = 0$:
(a) Interface line concentration; (b) Bottom line concentration; (c) Concentration difference.

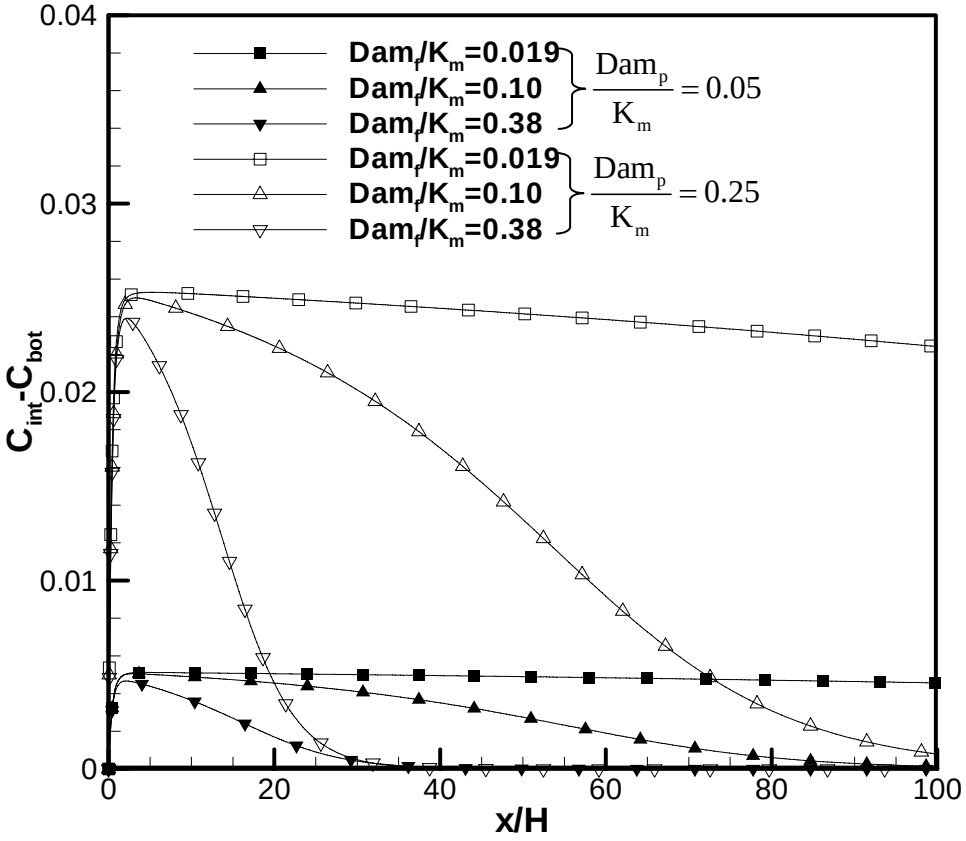

Figure 7.6c

Figure 7.6 Effects of different $\frac{Dam_p}{K_m}$ and $\frac{Dam_f}{K_m}$ for low reaction rate; h/H=0.5, $\varepsilon = 0.9$, $\beta = 0$ and $\beta_1 = 0$:
(a) Interface line concentration; (b) Bottom line concentration; (c) Concentration difference.

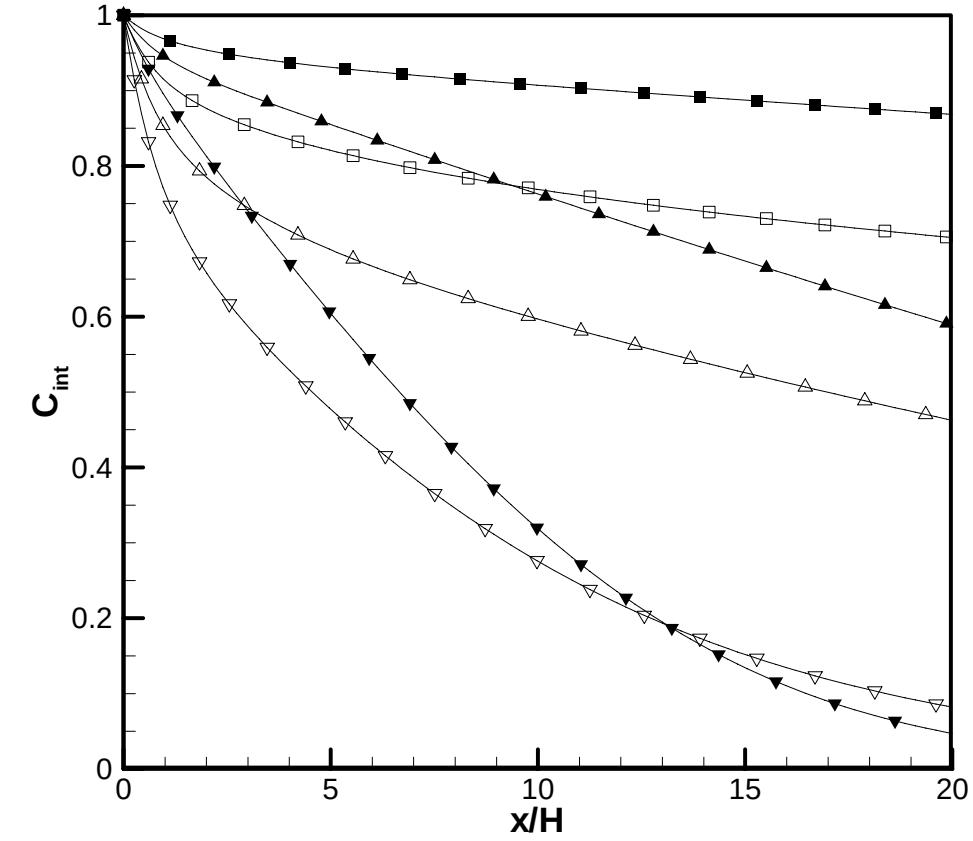

Figure 7.7a

Figure 7.7 Effects of different Dam_p and Dam_f for middle and high reaction rate; K_m =0.260, h/H=0.5, $\varepsilon = 0.9$, $\beta = 0$ and $\beta_1 = 0$:
(a) Interface line concentration; (b) Bottom line concentration; (c) Concentration difference.

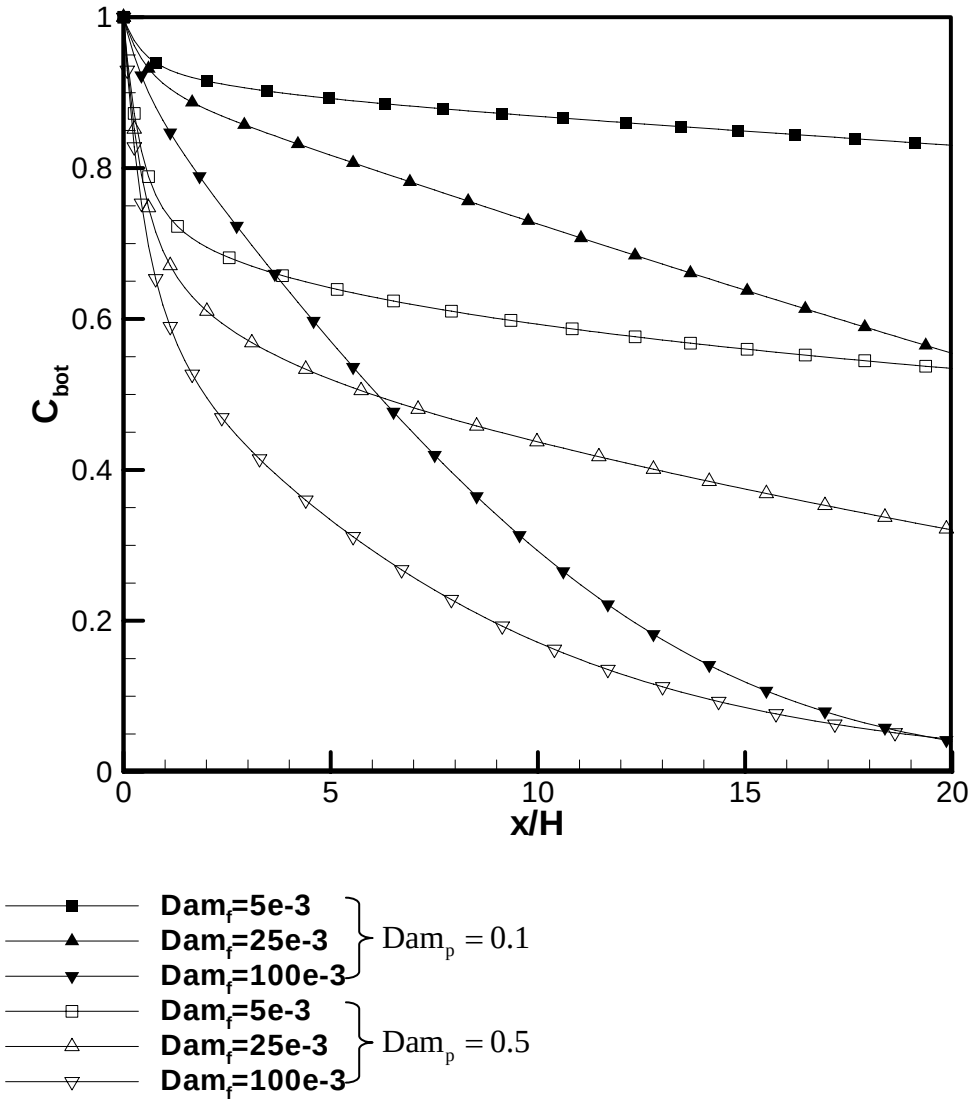

Figure 7.7b

Figure 7.7 Effects of different Dam_p and Dam_f for middle and high reaction rate; K_m=0.260, h/H=0.5, $\varepsilon = 0.9$, $\beta = 0$ and $\beta_1 = 0$:
(a) Interface line concentration; (b) Bottom line concentration; (c) Concentration difference.

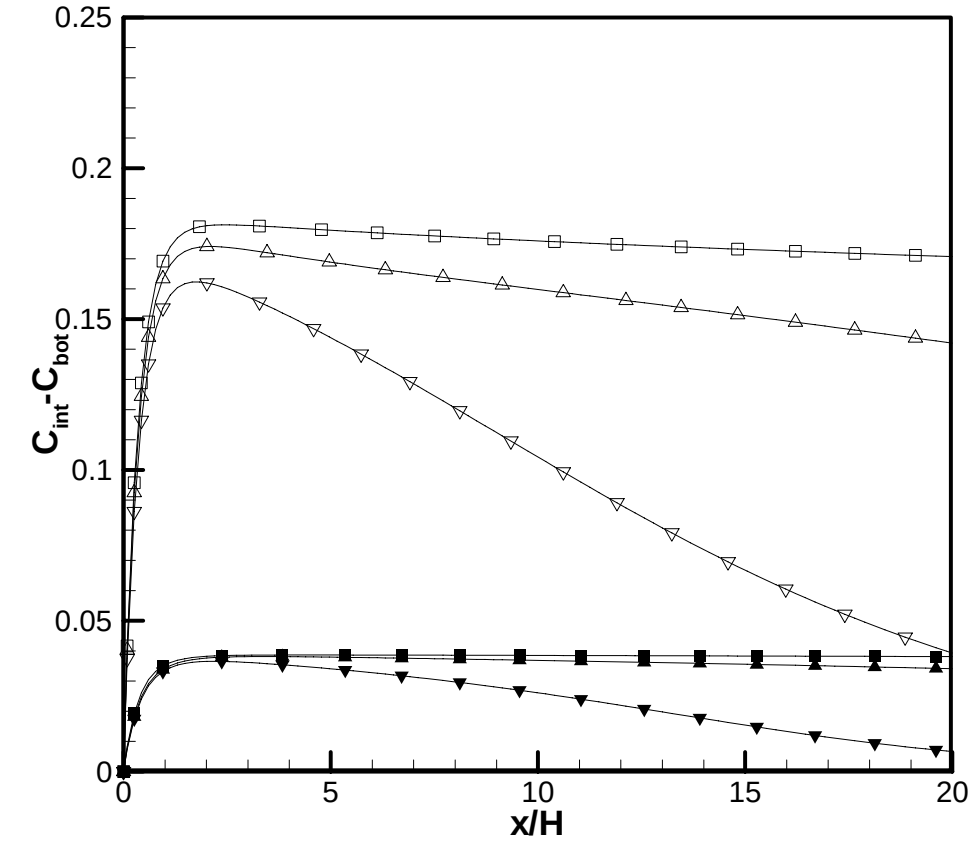

Figure 7.7c

Figure 7.7 Effects of different Dam_p and Dam_f for middle and high reaction rate; K_m =0.260, h/H=0.5, $\varepsilon = 0.9$, $\beta = 0$ and $\beta_1 = 0$:
(a) Interface line concentration; (b) Bottom line concentration; (c) Concentration difference.

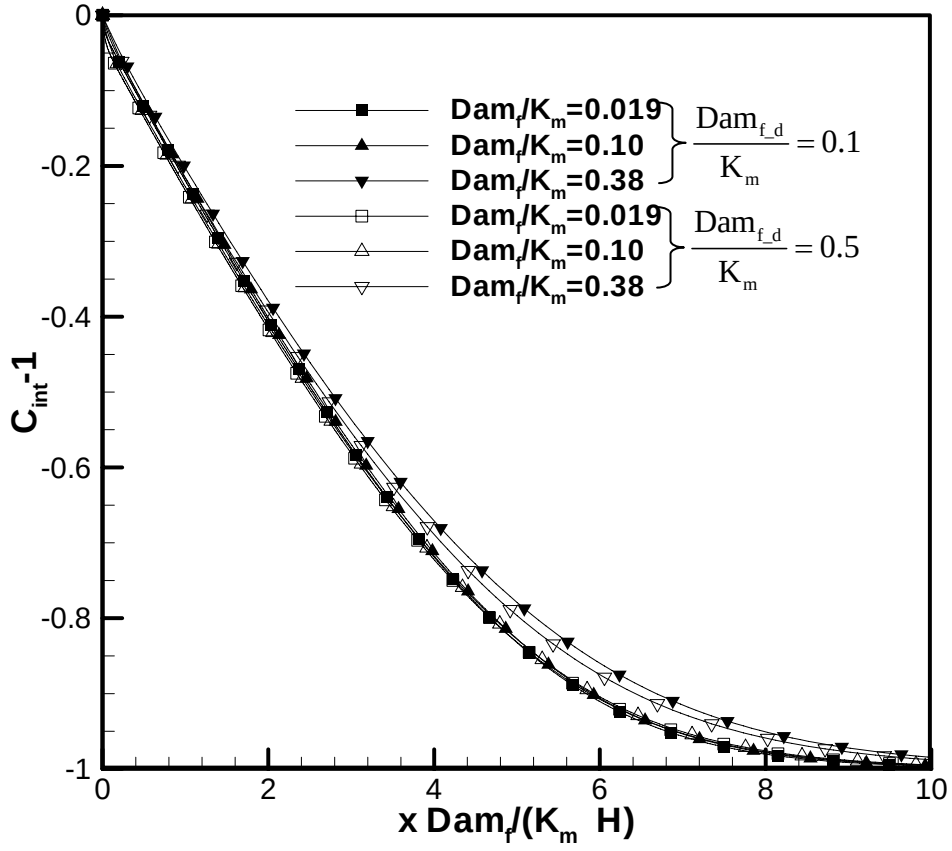

Figure 7.8 Concentration at the interface as a function of reaction-convection distance parameter with different $\frac{Dam_f}{K_m}$ and $\frac{Dam_{f\_d}}{K_m}$ for first-order reaction; $\varepsilon = 0.9$, $\beta = 0$ and $\beta_1 = 0$.

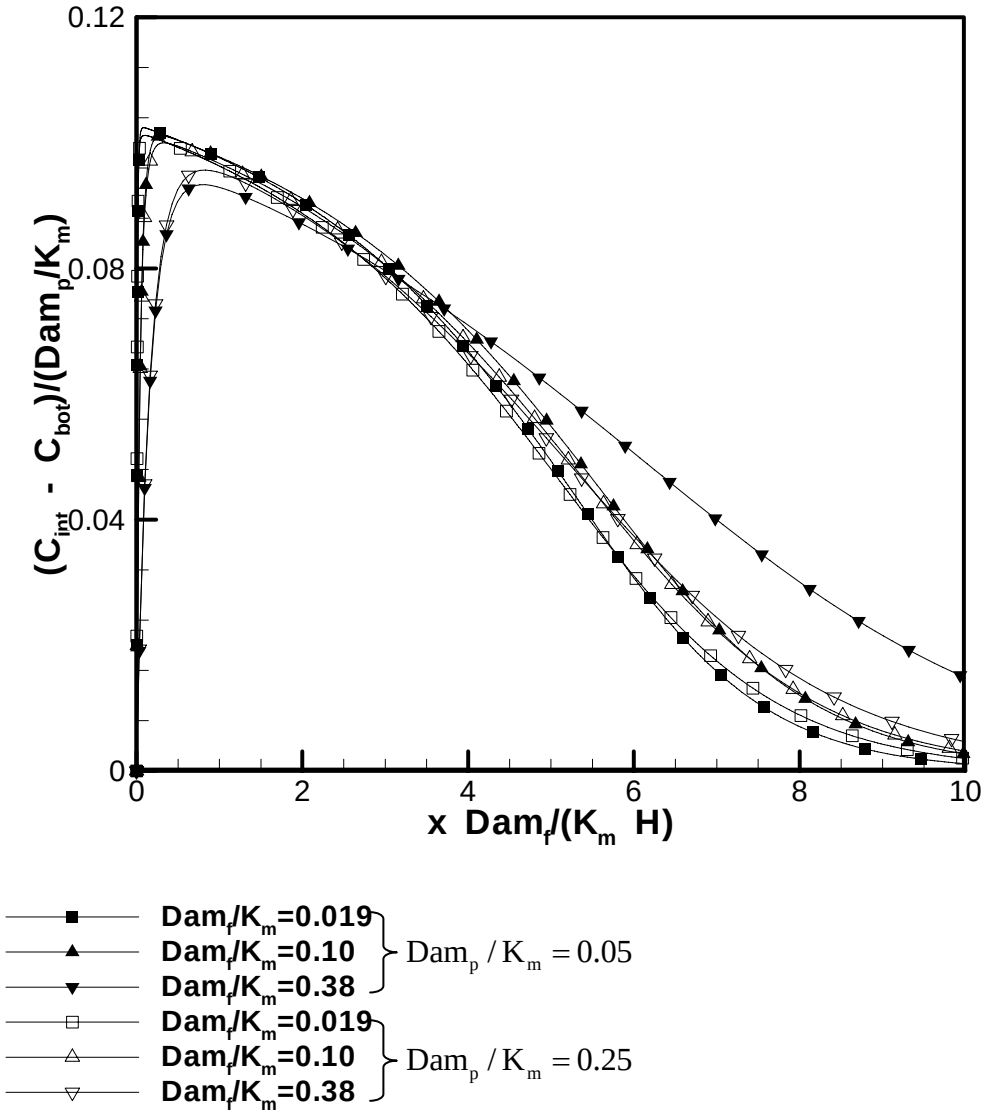

Figure 7.9 Concentration difference parameter as a function of reaction-convection distance parameter with different $\frac{Dam_f}{K_m}$ and $\frac{Dam_p}{K_m}$ for first-order reaction; $\varepsilon = 0.9$, $\beta = 0$ and $\beta_1 = 0$.

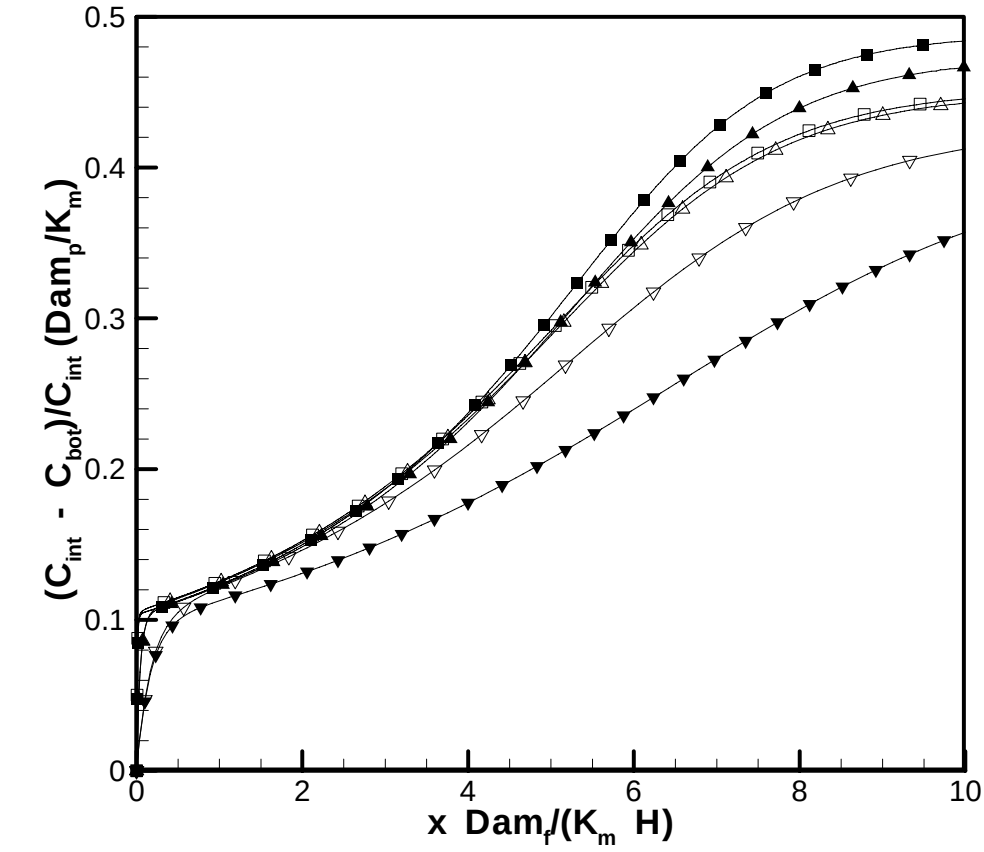

Figure 7.10 Reaction effectiveness factor as a function of reaction-convection distance parameter with different $\frac{Dam_f}{K_m}$ and $\frac{Dam_p}{K_m}$ for first-order reaction; $\varepsilon = 0.9$, $\beta = 0$ and $\beta_1 = 0$.

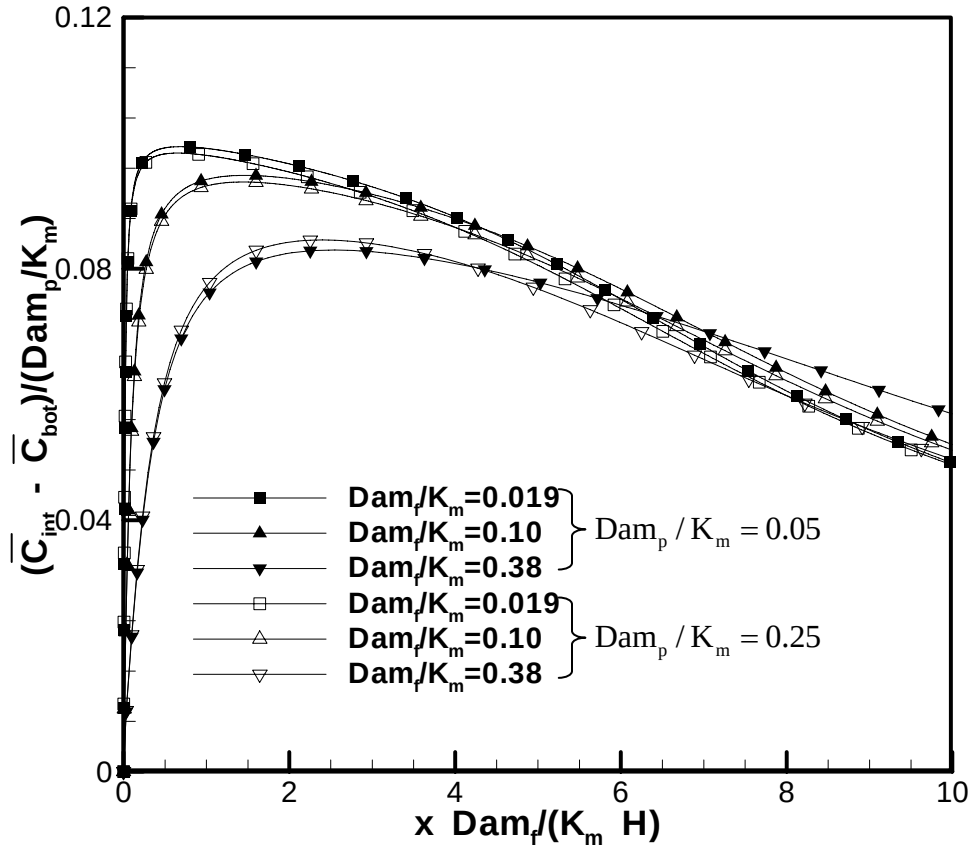

Figure 7.11 Reactor efficiency as a function of reaction-convection distance parameter with different $\frac{Dam_f}{K_m}$ and $\frac{Dam_p}{K_m}$ for first-order reaction; $\varepsilon = 0.9$, $\beta = 0$ and $\beta_1 = 0$.

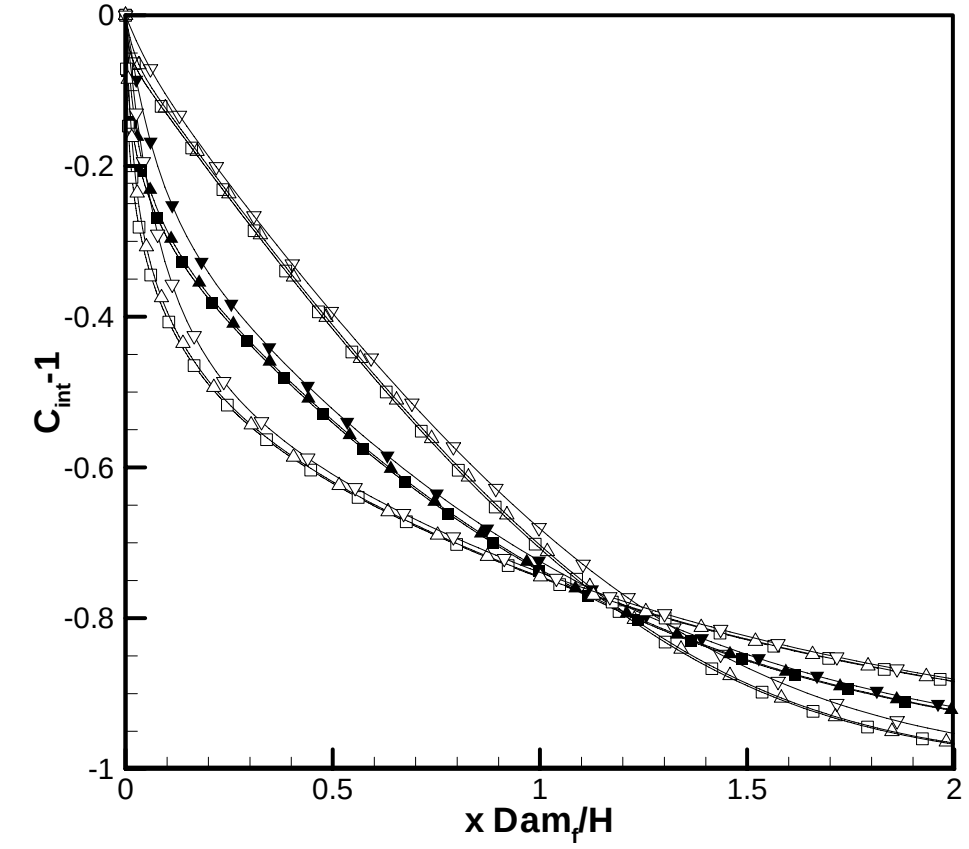

Figure 7.12a

Figure 7.12 Concentration at the interface as a function of reaction-convection distance parameter with different Dam_f for Michaelis-Menten reaction; $\varepsilon = 0.9$, $\beta = 0$ and $\beta_1 = 0$:
(a) At different Dam_{f_d}; (b) At different K_m.

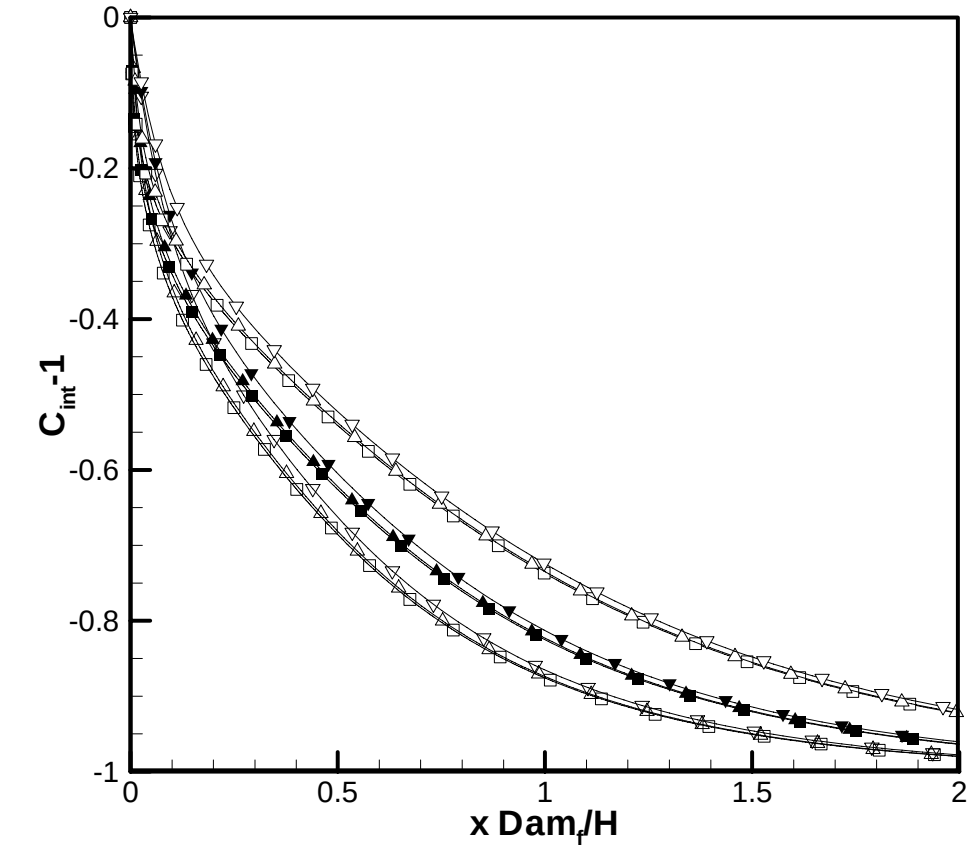

Figure 7.12b

Figure 7.12 Concentration at the interface as a function of reaction-convection distance parameter with different Dam_f for Michaelis-Menten reaction; $\varepsilon = 0.9$, $\beta = 0$ and $\beta_1 = 0$:
(a) At different Dam_{f_d}; (b) At different K_m.

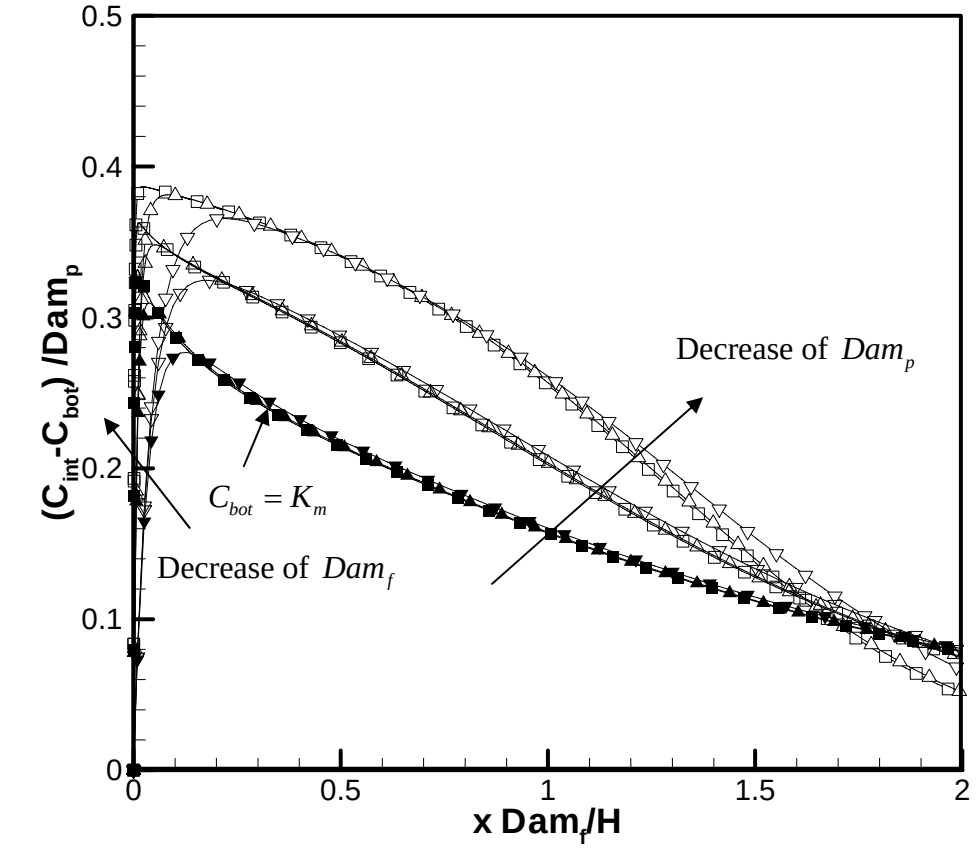

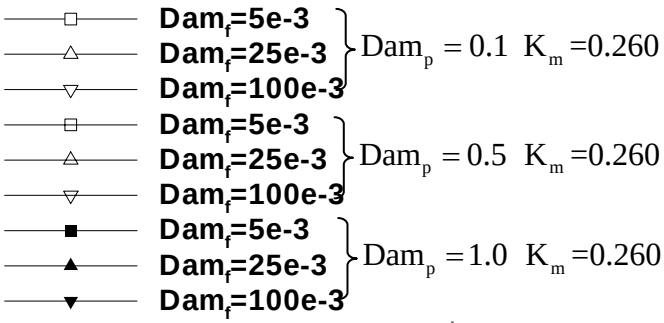

Figure 7.13a

Figure 7.13 Concentration difference parameter as a function of reaction-convection distance parameter with different Dam_f for Michaelis-Menten reaction; $\varepsilon = 0.9$, $\beta = 0$ and $\beta_1 = 0$:

(a) At different Dam_p; (b) At different K_m.

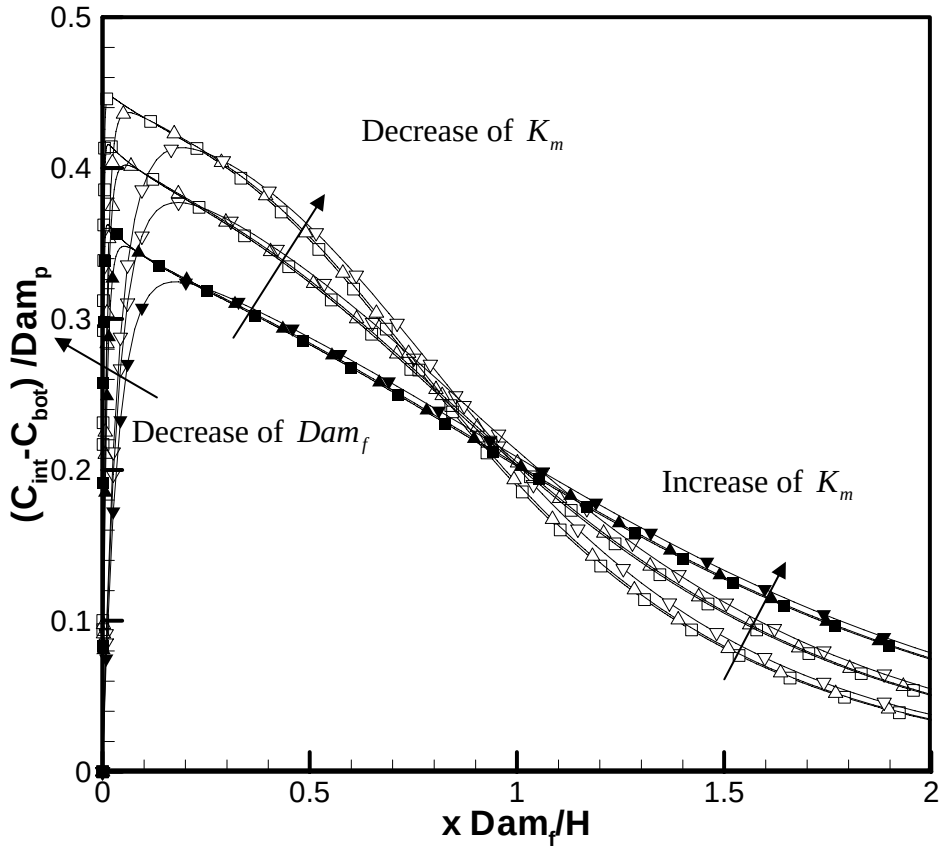

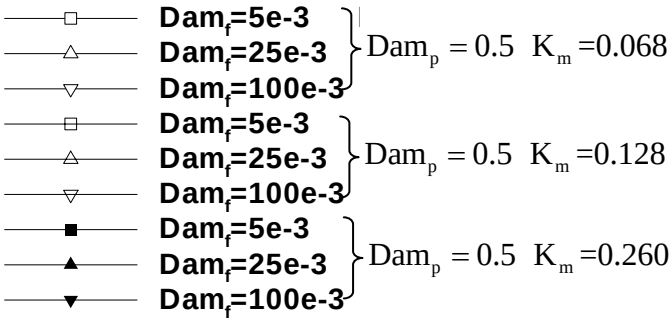

Figure 7.13b

Figure 7.13 Concentration difference parameter as a function of reaction-convection distance parameter with different Dam_f for Michaelis-Menten reaction; $\varepsilon = 0.9$, $\beta = 0$ and $\beta_1 = 0$:
(a) At different Dam_p; (b) At different K_m.

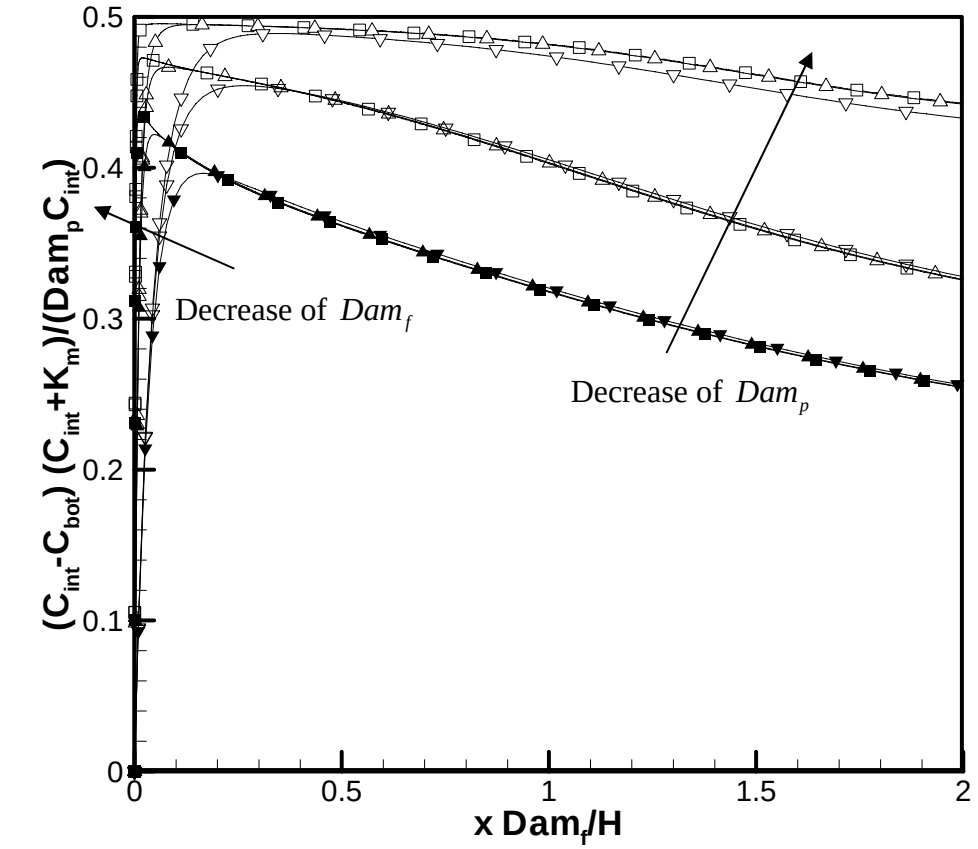

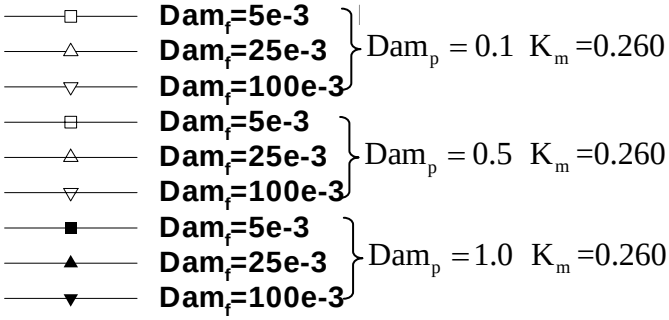

Figure 7.14a

Figure 7.14 Reaction effectiveness factor as a function of reaction-convection distance parameter with different Dam_f for Michaelis-Menten reaction; $\varepsilon = 0.9$, $\beta = 0$ and $\beta_1 = 0$:

(a) At different Dam_p; (b) At different K_m.

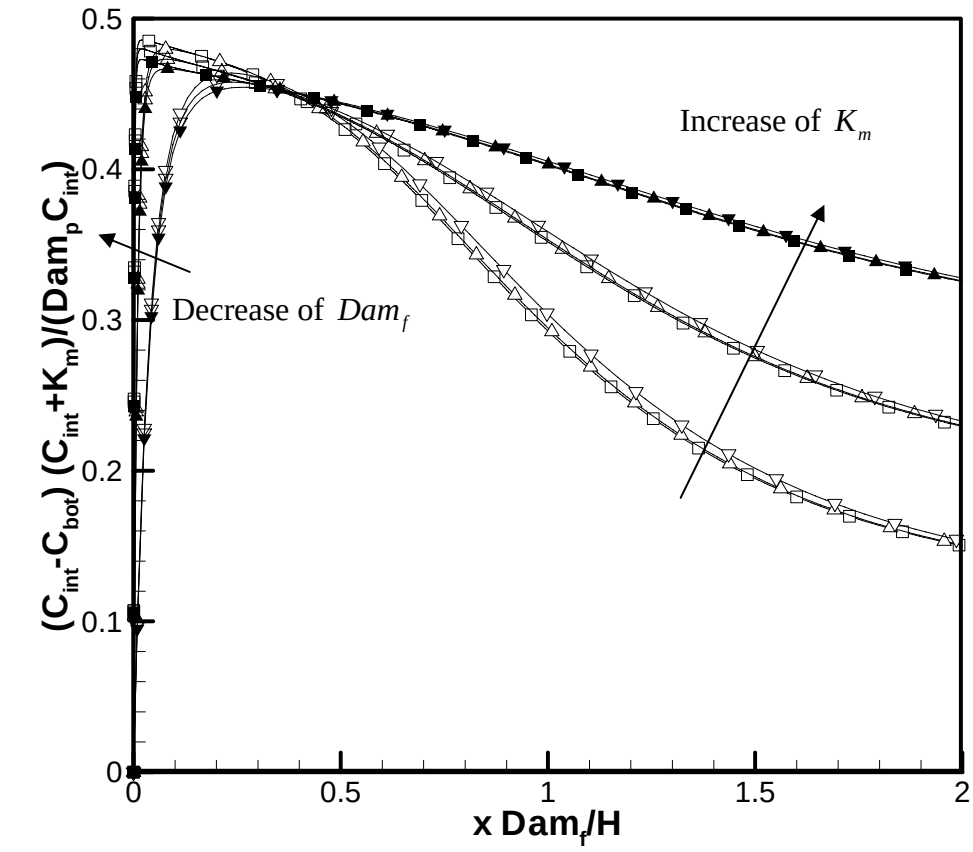

Dam_f=5e-3
Dam_f=25e-3 } $Dam_p = 0.5$ K_m =0.068
Dam_f=100e-3

Dam_f=5e-3
Dam_f=25e-3 } $Dam_p = 0.5$ K_m =0.128
Dam_f=100e-3

Dam_f=5e-3
Dam_f=25e-3 } $Dam_p = 0.5$ K_m =0.260
Dam_f=100e-3

Figure 7.14b

Figure 7.14 Reaction effectiveness factor as a function of reaction-convection distance parameter with different Dam_f for Michaelis-Menten reaction; $\varepsilon = 0.9$, $\beta = 0$ and $\beta_1 = 0$:
(a) At different Dam_p; (b) At different K_m.

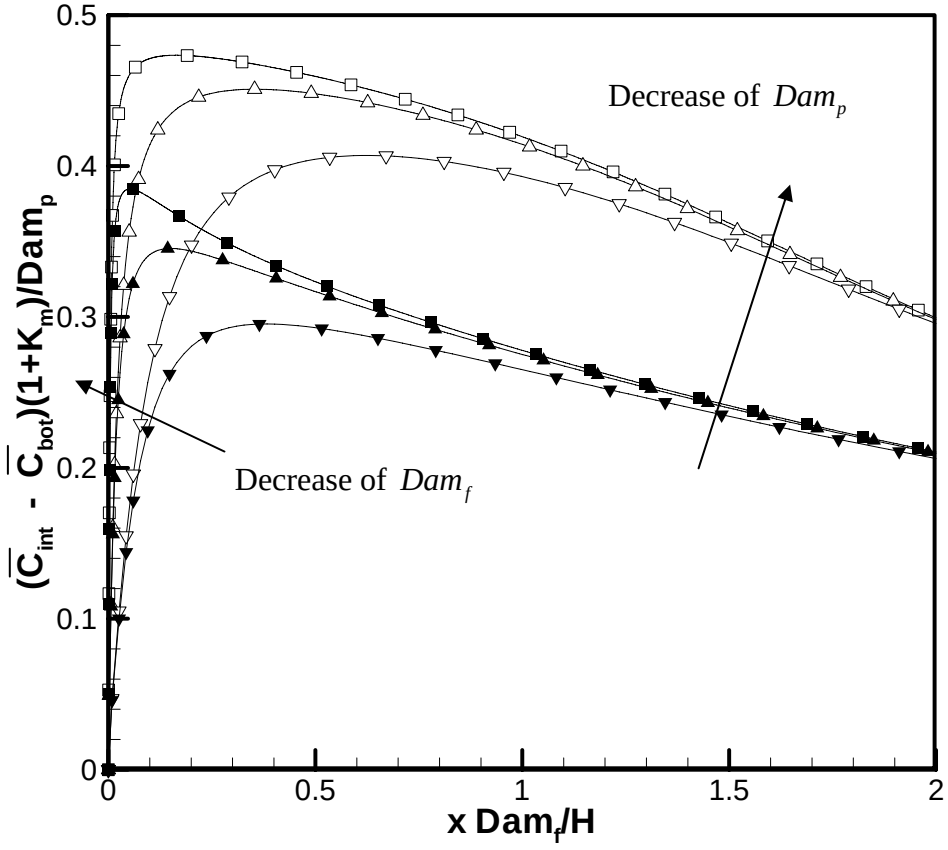

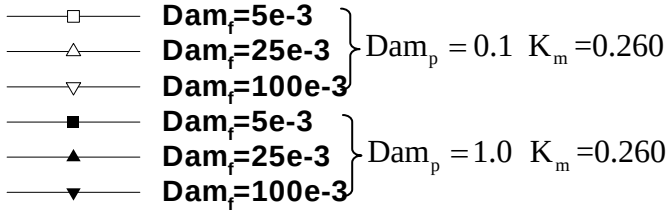

Figure 7.15a

Figure 7.15 Reactor efficiency as a function of reaction-convection distance parameter with different Dam_f for Michaelis-Menten reaction; $\varepsilon = 0.9$, $\beta = 0$ and $\beta_1 = 0$:

(a) At different Dam_p; (b) At different K_m.

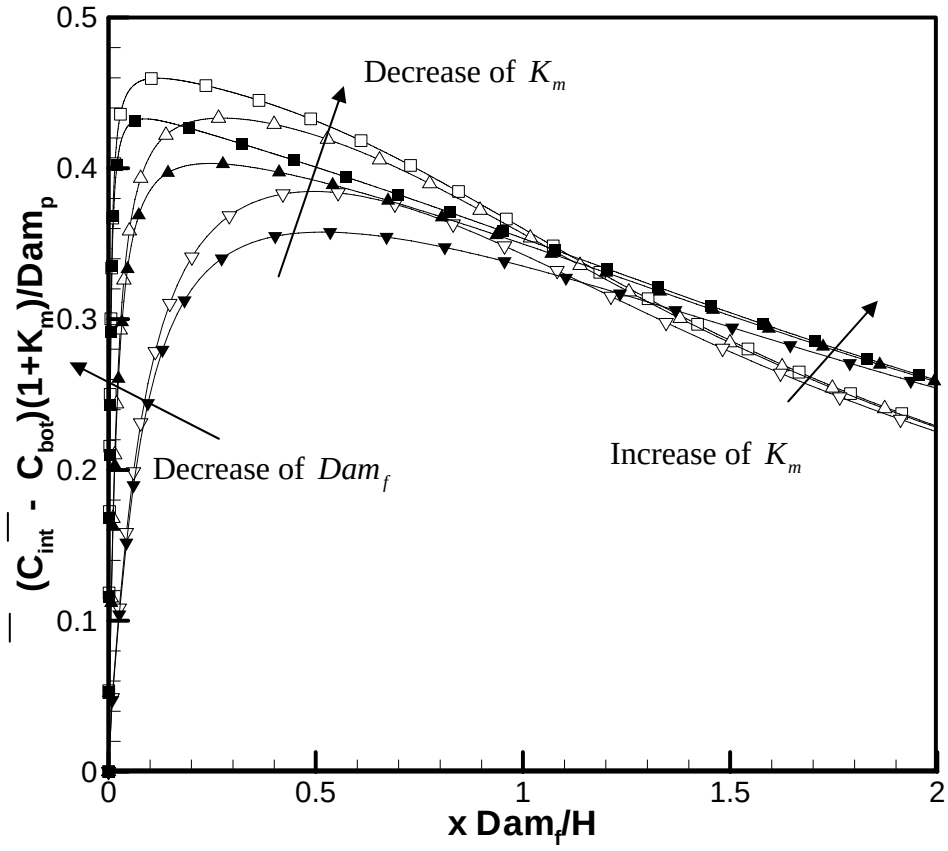

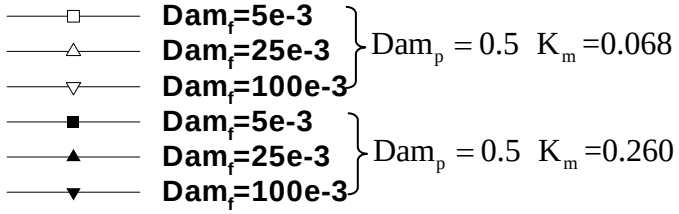

Figure 7.15b

Figure 7.15 Reactor efficiency as a function of reaction-convection distance parameter with different Dam_f for Michaelis-Menten reaction; $\varepsilon = 0.9$, $\beta = 0$ and $\beta_1 = 0$:

(a) At different Dam_p; (b) At different K_m.

Chapter 8

Conclusions and Recommendations

8.1 Conclusions

The main objective of current research was to develop and implement a numerical method for transport phenomena in porous media and porous/fluid coupled domains with complex geometries. For the interface between porous and homogeneous fluid domains, the Ochoa-Tapia and Whitaker's stress jump interfacial condition (1998b) was used to investigate its effects on heat and mass transfer. The current study also considered porous media effects on the flow pattern, heat and mass transfer in such porous/fluid coupled domains.

A two-domain method was implemented for more realistic and reasonable treatments on local velocity, stress, temperature and mass at the porous/fluid interface. It was based on finite volume method together with body-fitted grids and multi-block technology. For the homogeneous fluid region, the governing equation was Navier-Stokes equation; and for the porous medium region, the generalized Darcy-Brinkman-Forchheimer extended model was used. At the interface between porous and homogeneous fluid domains, the flow boundary conditions imposed was a shear stress jump, which included both viscous and inertial effects, together with a continuity of normal stress. The thermal or mass interfacial boundary conditions were continuities of temperature and heat flux, or mass and mass flux. Such thermal and

mass interfacial conditions have not been combined with stress jump condition in previous studies.

The developed numerical technique was applied to several cases in heat and mass transfer: a) unsteady external flows past a porous square or trapezoidal cylinder, b) natural convective heat-transfer in a porous wavy cavity, c) forced convective heat-transfer after a backward facing step with a porous insert or with a porous floor segment, d) mass transfer in a microchannel reactor with a porous wall. The implementations of the numerical technique are different from those of previous studies which were mainly based on one-domain method with either Darcy's law or Brinkman's equations for the porous medium.

The present work contributes a numerical implementation that can deal with general transport problems in porous and homogeneous fluid domains. The developed numerical technique is able to incorporate different flow-thermal or flow-mass boundary conditions at the porous-fluid interface, and can address problems in which the flow and thermal or mass interfacial conditions need to be considered in detail. The technique is suitable for more complex geometries as it implements body fitted grids and multi-block approach.

8.1.1 Unsteady External Flows past a Porous Square or Trapezoidal Cylinder

Different from flows past solid bodies, the flow penetrated into the porous bodies and resulting flow is steady or unsteady flow depending on both the Reynolds

number and Darcy number. With a larger Darcy number, the Reynolds number has to be higher before the vortex shedding phenomena occurs. The Darcy number effect becomes smaller when $Da \le 10^{-4}$; and the fluctuation-amplitude of drag coefficient decreases with a larger Darcy number. Generally, a larger porosity cylinder results in smaller drag coefficient and lift amplitude.

The effects of the stress jump parameters are given for the flow condition from *Re* = 20 to 200. The first coefficient β has a more noticeable effect whereas the second coefficient β_1 has small effect, even for *Re* = 200. It was interesting to find that stress jump parameters affected flow pattern, for example, unsteady flow phenomena when *Re* = 40 with $\beta = 1$ and $\beta_1 = 0$ for porous square case, while for trapezoidal one, there was no such phenomenon. The stress jump parameters could also play an important role for the flow pattern past porous bodies, depending on the body shapes.

8.1.2 Natural Convective Heat-transfer in a Porous Wavy Cavity

Natural convection in a porous wavy cavity was studied using the generalized Brinkman-Forcheimmer extended model. Different from previous studies using Darcy's law (Misirlioglu, et al, 2005), the isotherms and streamlines show interesting phenomena, e.g., multi-cellular circulations to single-cellular circulation. This is due to the shortcomings of Darcy's law; for example, it neglects inertia, convection, and

viscous effects, while the generalized Brinkman-Forcheimmer extended model can depict the porous flow better.

Thus the results are shown with a wider range of Rayleigh and Darcy numbers than those of previous studies. At low Darcy-Rayleigh number another recirculation zone may appear at both the top and bottom regions, which are additional to the main recirculation at the middle. At large Darcy-Rayleigh number, the top and bottom recirculations vanished and the middle recirculation was distorted into two. The results of local Nusselt number show that the dependence on Darcy number and porosity is not small if the Darcy-Rayleigh number is large. For the wavy geometry effect, slightly negative Nusselt numbers were found with small aspect ratio and large waviness values. This indicated negative temperature gradient there, which was mainly due to local large inertia effect. This showed that the inertial effect played an important role at large Rayleigh numbers or waviness values.

8.1.3 Forced Convective Heat-transfer after a Backward Facing Step with a Porous Insert or a Porous Floor Segment

Forced convections after the backward facing step with the addition of a porous insert or with a porous floor segment were simulated. The heat transfer was enhanced globally with a porous insert or enhanced locally with a porous floor segment. For those with a porous insert, to minimize frictional losses and to attain heat enhancement, a medium length of insert with medium Darcy number, and larger Reynolds number was preferred. With the addition of a porous insert, the circulation

after the step was eliminated, which increased heat convection there. Increasing Reynolds number meant increasing the convection effect, while further decreasing the Darcy number to 10^{-5} did not increase the convection after the step due to the high resistance provided by the insert. For those cases with a porous floor segment, heat transfer was enhanced locally after the porous segment while the flow attachment point was located around the end of the segment. With the addition of a porous floor segment, the circulation after the step was elongated, which helped more flow to entrain back for heat convection there.

The stress jump parameter effects on the global and local Nusslet number were more noticeable for the flow along porous/fluid interface in the porous floor segment case, due to the sensitive change in local velocity and temperature profiles with different combinations of stress jump parameters. Generally the first stress jump parameter has much more effect if the Darcy number is small; the second stress jump parameter effect can not be neglected for parallel flow.

8.1.4 Mass Transfer in a Microchannel Reactor with a Porous Wall

The flow and mass transfer in a microchannel reactor with a porous wall was numerically investigated. Two parameters are defined to characterize the mass transports in the fluid and porous regions. The porous Damkohler number Dam_p is the ratio of consumption to diffusion of the substrates in the porous medium. The fluid Damkohler number Dam_f is the ratio of substrate consumption in the porous

medium to substrate convection in the fluid region. It is shown that the apparent effect of the conventionally used fluid Peclet number Pe_f is actually due to the change of Dam_f. As the consumption is considered over an axial distance, and Dam_f relates to consumption per unit length, the combined parameter $\frac{x \bullet Dam_f}{H}$ is defined from a simplified analysis for Michaelis-Menten reaction. Another parameter is the fluid-diffusion Damkohler number Dam_{f_d} which is the ratio of substrate consumption in the porous medium and substrate diffusion in the fluid region. The concentration difference between the interface and base of the porous medium are normalized to form a concentration difference parameter $\frac{C_{\text{int}} - C_{bot}}{Dam_p}$. The numerical results are found to be well correlated by the use of these parameters.

The interface concentration C_{int} is found to be a function of the reaction-convection distance parameter $\frac{x \bullet Dam_f}{H}$ and the fluid-diffusion Damkohler number Dam_{f_d} whose influence is relatively smaller at $\frac{x \bullet Dam_f}{H}$ >1. The concentration difference parameter $\frac{C_{\text{int}} - C_{bot}}{Dam_p}$ is not completely normalized by Dam_p which is based on various maximum values of the Michaelis–Menten reactions. For reactions close to first-order type, similar parameters are involved except all the Damkohler numbers are divided by the Michaelis-Menten constant K_m.

The influence of $\frac{Dam_{f\_d}}{K_m}$ and $\frac{Dam_p}{K_m}$ are small as these could not be varied much for reactions close to first-order type.

The reaction effectiveness factor and reactor efficiency for both of the above two reaction types are presented with the use of the combined parameters. For Michaelis-Menten type reactions, the reactor efficiency reduces with $\frac{x \bullet Dam_f}{H}$ due to the lower reaction (or flux) because of the low concentration; furthermore the local effectiveness factor becomes lower. The effectiveness drops because the concentration in the porous medium is low which gives small Michaelis- Menten reaction. A larger Dam_p (smaller diffusion) also gives smaller reactor efficiency. For reactions close to first-order type, the reactor efficiency reduces with $\frac{x}{H}\frac{Dam_f}{K_m}$ because of the reduced reaction (or flux) due to low concentration. Although increased fluid convection (smaller $\frac{Dam_f}{K_m}$) does increase the efficiency, the effect is not large. There is no advantage in reducing $\frac{Dam_f}{K_m}$ below 0.02 because the effectiveness is poor due to the diffusion limitation in the fluid region.

The general correlated results may be useful for the design of such reactor with porous walls. From the plots, the concentration in the porous medium could be predicted for a given reactor geometry. The critical length to avoid concentration

insufficiency could also be determined. The flow and geometry conditions could be designed to achieve high reactor efficiency.

8.2 Recommendations

Future study can extend current numerical method to three-dimensional and more practical cases with more complex geometries. Attention should be paid to those with singularity domains which may give difficulties in getting stable, consistent and convergent solutions. Unstructured grid and multi-block technology with different size grids may also be used for complex geometries. To avoid the instability and un-convergency problems due to the abrupt fluid property changes along the interface, self-adaptive grid could also be used.

For unsteady flow, mass transfer can be considered from the porous cylinders to the environment around with vortex shedding (Bhattacharyya et al, 2006b). An extension of the mass jump interfacial conditions and their effects on flow and mass transfer can also be conducted theoretically or numerically (Valdes-Parada et al, 2007b). From the practical point of view, the flow past an array of porous square cylinders can also be conducted.

For heat and mass convection problems, mixed convection problems (with both external convection and gravity effects) can be considered in a cavity filled with porous or porous/fluid media. The stress jump conditions may have different effects on heat and mass transfer in such mixed convection problems. To enhance heat transfer, turbulent heat transfer models can be added in current work together with the

existence of porous media (Assato et al., 2005). With the existence of turbulence, the stress jump parameters may affect the flow and heat transfer more significantly.

For mass transfer in microchannel reactors with a porous wall, other types of reaction for mass consumption models can be attempted, for example the inhibitory kinetics (Pathi et al., 2005). The reaction efficiency and reactor effectiveness factor can be defined based on local concentration to more accurately measure the reactor performance. More realistically, the reaction kinetics can also be assumed to be with time-dependent consumption rate and variable porosity and permeability in porous region (for example, due to the change of cell density). Additionally, local non-averaged mass transfer model can also be assumed to model the solid and fluid phases in porous region, respectively.

For interface coupled conditions, experiments on stress jump parameter values can be addressed with different porous materials. Likewise theoretical derivation of the interface treatment for heat or mass transfer can be continued and their effects on transport phenomena may also be implemented for numerical simulations. Different porous material with different interfacial porous structures can be combined to test their effects on natural, forced and mixed convective heat transfer, and mass transfer problems.

References

Abu-Hijleh, B., Convection heat transfer from a laminar flow over a 2-D backward facing step with asymmetric and orthotropic porous floor segments, Numerical Heat Transfer A, 31, pp. 25-335, 1997.

Abu-Hijleh, B., Heat transfer from a 2D backward facing step with isotropic porous floor segments, International Journal of Heat and Mass Transfer, 43, pp. 2727-2737, 2000.

Alazmi, B. and Vafai, K., Analysis of fluid flow and heat transfer interfacial conditions between a porous medium and a fluid layer, International Journal of Heat and Mass Transfer, 44, pp. 1735-1749, 2001.

Al-Muftah., A. E. and Abu-Reesh, I. M., Effects of simultaneous internal and external mass transfer and product inhibition on immobilized enzyme-catalyzed reactor, Biochemical Engineering Journal, 27 (2), pp. 167-178, 2005.

Assato, M., Pedras, M. H. J. and Delemos, M. J. S., Numerical solution of turbulent channel flow past a backward-facing-step with a porous insert using linear and non-linear k-ε models, Journal of Porous Media, 8, pp. 13-29, 2005.

Bancroft, G. N., Sikavitsas, V. I. and Mikos A. G., Design of a flow perfusion bioreactor system for bone tissue-engineering applications, Tissue Engineering, 9 (3), pp. 549-554, 2003.

Basu, A. J., and Khalili, A., Computation of flow through a fluid-sediment interface in a benthic chamber, Physics of Fluids, 11, pp. 1395-1405, 1999.

Beavers, G. S., and Joseph, D. D., Boundary condition at a naturally permeable wall, Journal of Fluid Mechanics, 30, pp. 197-207, 1967.

Bennacer, R., Beji, H. and Mohamad, A. A., Double diffusive convection in a vertical enclosure inserted with two saturated porous layers confining a fluid layer. International Journal of Thermal Sciences, 42, pp. 141-151, 2003.

Bera, P., Eswaran, V. and Singh, P., Numerical study of heat and mass transfer in an anisotropic porous enclosure due to constant heating and cooling, Numerical Heat Transfer A, 34, pp. 887-905, 1998.

Betchen, L., Straatman, A. G. and Thompson, B. E., A nonequilibrium finite-volume model for conjugate fluid/porous/solid domains, Numerical Heat Transfer A, 49, pp. 543-565, 2006.

Bhatia, S., Long, W. S. and Kamaruddin, A. H., Enzymatic membrane reactor for the kinetic resolution of racemic ibuprofen ester: modeling and experimental studies Chemical Engineering Science, 59 (22-23), pp. 5061-5068, 2004

Bhattacharya, A. and Mahajan, R. L., Finned metal foam heat sinks for electronics cooling in forced convection, Journal of Electronic Packaging, 124, pp. 155-163, 2002.

Bhattacharyya, S., Dhinakaran, S. and Khalili, A., Fluid motion around and through a porous cylinder, Chemical Engineering Science, 61, pp. 4451-4461, 2006a.

Bhattacharyya, S., Maiti, D. K. and Dhinakaran, S., Influence of buoyancy on vortex shedding and heat transfer from a square cylinder in proximity to a wall, Numerical Heat Transfer A, 50, pp. 585-606, 2006b.

Boschetti, F., Raimondi, M. T., Migliavacca, F. and Dubini, G., Prediction of the micro-fluid dynamic environment imposed to three-dimensional engineered cell systems in bioreactors, Journal of Biomechanics, 39, pp. 418-425, 2006.

Braza, M., Chassaing, P. and Minh, H. Ha., Numerical study and physical analysis of the pressure and velocity fields in the near wake of a circular cylinder, Journal of Fluid Mechanics, 165, pp. 79-130, 1986.

Brinkman, H. C., A calculation of the viscous force exerted by a flowing fluid on a dense swarm of particles, Applied Scientific Research, A1, pp. 27-34, 1947a.

Brinkman, H. C., On the permeability of media consisting of closely packed porous particles, Applied Scientific Research, A1, pp. 81-86, 1947b.

Calhoun, D., A Cartesian grid method for solving the two-dimensional streamfunction-vorticity equations in irregular regions, Journal of Computational Physics, 176, pp. 231-275, 2002.

Chandesris, M. and Jamet, D., Boundary conditions at a planar fluid-porous interface for a Poiseuille flow, International Journal of Heat and Mass Transfer, 49, pp. 2137-2150, 2006.

Chandesris, M. and Jamet, D., Boundary conditions at a fluid-porous interface: An a priori estimation of the stress jump coefficients, International Journal of Heat and Mass Transfer, 50, pp. 3422-3436, 2007.

Chen, X. B., Yu, P., Winoto, S. H. and Low, H. T., Free convection in a porous wavy cavity based on the Darcy-Brinkman-Forchheimer extended model, Numerical Heat Transfer A, 52, pp. 377-397, 2007.

Chen, X. B., Yu, P., Winoto, S. H. and Low, H. T., A numerical method for forced convection in porous and homogeneous fluid domains coupled at interface by stress jump, International Journal for Numerical Methods in Fluids, 56, pp. 1705-1729, 2008a.

Chen, X. B., Yu, P., Winoto, S. H. and Low, H. T., Forced convection over a backward facing step with a porous floor segment, Numerical Heat Transfer A, 53, pp. 1211-1230, 2008b.

Chen, X. B., Yu, P., Winoto, S. H. and Low, H. T., Numerical analysis for the flow past a porous square cylinder based on the stress-jump interfacial-conditions, International Journal of Numerical Methods for Heat and Fluid Flow, 18 (5), pp. 635-655, 2008c.

Chen, X. B., Yu, P., Winoto, S. H. and Low, H. T., Numerical analysis for the flow past a porous trapezoidal-cylinder based on the stress-jump interfacial-conditions, International Journal of Numerical Methods for Heat and Fluid Flow, 19 (2), pp. 223-241, 2009.

Chen, X. B., Yu, P., Winoto, S. H. and Low, H. T., Mass transport in a microchannel reactor with a porous wall, ASME Journal of Biomechanical Engineering, submitted for publication.

Cheng, M. and Liu, G. R., Effects of afterbody shape on flow around prismatic cylinders, Journal of Wind Engineering and Industrial Aerodynamics, 84, pp. 181-196, 2000.

Chow, D. C., Wenning, L. A., Miller, W. M. and Papoutsakis, E. T., Modeling pO2 distributions in the bone marrow hematopoietic compartment. I. Krogh's Model, Biophysical Journal, 81, pp. 675-684, 2001a.

Chow, D. C., Wenning, L. A., Miller, W. M. and Papoutsakis, E. T., Modeling pO2 distributions in the bone marrow hematopoietic compartment. II. Modified Krogh's Models, Biophysical Journal, 81, pp. 685-696, 2001b.

Chung, C. A., Chen, C. W., Chen, C. P. and Tseng, C. S., Enhancement of cell growth in tissue-engineering constructs under direct perfusion: Modeling and simulation, Biotechnology and Bioengineering, 97 (6), pp. 1603-1616, 2007.

Chung, Y. J. and Kang, S.-H., Laminar vortex shedding from a trapezoidal cylinder with different height ratios, Physics of Fluids, 12 (5), pp. 1251-1254, 2000.

Cohen, R. D., Predicting the effects of surface suction and blowing on the Strouhal frequencies in vortex shedding, JSME International Journal (Series II), 34, pp. 30-39, 1991.

Cooper, J. A., Lu, H. H. and Ko, F. K., Freeman, J. W., Laurencin, C. T., Fiber-based tissue-engineered scaffold for ligament replacement: design considerations and in vitro evaluation, Biomaterials, 26, pp. 1523-1532, 2005.

Costa, V. A. F., Oliveira, L. A., Baliga, B. R. and Sousa, A. C. M., Simulation of coupled flows in adjacent porous and open domains using a control-volume finite-element method, Numerical Heat Transfer A, 45, pp. 675-697, 2004.

de Vahl Davis, G., Natural convection of air in a square cavity: a bench mark numercal solution, International Journal for Numerical Methods in Fluids, 3, 249-264, 1983.

Davis, R. W. and Moore, E. F., A numerical study of vortex shedding from rectangles. Journal of Fluid Mechanics, 116, pp. 475-506, 1982.

Davis, R.W., Moore, E.F., Purtell, L. P., A numerical-experimental study of confined flow around rectangular cylinders, Physics of Fluids, 27 (1), pp. 46-59, 1984.

Dennis, S.C.R. and Chang, G., Numerical solutions for steady flow past a circular cylinder at Reynolds number up to 100, Journal of Fluid Mechanics, 42 (3), pp. 471-489, 1970.

Drott, J., Lindstrom, K., Rosengren, L. and Laurell, T., Porous silicon as the carrier matrix in microstructured enzyme reactors yielding high enzyme activities, Journal of Micromechanics and Microengineering, 7 (1), pp. 14-23, 1997.

Drott, J., Rosengren, L., Lindstrom, K. and Laurell, T., Porous silicon carrier matrices in micro enzyme reactors-influence of matrix depth, Mikrochimica Acta, 131, pp. 115-120, 1999.

Dusting, J., Sheridan, J. and Hourigan, K., A fluid dynamic approach to bioreactor design for cell and tissue culture, Biotechnology and Bioengineering, 94, pp. 1197 – 1208, 2006.

Ettefagh, J., Vafai, K., and Kim, S. J., Non-Darcian effects in open-ended cavities filled with a porous medium, ASME Journal of Heat Transfer, 113, pp. 747-756, 1991.

Ferziger, J. H. and Perić, M., Computational methods for fluid dynamics, 2nd ed., pp. 222-233, Springer, Berlin, 1999.

Forchheimer, P., Wasserbewegung durch Boden, Zeits. Ver. Deutsch. Ing., 45, pp. 1782-1788, 1901.

Franke, R., Rodi, W. and Schönung, B., Numerical calculation of laminar vortex shedding past cylinders, Journal of Wind Engineering and Industrial Aerodynamics, 35, pp. 237-257, 1990.

Fu, W.-S., Huang, H..-C. and Liou, W.-Y., Thermal enhancement in laminar channel flow with a porous block, International Journal of Heat and Mass Transfer, 39 (10), pp. 2165-2175, 1996.

Gartling, D. K., A test problem for outflow boundary conditions flow over a backward-facing step, International Journal for Numerical Methods in Fluids, 11, pp. 953-967, 1990.

Gartling, D. K., Hickox, C. E. and Givler, R. C., Simulation of coupled viscous and porous flow problems, International Journal of Computational Fluid Dynamics, 7, pp. 23-48, 1996.

Gemmiti, C. V. and Guldberg, R. E., Fluid flow ineases Type II collagen Deposition and Tensile Mechanical Properties in Bioreactor Grown Tissue Engineered Cartilage, Tissue Engineering, 12, pp. 469–479, 2006.

Ghia, U., Ghia, K. N. and Shim, C. T., High-Re solutions for incompressible flow using the Navier-Stokes equations and a multigrid method, Journal of Computational Physics, 48, pp. 387-411, 1982.

Gobin, D., Goyeau, B. and Neculae, A., Convective heat and solute transfer in partially porous cavities, International Journal of Heat and Mass Transfer, 48, pp. 1898-1908, 2005.

Goyeau, B., Lhuillier, D., Gobin, D. and Velarde, M. G., Momentum transport at a fluid-porous interface, International Journal of Heat and Mass Transfer, 46, pp. 4071-4081, 2003.

Greenkorn, R. A., Steady flow through porous media, AICHE Journal, 27, pp. 529-545, 1981.

Griffith, L. G. and Swartz, M. A., Capturing complex 3D tissue physiology in vitro, Nature Reviews Molecular Cell Biology, 7, pp. 211-224, 2006.

Haddad, O. M., Al-Nimr, M. A. and Al-Omary, J. Sh., Forced convection of gaseous slip flow in porous micro-channels under local-thermal non-equilibrium conditions, Transport in Porous Media, 67, pp. 453-471, 2007.

Holzbecher, E., Free Convection in open-top enclosures filled with a porous medium heated from below, Numerical Heat Transfer A, 46, pp. 241-254, 2004.

Horta, A., Alvarez, J. R. and Luque, S., Analysis of the transient response of a CSTR containing immobilized enzyme particles - Part I. Model development and analysis of the influence of operating conditions and process parameters Biochemical Engineering Journal, 33 (1), pp. 72-87, 2007.

Hsiao, S.W. and Chen, C.K., Natural convection heat transfer from a corrugated plate embedded in an enclosed porous medium, Numerical Heat Transfer A, 25, pp. 331-345, 1994.

Hsu, C. T. and Cheng, P., Thermal dispersion in a porous medium, International Journal of Heat and Mass Transfer, 33, pp. 1587-1597, 1990.

Huang, P. C. and Vafai, K., Analysis of forced convection enhancement in a channel using porous blocks, Journal of Thermophysics and Heat Transfer, 8 (3), pp. 563-573, 1994a.

Huang, P. C. and Vafai, K., Internal heat transfer augmentation in a channel using an alternate set of porous cavity-block obstacles, Numerical Heat Transfer A, 25, pp. 519-539, 1994b.

Jang, J. Y. and Chen, J. L., Forced convection in a parallel plate channel partially filled with a high porosity medium, International Communication of Heat and Mass Transfer, 19, pp. 263-273, 1992.

Jue, T. C., Numerical analysis of vortex shedding behind a porous cylinder, International Journal of Numerical Methods for Heat and Fluid Flow, 14, pp. 649-663, 2003.

Karimi-Fard, M., Charrier-Mojtabi, M. C., and Vafai, K., Non-Darcian effects on double diffusive convection within a porous medium, Numerical Heat Transfer, A, 31, pp. 837-852, 1997.

Khashan, S. A., Al-Amiri, A. M. and Pop, I., Numerical simulation of natural convection heat transfer in a porous cavity heated from below using a non-Darcian and thermal non-equilibrium model, International Journal of Heat and Mass Transfer, 49, pp. 1039-1049, 2006.

Kim, S. J. and Choi, C. Y., Convective heat transfer in porous and overlying layers heated from below, International Journal of Heat and Mass Transfer, 39, pp. 319-329, 1996.

Kiwan, S., and AI-Nimr, M. A., Using porous fins for heat transfer enhancement, ASME Journal of Heat Transfer, 123, pp. 790-795, 2001.

Klekar, K. M., Patankar, S. V., Numerical predication of vortex shedding behind square cylinders, International Journal for Numerical Methods in Fluids, 14, pp. 327-341, 1992.

Kondoh, T., Nagano, Y. and Tsuji, T., Computational study of laminar heat transfer downstream of a backward-facing step, International Journal of Heat and Mass Transfer, 36 (33), pp. 577-591, 1993.

Kuznetsov, A. V., Fluid mechanics and heat transfer in the interface region between a porous medium and a fluid layer: a Boundary Layer Solution, Journal of Porous Media, 2 (3), pp. 309-321, 1999.

Lapwood, E. R., Convection of a fluid in a porous medium, Proceedings of Cambridge Philosophical Society, 44, pp. 208-521, 1948.

Lauriat, G. and Prasad, V., Non-Darcian effects on natural convection in a vertical porous enclosure, International Journal of Heat and Mass Transfer, 32 (11), pp. 2135-2148, 1989.

Lee T. S., Early stages of an impulsively started unsteady laminar flow past tapered trapezoidal cylinders, International Journal for Numerical Methods in Fluids, 26, pp. 1181-1203, 1998a.

Lee, T. S., Numerical study of early stages of an impulsively started unsteady laminar flow past expanded trapezoidal cylinders, International Journal of Numerical Methods for Heat and Fluid Flow, 8, pp. 934-955, 1998b.

Lilek, Ž., Muzaferija, S., Perić, M. and Seidl, V., An implicit finite-volume method using nonmatching blocks of structured grid, Numerical Heat Transfer B, 32, pp. 385-401, 1997.

Ling, L. M., Ramaswamy, B., Cohen, D. R. and Jue, T. C., Numerical analysis on Strouhal frequencies in vortex shedding over square cylinders with surface suction and blowing, International Journal of Numerical Methods for Heat and Fluid Flow, 3, pp. 458-67, 1993.

Liu, C., Sheng, X., and Sung, C. H., Preconditioned multigrid methods for unsteady incompressible flows, Journal of Computational Physics, 139, pp. 35-57, 1998.

Lysenko, V., Vitiello, J., Remaki, B. and Barbier, D., Gas permeability of porous silicon nanostructures, Physical Review E, 70 (1), 017301, Part 2, 2004.

Ma, T., Yang, S. T. and Kniss, D. A., Development of an in vitro human placenta model by the cultivation of human trophoblasts in a fiber-based bioreactor system, Tissue Engineering, 5 (2), pp. 91-102, 1999.

Mahmoudifar, N. and Doran, P. M., Tissue Engineering of human cartilage in bioreactors using single and composite cell-seeded scaffolds, Biotechnology and Bioengineering, 91 (3), pp. 338-55, 2005

Mahmud, S. and Fraser, R. D., Free convection and entropy generation inside a vertical inphase wavy cavity, International Communication of Heat and Mass

Transfer, 31, pp. 455-466, 2004.

Martin, A.R., Satiel, C. and Shyy, W., Heat transfer enhancement with porous inserts in recirculating flow, ASME Journal of Heat Transfer, 120, pp. 458-467, 1998.

McClelland, R. E., MacDonald, J. M. and Coger, R. N., Modeling O_2 transport within engineered hepatic devices, Biotechnology and Bioengineering 82 (1), pp. 12-27 MAR 30, 2003.

Melander, C., Tüting, W., Bengtsson, M., Laurell, T., Mischnick, P. and Gorton, L., Hydrolysis of maltoheptaose in flow through silicon wafer microreactors containing immobilised α -Amylase and glycoamylase, Starch-Stärke, 58, pp. 231-242, 2006.

Michael, L. S. and Fikret, K., Bioprocess engineering: Basic concepts, Prentice-Hall, Englewood Cliffs, NJ, 1992.

Min, J. Y. and Kim, S. K., A novel methodology for thermal analysis of a composite system consisting of a porous medium and an adjacent fluid layer, ASME Journal of Heat Transfer, 127, pp. 648-656, 2005.

Misirlioglu, A. Aydin, Baytas, C. and Pop, I., Free convection in a wavy cavity filled with a porous medium, International Journal of Heat and Mass Transfer, 48, pp.1840-1850, 2005.

Murthy, P. V. S. N., Rathish, Kumar B. V. and Singh, P., Natural convection heat transfer from a horizontal wavy surface in a porous enclosure, Numerical Heat Transfer A, 31, pp.207-221, 1997.

Muzaferija, S., Adapative Finite volume method for flow predictions using unstructured meshes and multigrid approach, PhD Thesis, University of London, 1994.

Neale, G. and Nader, W., Practical significance of brinkman's extension of Darcy's law: coupled parallel flows within a channel and a bounding porous medium, Canadian Journal of Chemical Engineering., 52, pp. 475-478, 1974.

Nield, D. A., Junqueira, S. L. M. and Lage, J. L., Forced convection in a fluid-saturated porous-medium channel with isothermal or isoflux Boundaries, Journal of Fluid Mechanics, 322, pp. 201-214, 1996.

Nithiarasu, P., Seetharamu, K. N. and Sundararajan, T., Double-diffusive natural convection in an enclosure filled with fluid-saturated porous medium: A generalized non-Darcy approach, Numerical Heat Transfer A, 30, pp. 413-426, 1996.

Nithiarasu, P., Seetharamu, K. N. and Sundararajan, T., Natural convective heat transfer in a fluid saturated variable porosity medium, International Journal of Heat and Mass Transfer, 40(16), pp. 3955-3967, 1997.

Nithiarasu, P., Seetharamu, K. N. and Sundararajan, T., Finite element modelling of flow, heat and mass transfer in fluid saturated porous media, Archives of Computational Methods in Engineering, 9, pp. 3-42, 2002.

Ochoa-Tapia, J. A. and Whitaker, S., Momentum transfer at the boundary between a porous medium and a homogeneous fluid I: Theoretical development, International Journal of Heat and Mass Transfer, 38, pp. 2635-2646, 1995a.

Ochoa-Tapia, J. A. and Whitaker, S., Momentum transfer at the boundary between a porous medium and a homogeneous fluid II: Comparison with experiment, International Journal of Heat and Mass Transfer, 38, pp. 2647-2655, 1995b.

Ochoa-Tapia, J. A. and Whitaker, S., Heat transfer at the boundary between a porous medium and a homogeneous fluid, International Journal of Heat and Mass Transfer, 40, pp. 2691-2707, 1997.

Ochoa-Tapia, J. A. and Whitaker, S., Heat transfer at the boundary between a porous medium and a homogeneous fluid: the One-equation model, Journal of Porous Media, 1, pp. 31-46, 1998a.

Ochoa-Tapia, J. A. and Whitaker, S., Momentum jump condition at the boundary between a porous medium and a homogeneous fluid: Inertial effect, Journal of Porous Media, 1, pp. 201-217,1998b.

Pathi, P., Ma, T. and Locke, B. R., Role of nutrient supply on cell growth in bioreactor design for tissue engineering of hematopoietic cells, Biotechnology and Bioengineering, 89 (7), pp. 743-758, 2005.

Pierre, J., Gemmiti, C. V., Kolambkar, Y. M., Oddou, C. and Guldberg, R. E., Theoretical analysis of engineered cartilage oxygenation: influence of construct thickness and media flow rate, Biomechanics and Modeling in Mechanobiology, 7 (6), pp. 497-510, 2008.

Porter, B., Zauel, R., Stockman, H, Guldberg, R. and Fyhrie, D., 3-D computational modeling of media flow through scaffolds in a perfusion bioreactor, Journal of Biomechamics, 38 (3), pp. 543-549, 2005.

Ratish, Kumar B. V., Singh, P., and Murthy, P. V. S. N., Effects of surface undulations on natural convection in a porous square cavity, ASME Journal of Heat Transfer, 119, pp. 848-851, 1997.

Ratish, Kumar B. V., Murthy, P. V. S.,N., and Singh, P., Free convection heat transfer from an isothermal wavy surface in a porous enclosure, International Journal for Numerical Methods in Fluids, 28, pp. 633-661, 1998.

Rathish, Kumar B. V. and Shalini, Free convection in a non-Darcian wavy porous enclosure, International Journal of Engineering Science, 41, pp. 1827-1848, 2003.

Rhie, C. M. and Chow, W. L., Numerical study of the turbulent flow past an airfoil with trailing edge separation, AAIA Journal, 21, pp. 1525-1532, 1983.

Rudrauah, N. and Balachandra, R. S., Study of nonlinear convection in a sparsely packed porous medium using spectral analysis, Applied Scientific Research, 40, pp. 223-245, 1983

Russel, D. and Wang, Z. J., A cartesian grid method for modeling multiple moving objects in 2D incompressible viscous flow, Journal of Computational Physics, 191, pp. 177-205, 2003.

Sahraoui, M. and Kaviany, M., Slip and no-slip temperature boundary conditions at the interface of porous, Plain Media: Convection, International Journal of Heat and Mass Transfer, 37, pp. 1029-1044, 1994.

Sharma, A. and Eswaran, V., Heat and fluid flow across a square cylinder in the two-dimensional laminar flow regime, Numerical Heat Transfer A, 45, pp. 247-269, 2004.

Silva, R. A. and de Lemos, M. J. S., Numerical analysis of the stress jump interface condition for laminar flow over a porous layer, Numerical Heat Transfer A, 43, pp. 603-617, 2003.

Suzuki, H., Inoue, Y., Nishimura, T., Fukutani, F. and Suzuki, K., Unsteady flow in a channel obstructed by a square rod (crisscross motion of vortex), International Journal of Heat and Fluid Flow, 14 (1), pp. 2-9, 1993.

Tmej, F., Limbergova, Z. and Hasal, P., Modelling and optimisation of enzymatic separating micro-reactor, Bioprocess and Biosystems Engineering, 28 (2), pp. 123-130, 2005.

Vafai, K., Handbook of porous media. Marcel Dekker, New York, pp. 201-441, 2000.

Vafai, K. and Kim, S. J., Fluid mechanics of the interface region between a porous medium and a fluid layer – an exact solution, International Journal of Heat and Fluid Flow, 11, pp. 254-256, 1990.

Vafai, K. and Thiyagaraja, R., Analysis of flow and heat transfer at the interface region of a porous medium, International Journal of Heat and Mass Transfer, 30, pp. 1391-1405, 1987.

Vafai, K. and Tien, C. L., Boundary and inertia effects on flow and heat transfer in porous media, International Journal of Heat and Mass Transfer, 24, pp. 195-203, 1981.

Valencia-Lopez, J. J. and Ochoa-Tapia, J. A., A study of buoyancy-driven flow in a confined fluid overlying a porous layer, International Journal of Heat and Mass Transfer, 44, pp. 4725-4736, 2001.

Valdes-Parada, F. J., Goyeau, B. and Ochoa-Tapia, J. A., Diffusive mass transfer between a microporous medium and an homogeneous fluid: Jump boundary conditions, Chemical Engineering Science, 61, pp. 1692-1704, 2006.

Valdes-Parada, F. J., Goyeau, B. and Ochoa-Tapia, J. A., Jump momentum boundary condition at a fluid-porous dividing surface: Derivation of the closure problem, Chemical Engineering Science, 62, pp. 4025-4039, 2007a.

Valdes-Parada, F. J., Ochoa-Tapia, J. A. and Alvarez-Ramirez, J., Diffusive mass transport in the fluid-porous medium inter-region: Closure problem solution for the one-domain approach, Chemical Engineering Science, 62, pp. 6054-6068, 2007b.

Valencia-Lopez, J. J., Espinosa-Paredes, G. and Ochoa-Tapia, J. A., Mass transfer jump condition at the boundary between a porous medium and a homogeneous fluid, Journal of Porous Media, 6 (1), 33-49, 2003.

van Doormal, J. P. and Raithby, G. D., Enhancements of the SIMPLE method for predicting incompressible fluid flows, Numerical Heat Transfer, 7, pp. 147-163, 1984.

Vasseur, P., Wang, C. H. and Sen, M., Brinkman model for natural convection in a shallow porous cavity with uniform heat flux, Numerical Heat Transfer A, 15, pp. 221-242, 1989.

Wang, S. and Tarbell, J. M., Effect of fluid flow on smooth muscle cells in a 3-dimensional collagen gel model, Arteriosclerosis, Thrombosis, and Vascular Boilogy, 20, pp. 2220-2225, 2000.

Williamson, C. H. K., Vortex dynamics in the cylinder wake, Annual Review of Fluid Mechanics, 28, pp. 477-539, 1996.

Ye, H., Das, D. B., Triffitt, J. T. and Cui, Z. F., Modelling nutrient transport in hollow fibre membrane bioreactors for growing three-dimensional bone tissue, Journal of Membrane Science, 272, pp. 169-178, 2006.

Ye, T., Mittal, Udaykumar H. S. and Shyy, W., An accurate Cartesian grid method for viscous incompressible flows with complex immersed boundary, Journal of Computational Physics, 156, pp. 209-240, 1999.

Yin, C. S., Dynamics of nonhomogeneous fluids, Macmillan, New York, 1965.

Yu, P., Lee, T. S., Zeng, Y. and Low, H. T., A numerical method for flows in porous and homogenous fluid domains coupled at the interface by stress jump, International Journal for Numerical Methods in Fluids, 53, pp. 1755-1775, 2007.

Zdravkovich, M. M., Flow around circular cylinders, vol. 1: Fundamentals, Oxford University Press, New York, 1997.

Zeng, Y., Lee, T. S., Yu, P. and Low, H. T., Mass transport and shear stress in a microchannel bioreactor: Numerical simulation and dynamic similarity, ASME Journal of Biomechanical Engineering, 128, pp. 185–193, 2006.

Zeng, Y., Lee, T. S., Yu, P. and Low, H. T., Numerical simulation on mass transport in a microchannel bioreactor for co-culture applications, ASME Journal of Biomechanical Engineering, 129, pp. 365–373, 2007.

Zeng, Y., Lee, T. S., Yu, P. and Low, H. T., Numerical simulation of mass transport in a microchannel bioreactor with cell micropatterning, ASME Journal of Biomechanical Engineering, 130, pp. 1883–1900, 2008.

Zhang, Baili and Zhao, Yong, A Numerical method for simulation of forced convection in a composite porous/fluid system, International Journal of Heat and Fluid Flow, 21, pp. 432-441, 2000.

Zhao, F., Chella, R. and Ma, T., Effects of shear stress on 3-D human mesenchymal stem cell construct development in a perfusion bioreactor system: Experiments and hydrodynamic modeling, Biotechnology and Bioengineering, 96 (3), 584-595, 2007.

Zhao, F. and Ma, T., Perfusion bioreactor system for human mesenchymal stem cell tissue engineering: Dynamic cell seeding and construct development, Biotechnology and Bioengineering, 91 (4), pp. 482-493, 2005.

Zhao, F., Pathi, P., Grayson, W., Xing Q., Locke, B. R. and Ma, T., Effects of oxygen transport on 3-D human mesenchymal stem cell metabolic activity in perfusion and static cultures: Experiments and mathematical model, Biotechnology Progress, 21 (4), pp.1269-1280, 2005.